

Ab-initio Electronic Structure Method for Substitutional Disorder Applied to Iron-Based Superconductors

Zur Erlangung des akademischen Grades eines
DOKTORS DER NATURWISSENSCHAFTEN
von der Fakultät für Physik am
Karlsruher Institut für Technologie (KIT)
genehmigte

DISSERTATION

von

Dipl.-Phys. Alexander Herbig
aus Heppenheim

Tag der mündlichen Prüfung: 12. Februar 2016

Referent: Prof. Dr. Hilbert von Löhneysen
Korreferent: Prof. Dr. Jörg Schmalian

1. Introduction

In a perfect world, crystalline solids are perfectly periodic. However, in reality this idealized model of perfect periodicity even under laboratory conditions can only be approached but never reached. There always remains a certain amount of lattice imperfections, grain boundaries and impurity atoms one has to deal with. Due to their random occurrence, such defects give rise to a certain level of disorder which in particular influences the dynamics of the crystal electrons which scatter on impurities. This, apart from thermal effects, for example gives rise to electrical resistivity or, speaking in a more microscopic language to finite lifetimes of the electronic quasiparticle states. Sometimes, such disorder effects are even desired because they can be used to tune the electronic properties of a system. A very prominent example is the large field of semiconductor devices, where the introduction of impurities leads to charge carrier doping and thus spatially dependent electronic properties. Without this technology, the present work could not have been performed. Essentially, disorder gives rise to plenty of interesting phenomena in solid state physics. The success of solid state theory in describing, more interestingly also explaining and sometimes even predicting experiments is to a large extent founded on the translational symmetry of the mathematical problems to be solved. But exactly that translational symmetry is violated in the presence of disorder. Thus, a proper description of disorder phenomena in realistic calculations is a nontrivial task. Especially in the otherwise well established field of first principles calculations of the electronic structure, the incorporation of disorder phenomena still is a challenge.

A special type of disorder arises from chemical substitution, where a certain atomic species of the crystalline host material is randomly substituted by impurity atoms at a prescribed concentration. A widely used approach based on supercells only works for special impurity concentrations but for arbitrary concentrations suffers from a dramatic increase of the computational effort, as will become clear later. For the theoretical investigation of systems with arbitrary impurity concentrations, the so-called effective medium approaches are more promising. A main goal of this thesis is to develop an extension of the coherent potential approximation (CPA) [1–4], being a famous representative of such effective medium approaches, within a pseudopotential density functional theory (DFT) framework [5–10] for electronic bandstructures based on earlier work [11]. The CPA in the past has been successfully applied in particular within the Kohn-Korringa-Rostocker [12, 13] (KKR) DFT framework [14–19], but rarely has been implemented within other approaches. The pseudopotential method however is one of the most frequently used. The developed method will allow the *ab-initio* treatment of substitutional disorder in arbitrarily complex real materials.

Apart from the above mentioned prominent example of semiconductor technology, substitutional disorder also plays an important role in many material classes being subject of fundamental research. One of these material classes, which is a hot topic in recent and ongoing research, is represented by the various families of iron based superconductors first discovered in 2008 [20]. This discovery marks the starting point of a new era of high temperature superconductivity with transition temperatures up to 56 K [21]. Su-

perconductivity, which was first discovered by Heike Kammerlingh Onnes in 1911, on the one hand is characterized by an abruptly vanishing electrical resistivity below a critical temperature which makes it interesting for technological applications. In addition, in this state the magnetic field gets expelled from the bulk of the sample due to the Meissner effect [22]. This means that rising the temperature and increasing an external magnetic field can destroy superconductivity, where the latter is a reason why superconductivity was not expected to appear in compounds containing iron, being a magnetic element.

These compounds exhibit a rich phase diagram [23–27]. In most stoichiometric iron based compounds superconductivity is not present at normal conditions and only appears either under hydrostatic pressure or, being relevant for the present work, when substitutional disorder is present. In the temperature versus substitution phase diagram, the superconducting state competes with an antiferromagnetic orthorhombic phase at low temperatures and a paramagnetic tetragonal phase at high temperatures. The temperature of this structural / magnetic transition can be tuned by chemical substitution. Also the superconducting transition temperature depends on the impurity concentration and for the most compounds forms a dome in the phase diagram: at a certain finite impurity concentration, superconductivity sets in and the transition temperature increases with impurity concentration up to a maximum, usually called "optimally doped" and then again decreases with further rising impurity concentration until it gets totally suppressed. This clearly shows that substitutional disorder plays a key role for understanding the complex phase interplay in these materials. But despite intensive recent and ongoing research there is still no consensus about the detailed impact of chemical substitution on the superconducting state in these materials. Furthermore, it is even not clear if substitution really leads to charge carrier doping in these systems [28–32]. In the study of other materials, ab-initio electronic structure calculations could contribute to a fundamental understanding but in the case of substitutional disorder in the iron based systems, until now there is no coherent picture from such calculations.

The ab-initio method developed in the present work is ideally suited for the study of this material class. A systematic in-depth study of various substitutions in the BaFe_2As_2 system considering the impact of disorder on the electronic structure will be performed in this work. Hereby, the focus will be set on the influence of disorder on individual bands near the Fermi level, which are in particular three hole like bands next to the center of the first Brillouin zone and two electron like bands next to the zone edge. The disorder induced level shifts provide information about the aspect of charge doping. Furthermore, the lifetimes of these states become finite due to disorder. Comparing the inverse lifetimes, which can be extracted from spectral broadenings of the states next to the Fermi level, allows to compare the scattering strengths of the different impurity species. Impurity scattering is crucial for the suppression of superconductivity: in the popular s^{+-} pairing scenario [33–37], being the most important candidate for the iron based superconductors where the superconducting order parameter changes sign between different Fermi surface sheets, interband scattering on nonmagnetic impurities leads to breaking of Cooper pairs [38] and thus a suppression of superconductivity. To investigate the robustness of this s^{+-} pairing scenario and compare how effective the various substitutions are in suppressing superconductivity, a first principles study distinguishing intraband and interband scattering will be presented.

This thesis is structured as follows: In the first part of the thesis, an introduction into the field of the electronic structure of substitutionally disordered systems will be given

and the theoretical framework as well as its particular implementation will be outlined in detail in Chapter 2. Further technical aspects of the method development also concerning the structure and usage of the program package can be found in Appendices A - D. The theoretical approach itself will be validated for a simple toy model against a more exact approach in Chapter 3. In Chapter 4, the implemented *ab-initio* method will be tested for simple binary $\text{Cu}_{1-x}\text{Zn}_x$ alloys. In this chapter, also essential concepts of representing the numerical data (in particular the spectral functions) will be introduced.

In the second part of the thesis in Chapter 5, the developed method will be applied to BaFe_2As_2 focussing on disorder induced level shifts and spectral broadenings of the individual bands at the Fermi level comparing different substitutions. This chapter starts with an introduction into the essential facts obtained by others about this material class which are needed to understand the impact of the results obtained in the present work. In the end, a specialized method will be developed to analyze intraband versus interband scattering caused by a single impurity from first principles to study, together with the spectral broadenings, the influence of the various substitutions on superconductivity. Finally, a summary, concluding remarks and ideas about possible related future work will be presented in Chapter 6.

Contents

1. Introduction	3
2. Computational method	9
2.1. Density functional theory	9
2.1.1. Statement of the problem	9
2.1.2. The theorems of Hohenberg and Kohn	10
2.1.3. The mixed basis pseudopotential approach	11
2.2. Substitutional disorder	12
2.2.1. Early approaches	13
2.2.2. Coherent potential approximation	14
2.2.3. Incorporation of environmental disorder effects	18
2.2.4. Orbital-based <i>ab-initio</i> implementation using pseudopotentials	20
2.3. Charge self-consistency	26
3. Model studies	31
3.1. The model	31
3.2. Conventional coherent potential approximation	32
3.3. Extension for environmental disorder	35
4. $\text{Cu}_{1-x}\text{Zn}_x$ alloys as benchmark	37
4.1. Crystal structure and details of the calculation	37
4.2. Density of states	39
4.3. Bloch spectral function	41
4.4. Partial substitutions	43
5. Substitutionally disordered BaFe_2As_2	47
5.1. Iron based superconductors: brief introduction	47
5.1.1. Various families of iron based superconductors	48
5.1.2. General properties of BaFe_2As_2	48
5.1.3. Open questions and goals of this work	51
5.2. Technical details of the calculation	53
5.3. $3d$ transition metal substitution	58
5.3.1. Densities of states	58
5.3.2. Band renormalization	61
5.4. $4d$ and $5d$ transition metal substitution	68
5.5. K and P substitution	72
5.6. General trends of band renormalization	76
5.7. Impact of impurity scattering on superconductivity	78
5.7.1. Dirty superconductors: theory essentials	78
5.7.2. Intraband and interband scattering from first principles	80

5.7.3.	Intraband versus interband scattering comparing different substitu- tions	84
5.7.4.	Implications for pair breaking	87
6.	Summary and conclusions	91
A.	The full <i>ab-initio</i> program	95
A.1.	How to perform calculations	96
A.2.	Output Files	101
A.3.	How to modify the behavior of the code	104
A.4.	Data structure	105
B.	Matrix elements	107
B.1.	Basis set	107
B.1.1.	Localized orbitals in real space	107
B.1.2.	Localized orbitals in reciprocal space	108
B.1.3.	Useful properties of real spherical harmonics	108
B.1.4.	Translation of the orbitals	109
B.2.	Overlap matrix elements	109
B.2.1.	Onsite overlap	110
B.2.2.	Offsite terms	110
B.3.	Electronic density	111
B.4.	Hamiltonian matrix elements	113
B.4.1.	Potential contributions	113
B.4.2.	The local potential	114
B.4.3.	The nonlocal pseudopotential	115
B.4.4.	The Hartree potential	115
B.4.5.	Exchange and correlation	116
B.4.6.	The mixing-potential or averaged crystal potential	119
B.4.7.	Onsite Hamiltonian matrix elements	120
B.4.8.	Offsite Hamiltonian matrix elements	121
B.5.	Symmetrization	123
C.	The impurity solver	127
D.	Green's functions in a nonorthogonal basis	131
D.1.	Local basis and field operators	131
D.2.	Bloch basis and field operators	132
D.3.	Retarded Green's function	133
D.4.	Bloch spectral function	134
	List of Figures	137
	Bibliography	139
	Acronyms	149
	Danksagung	151

2. Computational method

2.1. Density functional theory

Density functional theory (DFT) [5, 6] can be seen as up to date's standard first principles approach to the calculation of the electronic structure of a system of many electrons and ions in general and crystalline solids in particular. It was very successful in the past in the theoretical treatment of real materials and nowadays a variety of different highly developed program packages exist which allow efficient calculations for complex systems at relatively cheap computational cost. In condensed matter physics DFT has a manifold of useful applications: It can help to analyze experimental data, especially in scattering experiments. It can provide an overview about possible effects in a recently discovered new material and even when it disagrees with experimental observations this can be helpful in explaining the origin of certain physical effects.

Some of these disagreements with experiments can be attributed to serious shortcomings of DFT which gave rise to the development of highly specialized methods to overcome these problems at least for certain limiting cases. The most prominent example is its insufficiency in a proper description of systems with strong electronic correlations where an enormous amount of work is still going to address this issue - for example by dynamical mean field theory [39–41] and related methods. Less known but of particular interest for this work is the problem of a DFT-based treatment of disordered systems.

Nevertheless, when dealing with real materials, almost all of those more specialized methods to treat a certain physical effect more accurately, including the one developed in this work, start from a DFT calculation. This together with its universal applicability is another reason for the great importance of DFT in condensed matter physics and makes it worthwhile to present a brief review in the following which is to a large extent based on my diploma thesis [42] and Meyer's PhD-thesis [10].

2.1.1. Statement of the problem

Usually, in the field of molecular and solid states physics, one is interested in the dynamics of many electrons interacting with themselves and the ions. The most general Hamiltonian describing such a system is

$$H = T_{el} + T_{ion} + V_{el-el} + V_{el-ion} + V_{ion-ion} \quad (2.1)$$

T_{el} (T_{ion}) being the kinetic energy of and V_{el-el} ($V_{ion-ion}$) the interaction potential between the electrons (ions). V_{el-ion} is the interaction between the electrons and ions. This general many body problem is of course not exactly solvable and further approximations are needed. One important approximation which is the basis of practically all electronic structure calculations in solids and valid as long as lattice dynamics is not considered, is the Born-Oppenheimer approximation [43]. Here it is assumed that the dynamics of the electrons will instantaneously follow the movements of the ions because of the huge mass

difference $M_{ion} \gg m_{el}$. This allows a decoupling of the dynamics of the electrons from that of the ions and the remaining problem is to independently solve two Schrödinger equations for the electrons and the ions

$$(T_{el} + V_{el-el} + V_{el-ion})|\psi\rangle = E_{el}(\{\mathbf{R}_I\})|\psi\rangle \quad (2.2)$$

$$(T_{ion} + V_{ion-ion} + E_{el}(\{\mathbf{R}_I\}))|\phi\rangle = E_{tot}|\phi\rangle \quad (2.3)$$

where the total energy of the electrons E_{el} (often referred to as the Born-Oppenheimer energy surface) parametrically depends on the positions of the ions \mathbf{R}_I . The electronic problem Eq. (2.2) thus got simplified but still remains a many body problem due to the many body nature of V_{el-el} .

2.1.2. The theorems of Hohenberg and Kohn

Instead of finding a wave-function based ansatz to this problem, DFT provides an alternative approach where the basic quantity is the electronic density $n(\mathbf{r})$. DFT is based on the theorems of Hohenberg and Kohn [5]:

1. From elementary quantum mechanics it is known that an external potential $v_{ext}(\mathbf{r})$ uniquely defines the ground state and thus the electronic density $v_{ext}(\mathbf{r}) \rightarrow H \rightarrow |\psi\rangle \rightarrow n(\mathbf{r})$. It can be proven that this can be reversed: knowledge of the electronic density defines the potential up to a constant $n(\mathbf{r}) \rightarrow v_{ext}(\mathbf{r})$. The total energy then is a functional of the electronic density

$$E_{el}[n(\mathbf{r})] = F[n(\mathbf{r})] + \int n(\mathbf{r})v_{ext}(\mathbf{r})d^3r \quad (2.4)$$

F being a universal functional of the electronic density independent of the external potential which in a solid describes the influence of the ions.

2. This energy functional is minimal for the density of the ground state and then assumes the value of the ground state energy.

These two theorems provide a variational principle to determine the ground state properties of the system. Instead of directly minimizing the energy functional, in most practical applications a different route originally due to Kohn and Sham [6] is chosen. Mapping the real system of interacting electrons to an auxiliary system of noninteracting electrons with the same density and minimization of the energy functional via a Lagrange ansatz leads to the following set of (Euler-Lagrange) equations:

$$\left(-\frac{\hbar^2}{2m}\Delta + v_{eff}(\mathbf{r})\right)\varphi_i(\mathbf{r}) = \epsilon_i\varphi_i(\mathbf{r}) \quad (2.5)$$

$$n(\mathbf{r}) = \sum_{i=1}^N |\varphi_i(\mathbf{r})|^2 \quad (2.6)$$

$$v_{eff}(\mathbf{r}) = v_{ext}(\mathbf{r}) + v_H[n](\mathbf{r}) + v_{XC}[n](\mathbf{r}) \quad (2.7)$$

where φ_i are the Kohn-Sham orbitals and ϵ_i the associated energy eigenvalues. The ionic potential v_{ext} describes the influence of the crystal lattice in case of a solid and v_H is the

Hartree potential

$$v_H[n](\mathbf{r}) = e^2 \int \frac{n(\mathbf{r}')}{|\mathbf{r} - \mathbf{r}'|} d^3r' \quad (2.8)$$

describing density-density interaction. All many body effects beyond the Hartree term are absorbed into the exchange and correlation (XC) potential v_{XC} . This ansatz allows to reduce the solution of a complicated N -body problem to a more tractable effective one particle problem. This simplification is paid with the price of the Eqs. (2.5) - (2.7) being self-consistent because the single particle Schrödinger Eq. (2.5) for the orbitals φ_i is governed by a potential v_{eff} Eq. (2.7) which depends on the density via the Hartree and the XC contribution and this density again depends on the orbitals φ_i via Eq. (2.6). Such a system of self-consistent equations has to be solved iteratively usually starting from an initial guess for the potential or the density which is performed in the most DFT codes. The XC potential, which was needed for the decoupling of the many body problem into one particle problems, is crucial for the description of electronic correlations. There exists no general expression for this potential and one has to resort to approximations. Until now, no approximation has been found which leads to satisfactory results in the description of (strongly) correlated electron systems, which is the main reason for the initially mentioned shortcomings of DFT when applied to such systems. However, the most common approximation for v_{XC} , which also will be used in the present work, is the local density approximation (LDA) [6]: The XC energy of a homogeneous, *interacting* electron gas to high accuracy has been determined numerically by quantum monte carlo methods and several parametrizations of this energy exist (which parametrization is used in calculations in this work, will be mentioned later). In the LDA, the XC energy which in general is a functional of the density depending on several positions (inhomogeneous electron gas) is just replaced by that energy of a homogeneous electron gas. Thus, the XC energy then is only a functional of the density depending on one single position. Despite the fact, that this is a strong approximation for all kind of realistic systems, it turned out to perform astonishingly well for many realistic systems as far as electronic correlations are not too strong. This success of the LDA for sure is a main reason for the success of DFT in general.

2.1.3. The mixed basis pseudopotential approach

As stated above in Sec. 2.1.2, the most DFT implementations solve the same set of self-consistent equations but they differ in the details about how the solution is obtained. The first important difference lies in the treatment of the electron-ion interaction potential v_{ext} . Here essentially two different approaches have to be distinguished: the all-electron methods and the pseudopotential approach. In the all-electron methods one uses the bare nuclear potential for v_{ext} and the Kohn-Sham equations have to be solved for all electrons on the same footing. In contrast, in the pseudopotential approach [44], the electrons are divided into core- and valence electrons and v_{ext} then has the meaning of an effective potential of a nucleus screened by the core electrons. Thus, the set of self-consistent equations (2.5)-(2.7) only has to be solved for the valence electrons which in general reduces the computational effort.

The second difference arises from the choice of basis set for the representation of the Kohn-Sham orbitals φ_i . Many codes use plane waves which have the advantage of simple mathematical treatment but the problem of slow convergence for elements with strongly

localized electrons (for example the $3d$ transition metals). On the other hand, a couple of codes use atom centered functions which are better suited for localized electrons but are not ideal for quasi-free electrons and require a more sophisticated mathematical treatment. The DFT code referred to in this work is a so-called mixed-basis pseudopotential code using norm-conserving pseudopotentials constructed after Vanderbilt [7] together with a basis set comprising a linear combination of plane waves and a few localized atomic functions to benefit from the advantages of both basis schemes. This MBPP code was originally developed by Steven Louie and co-workers [8] in Berkeley in the 70's and redeveloped by Bernd Meyer and co-workers [9, 10] in Stuttgart in the 90's. This code, which is currently not available public, is still frequently used and maintained by several groups in Germany. In particular it serves as a starting point for several extensions as for example a program to perturbatively calculate phonons developed by Rolf Heid [45] and an implementation of dynamical mean-field theory for strongly correlated systems developed by the group of Frank Lechermann [46]. In this work I have developed a new extension to this code for the treatment of substitutionally disordered compounds from first principles.

2.2. Substitutional disorder

An idealized solid exhibits perfect periodicity which in particular allows theoretical calculations to be restricted to just one unit cell as long as bulk properties are considered. But in the real world no solid is perfectly periodic and randomly distributed impurities lead to disorder effects which manifest themselves in many different properties such as thermodynamics or transport. Sometimes such disorder effects are even desired and can be used to tune selected material properties. Often the phase diagrams of whole material classes are governed by disorder as for example in the cuprate [47] or iron pnictide [20] high temperature superconductors.

Among different types of disorder I will specifically focus on substitutional disorder in this work where the following situation is assumed: Given a perfectly periodic crystalline host or parent compound, a certain atomic species is substituted by another. Generally, in a complicated compound where only a part of the constituent atomic species is substituted and the rest is unaffected, the sublattices of these possibly substituted atomic types are assumed to be known. However, it is completely random at which geometrical site in the bulk crystal an actual substitution occurs. The only control parameter herein is the impurity concentration. This provides a realistic modelling of the experimental situation when chemical substitution is performed in a stoichiometric parent compound.

The most DFT implementations are suited for the treatment of a few tens up to a hundred of atoms at reasonable computational effort. In the last decades, method developments and technical advances in supercomputing have raised projects to treat several thousands of atoms within DFT but even this is far from sufficient to treat each of the $\approx 10^{23}$ atoms in a bulk solid individually. For this reason, in most cases the periodicity of the crystal lattice is used and the actual calculation is only performed for one unit cell when DFT is applied to bulk solids. On the one hand this allows to handle complex compounds with large unit cells but on the other hand makes it impossible to directly address the problem of disorder in bulk solids via DFT because the periodicity gets destroyed by disorder. This raises the necessity of more specialized approaches.

2.2.1. Early approaches

Before focusing on a special method dedicated to the treatment of substitutional disorder based on DFT, which was implemented in this work, it is instructive to first give a brief review about some exemplary earlier approaches. The most straight forward among them relies on supercells, essentially meaning an enlarged unit cell where a certain portion of the host lattice sites is occupied by the substituent species, corresponding to the actual impurity concentration. To really account for the randomness of the substitutions, it is of course necessary to average over several distinct configurations. As a consequence, it is for example not sufficient to simply use a supercell twice as large as the unit cell of the parent compound in case of 50% substitution, in order to obtain a good thermodynamic average. First of all, this shows that this method can only be practicable for special impurity concentrations like 50%, 25%, 12,5% and secondly even at such special impurity concentrations the size of the supercell and thus the computational effort grows with increasing quality of the thermodynamic average. The proper description of a system at arbitrary impurity concentration (e.g. 42%) would thus require a very large supercell which simply rules out the use of this method in general cases. Nevertheless one can already learn a lot from supercell calculations at those special impurity concentrations, which led to sophisticated computational schemes, for example in [48, 49] applied to iron-pnictides.

In fact, there exist material classes where experiments observe interesting effects at small impurity concentrations (e.g. in the iron pnictide superconductors sometimes less than 10%, in semiconductors even much less). The desire to investigate them by *ab-initio* methods requires to look for alternatives to supercells which can handle arbitrary impurity concentrations. This class of methods is usually summarized by the term of effective medium theories and the simplest among them is the virtual crystal approximation (VCA) [50]. Here the individual atomic potentials at the lattice sites, where substitutions are possible, simply get replaced by an average over the atomic potentials of the host and the impurity species, weighted by the respective atomic concentrations

$$\{V_A(\mathbf{R}_i), V_B(\mathbf{R}_i)\} \quad \rightarrow \quad V_{VCA}(\mathbf{R}_i) = c_i^A V_A(\mathbf{R}_i) + c_i^B V_B(\mathbf{R}_i) \quad (2.9)$$

where V_A is the atomic potential and c_i^A the atomic concentration of species A at site i . So the real physical medium of the crystal gets replaced by an effective medium containing artificial atoms at the substitutional sites. This method is relatively simple to implement and also provided successful results especially in the context of lattice dynamics and electron-phonon coupling [51, 52]. But on the other hand, in many cases it tends to lead to physically incorrect results [19, 53] - for example it fails in the split band limit of an alloy. This limit describes the separation of one band into two individual bands with increasing impurity concentration and can for example be observed via exact diagonalization of tight-binding models as well as in real $\text{Cu}_{1-x}\text{Zn}_x$ alloys as will become clearer in Chaps. 3 and 4. The reason of this failure lies in the simplicity of the VCA [53]: in a real disordered A_{1-x}B_x alloy the electronic density for sure is inhomogeneous due to the different potentials of A and B and the random distributions of these two species. Thus in general, the probability to find an electron next to an A atom is expected to be different from the probability to find it next to a B atom. This realistic behavior is neglected by averaging over the two atomic potentials as it is done in the VCA.

2.2.2. Coherent potential approximation

After having clarified the insufficiency of the VCA in the last section, it turns out to be worthwhile for the treatment of generic substitutionally disordered systems to further pursue the thought of the effective medium theories on a more rigorous mathematical basis. For the most more elaborate methods, the apparatus of Green's functions is a powerful tool. One usually starts (as for example suggested in [3, 19]) by formulating the problem of a substitutionally disordered system of noninteracting electrons in the tight-binding language by the following Hamiltonian

$$\hat{H} = \sum_{ij} W_{ij} c_i^\dagger c_j + \sum_i \epsilon_i c_i^\dagger c_i \quad (2.10)$$

where W_{ij} describes the hopping of an electron from site i to site j and ϵ_i is the electron's onsite energy. The operators c_i^\dagger (c_i) create (annihilate) an electron at site i and obey the fermionic commutation relations maintaining the Pauli principle and the antisymmetry of the wavefunction under particle exchange

$$\{c_i, c_j^\dagger\} \equiv c_i c_j^\dagger + c_j^\dagger c_i = \delta_{ij} \quad \{c_i, c_j\} = \{c_i^\dagger, c_j^\dagger\} = 0 \quad (2.11)$$

where $\{\cdot, \cdot\}$ denotes the anticommutator of two operators and δ_{ij} is a Kronecker-delta. The simplest way of including disorder effects into this model consists in assuming the disorder to be only connected with the onsite terms of the Hamiltonian Eq. (2.10). These onsite terms then can assume different values depending on the species which actually occupies a site in a random configuration. This means that for an electron the random atomic occupation of the site where it is currently located is decisive but the atomic occupations of the surrounding sites are unimportant, i.e. off-diagonal disorder or environmental effects are neglected. To approach this problem, it is useful to consider the onsite term ϵ_i as a perturbation which leads to the following Born's series or closed reformulation as a Dyson's equation [3, 19] for the Green's function in frequency domain of the disordered system

$$G_{ij}(\omega) = G_{ij}^0(\omega) + \sum_k G_{ik}^0 \epsilon_k G_{kj}^0 + \sum_{kl} G_{ik}^0 \epsilon_k G_{kl}^0 \epsilon_l G_{lj}^0 + \dots \quad (2.12)$$

$$= G_{ij}^0(\omega) + \sum_k G_{ik}^0(\omega) \epsilon_k G_{kj}(\omega) \quad (2.13)$$

$$G_{ij}^0(\omega) = [(\omega - W)^{-1}]_{ij} \quad (2.14)$$

where G_{ij}^0 , being the Green's function of the unperturbed Hamiltonian, is solely determined by the hopping terms and is assumed to be known. The physical observables in a disordered system are thermodynamic averages and therefore it is straight-forward to configurationally average the series Eq. (2.12) term by term

$$\langle G_{ij}(\omega) \rangle = G_{ij}^0(\omega) + \sum_k G_{ik}^0 \langle \epsilon_k \rangle G_{kj}^0 + \sum_{k,l} G_{ik}^0 \langle \epsilon_k G_{k,l}^0 \epsilon_l \rangle G_{lj}^0 + \dots \quad (2.15)$$

$$= G_{ij}^0(\omega) + \left(G^0(\omega) \Sigma(\omega) \langle G(\omega) \rangle \right)_{i,j} \quad (2.16)$$

In the last step Eq. (2.16), the averaged series was reconverted into the closed form of a Dyson's equation by *defining* a complex, frequency dependent self-energy $\Sigma(\omega)$ where

all repeated averaging processes are absorbed into. However, it is an absolutely non-trivial task to determine this self-energy and impossible without further approximations. Eq. (2.16) receives a considerable simplification if the self-energy is assumed to be a single-site quantity $\Sigma_{ij} = \Sigma_i \delta_{ij}$. At least from the original Hamiltonian, where the disorder was considered to be associated with an onsite quantity, such a similar approximation for the self-energy seems reasonable. Among several earlier approaches to solve such a problem [3, 19, 54–56], the coherent potential approximation (CPA) turned out to be the most sophisticated. This approximation first was simultaneously published in 1967 by Soven [1] for electronic dynamics and Taylor [2] for lattice dynamics. Before diving into the formal subtleties of this approximation, it is instructive to provide a brief pictorial sketch about its principle. In the CPA, the sites of the actual disordered crystal are replaced by an initially unknown effective medium associated with an effective medium Green's function $\Gamma(\omega)$ and a self-energy $\Sigma(\omega)$ which both depend on the (complex) frequency ω . Then, one site in the effective medium - which one does not matter due to the single site nature of the CPA - is replaced by a real impurity with a well defined onsite energy. This replacement is done with all possible species which are allowed to be substituted at the site and it is demanded that the average of these replacements is the same as the effective medium. This self-consistent CPA condition provides an iterative scheme to determine the initially unknown effective medium: the medium will be slightly changed until the condition is fulfilled. In Fig. 2.1 this scheme is depicted for the example of a binary A-B-alloy on a two dimensional lattice, based on a similar cartoon in [57]. This CPA condition can be math-

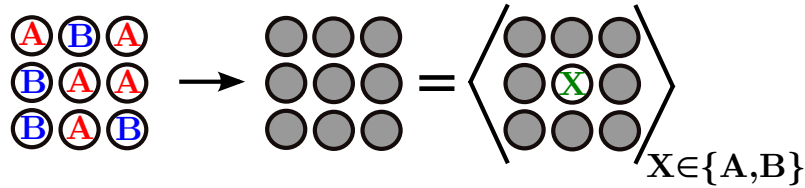


Figure 2.1.: The random A-B-alloy gets replaced by the CPA effective medium (shaded) which should be the same as the average over all insertions of real impurities into the effective medium

ematically formulated in different ways which for example is summarized in an extensive review by Elliott et al.[3].

As a preparation for the next section, it is useful to derive the self consistent equations in the locator framework following the work of Brouers [58] and Rowlands [19]. In particular, the equivalence to the traditional approaches has previously been shown by Leath [59] using diagrammatic techniques. As introduced by Matsubara [60], Eq. (2.12) can equivalently be expressed in terms of the so-called locator $g_i(\omega) = (\omega - \epsilon_i)^{-1}$ and the hopping matrix elements W_{ij} :

$$G_{ij}(\omega) = g_i(\omega)\delta_{ij} + \sum_{k \neq i} g_i(\omega)W_{ik}G_{kj}(\omega) \quad (2.17)$$

The locator $g(\omega)$ is nothing else than a Green's function of a localized state with energy ϵ_i . The locator equation of motion Eq. (2.17) is equivalent to the Dyson's equation Eq. (2.13) for the complementary approach of starting from localized atomic states and perturbatively including the interatomic hopping W . The diagonal elements of this equation can be

rewritten without the summation restriction by introducing the so-called interactor Δ [58]

$$G_{ii} = (g_i^{-1} - \Delta_i)^{-1} \quad (2.18)$$

$$\Delta_i = \sum_{j \neq i} W_{ij} g_j W_{ji} + \sum_{j \neq i} \sum_{k \neq i} W_{ij} g_j W_{jk} g_k W_{ki} + \dots \quad (2.19)$$

The only purpose of the interactor is to reformulate the locator equation of motion into a closed expression similar to what was done before by introducing the self-energy into the configurationally averaged Dyson's equation Eq. (2.16). This form of the locator equation of motion then is convenient for the introduction of the effective CPA-medium by the self-energy $\Sigma(\omega)$ and the effective medium Green's function $\Gamma(\omega)$ or, using the respective equivalents in the local approach, the effective medium interactor $\bar{\Delta}(\omega)$ and locator $\gamma(\omega)$

$$\gamma_i(\omega) = (\omega - \Sigma_i(\omega))^{-1} \quad (2.20)$$

$$\Gamma_{ii}(\omega) = (\gamma_i^{-1}(\omega) - \bar{\Delta}_i(\omega))^{-1} \quad (2.21)$$

where (2.18) was used. For a mathematical description of the insertion of a real impurity of species q into the effective medium, being essential for the CPA condition, an impurity Green's function ${}^q G(\omega)$ can be defined. Replacing γ in Eq. (2.21) by an impurity locator $g_i^q(\omega) = (\omega - \epsilon_i^q)^{-1}$ with species dependent onsite energy ϵ_i^q , ${}^q G$ is found to be

$${}^q G_{ii} = \left((g_i^q)^{-1} - \bar{\Delta}_i \right)^{-1} = \left(\Gamma_{ii}^{-1} + \Sigma_i - \epsilon_i^q \right)^{-1} \quad (2.22)$$

where in the last step a combination of Eqs. (2.20) and (2.21) was used to get rid of $\bar{\Delta}$. This impurity Green's function now allows a direct mathematical formulation of the CPA condition illustrated in Fig. 2.1

$$\Gamma_{ii}(\omega) \stackrel{!}{=} \sum_q c_i^q {}^q G_{ii}(\omega) \quad (2.23)$$

where c_i^q is the atomic concentration of species q at site i . The effective medium was introduced to get an approximation for the configurational averaged Green's function $\langle G \rangle$ of the real physical system as defined in Eq. (2.15) and therefore under this approximation, Γ has to be identical with $\langle G \rangle$. The same then holds for the self-energy and Dyson's equation Eq. (2.16) together with Eq. (2.14) yields

$$\Gamma_{ii} \stackrel{!}{=} \langle G_{ii} \rangle = \left[(G_{ii}^0)^{-1} - \Sigma_i \right]^{-1} = [\omega - W_{ii} - \Sigma_i]^{-1} \quad (2.24)$$

The effective medium exhibits the full translational symmetry of the parent compound and the local effective medium Green's function $\Gamma_{ii}(\omega)$ can be obtained from a representation in \mathbf{k} -space using a Fourier transformation. Here it is necessary to divide the combined local index i into a lattice index L and an atomic index inside the unit cell s

$$\mathbf{R}_i = \mathbf{R}_L + \mathbf{R}_s \quad (2.25)$$

This allows a Fourier transformation of the hopping terms according to the following convention

$$W_{s,t}(\mathbf{k}) = \frac{1}{(2\pi)^3} e^{-i\mathbf{k}(\mathbf{R}_s - \mathbf{R}_t)} \sum_L e^{-i\mathbf{k}\mathbf{R}_L} W_{Ls,t} \quad (2.26)$$

which will be used throughout this work also for all other translational invariant matrix elements. Then the effective medium Green's function, of which in the CPA cycle only the onsite elements are needed, can be calculated

$$\Gamma_{ss}(\omega) = \int_{1.BZ} d^3k \Gamma_{ss}(\mathbf{k}, \omega) = \int_{1.BZ} d^3k [\omega - W(\mathbf{k}) - \Sigma]^{-1} \Big|_{ss} \quad (2.27)$$

where the integration is performed over the first Brillouin zone. Finally, eqs. (2.22), (2.23) and (2.27) together form a set of self-consistent equations which can be solved by the following iterative scheme:

1. In iteration n , calculate the effective medium Green's function ${}^{n-1}\Gamma$ by Eq. (2.27) from the hopping matrix elements and the self-energy from the previous iteration
2. For every substituent species, calculate an impurity Green's function from Eq. (2.22)
3. Calculate a new effective medium Green's function ${}^n\Gamma$ from the CPA condition Eq. (2.23)
4. From the difference of those two Green's functions calculate a self-energy update via $d\Sigma_i = ({}^{n-1}\Gamma)^{-1} \Big|_{ii} - ({}^n\Gamma)^{-1} \Big|_{ii}$
5. If $d\Sigma$ is small enough, the scheme is finished, otherwise repeat at step 1 with iteration $n + 1$

In the first iteration, the initial self-energy has to be guessed. The update formula for $d\Sigma$ can be derived by recognizing that Eqs. (2.27) and (2.23) hold for every iteration but Γ as well as Σ will change between two iterations in contrast to ω and W which will stay the same in every iteration.

In the beginning of this section, it was stated that due to the single-site nature of this approach, environmental disorder effects are neglected. On the other hand, this provides a computational feasible method to obtain the thermodynamic average of a disordered system where the computation time does not scale with the impurity concentration. For that reason it has been successfully applied within *ab-initio* frameworks and among them especially within the Kohn-Korringa-Rostoker (KKR) method [12–19], which is a multiple-scattering Green's function based DFT approach. When applying the CPA within a wave function based approach, extended overlapping basis sets like the popular linear combination of atomic orbitals (LCAO) basis, not even to mention plane waves, are not well suited due to its local nature. Because of that there exist only few implementations of this powerful method within other frameworks apart from KKR.

It is thus desirable to have a method which can also handle off-diagonal disorder effects beyond the CPA with maybe less requirements to a basis set. At least on the route towards off-diagonal disorder, a couple of cluster-extensions to the CPA have been developed over the years. The most prominent ones are for example the molecular coherent potential approximation (MCPA) [61] from the 1970's, where essentially a finite cluster sits at every "site" in the effective medium. Its more famous successor is the nonlocal coherent potential approximation (NLCPA), first discussed in 2001 [62], where such clusters are embedded into the effective medium in a more sophisticated way. Recently in 2013, the dual-fermion approach, being a field theoretical method originally developed for strongly correlated systems [63], was discussed in the context of disordered systems [64]. As summarized

in [19], the MCPA and its successors suffer from several shortcomings like violation of symmetries and non analyticity. The NLCPA seems to be a quite successful approach [18, 19] but also is told to be computationally expensive in some cases. In particular in [64] it is stated, that (unlike conventional CPA) the NLCPA can capture effects leading to Anderson localization but does not describe the Anderson transition properly.

2.2.3. Incorporation of environmental disorder effects

An alternative approach towards improving the CPA for off-diagonal disorder by taking into account disordered hopping terms but still relying on a single-site self-energy, is the formalism of Blackman, Esterling and Berk (BEB) [4]. This approach has later proven to be analytic [65], correctly recovers all symmetries of the parent compound as will become clear below and has been successfully applied also within nonorthogonal, overlapping basis sets [11]. First of all, BEB introduced the following binary occupation variables (notation follows [11])

$$\eta_i^P = \begin{cases} 1 & \text{if site } i \text{ is occupied with species } P \\ 0 & \text{otherwise} \end{cases}$$

To ensure that these random occupation variables describe a physical realistic situation, they have to obey several rules:

1. Avoid occupation by multiple species at the same site

$$\eta_i^P \eta_i^Q = \delta_{PQ} \eta_i^P \quad (2.28)$$

2. Ensure occupation with one species

$$\sum_P \eta_i^P = 1 \quad (2.29)$$

3. Relation of random occupation variables to atomic concentration

$$\langle \eta_i^P \rangle = c_i^P \quad (2.30)$$

4. Statistical independence of the occupation of two sites

$$\langle \eta_i^P \eta_j^Q \rangle = c_i^P c_j^Q \quad (2.31)$$

These rules are frequently used as an algebra in later calculations. Via these η , a transformation of the Hamiltonian between the Hilbert space of *one special* configuration (normal symbols) and a non stochastic extended Hilbert space containing *all* configurations (underlined symbols) can be established

$$\hat{H} = \sum_{i,j,P,Q} \underline{H}_{i,j}^{P,Q} \eta_i^P \eta_j^Q c_i^\dagger c_j = \sum_{i,j,P,Q} \eta_i^P \underline{W}_{ij}^{PQ} \eta_j^Q c_i^\dagger c_j + \sum_{i,P} \eta_i^P \underline{\epsilon}_i^P c_i^\dagger c_i \quad (2.32)$$

This means that the Hamiltonian \hat{H} of a *specific* configuration is selected from a more general Hamiltonian $\underline{\hat{H}}$ by specifying the set of η . It is essential for this approach that the only stochastic quantities under consideration are the η . They encode a random configuration, whereas the quantities in the extended Hilbert space \underline{H} and \underline{S} are non

stochastic and thus possess the full translational and point group symmetry of the parent compound. Additionally, in this formalism the disorder effects are no longer encoded just in the onsite terms ϵ_i . Moreover, the hopping elements $W_{ij} = \eta_i^P \underline{W}_{ij}^{PQ} \eta_j^Q$ of a specific random configuration encoded in the η are random and take into account the disordered environment of a site in the crystal.

Instead of presenting the original derivation of the self-consistent equations as in [4], I will take an alternative and maybe more comprehensive route similar to that given in [65]. It essentially is a generalization of the approach due to [19, 58] given in the preceding section to the extended Hilbert space. Application of the BEB-transformation Eq. (2.32) causes the site matrix elements (e.g. $G_{i,j}$, $H_{i,j}$), being complex numbers in Sec. 2.2.2, to resemble matrices in species space. In particular, for the Green's function and the locator of Sec. 2.2.2 this yields

$$\underline{G}_{ij}^{PQ} = \eta_i^P G_{ij} \eta_j^Q \quad \underline{g}_i^P = \eta_i^P g_i \quad (2.33)$$

The locator \underline{g}_i^P is special in that respect: due to its original definition as a site diagonal quantity and the BEB rule Eq. (2.28) it is also species diagonal. As a consequence, the locator equations of motion for the actual physical system and the effective medium have the same form in site indices in extended Hilbert space as their counterparts in conventional CPA, Eqs. (2.18) and (2.21), but additionally become matrix equations in species space

$$\underline{G}_{ii} = (\underline{g}_i^{-1} - \underline{\Delta}_i)^{-1} \quad \underline{\Gamma}_{ii} = (\underline{\gamma}_i^{-1} - \underline{\bar{\Delta}}_i)^{-1} \quad (2.34)$$

In the same way as done in conventional CPA Eq. (2.20), the BEB-CPA self-energy $\underline{\Sigma}$ can be defined via

$$\underline{\gamma}_i = (\omega - \underline{\Sigma}_i)^{-1} \quad (2.35)$$

with the important remark that this self energy is *not* related to the one in conventional CPA by a BEB-transformation. This property is only maintained by the Green's function, locator and Hamiltonian. In analogy to the route which was selected in Sec. 2.2.2, an impurity locator which replaces the BEB-CPA medium, i.e. the self-energy, with the onsite energy of a particular species q at site i can be written as

$${}^q \underline{g}_i^P = \left[\omega - \delta_{Pq} \epsilon_i^q - (1 - \delta_{Pq}) \underline{\Sigma}_i^{PP} \right]^{-1} \quad (2.36)$$

which leaves the effective medium locator unchanged elsewhere. In the same way as Eq. (2.22) was obtained, this yields for the impurity Green's function and the CPA condition

$$({}^q \underline{G})^{-1} \Big|_{ii}^{PQ} = (\underline{\Gamma}^{-1})_{ii}^{PQ} + (\underline{\Sigma}_i^{PQ} - \epsilon_i^q) \delta_{PQ} \delta_{Pq} \quad (2.37)$$

$$\underline{\Gamma}_{ii}^{PQ} = \sum_q c_i^q {}^q \underline{G}_{ii}^{PQ} \quad (2.38)$$

To complete the set of self-consistent equations, the fact that the underlined quantities in extended Hilbert space maintain the translational symmetry of the parent compound can be used to obtain in analogy to Eq. (2.27)

$$\underline{\Gamma}_{ii}^{PQ} = \int_{1.BZ} d^3 k [\omega \mathbf{1} - \underline{W}(\mathbf{k}) - \underline{\Sigma}_i]^{-1} \Big|_{ii}^{PQ} \quad (2.39)$$

where the translational symmetry of $\underline{W}(\mathbf{k})$ and site diagonality of $\underline{\Sigma}$ restricts the matrix inversion in orbital space to one unit cell.

The obtained self-consistent Eqs. (2.39), (2.38) and (2.37) have exactly the same form as the respective Eqs. (2.27), (2.23) and (2.22) obtained for the conventional CPA in the previous section - the only difference is that the quantities, being complex numbers in the conventional CPA, now are matrices in species indices. Apart from this fact, the iterative scheme to solve these self-consistent equations is completely analog to the one outlined in the last section.

This method preserves the single site property of the self-energy which is advantageous for efficient numerical implementation but goes a step beyond the conventional CPA in its ability to treat environmental disorder effects based on disordered hopping terms. A verification of these qualities based on numerical model studies will be presented in Chap. 3.

2.2.4. Orbital-based *ab-initio* implementation using pseudopotentials

In the last section, the BEB-CPA, being a method dedicated to the treatment of substitutional disordered systems at arbitrary impurity concentrations including off-diagonal disorder effects, was presented. The physical, material specific quantities this scheme is governed by, are the Hamiltonian matrix elements $\underline{H}_{i,j}^{P,Q}$ entering the self-consistent equations via hopping- and onsite-terms. Until now, these matrix elements are just free parameters of a certain physical model. The aim of this section is to show a way how to obtain them from a first-principles DFT calculation relying on the mixed-basis pseudopotential program (MBPP), mainly based on earlier work by Koepernik et al. [11] who did this in context of the full potential local orbital (FPLO) framework.

In principle, the idea is to generalize the site- and species-dependent matrix elements to another orbital degree of freedom $\underline{H}_{i,j}^{P,Q} \rightarrow \underline{H}_{i\mu,j\nu}^{P,Q}$ where i,j are site-, P,Q species- and $\mu = (l, m)$, $\nu = (l', m')$ are compound orbital indices, l being the quantum number of orbital angular momentum and $m \in \{-l, l\}$ the magnetic quantum number. Such matrix elements then can be understood as the Hamiltonian operator of our DFT method \hat{H}_{DFT} evaluated between LCAO orbitals $|iP\mu\rangle$

$$\underline{H}_{i\mu,j\nu}^{P,Q} = \langle iP\mu | \hat{H}_{DFT} | jQ\nu \rangle \quad \underline{S}_{i\mu,j\nu}^{P,Q} = \langle iP\mu | jQ\nu \rangle \quad (2.40)$$

Obviously, such an LCAO basis is not restricted to be orthonormal and exhibits a nontrivial overlap matrix \underline{S} . For such a basis, the unit operator is defined as

$$\mathbf{1} = \sum_{iP\mu, jQ\nu} |iP\mu\rangle \left(S^{-1}\right)_{i\mu, j\nu}^{P,Q} \langle jQ\nu| \quad (2.41)$$

The hopping matrix elements W can then be identified as offsite matrix elements \check{H} and the onsite terms ϵ_i as onsite matrix elements \dot{H} of the DFT-Hamiltonian. Unfortunately, the MBPP itself relies on localized atomic functions *and* plane waves of which the latter are definitely not suited for a local, site dependent method like the BEB-CPA. The MBPP contains on the other hand subroutines where the Kohn-Sham orbitals in mixed-basis representation of a converged bandstructure calculation can be transformed to an LCAO representation solely containing atom centered functions. These routines, originally developed for the purpose of local chemical analysis [10], essentially use the same atomic functions as in the mixed basis, modified by cutoff functions. The parameters of

these cutoff functions then are optimized to the actual bandstructure which leads to radial functions in the usual representation of the basis functions ϕ_{lm} in terms of real spherical harmonics K_{lm}

$$\langle \mathbf{r} | iP\mu \rangle = \phi_{i,\mu}^P(\mathbf{r}) = \phi_{lm}^P(\mathbf{r} - \mathbf{R}_i) \quad \phi_{lm}^P(\mathbf{r}) = i^l f_l^P(r) K_{lm}(\hat{\mathbf{r}}) \quad (2.42)$$

where $r = |\mathbf{r}|$ and $\hat{\mathbf{r}}$ is a unit vector pointing in the direction of \mathbf{r} . This optimization of the local orbitals is accomplished by minimizing the so-called spillage function [66, 67] which gives a measure about the difference in electronic density calculated within the original basis compared to the one calculated in the projected basis. Furthermore, this approximation is carried out in such a way that the agreement between the bandstructure obtained within the local basis and the original one is best below the Fermi level. The coincidence far above the Fermi level for unoccupied bands, where DFT as a ground state theory is not supposed to be reliable anyway, usually is not good but also not important. However, a good representation of the Kohn-Sham orbitals in terms of a local basis can only be achieved if the functions are heavily overlapping. In this work, the basis functions are normalized, meaning that the onsite part of the overlap matrix is always one

$$\underline{S}_{i\mu,\nu}^P = \underline{S}_{i\mu,j\nu}^{P,Q} \delta_{i,j} \delta_{P,Q} = \langle iP\mu | iP\nu \rangle = \delta_{\mu,\nu} \quad (2.43)$$

where the additional $\delta_{P,Q}$ is a consequence of the BEB-rule Eq. (2.28). This allows, as becomes obvious later in this section, to simply generalize the derivation of the BEB-CPA in the locator framework as presented in Sec. 2.2.3 to such a special non-orthogonal basis. For the local decomposition of the potentials needed to evaluate the Hamiltonian matrix elements we first need to assume a local decomposition of the electronic density in the following way

$$n(\mathbf{r}) = \sum_{iP} \eta_i^P n_i^P(\mathbf{r}) \quad (2.44)$$

For a clean system, such a decomposition in principle can be derived from the fundamental Kohn-Sham equation for the density Eq. (2.6)

$$\begin{aligned} n(\mathbf{r}) &= \sum_{n=1}^N |\varphi_n(\mathbf{r})|^2 \\ &= \sum_{iP\mu} \phi_{i\mu}^P(\mathbf{r}) \sum_{jQ\nu} C_{i\mu,j\nu}^{P,Q} [\phi_{j,\nu}^Q(\mathbf{r})]^* \end{aligned} \quad (2.45)$$

where n is a band index and the expansion coefficients C of the Kohn-Sham orbitals φ_n with respect to the local orbitals ϕ are given by

$$C_{i\mu,j\nu}^{P,Q} = \sum_{i'P'\mu'} \sum_{j'Q'\nu'} \sum_n (S^{-1})_{i\mu,i'\mu'}^{P,P'} \langle i'P'\mu' | n \rangle \langle n | j'Q'\nu' \rangle (S^{-1})_{j'\nu',j\nu}^{Q',Q} \quad (2.46)$$

which are calculated by the LCAO routines in the MBPP (in a slightly different form in \mathbf{k} -space). More details of such a decomposition are described in the next section about charge self-consistency and in App. B.3. This leads to a local decomposition of the potential

$$V(\mathbf{r}) = \sum_{iP} \eta_i^P V_i^P(\mathbf{r}) = V_{pseudo}(\mathbf{r}) + V_{Hartree}[n(\mathbf{r})] + V_{XC}[n(\mathbf{r})] \quad (2.47)$$

2. Computational method

where the pseudopotential is already decomposed in terms of species and angular momentum by construction. The decomposition of the Hartree term can be obtained by the decomposition of the density after Eq. (2.44) due to its linear dependence on the electronic density. Only the decomposition of the XC-potential is not straight forward and will be discussed later in this section. The Hamiltonian matrix elements of a random configuration are given by

$$H_{i\mu,j\nu} = \eta_i^P \underline{H}_{i\mu,j\nu}^{PQ} \eta_j^Q = \eta_i^P \left\langle iP\mu \left| \hat{T} + \sum_{k,R} \eta_k^R V_k^R(\mathbf{r}) \right| jQ\nu \right\rangle \eta_j^Q \quad (2.48)$$

where \hat{T} is the kinetic energy operator. The problem is that this matrix element exhibits additional stochastic contributions due to the decomposition of the local potential. This is a drawback compared to BEB's original idea of non-stochastic matrix elements defined in an extended Hilbert space which exhibits the full translational symmetry and choosing a random configuration by multiplying with the stochastic η from both sides. Following [11], this problem can be approached by only treating the potentials located at the terminal sites out of the sum in the middle exactly and take the rest into account by a configurational average over the whole crystal

$$\underline{H}_{i\mu,j\nu}^{PQ} = \left\langle iP\mu \left| \hat{T} + V_i^P + V_j^Q + \sum_{k \neq (i,j), R} c_k^R V_k^R \right| jQ\nu \right\rangle \quad (2.49)$$

which ensures the translational symmetry of the \underline{H} being required by the BEB scheme. Then the decomposition into onsite- and offsite contributions is straight forward:

$$\underline{\dot{H}}_{i\mu,j\nu}^{P,Q} = \delta_{i,j} \delta_{P,Q} \left\langle iP\mu \left| T + V_i^P + \sum_{k \neq i, R} c_k^R V_k^R \right| iP\nu \right\rangle \quad (2.50)$$

$$\underline{\check{H}}_{i\mu,j\nu}^{P,Q} = (1 - \delta_{i,j}) \left\langle iP\mu \left| T + V_i^P + V_j^Q + \sum_{k \neq (i,j), R} c_k^R V_k^R \right| jQ\nu \right\rangle \quad (2.51)$$

where again the additional factor δ_{PQ} in the onsite term originates from the BEB-rule Eq. (2.28). To efficiently calculate these multi-center integrals between wavefunctions expressed by spherical harmonics Eq. (2.42), it is convenient to also perform a multipole expansion of the potentials. The resulting expressions containing only one dimensional radial integrals which were actually implemented, are shown in full detail in App. B.

As stated before, only for the exchange correlation (XC) potential such a multipole expansion cannot be carried out analytically because it is a nonlinear functional of the density. In [11] this issue was solved by an atomic sphere approximation (ASA) where V_{XC} should assume the value for the total density of the disordered system for \mathbf{r} within this sphere and a constant, interstitial value outside the sphere. By introducing these spheres, an artificial site index is given to V_{XC} . But this works only under an isotropic approximation where this site decomposition of V_{XC} is assumed to only have an $l = 0$ contribution and any higher angular momenta are neglected.

In practical calculations for real materials carried out in this work, this approximation worked as long as the systems were close to isotropic, i.e. the angle dependence of the density was not important and contributions with $l > 0$ could be neglected. For anisotropic

systems, this approximation turned out to fail: in the BaFe₂As₂ it yielded an additional spurious electron pocket. This problem led to the implementation of a more sophisticated approach within this work based on so-called shape functions. Such shape functions \mathcal{S} are spherically symmetric and characterized by a site- and species-dependent cutoff radius $C R_i^P$

$$\mathcal{S}_i^P(\mathbf{r}) = \mathcal{S}_i^P(|\mathbf{r}|) = \mathcal{S}^P\left(\frac{|\mathbf{r}|}{C R_i^P}\right) \quad \mathcal{S}^P(1) = 0 \quad (2.52)$$

$$\mathcal{N}(\mathbf{r}) = \sum_{i,P} c_i^P \mathcal{S}_i^P(\mathbf{r} - \mathbf{R}_i^P) \quad (2.53)$$

where a proper normalization is maintained by $\mathcal{N}(\mathbf{r})$. The exact functional form for these shape functions chosen in this work are shown in App. B.4.5. These shape functions are allowed and also required to overlap and the following definition guarantees a well-defined result without any double-counting

$${}^{XC}V_i^P(\mathbf{r}) = V_{XC} \left[{}^{XC}n_i^P(\mathbf{r}) \right] \frac{\mathcal{S}_i^P(\mathbf{r} - \mathbf{R}_i)}{\mathcal{N}(\mathbf{r})} \quad (2.54)$$

where ${}^{XC}n_i^P(\mathbf{r})$ is a conditionally averaged density under the constraint that site i is occupied by an atom of type P

$${}^{XC}n_i^P(\mathbf{r}) = n_i^P(\mathbf{r}) + \sum_{j \neq i, Q} c_j^Q n_j^Q(\mathbf{r} - (\mathbf{R}_j - \mathbf{R}_i)) \quad (2.55)$$

In a clean compound, where a single well defined species is associated with every site, the species-dependence of the shape functions simply reduce to their site dependence. In addition, Eqs. (2.53) and (2.55) then become

$$\mathcal{N}(\mathbf{r}) = \sum_i \mathcal{S}_i(\mathbf{r} - \mathbf{R}_i) \quad (2.56)$$

$${}^{XC}n_i^P(\mathbf{r}) = n_i^P(\mathbf{r}) + \sum_{j \neq i, Q} n_j^Q(\mathbf{r} - (\mathbf{R}_j - \mathbf{R}_i)) = n(\mathbf{r}) \quad (2.57)$$

where the density simply reduces to the total density. To be physically meaningful, such a decomposition has to add up to the full XC-potential

$$\begin{aligned} V_{XC}[n(\mathbf{r})] &\stackrel{!}{=} \sum_i {}^{XC}V_i(\mathbf{r} - \mathbf{R}_i) = \sum_i V_{XC}[n(\mathbf{r})] \frac{\mathcal{S}_i(\mathbf{r} - \mathbf{R}_i)}{\mathcal{N}(\mathbf{r})} \\ &= V_{XC}[n(\mathbf{r})] \frac{\mathcal{N}(\mathbf{r})}{\mathcal{N}(\mathbf{r})} \end{aligned} \quad (2.58)$$

which proves the consistency of this approach for clean compounds. In a disordered system, the one to one correspondence between site and species indices is no longer fulfilled, such a formal proof is not possible anymore and the decomposition becomes approximative.

This allows to build up the following scheme: First, the XC-potential is calculated from the conditionally averaged density which is afterwards locally and species-selectively decomposed via the shape functions. Then follows an additional angular momentum decom-

position which is carried out completely numerical by a Gauß-Legendre integration [68–71] over the whole angle. This approach is discussed in more detail in App. B.4.5

After having outlined the computation of the required matrix elements, the central self-consistent equations of the BEB-CPA in the special non-orthogonal basis, which have been implemented in this work, shall be derived in the following. Because Green's functions in a non-orthogonal basis is usually not a topic readers are supposed to be familiar with, their most important properties should be summarized here based on other work [72, 73] (see also App. D for more details). Without loss of generality, in this repetition the species indices P, Q and underlines will be omitted for a moment. Depending on the set of fermionic operators, in a non-orthogonal basis there are in general two sets of retarded Green's functions which are defined as

$$G_{i\mu, j\nu}(t) = -i\theta(t) \langle \{ a_{i\mu}(t), a_{j\nu}^\dagger \} \rangle \quad (2.59)$$

$$\mathcal{G}_{i\mu, j\nu}(t) = -i\theta(t) \langle \{ c_{i\mu}(t), c_{j\nu}^\dagger \} \rangle \quad (2.60)$$

where $\{ \cdot, \cdot \}$ denotes the anticommutator of two operators like before. In the first variant Eq. (2.59), the operator $a_{i\mu}^\dagger$ ($a_{i\mu}$) creates (annihilates) an electron in orbital $\phi_\mu(\mathbf{r} - \mathbf{R}_i)$ and the commutation relations are connected with the overlap matrix

$$\{ a_{i\mu}, a_{j\nu}^\dagger \} = S_{i\mu, j\nu} \quad (2.61)$$

In the second variant Eq. (2.60), the operators $c_{i\mu}$ are defined by the field-operators $\psi(\mathbf{r}) = \sum_{i\mu} c_{i\mu} \varphi_\mu(\mathbf{r} - \mathbf{R}_i)$ from which their commutation relations are derived to be

$$\{ c_{i\mu}, c_{j\nu}^\dagger \} = S_{i\mu, j\nu}^{-1} \quad (2.62)$$

Performing the same analysis using the insertion of a complete set of eigenstates $\sum_n |n\rangle\langle n| = \mathbf{1}$ as performed in standard textbooks like [74], considering a system of non-interacting electrons and Fourier transformation to frequency domain, the Green's matrices are found to be

$$\mathcal{G}(\omega) = (\omega^+ S - H)^{-1} \quad (2.63)$$

$$G(\omega) = S \mathcal{G}(\omega) S = S(\omega^+ S - H)^{-1} S \quad (2.64)$$

where H is the Hamiltonian matrix in LCAO indices and $\omega^+ = \omega + i\delta$ with a small imaginary part δ accounts for the analyticity of the retarded functions in the upper complex half plane. To establish the locator concept in the nonorthogonal basis, it is convenient to start from the equation of motion for \mathcal{G} Eq. (2.63)

$$\underbrace{(\omega \dot{S} - \dot{H})}_{g^{-1}} \mathcal{G} + (\omega \check{S} - \check{H}) \mathcal{G} = \mathbf{1} \quad (2.65)$$

where again the decomposition of the Hamiltonian and overlap matrices into onsite and offsite contributions has been performed. The first bracket in Eq. (2.65) can be identified as the inverse of the locator g which becomes clearer from converting Eq. (2.65) into the

form of a locator equation of motion similar to Eq. (2.17)

$$\mathcal{G} = g + g \left(\check{H} - \omega \check{S} \right) \mathcal{G} \quad g = \left(\omega \dot{S} - \dot{H} \right)^{-1} \stackrel{\dot{S}=\mathbf{1}}{=} \left(\omega - \dot{H} \right)^{-1} \quad (2.66)$$

where the term $\check{H} - \omega \check{S}$ could be understood as a generalized hopping matrix and the normalization of the wave functions $\dot{S} = \mathbf{1}$ selected in this work was used. This allows to generalize the self-consistent BEB-CPA equations Eqs. (2.37) - (2.39) to a non-orthogonal basis set by substituting $W \rightarrow \check{H} - \omega \check{S}$ in the expressions for the medium Green's function Γ of Sec. 2.2.3 which leads to

$$\underline{\Gamma}_{i,\mu\nu}^{PQ} = \int_{1.BZ} d^3k \left[\omega \left(\mathbf{1} + \check{S}(\mathbf{k}) \right) - \check{H}(\mathbf{k}) - \underline{\Sigma} \right]^{-1} \Big|_{i\mu, i\nu}^{PQ} \quad (2.67)$$

$$\left({}^q \underline{G} \right)^{-1} \Big|_{i,\mu\nu}^{PQ} = \left(\underline{\Gamma}^{-1} \right)_{i,\mu\nu}^{PQ} + \left(\underline{\Sigma}_{i,\mu\nu}^{PQ} - \dot{H}_{i,\mu\nu}^q \right) \delta_{PQ} \delta_{Pq} \quad (2.68)$$

$$\underline{\Gamma}_{i,\mu\nu}^{PQ} = \sum_q c_i^q {}^q \underline{G}_{i,\mu\nu}^{PQ} \quad (2.69)$$

where the shorthand notation $X_{i\mu, i\nu} = X_{i,\mu\nu}$ for site diagonal quantities was introduced. In Eq. (2.67) the matrix inversion for each \mathbf{k} -point is performed in orbital-, species- and site- space if the unit cell contains more than one atom. The translational invariance of $\check{H}(\mathbf{k})$ and $\check{S}(\mathbf{k})$ together with the site diagonality of the self-energy ensure that this possible site index does not exceed one unit cell.

For the implementation of an iterative scheme to solve these three self-consistent equations, the same update formula as introduced in the discussion of the conventional CPA Sec. 2.2.2 combined with Eq. (2.69) yields after some manipulations

$$d\underline{\Sigma}_{i,\mu\nu}^{PQ} = \left(\underline{\Gamma}_i^{-1} \right)_{\mu\nu}^{PQ} + \sum_q \frac{1}{c_i^q} \left[\dot{H}_i - \underline{\Sigma}_i - \underline{\Gamma}_i^{-1} \right]_{\mu\nu}^{qq} \delta_{PQ} \delta_{Pq} \quad (2.70)$$

which was actually implemented in the program instead of Eqs. (2.68) and (2.69) because one additional matrix inversion can be avoided in this way and the involved matrix inversions can be performed for each site separately due to the site diagonality of the involved quantities.

In principle, the self consistent scheme outlined above is equivalent to that obtained in [11] in a different formal approach. Our scheme experienced two simplifications compared to [11]: We do not have to consider contributions from core electrons in the matrix elements which need an extra treatment because the pseudopotential method only deals with valence electrons and our basis functions are normalized ($\dot{S} = \mathbf{1}$).

It is important to note that the effective medium Green's function $\underline{\Gamma}$ is defined in the same way as \mathcal{G} in Eq. (2.63). This is crucial for the calculation of physical properties from $\underline{\Gamma}$. In particular, the density of states (DOS) $\nu(\omega)$ is defined in terms of the other Green's function $\underline{G} = \underline{S} \underline{\Gamma} \underline{S}$ Eq. (2.64) which is associated with annihilation and creation of electrons

$$\begin{aligned} \nu(\omega) &= -\frac{2}{\pi} \text{Im Tr} \left[\underline{S} \underline{\Gamma}(\omega^+) \right] \\ &= -\frac{2}{\pi} \text{Im Tr} \left\{ \int_{1.BZ} d^3k S(\mathbf{k}) \left[\omega \left(\mathbf{1} + \check{S}(\mathbf{k}) \right) - \check{H}(\mathbf{k}) - \underline{\Sigma} \right]^{-1} \right\} \end{aligned} \quad (2.71)$$

which is analog to [75] and an additional factor \underline{S}^{-1} arising from taking a trace of an operator in a nonorthogonal basis has been considered. Tr in Eq. (2.71) means the summation over the diagonal elements (see also App.D for more details). The factor 2 takes into account the spin degree of freedom in a non spin-polarized calculation and the frequency $\omega^+ = \omega + i\delta$ with infinitesimal δ is slightly shifted above the real axis where the retarded Green's function is analytic. The smaller δ is chosen, the more fine structure but unfortunately also the more numerical noise the DOS will show. Thus in practical calculations one always has to check δ to find a good compromise between noise and resolution. Another important quantity is the Bloch spectral function which is usually defined as

$$A(\mathbf{k}, \omega) = -\frac{1}{\pi} \text{Im Tr} \left[\sum_{L \in \text{lattice}} e^{i\mathbf{k}\mathbf{R}_L} \int_{\text{P.U.}} d^3r \underline{\Gamma}(\mathbf{r} - \mathbf{R}_L, \mathbf{r}, \omega^+) \right] \quad (2.72)$$

being a discrete Fourier transform of the Green's function in real space on the crystal lattice together with an integration over one unit cell. The real space Green's function is defined via the field operators and thus no overlap matrix is needed. It can be shown (see App.D) that this is indeed equivalent to

$$A(\mathbf{k}, \omega) = -\frac{1}{\pi} \text{Im Tr} \left[\underline{S}(\mathbf{k}) \underline{\Gamma}(\mathbf{k}, \omega^+) \right] \quad (2.73)$$

where $\underline{\Gamma}(\mathbf{k}, \omega^+)$ is just the kernel of the integral in Eq. (2.67). This is of course just the same expression (per spin degree of freedom) as Eq. (2.71) without integration. This spectral function contains all information about the band structure of the disordered system as will be visualized later. Often, when $A(\mathbf{k}, \omega)$ is calculated, δ has to be chosen smaller than for the calculation of the DOS in order to resolve dense bands which led to two different δ in the actual implementation as discussed in detail in Apps. A.1 and C.

2.3. Charge self-consistency

The method which has been outlined in the last section contains all essential ingredients needed for the calculation of the electronic structure of an arbitrary substitutionally disordered system from first principles. Such a generic calculation would be accomplished by several steps: First, an MBPP-DFT calculation is carried out for the parent compound which provides the pseudopotentials for each atomic species, the local basis functions obtained from the LCAO fit and general information about the crystal structure and its symmetries. Then for each substitutional end member DFT calculations are performed, which in addition deliver the required pseudopotentials and local orbitals of the substituent species. Instead of just doing DFT calculations for the bare substituent, this approach has the advantage of optimizing the basis functions to the crystal structure and the surrounding part of the parent compound which is not substituted. This provides the best possible starting point for achieving rapid convergence of the CPA solver. To be consistent, the crystal structures have to be the same in all of these different DFT calculations which has to be taken into account when variations of lattice parameters due to disorder are considered.

In the CPA program, the overlap matrix is calculated and the locally decomposed electronic density Eq. (2.44) is computed from the local basis functions as sketched in Eq. (2.45). The density is needed for the local decomposition of the Hartree potential and the local

decomposition of the XC potential is performed by the shape function approach, also relying on the density. Finally, the Hamiltonian matrix elements Eqs. (2.50) and (2.51) can be evaluated. This is actually the most time-consuming part of the CPA-program. Via these matrix elements the self-consistent CPA equations are solved via Eqs. (2.67) and (2.70) which in the end delivers an effective medium Green's function $\underline{\Gamma}(\omega)$. In principle the procedure then would be finished as the most physical information is contained in the Green's function or the spectral function.

However, this approach alone suffers from a significant shortcoming: The starting point were several isolated DFT calculations which mutually neglect the presence of the respective substitutional species. One may argue that they get coupled to each other in a sense by the species off-diagonal terms of the Hamiltonian but therein in particular the Hartree- and the XC-potential depend on the density which initially can only be calculated from the (mutually isolated) local basis functions and thus does not contain any disorder effects. This was already recognized in [11] and solved by a charge self-consistency condition which was also adapted in this work. The essential idea is to calculate a new charge density from the Green's function of a converged CPA calculation and then to feed it back into the Hamiltonian. Repeatedly applied until the density does not change significantly anymore, this successively improves the Hamiltonian of the disordered system. The electronic density can be calculated from the Green's function in real space via the expression

$$n(\mathbf{r}) = -\frac{1}{\pi} \int_{-\infty}^{E_F} \text{Im} G(\mathbf{r}, \mathbf{r}, \omega^+) d\omega \quad (2.74)$$

where the upper limit of the integration is the system's Fermi energy E_F in order to take into account only occupied states. Within the LCAO framework in the disordered system, the Green's function in real space can be connected to the matrix \mathcal{G} (see App. D) using the basis functions in real space $\varphi_{i,\mu}^P(\mathbf{r})$ and thus the electronic density of one random configuration is given by

$$n(\mathbf{r}) = -\frac{1}{\pi} \sum_{iP\mu, jQ\nu} \varphi_{i,\mu}^P(\mathbf{r}) \int_{-\infty}^{E_F} \text{Im} \eta_i^P \mathcal{G}_{i\mu, j\nu}(\omega^+) \eta_j^Q d\omega \left(\varphi_{j\nu}^Q(\mathbf{r}) \right)^* \quad (2.75)$$

where additionally the BEB transformation has been applied. Of course, Eq. (2.75) alone is not physically meaningful because in the end only configurational averages can be compared with experiments. The configurationally averaged version of Eq. (2.75) immediately follows to be

$$\bar{n}(\mathbf{r}) = -\frac{1}{\pi} \sum_{iP\mu, jQ\nu} \varphi_{i,\mu}^P(\mathbf{r}) \int_{-\infty}^{E_F} \text{Im} \underbrace{\langle \eta_i^P \mathcal{G}_{i\mu, j\nu}(\omega^+) \eta_j^Q \rangle}_{\stackrel{CPA}{=} \Gamma_{i\mu, j\nu}^{PQ}} d\omega \left(\varphi_{j\nu}^Q(\mathbf{r}) \right)^* \quad (2.76)$$

This is the required expression to evaluate the total physical density in a disordered system but on the other hand, this is not helpful for the calculation of the Hamiltonian matrix elements which are defined in the extended Hilbert space containing all configurations. For these matrix elements, which are *not* configurationally averaged, the site and species decompositions of the potential and thus the respective decompositions of the density are essential. Thus the aim is to return to Eq. (2.75) and find a decomposition in the form

mentioned above

$$n(\mathbf{r}) = \sum_{iP} \eta_i^P n_i^P(\mathbf{r}) \quad (2.77)$$

and derive expressions for the local components n_i^P using the effective medium Green's function to close the self-consistency cycle. This is a difficult task and not possible without further approximations and has been approached in [11] by the so-called terminal point approximation which will be sketched in the following. Essentially, in this approximation the Green's function in extended Hilbert space is replaced by its twofold conditional average in the following way

$$\underline{\mathcal{G}}_{i\mu,j\nu}^{PQ} = \eta_i^P \mathcal{G}_{i\mu,j\nu} \eta_j^Q \quad \rightarrow \quad \eta_i^P \langle \underline{\mathcal{G}}_{i\mu,j\nu}^{PQ} \rangle_{P_i, Q_i} \eta_j^Q \quad (2.78)$$

where $\langle \dots \rangle_{P_i, Q_i}$ means averaging under the constraint that the occupations of site i with species P and site j with species Q are fixed. Then, an additional average is performed on the η on the right index because we want the η_i^P to be the only stochastic quantity in the decomposition Eq. (2.77) but the $n_i^P(\mathbf{r})$ to be non stochastic. This yields

$$\begin{aligned} n_i^P(\mathbf{r}) = & -\frac{1}{\pi} \sum_{j, Q, \mu, \nu} \varphi_{i\mu}^P(\mathbf{r}) \int_{-\infty}^{E_F} \text{Im} \langle \underline{\mathcal{G}}_{i\mu, j\nu}^{PQ}(\omega^+) \rangle_{P_i, Q_i} d\omega \times \\ & \times \left(\varphi_{j\nu}^Q(\mathbf{r}) \right)^* \left[\delta_{ij} + (1 - \delta_{ij}) c_j^Q \right] \end{aligned} \quad (2.79)$$

where the expression $\left[\delta_{ij} + (1 - \delta_{ij}) c_j^Q \right]$ maintains the fourth BEB-rule Eq. (2.31) upon averaging. In [11] it is shown that the required conditionally averaged Green's functions can be obtained from the effective medium Green's function via

$$\langle \underline{\mathcal{G}}_{i\mu, i\nu}^{PP} \rangle_{P_i} = \frac{\Gamma_{i\mu, i\nu}^{PP}}{c_i^P} \quad \langle \underline{\mathcal{G}}_{i\mu, j\nu}^{PQ} \rangle_{P_i, Q_j} = \frac{\Gamma_{i\mu, j\nu}^{PQ}}{c_i^P c_j^Q} \quad (2.80)$$

Putting it all together then leads to the following local species resolved density contributions

$$n_i^P(\mathbf{r}) = -\frac{1}{\pi} \frac{1}{c_i^P} \sum_{j, Q, \mu, \nu} \varphi_{i\mu}^P(\mathbf{r}) \int_{-\infty}^{E_F} \text{Im} \underline{\Gamma}_{i\mu, j\nu}^{PQ}(\omega^+) d\omega \left(\varphi_{j\nu}^Q(\mathbf{r}) \right)^* \quad (2.81)$$

As a consistency check, calculating the configurationally averaged density which comes along with replacing η_i^P by c_i^P in Eq. (2.77) and inserting Eq. (2.81) indeed yields the expression for the configurationally averaged density in Eq. (2.76). For numerical reasons, the new density at the end of a charge iteration cannot be directly plugged into the Hamiltonian because this would immediately lead to an unstable result. This is a common problem in many self-consistent methods and is usually solved by mixing the old and new density in the next iteration. The simplest method is to use linear mixing but especially in the case of the iron pnictides this turned out to converge extremely slow and was very prone to instabilities. For that reason in this work a modified Broyden mixing after [76] was used.

The Fermi energy which is needed for the charge self-consistency but also for the interpretation of the numerical results is calculated in a similar fashion. The number of electrons (valence electrons in the pseudopotential framework) can be obtained from the density of

states via

$$N = \int_{-\infty}^{E_F} \nu(\omega) d\omega = -\frac{2}{\pi} \int_{-\infty}^{E_F} \text{Im Tr} \left[\underline{S}\Gamma(\omega^+) \right] d\omega \quad (2.82)$$

From particle number conservation then the the upper integration limit in Eq. (2.82) is successively shifted until the actual number of electrons is obtained. In the program, this is implemented via a bisection method where the width of the search interval for E_F is divided by two in each search step. In a complex disordered compound the valence electron number is given due to the constraint of charge neutrality by

$$N = \sum_{i,P} c_i^P N_i^P \quad (2.83)$$

where the N_i^P are the electron numbers of the individual atoms.

There is a special problem left in the practical implementation of Eqs (2.81) and (2.82) considering the involved integrations of the Green's function over frequency. As mentioned in the end of Sec 2.2.4, the fine structure of the results sensitively depends on the infinitesimal imaginary part δ of the frequency. The integration can be written in the following form as well

$$\int_{-\infty}^{E_F} \Gamma(\omega) d\omega = \int_{-\infty}^{\infty} \Gamma(\omega) \theta(E_F - \omega) d\omega \quad (2.84)$$

where θ is the Heaviside step function. Such an integration can be converted to a contour integral in the complex plane using the residual theorem. In this work we select a closed rectangular box far away from the real axis enclosing all poles of the Green's function. The boundaries of the box are chosen in a practical application in such a way, that a change of the boundaries does not affect the result anymore. Such a test of course has to be carried out for each material class under consideration. In order to achieve a reasonable accuracy it turned out that the usual numerical Simpson integration [68, 69, 77], being a Newton-Cotes formula [68, 69, 78, 79] of second order, is not sufficient any more and it was necessary to resort to the so-called Weddle-rule [68, 69, 79], being a Newton-Cotes formula of sixth order. This has the curious effect that the number of frequency sampling points has to be dividable by six plus one. By using the symmetry of the Green's function $G_{i,j}(\omega^*) = (G_{j,i}(\omega))^*$ it is possible to restrict the integration to a "half-box" in the upper half-plane. The results obtained within this scheme do not depend any more on the choice of a parameter like δ .

Another problem arises from the θ -function appearing in Eq. (2.84). The numerical treatment of such an abrupt, step-like change is always critical and can lead to instabilities. Thus it is well established in the *ab-initio* community to replace θ by a smooth cutoff function. The most physical choice in the case of particle numbers or densities is the Fermi distribution function

$$f(\omega, T) = \frac{1}{e^{\beta(\omega-\mu)} + 1} \quad (2.85)$$

where $\beta = \frac{1}{k_B T}$, T is the temperature, k_B the Boltzmann constant and μ the temperature dependent chemical potential obeying the relation $\mu(T = 0) = E_F$. This way to avoid step functions comes with the cost of another complication: $f(\omega)$, when evaluated in the complex plane, has singularities on the fermionic Matsubara frequencies $\omega_n = (2n + 1)\pi k_B T$, n being an integer. Due to the residual theorem, they just have to be subtracted from the

2. Computational method

integral because they were counted by the complex contour integration surrounding them. This in the end leads to the following expression for the frequency integration

$$\oint_{\text{box}} \underline{\Gamma}(\omega) f(\omega, T) d\omega - \sum_n \frac{2n\pi i}{\beta} \underline{\Gamma}(\mu + i\omega_n) \quad (2.86)$$

This introduces an artificial temperature scale into the calculation which should not be compared with experimental temperature scales because this is only the bare temperature of a system of noninteracting electrons. In practical calculations, temperatures below 300K turned out to be inconvenient because then the number of Matsubara frequencies and thereby the computation time increases and additionally the Fermi function gets very narrow which requires a huge number of sampling points and thus negates all advantages of this finite temperature method. The chemical potential can be calculated several temperatures and the Fermi energy can be extrapolated to $T = 0$. More technical details involved in these frequency integrations are outlined in App. C.

An overview over the full charge self-consistent process which I implemented in this work is visualized in Fig.2.2.

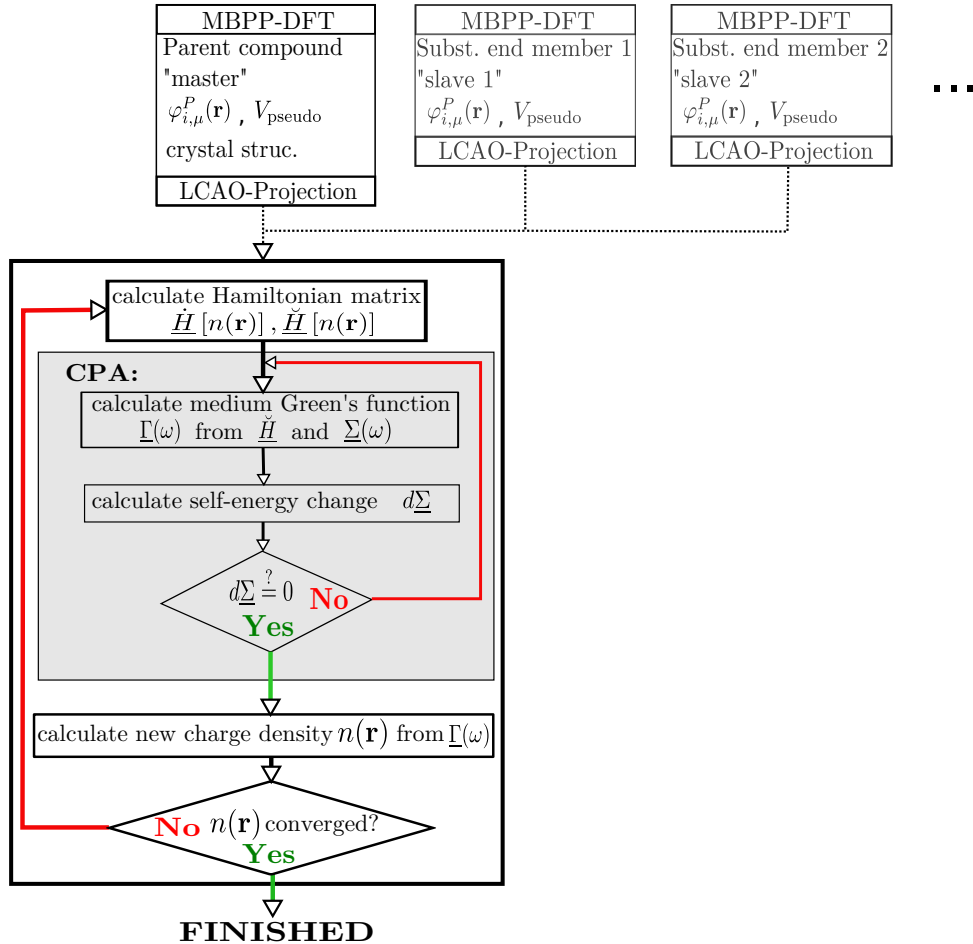


Figure 2.2.: Schematic working flow of the ab-initio program: In an inner self-consistency loop the CPA-medium is calculated and in an outer loop a charge self-consistent Hamiltonian is achieved

3. Model studies

In the last chapter, the BEB-CPA as a method dedicated to the calculation of the electronic structure of substitutionally disordered materials was introduced. From the underlying theoretical model it was obvious that unlike the conventional CPA also offsite disorder effects can be treated because the method assumes that disorder influences the onsite matrix elements as well as the hopping matrix elements. Which physical phenomena are captured or, to be more specific, which impact on the density of states such an incorporation of disordered hopping terms has, was not yet clarified and has to be elucidated before applying the method to particular problems of interest.

The analytic properties, limiting cases and quality of approximation of the conventional CPA have been studied elsewhere both numerically and analytically as for example in the extensive review by Elliott et al. [3]. First results for the BEB-CPA for different limiting cases were shown in the original paper by Blackman et al. [4]. Analytical work on simple model test systems like linear chains has been presented by Koepernik et al. [75]. This chapter is devoted to a numerical parameter study where the density of states (DOS) obtained within the BEB-CPA for a three dimensional model system is compared to results obtained from exact diagonalization which to my knowledge has not been performed before.

3.1. The model

For this study, rather than the *ab-initio* program, an implementation of the BEB-CPA for a tight binding Hamiltonian of the form

$$H = \sum_{i,j,P,Q} \eta_i^P W_{i,j}^{P,Q} \eta_j^Q c_i^\dagger c_j + \sum_{i,P} \eta_i^P \epsilon_i^P c_i^\dagger c_i \quad (3.1)$$

was chosen containing a species-dependent hopping matrix element W and onsite term ϵ - the same tight binding model, the original BEB-CPA was formulated for [4]. A binary alloy with two species A and B with the atomic concentrations c^A and $c^B = 1 - c^A$ on a three dimensional simple cubic lattice with nearest neighbor hopping was assumed. Apart from the concentrations, the free parameters are the hoppings W^{AA} , $W^{AB} = W^{BA}$, W^{BB} and the onsite energies ϵ^A and ϵ^B . For the desired comparison with a more exact method, a program developed by Robert Eder [80] was used which solves the model Eq. (3.1) on a finite cluster using exact diagonalization by means of the Lanczos' Method [81]. This finite cluster comprising 40x40x40 sites was randomly occupied with either A or B atoms and for configurational averaging the spectral function was evaluated at 6400 randomly chosen sites. At this cluster size, no substantial differences between a system with open or periodic boundary conditions were apparent. Without loss of generality we choose symmetric onsite energies $\epsilon^A = -\epsilon^B$ for the rest of this chapter.

3.2. Conventional coherent potential approximation

If all species dependent hopping matrix elements are set equal to each other, in particular in this section $W^{AA} = W^{BB} = W^{AB} = W^{BA} = 1.0$, the conventional CPA is recovered as a limiting case of the BEB-CPA. For this special case, where only onsite disorder is present, the density of states for equal concentrations $c^A = c^B = 0.5$ calculated from the conventional CPA is compared against the results obtained from exact diagonalization (ED) for several onsite energies in Fig. 3.1. The black curves for $\epsilon^A = 0$ correspond to the clean system without disorder. Upon increasing the difference between the onsite energies,

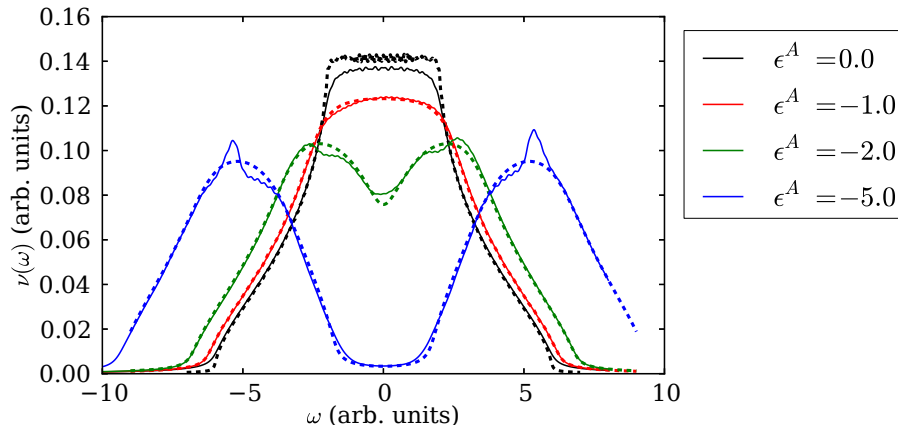


Figure 3.1.: Densities of states for $W^{AA} = W^{BB} = W^{AB} = W^{BA} = 1.0$ and $c^A = c^B = 0.5$ for several symmetric onsite energies $\epsilon^A = -\epsilon^B$ (different colors). Dashed thick lines: conventional CPA, solid thin lines: ED. Like all subsequent data plots in this thesis, this plot was generated via Matplotlib [82], an open-source python project for scientific plots

the single spectral peak first gets broadened until it starts to split into two local maxima which finally get separated from each other. Obviously, the transition to the split-band limit is qualitatively and quantitatively well reproduced by the CPA. At the same time, this also provides a nice example where the simpler virtual crystal approximation (VCA) fails, as already mentioned in Sec. 2.2.1, because just by averaging atomic potentials this band splitting cannot be captured.

Next, it is interesting to investigate the dependence of the DOS on the atomic concentrations. In order to reveal as much details as possible also by taking into account effects on single bands, this analysis was performed in the split-band limit for $\epsilon^A = -4.0$ for various concentrations in Fig. 3.2. The black curves here unlike before correspond to an ordered system with a single atomic species ($c^A = 1, c^B = 0$) with a *shifted* onsite energy $\epsilon^A = -4.0$ which just results in a rigid band shift of the peak obtained before in Fig. 3.1 in frequency to a position centered around ϵ_A but does not affect the shape of the peak. Upon lowering c^A and increasing c^B the height of the respective peaks also get lowered and increased in roughly the same ratio.

In summary, the concentration has a major influence on the peak height whereas the onsite energy is mainly responsible for the position in energy the peak is centered around. The slight asymmetry in the ED results at $c^A = 0.5$, which is obvious especially in the green curve of Fig. 3.2, is due to finite size effects of the considered cluster.

These two parameter studies exhibit an overall qualitative and quantitative agreement

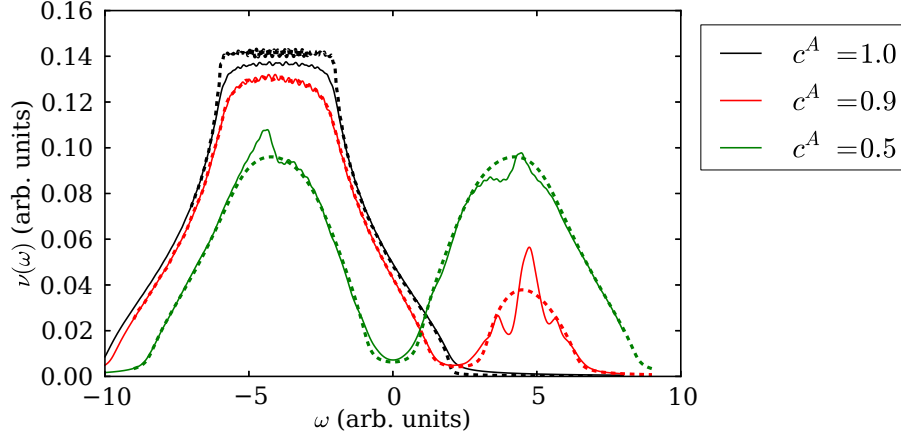


Figure 3.2.: Densities of states for $W^{AA} = W^{BB} = W^{AB} = W^{BA} = 1.0$ and symmetric onsite energies $\epsilon^A = -\epsilon^B = -4.0$ (split band limit) for several concentrations $c^A = 1 - c^B$ (different colors). Dashed thick lines: conventional CPA, solid thin lines: ED

between the CPA and ED apart from some fine structured features at the peaks in the ED results which are not reproduced by the CPA. At least in the green and blue curves in Fig. 3.1 as well as the green curve in Fig. 3.2 they look similar to a Fano lineshape [83], which is depicted in Fig. 3.3. Behind these curves lies the Fano-Anderson model [83] which describes the coupling of a single localized state to a continuum of states via the following Hamiltonian:

$$H_{FA} = \epsilon b^\dagger b + \sum_k \epsilon_k c_k^\dagger c_k + \sum_k V_k (b^\dagger c_k + c_k^\dagger b) \quad (3.2)$$

The operators b^\dagger (b) describe creation (annihilation) of a localized state with energy ϵ whereas the operators c_k^\dagger (c_k) create (annihilate) a continuum (or band) state k with energy ϵ_k . V_k is the hybridization between the localized state and a band state k . The single-particle Green's function of this model can be analytically calculated and the terms,

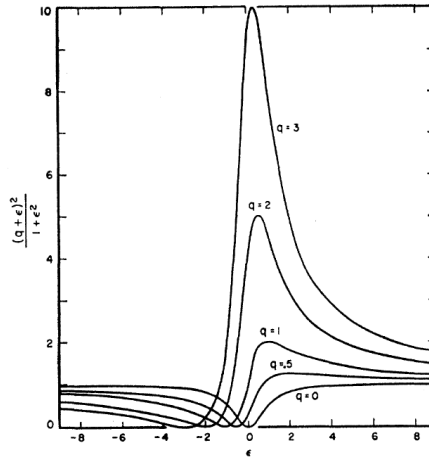


Figure 3.3.: Typical Fano lineshapes, taken from the original paper [83]

which describe the coupling of the localized state to the continuum just exhibit the above-mentioned lineshape depicted in Fig. 3.3. Thus, the similarity between the extra features in the ED results compared to the CPA and the Fano lineshape points towards an interpretation of these features as occurrence of localized electronic states. Such states could arise due to clusters inside the disordered system where an atom of type A is surrounded essentially by atoms of type B and vice versa. To test this hypothesis, configurations in the ED calculation, called C_6 , where all six nearest neighbors of a site occupied with one species are occupied with the other species, were excluded from the configurational average. This is a primitive way to exclude clusters of equal atomic types formed around an atom of different type thus giving rise to the formation of a localized state. This calculation was repeated with a weaker criterion C_5 , where only five of the six nearest neighbors have a different species as the central site. The comparison of the respective DOS with the unrestricted ED calculation and the CPA result is shown in Fig. 3.4 for $\epsilon^A = -4.0$, $c^A = 0.4$ and $c^B = 0.6$. In the calculation where the C_6 configurations were

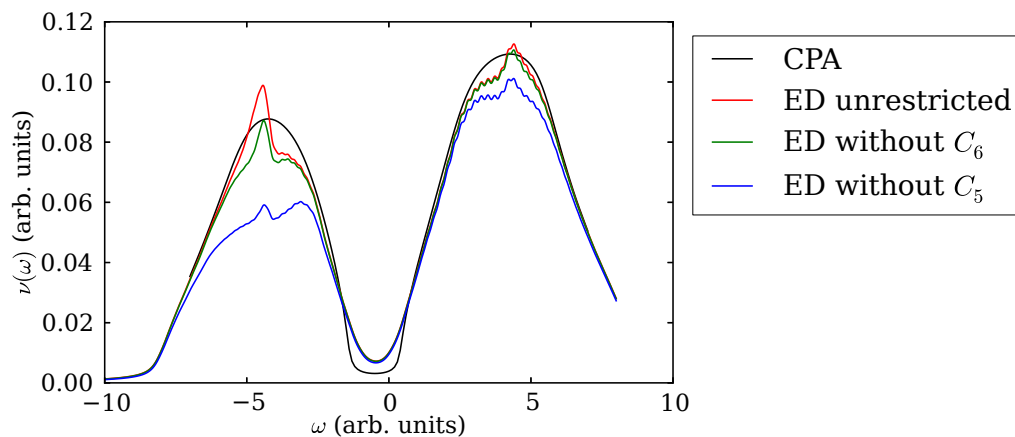


Figure 3.4.: Densities of states for $\epsilon^A = -\epsilon^B = -4.0$, $c^A = 0.4$ and $c^B = 0.6$ obtained within CPA (black), unrestricted ED of the full system (red), ED without clusters C_6 (green) and ED without clusters C_5 (blue)

excluded, the features in the DOS which were suspected to originate from localization get reduced. In the calculation without C_5 configurations they get more reduced. This is consistent because it holds $C_6 \subset C_5$ and for the probability of finding such a configuration $P(C_6) < P(C_5)$ so the C_5 configurations appear more frequently. This and the fact that these configurations really were removed from the DOS are the reasons why also the overall heights of the peaks decrease with a weaker criterion for cluster formation. Instead of removing such configurations, the CPA just smears them out by averaging which results in the smooth curves. Taking this into account, even if the smooth CPA curves could not be reproduced by this simple test, the observed behavior is sufficient to conclude that these features originate from clustering effects and obviously the CPA is not able to incorporate them. This could already have been guessed from the fact that the CPA is not sensitive to environmental disorder which is needed to identify clusters and has already been pointed out in several papers like for example [64].

3.3. Extension for environmental disorder

So far, the behavior of the CPA was illustrated and its overall agreement to ED was emphasized which certainly is one reason for the success of this method. However, these or similar results are already well established in the CPA community so the question arises which conclusions can be made for the BEB-CPA. Concerning the influence of the atomic concentrations and the onsite energies on the DOS, such an analysis revealed the same behavior as shown above for the conventional CPA and thus will not be repeated here. The more decisive issue is to figure out how the species dependent hopping matrix elements in Hamiltonian Eq. (3.1), which were not taken into account before, additionally affect the DOS. On the background that they extend the conventional CPA in providing a description of environmental disorder effects, it is interesting to see if the BEB-CPA may be able to capture localization effects. For fixed concentrations of $c^A = 0.4$, $c^B = 0.6$ as well as onsite energy $\epsilon^A = -4.0$ in the split band limit and fixed inter-species hopping $W^{AB} = W^{BA} = 1$, being the same set of parameters as used in test calculations in the original BEB-paper [4], a comparison of the DOS obtained from the BEB-CPA to ED results under variation of the intra-species hoppings W^{AA} and W^{BB} is shown in Fig. 3.5. For orientation, the black curve again shows the clean system parametrized by $c^A = 1$ and $\epsilon^A = 0$. The red curves show the results with all hopping terms being equal, which is the limiting case of the conventional CPA. Then, the W^{AA} -hopping is successively increased and the W^{BB} -hopping decreased. This causes a spectral broadening of the left peak centered around ϵ^A and a narrowing of the peak centered around ϵ^B . This can be understood because the bandwidth is proportional to the hopping in a tight-binding Hamiltonian. Because the particle number, being the area under the DOS, has to be conserved, the height of the broadened peak then gets reduced and the height of the narrowed peak gets increased. Again the DOS obtained by the BEB-CPA overall agrees very well with the ED results. Due to the fact that such a tight binding model with randomness in the onsite energies and the hopping terms is rather complicated, such an agreement of ED with a method which only relies on a single-site self-energy is striking. However, also in this calculation

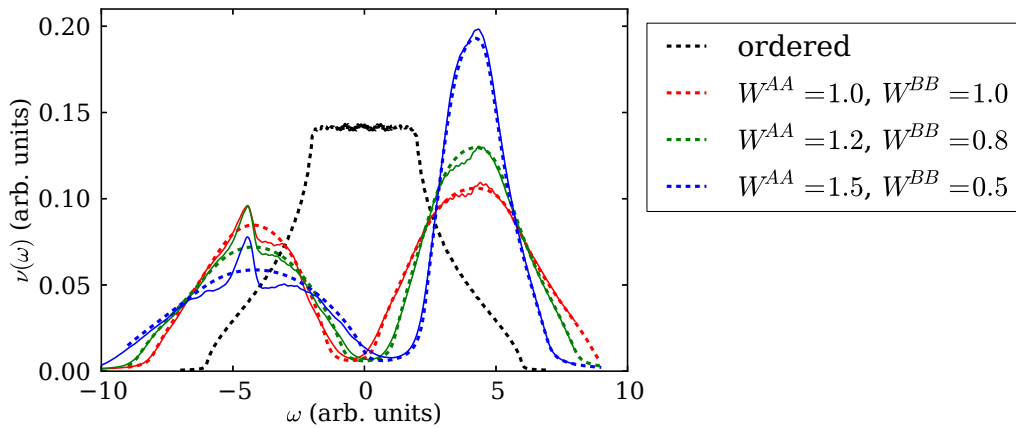


Figure 3.5.: Densities of states for $W^{AB} = W^{BA} = 1.0$ and symmetric onsite energies $\epsilon^A = -\epsilon^B = -4.0$ (split band limit), $c^A = 0.4$ and $c^B = 0.6$ for various species diagonal hopping matrix elements W^{AA}, W^{BB} (different colors). Dashed thick lines: conventional CPA, solid thin lines: ED

the ED results exhibit the same Fano-shaped features at the peaks which do not appear in the BEB-CPA, which is most obvious at the top of the left peak. This leads to the conclusion, that the BEB-CPA performs well in including environmental disorder effects beyond the conventional CPA in combination with the efficiency of a single site self-energy but is not sensitive to clustering phenomena.

4. $\text{Cu}_{1-x}\text{Zn}_x$ alloys as benchmark

In the last chapters I have introduced the BEB-CPA and outlined a scheme how to implement this method within a pseudopotential-LCAO framework to be able to tackle the problem of substitutionally disordered real materials from first principles. The BEB-CPA itself was verified on a simple tight-binding model against exact diagonalization to get an impression how well this method performs in the treatment of environmental disorder effects and where its principal limitations are.

The next step is to apply the full ab-initio implementation to a real material what will be the purpose of this chapter. Before applying the present methodology to rather complex materials, which are object of current research, one should start validating it with a simple compound which has well-known properties, has already been investigated by other implementations of a similar method and still may lead to instructive physical results. A typical system which satisfies these requirements and provides a realization of the split-band regime discussed in the last chapter in nature, is the binary $\text{Cu}_{1-x}\text{Zn}_x$ alloy where x is the impurity concentration. We are confronted with this metallic alloy in our everyday life - it is nothing else than brass and is most frequently used with a Zn-concentration of $x = 0.37$ [84].

4.1. Crystal structure and details of the calculation

This alloy exhibits several phases depending on the temperature and concentration. In this work only the so-called β -phase [84] was considered which has body-centered cubic (bcc) structure. The bcc-lattice constant was chosen $a = 2.86\text{\AA}$ after [18]. This bcc lattice is sketched in Fig. 4.1 (a) where the lattice vectors point along the space diagonals and the shading indicates random occupation. The unit cell contains only one atom with index 1. In the calculations an equivalent description in a simple-cubic (sc) lattice was chosen, as

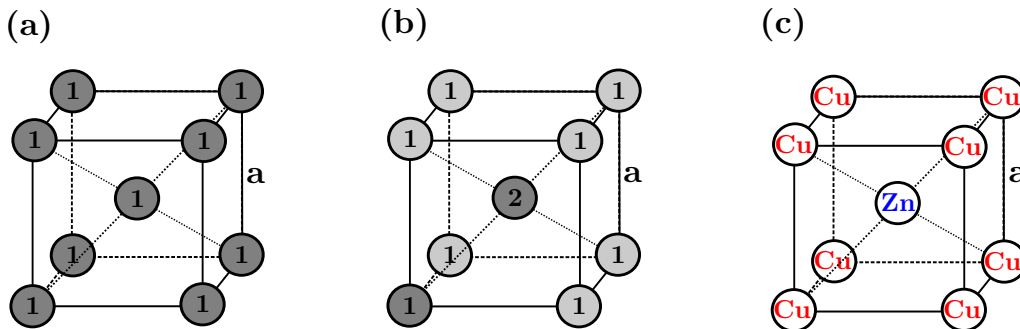


Figure 4.1.: (a): The randomly occupied (shaded) bcc lattice with one atomic site (indicated by 1) per unit cell, lattice constant a ; (b): The same structure described by a sc lattice with two sites (indicated by 1 and 2) per unit cell (darker shaded); (c): An ordered CuZn compound described in a sc lattice

depicted in Fig. 4.1 (b) with two atomic sites per unit cell, where site 1 is located at $(0,0,0)$ and site 2 is located at $\frac{a}{2}(1,1,1)$. The lattice vectors point along the solid lines and the two atomic sites belonging to the same unit cell are darker shaded. The main reason for this choice was to compare with an *ordered* CuZn compound which is shown in Fig. 4.1 (c). From a technical point of view, this was also needed to test the method for nontrivial unit cells.

The DFT calculations for both end-members were performed on a regular $8 \times 8 \times 8$ Monkhorst-Pack [85] \mathbf{k} -mesh for Brillouin zone integration using norm-conserving pseudopotentials constructed after Vanderbilt [7] by Rolf Heid [86] together with one local d -type function and plane waves up to a cutoff energy of 30 Ry. The XC-potential was treated within the local density approximation (LDA) using a parametrization after Hedin and Lundqvist [87]. For each atomic type, nine local basis functions up to angular momentum $l = 2$ are used in the CPA program where the radial functions were generated by the LCAO-fit from the bare localized functions $^{MBP}f_l^P(r)$ of the MBPP calculation via the cutoff function

$$f_l^P(r) = \left[1 - e^{-\gamma_l^P (R_{C,l}^P - \lambda_l^P r)^2} \right] ^{MBP} f_l^P(r) \quad (4.1)$$

The cutoff radii $R_{C,l}^P$ and function parameters $(\lambda_l^P, \gamma_l^P)$ yielded by the fit to achieve a good description of the bandstructure in the localized basis, are listed in Tab 4.1 and the corresponding radial functions are shown in Fig. 4.2.

Atomic type P	l	λ_l^P	γ_l^P	$R_{C,l}^P$ (Bohr)
Cu	0	0.9510	0.2375	6.0
Cu	1	0.9404	0.1669	6.0
Cu	2	0.9943	0.4817	6.0
Zn	0	0.9487	0.4135	6.0
Zn	1	0.9551	0.2960	6.0
Zn	2	0.9786	0.5012	6.0

Table 4.1.: LCAO fit parameters

Compared to the nearest neighbor distance of 4.68 Bohr in this compound, these wavefunctions, especially the $l = 0$ and $l = 1$ contribution, are rather extended and thus considerably overlapping which immediately shows the necessity of taking into account the overlap matrix when formulating the BEB-CPA for such a basis set. Furthermore, the wavefunctions are quite similar for Cu and Zn, the largest deviations occur for the more localized d -states.

As already mentioned in Sec. 2.2.4, in the LCAO fit the spillage function is optimized which measures the difference in the electronic density from the MBPP to the one obtained in the LCAO representation. For a last quality check of the LCAO fit in Fig. 4.3 the bandstructure obtained within the MBPP calculation is compared to the one calculated in the LCAO part and they both agree very well.

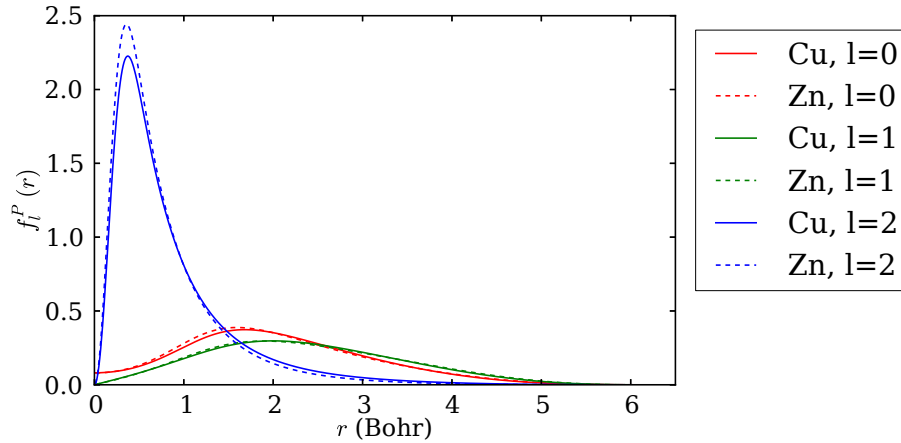


Figure 4.2.: Radial basis functions $f_l^P(r)$ used for the CPA-calculations for Cu (solid) and Zn (dashed) for different angular momenta l (color)

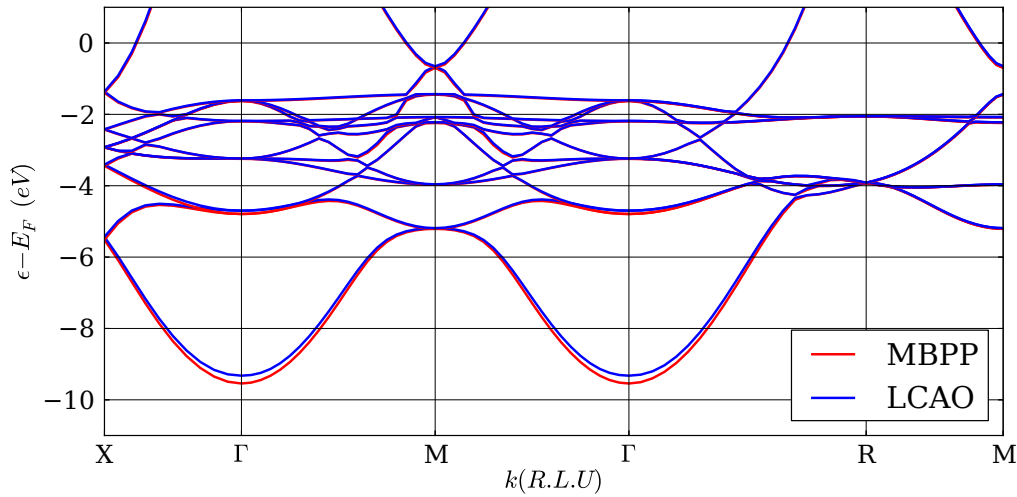


Figure 4.3.: Band structure of pure Cu obtained from the MBPP-DFT calculation (red) compared against the LCAO representation

4.2. Density of states

Especially for testing the method in this chapter but also in general applications to new terrain, the results obtained from a CPA calculation for the unsubstituted end members should be compared with those obtained from DFT to check if all cutoff parameters (see App. A) are appropriately chosen. In the left panel of Fig. 4.4 the density of states (DOS) of pure Cu obtained from the CPA program is compared against the DFT result and in the right panel the same is shown for pure Zn. Apart from some wiggles due to numerical noise in the tails of the DOS, these results agree very well, which shows that the CPA implementation works for the pure systems. These CPA results were obtained after one charge iteration but further charge iterations do not change anything which means that these calculations are already charge self-consistent. In more complicated compounds like e.g. the iron pnictides this is not self-evident because there the local basis representation

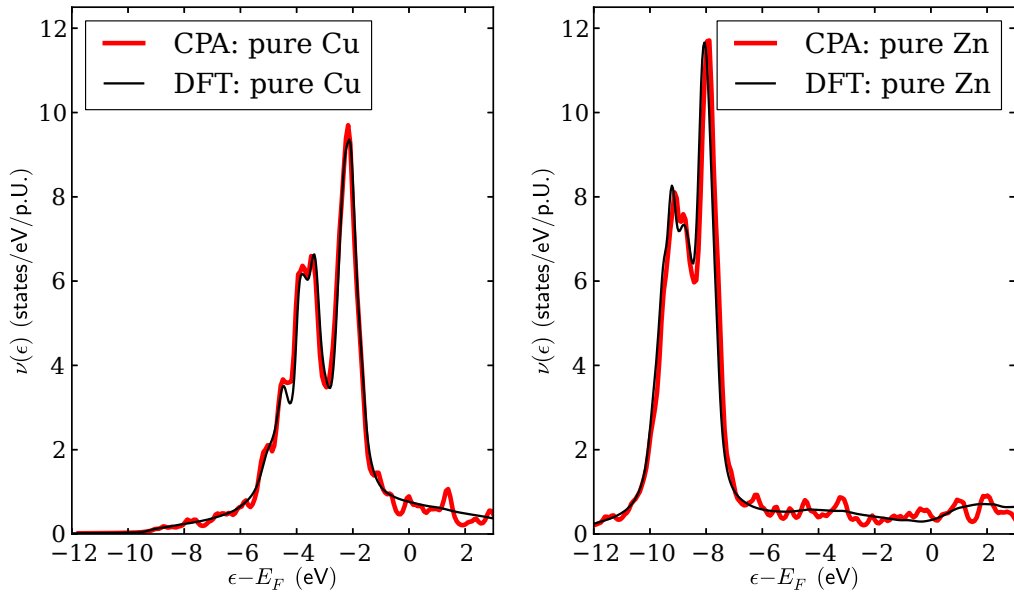


Figure 4.4.: Density of states of pure Cu (left) and pure Zn (right) obtained within the CPA (red) after one charge iteration against DFT (black)

and further approximations made in the CPA program in the treatment of the exchange correlation potential and summation cutoffs do not deliver such a good starting point like here and the program needs some charge iterations to converge already for the pure compounds. Physically, these results exhibit peaks with relatively strong localization which arises from the fact that mainly d -states contribute to the DOS in this energy regime. The peak of the Zn DOS is lower relative to the Fermi energy than the one of Cu which originates from a higher number of valence electrons for Zn. Those two effects together are responsible for these compounds ranging in the split-band regime. Furthermore, the peaks essentially consist of two secondary maxima which is a manifestation of the crystal field splitting of the e_g (at higher energy) and t_{2g} (at lower energy) states characteristic for these elements.

After having verified that the CPA leads to reasonable results for the clean case, let me now focus on the more interesting disordered case $\text{Cu}_{0.5}\text{Zn}_{0.5}$. In Fig. 4.5 the DOS of this disordered compound obtained by the CPA after one charge iteration and the self-consistent result after 17 iterations are compared against the DOS of an ordered CuZn compound. The changes due to charge self-consistency are rather small. The DOS of the ordered compound essentially contains peaks at the same positions in energy as already the pure Cu and Zn calculations in Fig. 4.4 did but they get narrower. Bearing in mind that the bandwidth is correlated to the hopping, this can be interpreted as a reduced probability of an electron e.g. located at a Zn atom to hop to another Zn atom because all nearest neighbors are now Cu atoms as can be seen from Fig. 4.1 (c). The DOS of the disordered system does not shift in energy compared to the ordered system but the peaks get broadened due to disorder. This can be understood as an enhanced probability compared to the ordered system for an electron e.g. located at a Zn atom to hop to another Zn atom because the atoms now are randomly distributed and not every nearest neighbor is a Cu atom. The same behavior was also obtained from a KKR-CPA calculation

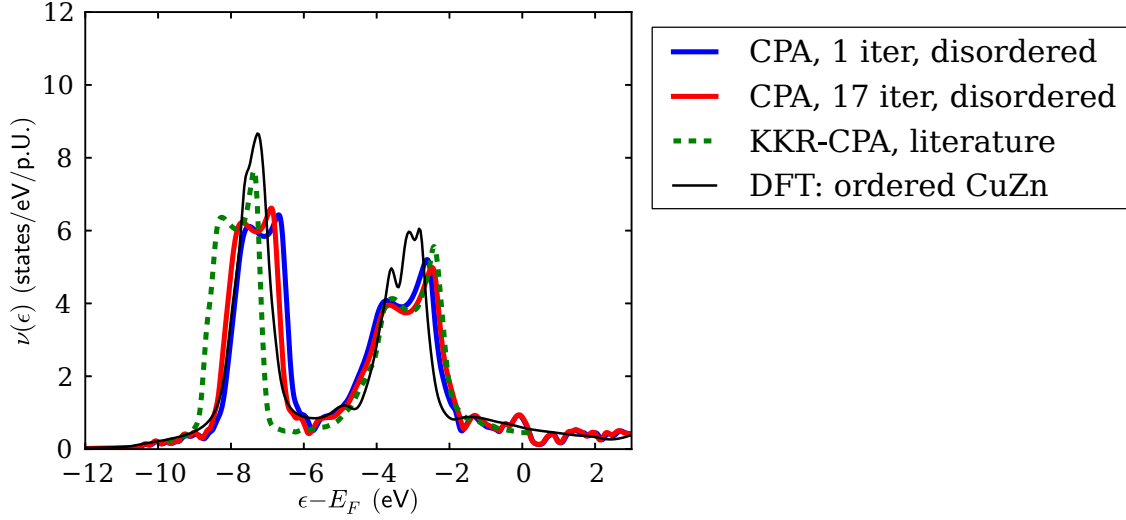


Figure 4.5.: Density of states of ordered CuZn (black) compared with the disordered case $\text{Cu}_{0.5}\text{Zn}_{0.5}$ obtained from the BEB-CPA within this work after one (blue) and 17 (red) charge iterations together with KKR-CPA results (dashed green) from [18]

[18] and the only difference to the present result consists in the positions of the peaks. This can be attributed to the different DFT approaches (KKR vs. MBPP) and is not a shortcoming of the present CPA implementation because already the results for the DOS of the ordered CuZn compound exhibit these shifts in the peak positions. As already mentioned before, this DOS is a realization of the split-band regime discussed in Chap. 3 and thus provides an example of a material class where a first principles implementation of the simpler virtual crystal approximation (VCA) would lead to wrong results. The calculations of the disordered alloy still exhibits the double-peak features due to the e_g - t_{2g} crystal field splitting but they get smeared due to disorder.

To study the behavior of the ab-initio method at arbitrary impurity concentrations, what was initially stated as the main goal, the DOS obtained after one charge iteration for several compositions are shown in Fig. 4.6. These results essentially show the same behavior for real materials as already obtained from the model calculations in Chap. 3 in the split-regime - the ratio of the peak heights correlates to the ratio of the concentrations. The peaks centered around the onsite energy of a species also in the general case exhibit the e_g - t_{2g} -splitting if the concentration of this species is sufficiently high.

4.3. Bloch spectral function

The Bloch spectral function $A(\omega, \mathbf{k})$ which was introduced in Sec. 2.2.4 and is given by Eq. (2.73) contains all information about the band structure of the disordered system. In addition to the DOS which is well suited to get a rough overview about the essential effects induced by disorder, $A(\omega, \mathbf{k})$ serves to study momentum-resolved disorder effects in detail. The Kohn-Sham band structure of a pure compound is essentially the Kohn-Sham energy eigenvalues obtained from solving Eq. (2.5) evaluated along a path in \mathbf{k} -space and thus only depends on the variable \mathbf{k} . The ω -dependence of the associated Bloch spectral func-

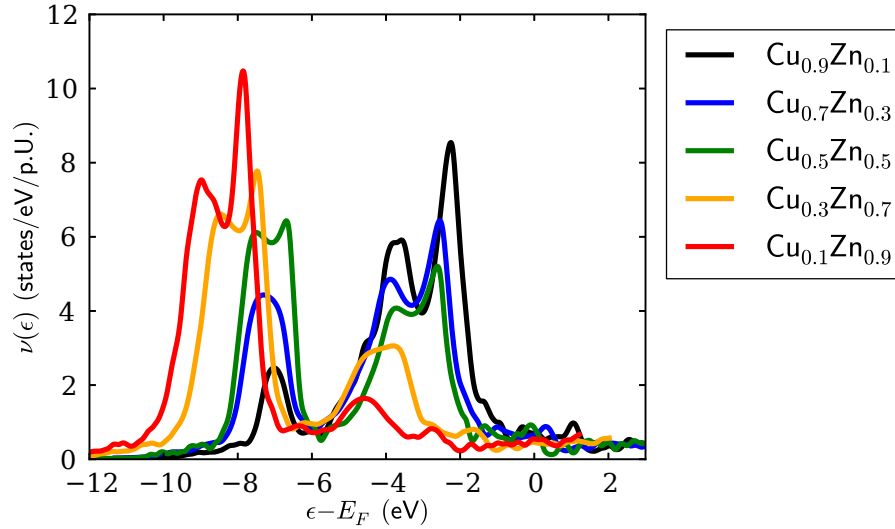


Figure 4.6.: Densities of states of disordered $\text{Cu}_{1-x}\text{Zn}_x$ obtained after one charge iteration for several compositions

tion is trivial - it is just a set of δ -peaks centered at the energy eigenvalues. In practice, $A(\omega, \mathbf{k})$ for a pure compound evaluated by the CPA becomes a set of Lorentz-peaks with a finite spectral width. This spectral width originates from the infinitesimal imaginary part of the frequency $\omega + i\delta$ needed for the evaluation of the Green's function but does not depend on \mathbf{k} . In contrast to this, $A(\omega, \mathbf{k})$ of a disordered system has a nontrivial frequency dependence and the spectral width can be \mathbf{k} -dependent. Comparing the spectral function of the disordered system to that of the clean system thus provides level shifts and spectral broadenings which are the real and imaginary part of the electronic self-energy due to disorder, respectively. In particular the spectral broadenings or imaginary parts of the self energy are proportional to the inverse lifetimes of the electronic states which are infinite in the pure system and become finite in the disordered system due to scattering of the electrons on impurities.

Whereas for the band structure of a pure system an ordinary two dimensional plot of $\epsilon(\mathbf{k})$ against \mathbf{k} is sufficient, $A(\omega, \mathbf{k})$ often is visualized in a color plot if it exhibits a nontrivial ω -dependence. Therein, the x -axis represents the path in \mathbf{k} -space, the y -axis the frequency and the actual value of $A(\omega, \mathbf{k})$ is shown as a false color code. This has the advantage that it still looks similar to a bandstructure and thus can be directly compared with the pure compound. For the charge self-consistent calculation of disordered $\text{Cu}_{0.5}\text{Zn}_{0.5}$, of which the DOS was shown in Fig. 4.5, such a color plot of $A(\omega, \mathbf{k})$ is shown together with the band structure of the ordered CuZn compound in Fig. 4.7. As already mentioned above, $A(\omega, \mathbf{k})$ of the pure system obtained from the CPA for numerical reasons exhibits a finite but trivial spectral width which is not contained in Fig. 4.7 because here just the DFT band structure of the pure compound is overlaid (overlying two color plots would not be helpful). This has to be kept in mind when interpreting such plots.

Doing so, from Fig. 4.7 it is still evident that the rather step bands next to the Fermi level and below -8 eV get hardly affected by disorder and in particular not broadened. In contrast, the rather flat bands in the region between -8 and -6 eV as well as between -4 and -2 eV get strongly affected, i.e. shifted and especially broadened due to impurity scat-

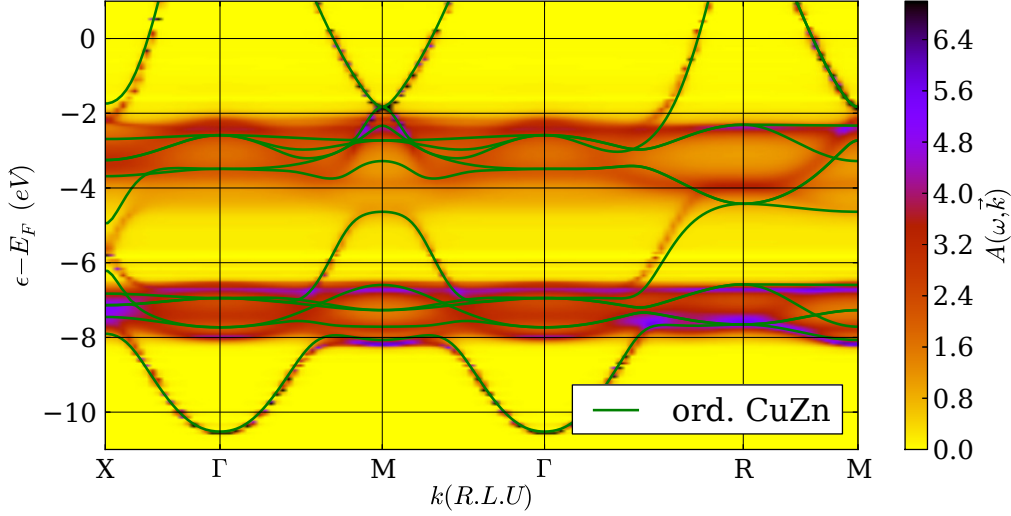


Figure 4.7.: Charge self-consistent Bloch spectral function $A(\omega, \mathbf{k})$ of disordered $\text{Cu}_{0.5}\text{Zn}_{0.5}$ (false color) together with band structure of ordered CuZn (green)

tering. These two regions correspond to the two peaks in the DOS. These color plots are well suited to provide a qualitative picture but for a quantitative analysis of these effects one needs to resort to more advanced techniques which will be done in Chap. 5 about the iron pnictides.

Further detailed information can be gained by instead of looking at the full spectral function just investigating a projection of $A(\omega, \mathbf{k})$ on a certain species and angular momentum. This was accomplished in this work by restricting the trace in the expression for the spectral function

$$A(\mathbf{k}, \omega) = -\frac{1}{\pi} \text{Im Tr} \left[\underline{S}(\mathbf{k}) \underline{\Gamma}(\mathbf{k}, \omega^+) \right] \quad (4.2)$$

to an appropriately chosen orbital subspace instead of evaluating it in the full Hilbert space. For the segment of the path in \mathbf{k} -space between Γ and P, the full spectral function of Fig. 4.7 is compared with its projections on Cu- d and Zn d -states in Fig. 4.8. From this plot we can conclude that only the Cu- d states (upper region of flat bands) and the Zn- d states (lower region of flat bands) get strongly affected by disorder and thus experience a reduction of lifetime whereas the s and p -states get at best slightly shifted. Of course, a similar analysis could also have been carried out on the level of the DOS which is also implemented in the program.

4.4. Partial substitutions

As a last example to conclude the discussion about this simple test system, I want to focus on a partially substituted alloy. On the one hand this provides further interesting physical insights and on the other hand it shows that the developed method can also handle arbitrarily complex compounds with different substitutions on different sites. Again, consider the disordered alloy in the simple cubic structure but assume that Zn substitutions are only allowed to occur on one of the two sublattices with $x = 0.5$ and the occupa-

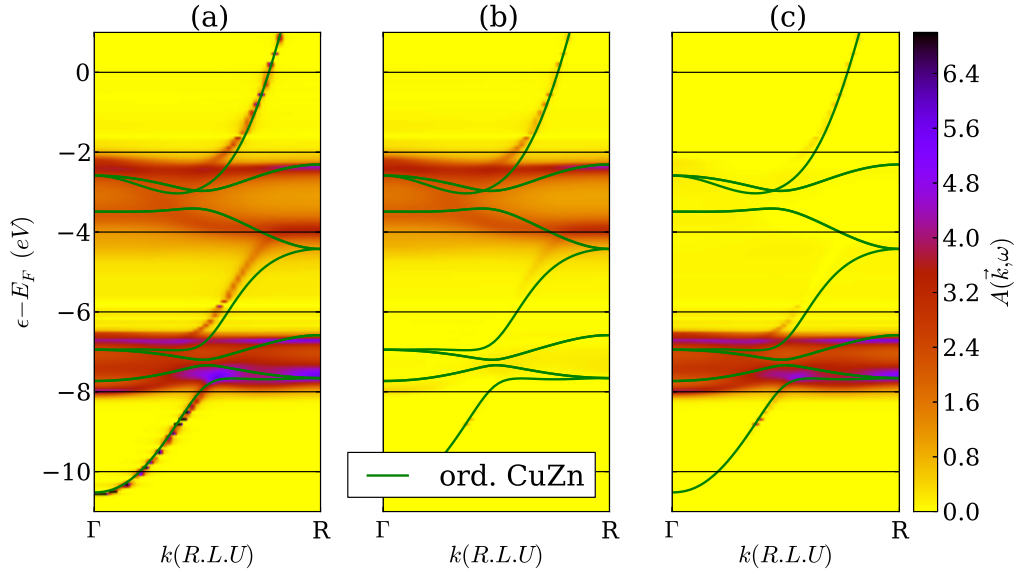


Figure 4.8.: (a): Total charge self-consistent Bloch spectral function $A(\omega, \mathbf{k})$ of disordered $\text{Cu}_{0.5}\text{Zn}_{0.5}$ (false color) together with band structure of ordered CuZn (green); (b): Projection on Cu-d -states; (c): Projection on Zn-d -states

tion with Cu on the other sublattice is unaffected, which is depicted in Fig. 4.9. Let us call this alloy configuration $\text{Cu}_{0.5}\text{Zn}_{0.5}\text{Cu}$ and the homogeneous substitutions, where both atoms are substituted as considered in the previous sections $(\text{Cu}_{1-x}\text{Zn}_x)_2$. The DOS of such a configuration is plotted in Fig. 4.10 together with those of the homogeneous alloys $(\text{Cu}_{0.5}\text{Zn}_{0.5})_2$ and $(\text{Cu}_{0.75}\text{Zn}_{0.25})_2$ as well as the ordered CuZn compound as a reference. These calculations are not charge self-consistent. Essentially, we obtain the same two-peak structure and the peaks do not get shifted with respect to the ordered system. The upper peak, which originates from the Cu-d -states, almost coincides with the respective peak of the $(\text{Cu}_{0.75}\text{Zn}_{0.25})_2$ calculation. The lower peak, which originates from the Zn-d -states, has a narrower spectral width than in the $(\text{Cu}_{0.75}\text{Zn}_{0.25})_2$ calculation but the same height as in the $(\text{Cu}_{0.5}\text{Zn}_{0.5})_2$ calculation. In Sec. 3.3 it was shown, that the species-diagonal hopping has considerable impact on the width of the DOS in the split-band limit. For an electron located at a Cu atom the probability to hop to another Cu atom does not change between the $(\text{Cu}_{0.75}\text{Zn}_{0.25})_2$ and the $\text{Cu}_{0.5}\text{Zn}_{0.5}\text{Cu}$ alloy configuration because in

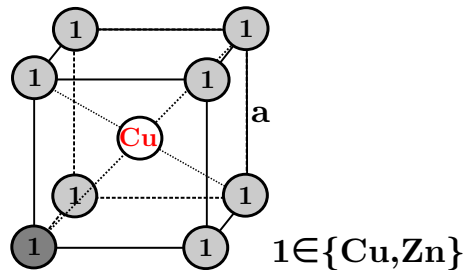


Figure 4.9.: Partially substituted CuZn alloy: only site 1 in the sc structure is substituted whereas the occupation of site 2 by Cu is held fixed

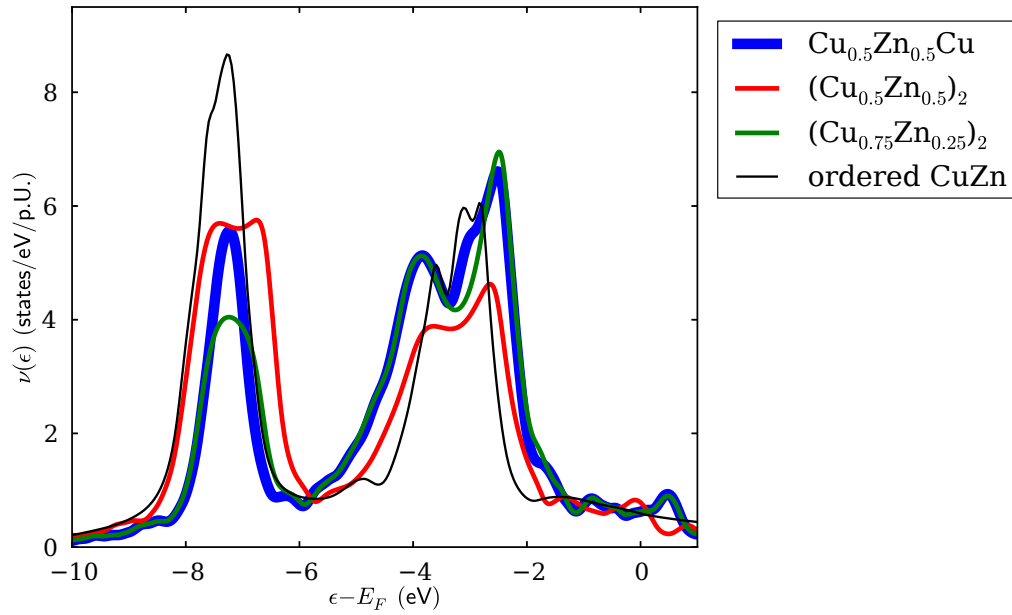


Figure 4.10.: Densities of states after one charge iteration of disordered partially substituted $\text{Cu}_{0.5}\text{Zn}_{0.5}\text{Cu}$ (blue) together with homogeneously substituted $(\text{Cu}_{0.5}\text{Zn}_{0.5})_2$ (red) and $(\text{Cu}_{0.75}\text{Zn}_{0.25})_2$ (green) and the ordered CuZn (black)

both cases effectively 25% of the Cu atoms are substituted by Zn. For an electron at the Zn atom the probability to hop to another Zn atom gets reduced compared to the $(\text{Cu}_{0.75}\text{Zn}_{0.25})_2$ case because one of its nearest neighbors is always fixed to be Cu. Due to particle number conservation the peak height then gets increased - that it just coincides with the height in the $(\text{Cu}_{0.5}\text{Zn}_{0.5})_2$ calculation has no deeper physical reason.

5. Substitutionally disordered BaFe_2As_2

Being armed with a powerful ab-initio method to treat substitutional disorder in complex real materials at arbitrary impurity concentrations and having convinced ourselves of its functionality in the last chapter, now the time has come to apply it to an interesting physical system being subject of ongoing research. The iron based superconductors (FeSC) represent a material class, where chemical substitution is an important tuning parameter. A huge amount of still ongoing experimental and theoretical work has been spent on these compounds in the last years by several groups in the condensed matter community. In the next sections, I will give a brief introduction into this field.

5.1. Iron based superconductors: brief introduction

Back in 2008, the group of Hideo Hosono in Tokyo were the first to discover superconductivity with a critical temperature of $T_c = 26$ K in $\text{LaFeAsO}_{1-x}\text{F}_x$ [20]. This discovery led to a rapid development in the study of different families of iron pnictides and iron chalcogenides with a big variety of chemical substitutions, where critical temperatures up to $T_c = 56$ K [21] were observed. After the research in the cuprates, defining the first era of high temperature superconductivity, was slowing down, this discovery was sort of revitalizing the field leading to a second era of research on high T_c materials, by some people also called "the iron age of superconductivity".

Superconductivity, which most prominently is characterized by an abrupt drop in electrical resistivity from a finite value to zero below a critical temperature T_c , was first discovered by Heike Kamerlingh Onnes in 1911 in elemental metals (mercury, tin and lead). Superconductivity seemed to be finally explained by the microscopic theory of Bardeen, Cooper and Schrieffer (BCS) [38] in 1957. This theory is founded on an idea by Cooper [88] who showed that in the presence of an arbitrarily weak attractive interaction between the electrons, the whole Fermi sea gets unstable and undergoes a phase transition into an energetically favorable state where the electrons form pairs, the so called Cooper pairs. In conventional superconductors, this attractive interaction, which is often called the "pairing glue" in the community, is mediated by electron-phonon coupling. Based upon this theoretical framework, all superconducting materials until the 1980's seemed to be understood and the interest in this field was decreasing at that time.

The discovery of the cuprate high T_c superconductors in 1986 by Bednorz and Müller [47] severely changed this belief because these compounds could not be explained by such a conventional picture and thus were considered as unconventional superconductors. Moreover, a generally accepted picture to understand the origin of superconductivity in the cuprates until now is still lacking.

The phenomenon of superconductivity is not only characterized by a drop in electrical resistivity below T_c . Furthermore, any magnetic field gets expelled from the bulk of a superconductor which is called the Meissner effect [22]. Vice versa, if a magnetic field exceeds a certain critical value, the superconducting state gets destroyed. For this reason, it was

hard to imagine to find superconductivity in a compound containing iron which is a magnetic element before Hosono's discovery. At this point, there is strong evidence that iron based superconductors are unconventional as well: From the theory side, Mazin et al. [34] found no sufficiently high electron-phonon coupling in first-principles calculations to explain the value of T_c in $\text{LaFeAsO}_{1-x}\text{F}_x$ and were the first to suggest an unconventional s^{+-} pairing scenario where the order parameter exhibits s -wave symmetry and changes sign between different Fermi surface sheets. In neutron-scattering experiments, an anisotropic superconducting gap [89] and a resonance mode was found in the superconducting state [90] where the latter was interpreted as signature of unconventional superconductivity mediated by spin fluctuations. In Josephson-effect measurements [91, 92], being a phase-sensitive technique to gain information about the gap symmetry, evidence for the s^{+-} pairing state was reported. Investigations of quasiparticle interference in $\text{FeSe}_{1-x}\text{Te}_x$ [93], being phase sensitive as well, measured by spectroscopic-imaging scanning tunneling microscopy, also agree with the s^{+-} pairing scenario. More generic model calculations [36] show that magnetic fluctuations in FeAs-based systems can lead to an s^{+-} -state as well. The enthusiasm causing a very huge scientific output in that field was certainly not least driven by the hope that understanding these compounds could maybe also be helpful to get a more coherent picture about the cuprates.

In most families of the iron pnictide compounds which I will give a brief overview about in the next section, there appears no superconducting state in the parent compound under normal conditions - one either has to apply pressure or perform chemical substitutions to make them superconducting. What chemical disorder actually accomplishes in these compounds, in particular, if it really leads to charge doping and how it influences superconductivity, is not yet fully understood and still discussed controversially as will be discussed in more detail later. This gave the motivation to address these questions by a systematic first-principles study of various substitutions in one prominent representative of the 122-family, the BaFe_2As_2 system, which this chapter is devoted to.

5.1.1. Various families of iron based superconductors

As already mentioned above, there exist different families of FeSC which can be distinguished by their composition. In Fig. 5.1 the four most prominent families are depicted after [94]. One structural element they all have in common, are layers consisting of iron atoms which form a planar square lattice surrounded by pnictogen (Pn) or chalcogen atoms in distorted tetrahedral coordination. These families differ in the spacer layers between the $\text{Fe}Pn$ -layers. The 11-family, being structurally the most simple, contains no spacer layer at all. In the 111-family one Li or Na atom is located between the $\text{Fe}Pn$ -layers. In the 1111-family, which is actually the family where the first FeSC $\text{LaFeAsO}_{1-x}\text{F}_x$ discovered by Hosono [20] belongs to, the $\text{Fe}Pn$ -layers alternate with rare-earth / oxygen layers. Last but not least, in the 122-family the intermediate layer is made up of one alkali or alkaline earth atom per two Fe atoms. This is the most intensively studied system. The BaFe_2As_2 compound belongs to this family and will be the system standing in the focus of the remaining part of this work.

5.1.2. General properties of BaFe_2As_2

Since superconductivity in K substituted $\text{Ba}_{0.6}\text{K}_{0.4}\text{Fe}_2\text{As}_2$ was first discovered by Rotter et al. [95] in 2008 with $T_c = 38\text{ K}$, this system was intensively studied with various

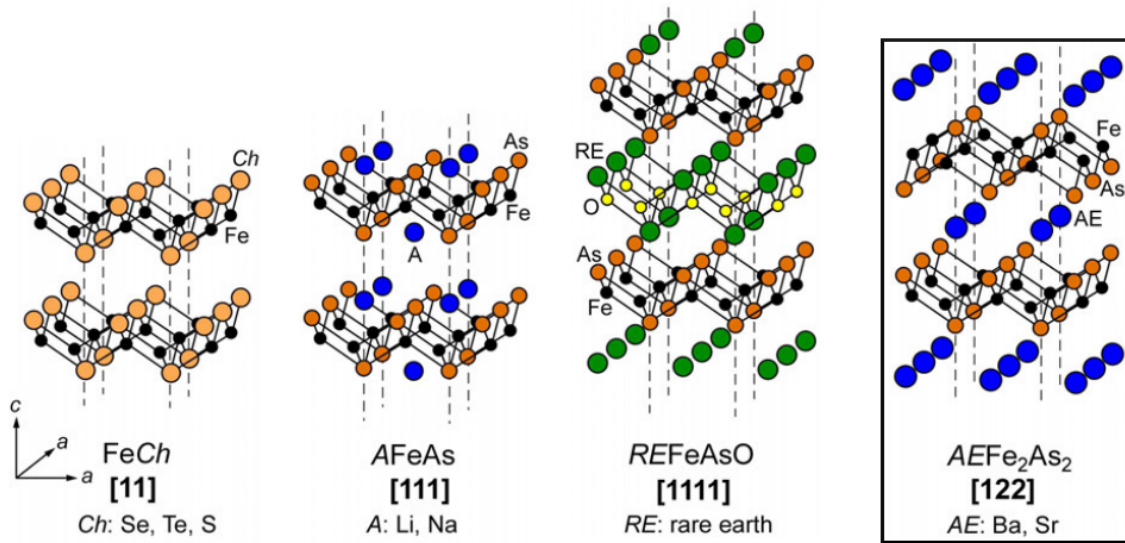


Figure 5.1.: Crystal structures of four most prominent families of FeSC (figure reproduced from [94]). Common among all: layers of planar iron atoms with tetrahedrally connected pnictogen or chalcogen atoms; Difference: type of spacer layers in between

substitutions - in particular also at the Fe site by other transition metals (TM). Belonging to the 122-family, the crystal structure has the space group $I4/mmm$. In this work, the crystal structure at room temperature is chosen, which can be described by a body-centered tetragonal (bct) lattice with five atoms per primitive unit cell, containing just one formula unit of $BaFe_2As_2$. A tetragonal cell containing two formula units of $BaFe_2As_2$ is visualized in Fig. 5.2, where the atoms of the primitive unit cell selected in this work are brighter and the remaining atoms are shaded for orientation. Therein, the Ba atom

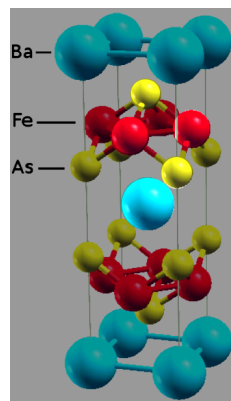


Figure 5.2.: Crystal structure of $BaFe_2As_2$ (modified figure from [96]). The five brighter atoms belong to the unit cell chosen in this work

sits at the origin of the unit cell such that they form the bct lattice. The lattice vectors

then are given by

$$\mathbf{a}_1 = \frac{1}{2} \begin{pmatrix} -a \\ a \\ c \end{pmatrix} \quad \mathbf{a}_2 = \frac{1}{2} \begin{pmatrix} a \\ -a \\ c \end{pmatrix} \quad \mathbf{a}_3 = \frac{1}{2} \begin{pmatrix} a \\ a \\ -c \end{pmatrix} \quad (5.1)$$

and the atomic positions

$$\begin{aligned} \mathbf{R}_{\text{Ba}} &= \begin{pmatrix} 0 \\ 0 \\ 0 \end{pmatrix} & \mathbf{R}_{\text{Fe}_1} &= \begin{pmatrix} a/2 \\ 0 \\ c/4 \end{pmatrix} & \mathbf{R}_{\text{Fe}_2} &= \begin{pmatrix} 0 \\ a/2 \\ -3c/4 \end{pmatrix} \\ \mathbf{R}_{\text{As}_1} &= z \begin{pmatrix} 0 \\ 0 \\ c \end{pmatrix} & \mathbf{R}_{\text{As}_2} &= z \begin{pmatrix} 0 \\ 0 \\ -c \end{pmatrix} \end{aligned} \quad (5.2)$$

The structural parameters used in all what follows were measured by Drotziger et al. [97] to be $a = 3.966\text{\AA}$, $c = 13.037\text{\AA}$ and $z = 0.354$.

Like the most other FeSC, also BaFe_2As_2 exhibits a complicated interplay of structural and magnetic phases with superconductivity, which is governed by chemical substitution. To get an overview for this interplay, Fig. 5.3 shows an experimental phase diagram which was compiled by Böhmer [26] comparing K-substitution, the two common TM substitutions Co and Ni, and P substitution. The individual data sets of this compilation were taken from references [26] ($\text{Ba}_{1-x}\text{K}_x\text{Fe}_2\text{As}_2$, thermal expansion), [25] ($\text{BaFe}_2(\text{As}_{1-x}\text{P}_x)_2$, thermal expansion), [23] ($\text{Ba}(\text{Fe}_{1-x}\text{Co}_x)_2\text{As}_2$, specific heat and thermal expansion) and [24] ($\text{Ba}(\text{Fe}_{1-x}\text{Ni}_x)_2\text{As}_2$, specific heat and transport). The degree of substitution is normalized such that 1.0 always corresponds to optimal doping. K substitution in the naive picture of a rigid band shift is expected to introduce holes to the system and is plotted to the right side of the phase diagram, whereas TM substitutions are expected to introduce electrons and are plotted to the left side. P substitution is isovalent but at least with respect to this normalized substitution behaves similarly to TM substitution and thus is

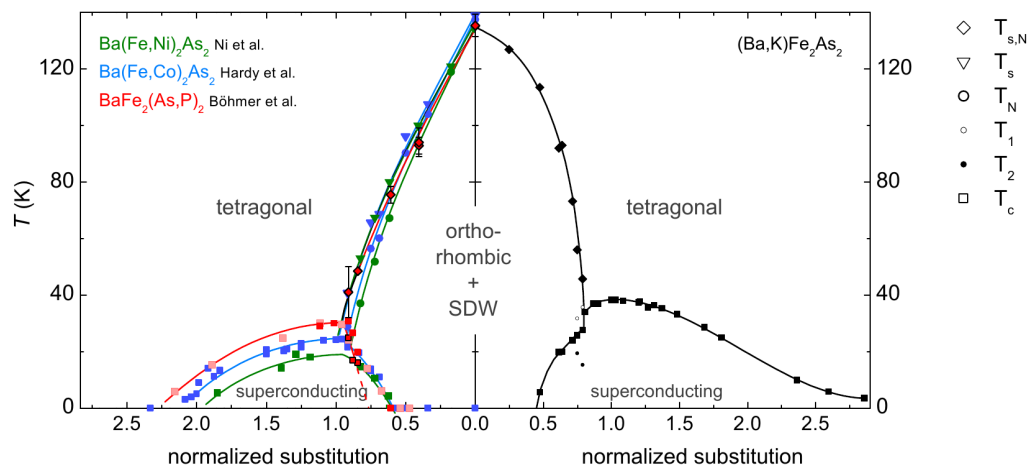


Figure 5.3.: Compilation of temperature - substitution phase diagrams for BaFe_2As_2 for different substitutions, substitution is normalized to optimal doping, figure taken from [26]

also plotted to the left side.

At room temperature, all compositions exhibit a tetragonal, paramagnetic phase. For a low degree of substitution, below the Néel temperature, which strongly depends on substitution, the compounds undergo a transition into an orthorhombic phase with stripe antiferromagnetic order, called the spin-density-wave (SDW) state in Fig. 5.3. The dependence of the Néel temperature on normalized substitution is similar for TM and P substitution but assumes a different shape for K substitution. Upon further lowering the temperature, the system can enter the superconducting state depending on the substitution, where a certain window exist within which this transition is possible. For obvious reasons this is called the superconducting dome. For K substitution appears the largest superconducting dome with highest T_c . Even on this normalized substitution scale it is obvious that the P substituted compounds exhibit a smaller superconducting dome which successively becomes smaller for Co and Ni substitution. As we shall see later, these effects are more drastic on the actual impurity concentration scale (see Fig. 5.5). This behavior will be revisited again in Sec. 5.7 about the impact of impurity scattering on superconductivity.

A 3d plot of the Fermi surface of stoichiometric BaFe_2As_2 obtained from an LDA-DFT calculation performed by Singh [98] is shown in Fig. 5.4. The hole-like and electron-like Fermi surfaces in general assume the form of warped (or twisted) cylinders around an axis parallel to \mathbf{k}_z . It exhibits three hole-like sheets (Fig. 5.4 resolves only two, because

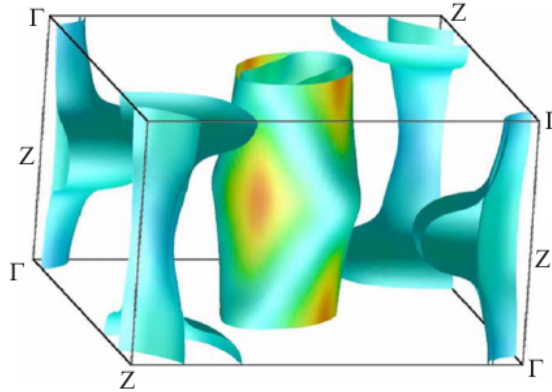


Figure 5.4.: The Fermi surface of stoichiometric BaFe_2As_2 obtained from LDA-DFT, figure from [98]

two of them are almost degenerate) around the zone center (Γ -point). Further, it exhibits two electron-like sheets around the zone edge (X -point). The projections of this Fermi-surface into the $(\mathbf{k}_x, \mathbf{k}_y)$ -plane, which I will deal later with, are essentially concentric ellipses around the Γ and X point. Obviously, the radius of the outer hole circle then depends on \mathbf{k}_z . Less obviously, also the angles between the axes of the ellipses of the electron Fermi surfaces depend on \mathbf{k}_z .

5.1.3. Open questions and goals of this work

In Fig. 5.5(a) the structural/magnetic and superconducting transition temperatures obtained from magnetization and resistivity measurements carried out by Canfield et al. [28] are plotted for various TM substitutions for Fe in the BaFe_2As_2 over the actual impurity

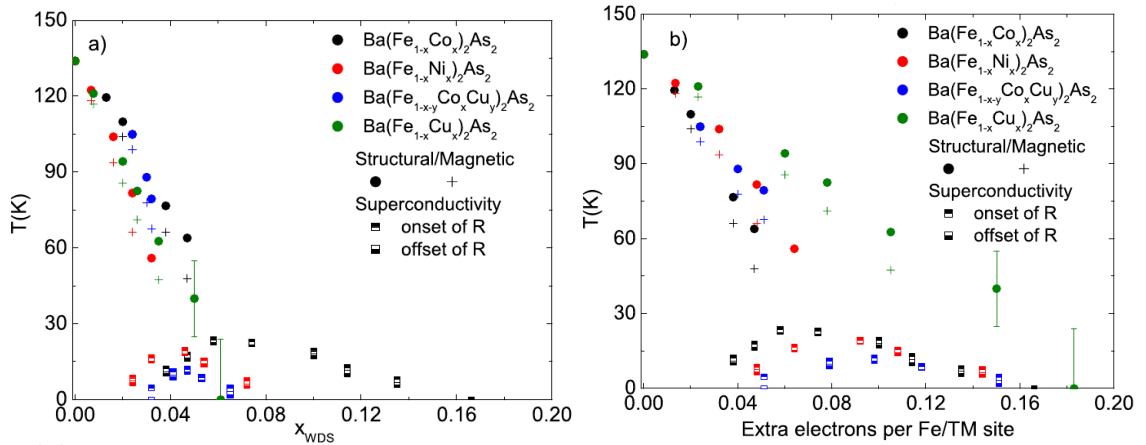


Figure 5.5.: Structural/magnetic and superconducting transition temperatures for different TM-substitutions in BaFe_2As_2 plotted over (a) the impurity concentration (b) the expected amount of extra electrons if charge doping is assumed, figure taken from [28]

concentration determined by wavelength-dispersive spectroscopy analysis (WDS). For Co and Ni substitution as well as Cu/Co co-substitution the heights and especially the widths of the superconducting domes are different. The solely Cu substituted samples show no superconductivity at all (in a more recent publication by partly the same authors [99], a very small superconducting dome for Cu substitution is reported). In spite of this, the structural/magnetic transition temperatures rather coincide among the different substitutions. This finding led these authors to the idea of alternatively plotting the same data over the amount of extra electrons which naively would be expected if the TM substitutions really accomplished charge doping. These results, which are shown in Fig. 5.5 (b), are in a sense complementary: the structural/magnetic transition temperatures now exhibit a large scattering whereas the widths of the superconducting domes rather coincide, again with the exception of the Cu substituted samples. This brought these authors to the conclusion that whereas for the structural/magnetic transition the impurity concentration, which is directly related to the atomic composition, is the relevant quantity, it is the charge doping, which governs the superconductivity in the case of Co and Ni substitution. Such a scenario of a rigid bandshift is in agreement with changes of Fermi surfaces which were observed in angular resolved photo emission spectroscopy (ARPES) measurements [29, 30].

On the other hand, there are X-ray absorption measurements (XANES, NEXAFS) [31, 32] which see at best a small change of valence at the Fe atom due to transition metal substitution which of course challenges the rigid bandshift picture. To close the circle, this would again be consistent with the relatively weak dependence of the structural/magnetic transition temperature on impurity concentration shown in Fig. 5.5 (a). From the *ab-initio* side, this dichotomy has been addressed by supercell calculations [100] and their combination with Wannier function based averaging techniques [49].

A further aspect of substitutional disorder besides the eventual effect of charge doping is impurity scattering. It is known since the early years of superconductivity that impurity scattering plays a crucial role in the suppression of T_c [33, 101–107]. In a conventional superconductor the Anderson theorem [108] states that superconductivity is only destroyed

by magnetic impurities which break the Cooper pairs. In the BaFe₂As₂ by now, a significant part of the community is convinced that the superconductivity is unconventional and exhibits an s^{+-} pairing state [35, 36]. This means that the superconducting order parameter has s -wave symmetry but changes sign between the hole and the electron pockets on the Fermi surface. For such a system it was shown that it is of great importance to differentiate between intraband and interband scattering and in particular intraband scattering on nonmagnetic impurities leads to Cooper pair breaking [33, 37].

In this work, the influence of substitutional disorder on the electronic structure will be analyzed in detail. In particular, the level shifts of electron-like and hole-like bands in the vicinity of the Fermi-level will shed light on the dichotomy between charge doping and static valences for TM substitution. Until now, at least to my knowledge, the issue of impurity scattering and especially intraband versus interband scattering has not yet been addressed by a systematic first-principles study. As already qualitatively shown in Chap. 4 about the Cu_{1-x}Zn_x alloys, the methodology developed in this work provides access to scattering strengths which gave motivation to a systematic investigation of band resolved impurity scattering effects in the BaFe₂As₂ for various substitutions. The subsequently presented work is partly based on my publication [109].

5.2. Technical details of the calculation

As mentioned in Sec. 5.1.2, the tetragonal crystal structure of BaFe₂As₂ at room temperature with two Fe atoms per unit cell as measured by [97] was used which was also considered for the substitutional end members (e.g. BaTM₂As₂). If not mentioned otherwise, this crystal structure was not changed with impurity concentration x to well separate disorder from structural effects. All calculations were performed without spin polarization because this is not yet implemented in the CPA method. The respective DFT calculations for the parent compound BaFe₂As₂ and substitutional end members were performed in the local density approximation (LDA) for the exchange correlation (XC) potential with a parametrization due to Perdew and Wang [110]. For the Brillouin zone integration a 8x8x4 Monkhorst-Pack [85] \mathbf{k} -mesh was selected, adapted to the tetragonal symmetry. Furthermore, norm-conserving pseudopotentials constructed after Vanderbilt [7] by Rolf Heid [111] were used together with local d -type functions for Fe or TM respectively and plane waves up to a cutoff energy of 22 Ry.

For each atomic species, nine local basis functions up to an orbital angular momentum of $l = 2$ were used in the CPA calculations which results in a size of the Hilbert space (dimensions of the quadratic matrices) of 45 for the parent compound and 63 for the disordered systems. Like already for the Cu_{1-x}Zn_x alloys in Chap. 4, the radial basis functions were obtained by the LCAO fit via minimizing the spillage function where the local pseudo wave functions $^{ps}f_l^P(r)$, obtained from the pseudopotential construction, are multiplied with cutoff functions

$$f_l^P(r) = \left[1 - e^{-\gamma_l^P (R_{C,l}^P - \lambda_l^P r)^2} \right] ^{ps} f_l^P(r) \quad (5.3)$$

The chosen cutoff radii $R_{C,l}^P$ and the functional parameters γ_l^P and λ_l^P as obtained by the LCAO fits are listed in Tab. 5.1. The so obtained radial basis functions for the three species of the parent compound Ba, Fe and As are shown in Fig. 5.6. The large cutoff radii ensure a good description of the band structure in the local basis. As a consequence,

Compound	Atomic type P	l	γ_l^P	$R_{C,l}^P$ (Bohr)	λ_l^P
$BaFe_2As_2$	Ba	0	0.1621	8.0	0.9864
	Ba	1	0.2176	8.0	0.9610
	Ba	2	0.2802	8.0	0.9745
	Fe	0	0.1974	6.0	0.8925
	Fe	1	0.1817	6.0	0.9068
	Fe	2	0.4642	6.0	0.9851
	As	0	0.2362	7.0	0.9790
	As	1	0.1495	7.0	0.9827
	As	2	0.0240	7.0	1.1117
$BaCo_2As_2$	Co	0	0.2023	6.0	0.9070
	Co	1	0.1986	6.0	0.9610
	Co	2	0.4657	6.0	0.9936
$BaNi_2As_2$	Ni	0	0.1886	6.0	0.9282
	Ni	1	0.1760	6.0	1.0113
	Ni	2	0.4505	6.0	1.0043
$BaCu_2As_2$	Cu	0	0.1505	6.0	0.9116
	Cu	1	0.1677	6.0	1.0105
	Cu	2	0.4704	6.0	0.9934
$BaZn_2As_2$	Zn	0	0.1602	6.0	0.9181
	Zn	1	0.1742	6.0	1.0113
	Zn	2	0.5014	6.0	0.9783
$BaMn_2As_2$	Mn	0	0.2012	6.0	0.8863
	Mn	1	0.1565	6.0	0.8567
	Mn	2	0.4665	6.0	0.9880
$BaPd_2As_2$	Pd	0	0.1947	6.0	0.9158
	Pd	1	0.1554	6.0	0.8585
	Pd	2	0.3828	6.0	1.0021
$BaPt_2As_2$	Pt	0	0.1880	6.0	0.9494
	Pt	1	0.1649	6.0	0.8813
	Pt	2	0.3084	6.0	1.0074
$BaFe_2P_2$	P	0	0.2426	7.0	0.9745
	P	1	0.1824	7.0	0.9845
	P	2	0.0010	7.0	0.6111
KFe_2As_2	K	0	0.2786	8.0	0.9850
	K	1	0.2493	8.0	1.0518
	K	2	0.2643	8.0	0.8049

Table 5.1.: LCAO fit parameters γ_l^P , λ_l^P and chosen cutoff radii $R_{C,l}^P$ for the individual end members

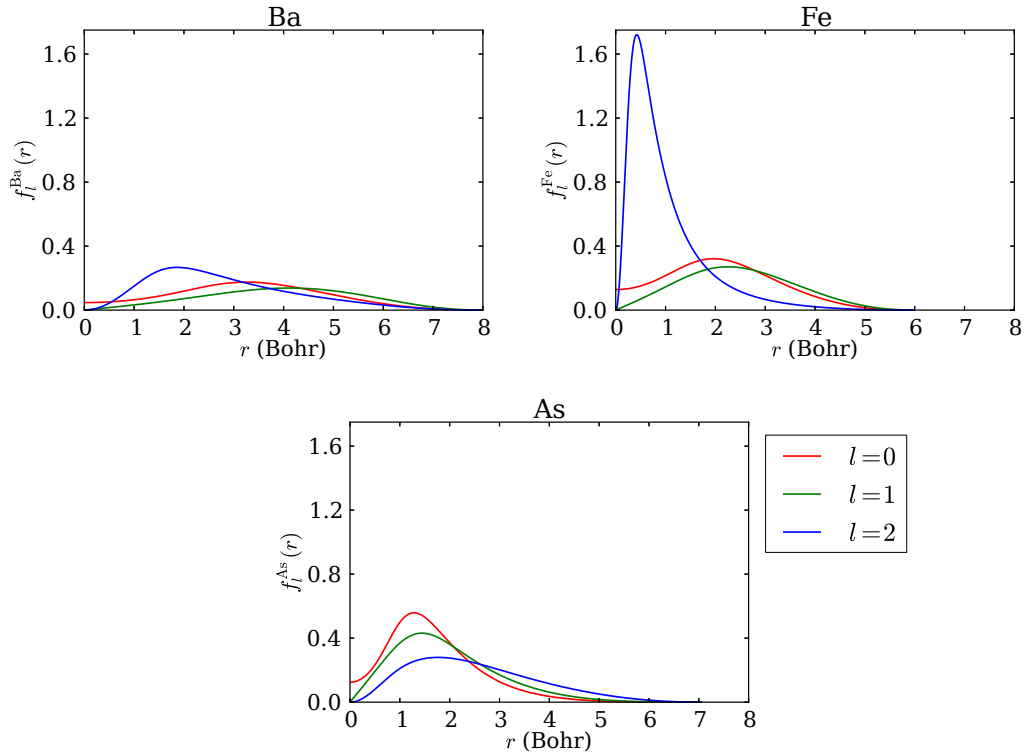


Figure 5.6.: Radial wavefunctions for Ba, Fe and As for $l = 0$ (red), $l = 1$ (green) and $l = 2$ (blue), respectively

even for the longest nearest neighbor distance Ba-As of 8.7 Bohr, these wavefunctions (apart from the Fe- d orbital) are heavily overlapping. Whereas for all species all angular momenta are used to obtain a good LCAO-fit, in particular for Fe the $3d$ -states play an important role for the valence which strongly enhances the Fe- d orbital. Especially in such spatially anisotropic systems like BaFe_2As_2 , a heavily overlapping local basis is needed for a reasonable description of the bandstructure. To get an impression of the quality of the LCAO fit, in Fig. 5.7 the bandstructure of the parent compound BaFe_2As_2 from the MBPP calculation is compared against the one obtained by the LCAO part of the MBPP. This gives a measure for the error in the energy levels due to the LCAO representation which are the basis for the CPA calculation. In the calculation of the matrix elements in the CPA program, further approximations in the XC-potential, charge density and summation cutoffs are made. To additionally get an estimate how this influences the error bar of the levels, in Fig. 5.8 the MBPP bandstructure is compared to the one obtained by diagonalizing the charge self-consistent "mixing Hamiltonian" (see Sec. B.4.6) which for an ordered compound is nothing else than the CPA-version of the crystal Hamiltonian. In the vicinity of the Fermi surface, the bandstructures agree well, especially for the three hole bands near the Γ -point and the two electron bands near the X-point. This good agreement is important for the further analysis of self-energy effects on these bands. It should be emphasized that the energy window of this plot is chosen rather small because BaFe_2As_2 obviously exhibits many dense bands in this region of interest. The band starting at the Γ -point approx. 0.2 eV above the Fermi level and then touching the Fermi level between Γ and Z caused particular problems and was the reason to develop the treatment of the XC-

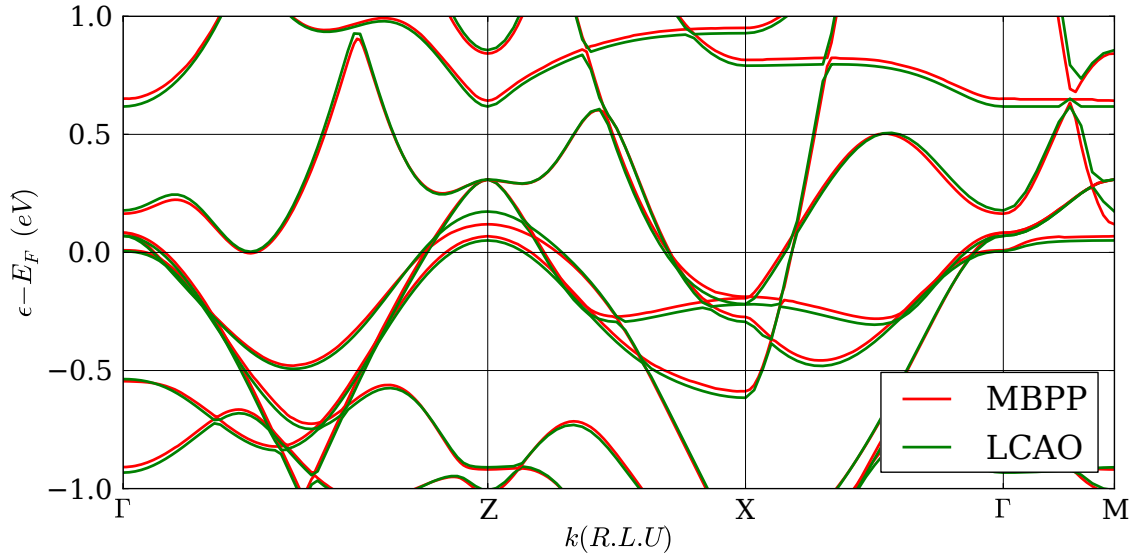


Figure 5.7.: Bandstructure of pure BaFe_2As_2 from MBPP-DFT (red) compared against the LCAO representation calculated within the MBPP (green)

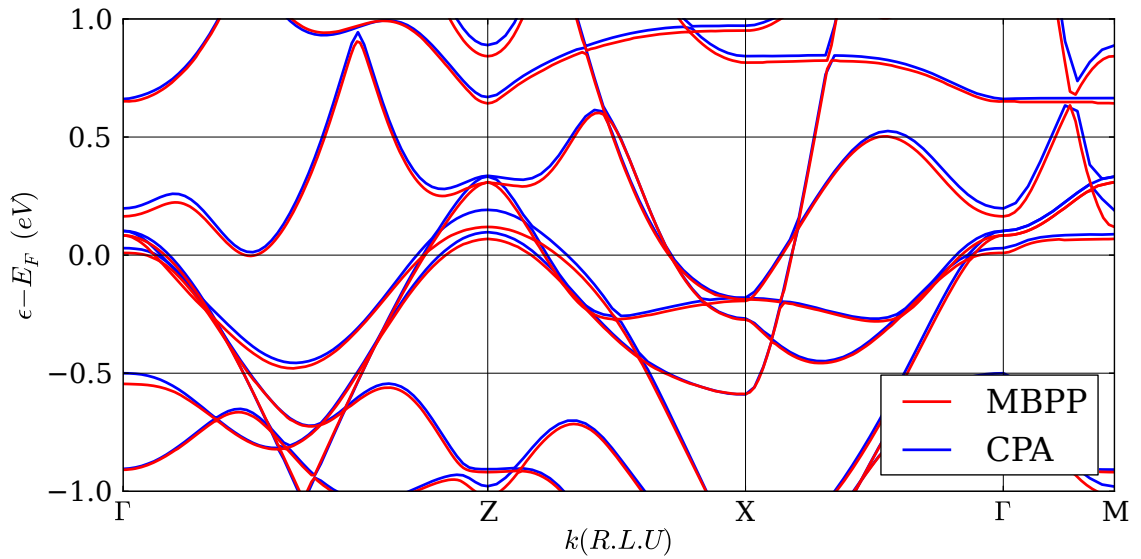


Figure 5.8.: Bandstructure of pure BaFe_2As_2 from MBPP-DFT (red) compared against the result from diagonalizing the charge self-consistent mixing Hamiltonian in the CPA program (blue)

potential based on shape functions explained in Secs. 2.2.4 and B.4.5. In the simpler atomic sphere approximation as proposed by Koepernik [11] this band significantly dropped below the Fermi level and thus formed a spurious electron pocket. The good agreement of all three calculations at that point shows how well the shape function approach together with charge self-consistency performs for such delicate bands. The shape functions were chosen

the same for all sites in the following form

$$S(x) = 1 - e^{-\gamma(1-x)^8} \quad x = \frac{|\mathbf{r}|}{R_C^P} \quad (5.4)$$

where the parameter $\gamma = 32.8$ was selected. The cutoff radii R_C^P are listed in Tab. 5.2. Another delicate parameter for the determination of the Fermi level in this particular

Atomic type P	R_C^P (Bohr)
Ba	10.5
Fe	6.9
As	6.5

Table 5.2.: Cutoff radii for the shape functions

system turned out to be the artificial temperature which was introduced for numerical reasons in Sec. 2.2.4. The Fermi level is extrapolated from two chemical potential values calculated at 300K and at 800K. The charge self-consistency is calculated at 800K.

As a last technical remark, I want to emphasize the importance of charge self-consistency in the BaFe_2As_2 system. A very nice example is shown in Fig. 5.9 where the total density of states (DOS) of $\text{Ba}(\text{Fe}_{0.9}\text{Zn}_{0.1})_2\text{As}_2$ calculated from the CPA effective medium Green's function according to Eq. (2.71) is plotted after the first charge iteration and for the charge self-consistent calculation after 32 charge iterations. Charge self-consistency has the most

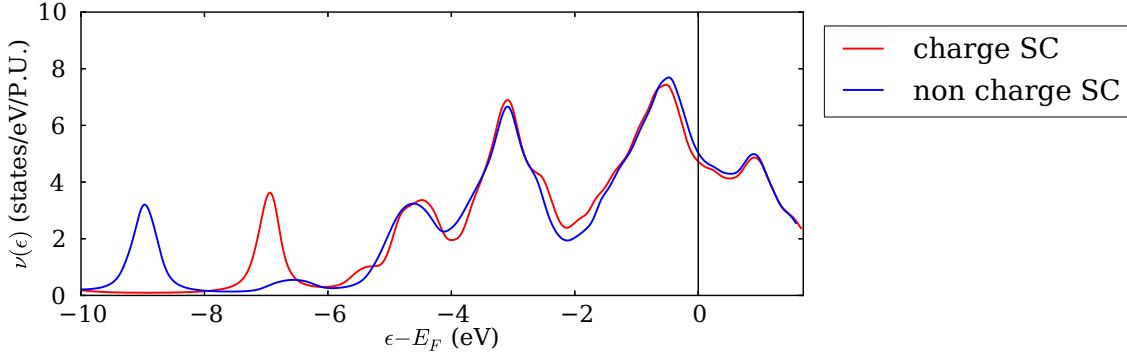


Figure 5.9.: Non charge self-consistent (blue) and charge self-consistent (red) total DOS of $\text{Ba}(\text{Fe}_{0.9}\text{Zn}_{0.1})_2\text{As}_2$

obvious impact on the position of the localized state appearing for Zn substitution which gets shifted from about -9 eV to about -7 eV with respect to the Fermi level. But also the shifts of the DOS in the vicinity of the Fermi level, which are rather small compared to the shift of the localized state, are important when band renormalization effects at the Fermi level are considered. This is of particular importance when one wants to determine at which concentration a hole or electron pocket vanishes. For that reasons, all subsequent calculations presented in this chapter are charge self-consistent if not mentioned otherwise. A second general important remark has to be made about the energy axis $\epsilon - E_F$ in plots of the DOS or the spectral function. If for example several DOS for different compositions are compared in a plot, then this implicitly means that every composition in general has a

different Fermi level where its respective energy axis refers to. If for example the difference of two peak positions ω_1 and ω_2 for two different compositions 1 and 2 is considered, this actually means

$$\omega_1 - \omega_2 = \epsilon_1 - E_{F,1} - \epsilon_2 + E_{F,2} \quad (5.5)$$

If not mentioned otherwise, this convention is used for DOS and spectral functions throughout this chapter.

5.3. $3d$ transition metal substitution

There are several possibilities to perform chemical substitutions in BaFe_2As_2 . One class of substitutions, which was frequently studied in experiments, is the substitution of both Fe atoms by another $3d$ transition metal via moving horizontally in the periodic table. In this chapter, substitution of Fe by $TM \in \{\text{Co}, \text{Ni}, \text{Cu}, \text{Zn}, \text{Mn}\}$ will be studied.

5.3.1. Densities of states

The DOS gives a space and momentum independent average information about the impact of substitutional disorder. It is well suited to get an overview about possible interesting effects which then can be studied in more detail for example by band or momentum resolved techniques with higher accuracy. In particular, the DOS contains information about level shifts due to chemical substitution and the depth of the impurity potential. Before the discussion of the results I want to establish the concept of a rigid band shift which will be needed throughout the remaining chapter. The idea is to calculate the necessary naively expected shift of the Fermi level if a certain amount of extra charge carriers is introduced to the system. Electrons are counted positively and holes negatively. For the particular case of TM substitution at the Fe site, the rigid band shift Δ^{TM} can be calculated from the valence electron number as follows

$$\int_0^{E_F + \Delta^{TM}} d\omega \nu(\omega) \stackrel{!}{=} Z_{\text{Ba}} + 2 \cdot Z_{\text{As}} + 2 \cdot (1 - x) \cdot Z_{\text{Fe}} + 2 \cdot x \cdot Z_{TM} \quad (5.6)$$

where E_F and $\nu(\omega)$ are the Fermi level and DOS of the parent compound and Z_P is the valence electron number of the atomic type P . The valence electron numbers of the substitutional end members are weighted by their concentrations which maintains charge neutrality of the composition. The DOS is integrated (in the present case numerically) up to the Fermi level plus Δ^{TM} to get a particle number and Δ^{TM} is adjusted until this particle number is equal to the number given on the right side of Eq. (5.6). This straight forwardly applies also to substitutions at other sites. At this point, it is important to remember that in the CPA calculations for the disordered systems the valence electron number, which is needed for the determination of the chemical potential (see Sec. 2.3 and App. C), is kept fixed due to particle number conservation. This particle number, which in the developed program has to be provided by the user, was calculated in exactly the same way as in the right side of Eq. (5.6).

In Fig. 5.10 the total DOS of $\text{Ba}(\text{Fe}_{0.9}\text{TM}_{0.1})_2\text{As}_2$ for different TM substitutions together with the DOS of the parent compound is plotted. In the inset, showing the behavior in a narrow region around the Fermi level, apart from Zn substitution the other TM -substitutions show a qualitative behavior which one might naively have expected: For the series from Co to Cu where the valence electron number of the substituent successively

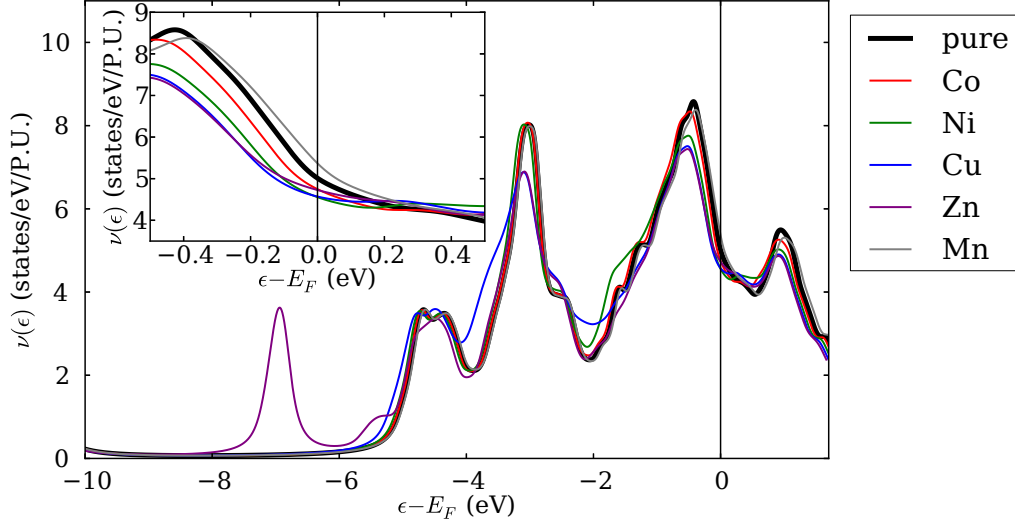


Figure 5.10.: Main plot: charge self-consistent total DOS of pure BaFe_2As_2 (black) together with disordered $\text{Ba}(\text{Fe}_{0.9}\text{TM}_{0.1})_2\text{As}_2$ with $\text{TM} \in \{\text{Co}, \text{Ni}, \text{Cu}, \text{Zn}, \text{Mn}\}$ (colors) over a large energy range w.r.t. the Fermi level of the respective composition; inset: the same quantities on a narrow energy range around the Fermi level

increases because of moving to the right in the periodic table, the DOS gets successively shifted to lower energies as if to account for these higher numbers of valence electrons. This behavior is also fulfilled by Mn which is to the left in the periodic table, thus has less valence electrons than Fe and the DOS shifts to higher energies as naively expected. This can be interpreted as first support of the picture of charge doping, but an analysis of the DOS can only give a rough overview. A more complete answer of this question thus will be postponed to the end of this chapter, where these effects on the actual bands at the Fermi level are more rigorously studied in detail.

The plot of the DOS in a larger energy interval reveals a qualitatively different behavior for Zn substitution. This is the only TM -substitution where a localized state forms at 7 eV below the Fermi energy. This behavior was already reported by Berlijn et al. [49] which used a combination of the supercell method and Wannier function based averaging techniques.

As already mentioned in Sec. 4.3, the present method can also calculate angular momentum and species projected DOS by restriction of the trace in Eq. (2.71) to an appropriately chosen subspace. In Fig. 5.11 such a projection on $l = 2$ (summed over all five d -states) and on the actual substituent species (e.g. for $\text{Ba}(\text{Fe}_{0.9}\text{Co}_{0.1})_2\text{As}_2$ a projection on Co- d states) was done for the same compositions as in Fig. 5.10. This is shown together with the respective projections (for each composition and the parent compound) on Fe- d states (black curves). From the last two chapters we know that the peak height in the DOS is to a large extent influenced by the concentration. Thus, the Fe peaks were scaled by a factor of 0.2 for the disordered systems and $0.2 \cdot 0.9$ for the parent compound (because the Fe concentration in the disordered system is 0.9) for better comparison. For the same reason, also the Zn peak was scaled by a factor of 0.3 because due to its sharpness it gets relatively high in order to ensure particle number conservation. Obviously, the peak positions of the respective substituents differ considerably whereas the respective Fe peaks hardly change

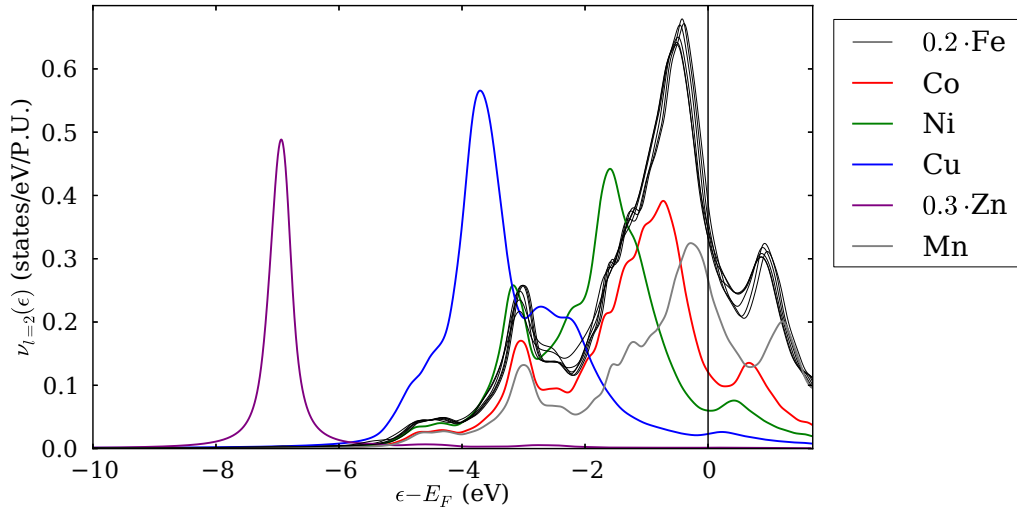


Figure 5.11.: Charge self-consistent sum over all $l = 2$ angular momentum contributions of TM -projected DOS of disordered $Ba(Fe_{0.9}TM_{0.1})_2As_2$ with $TM \in \{Co, Ni, Cu, Zn, Mn\}$ (colors, Zn scaled by 0.3) together with the respective projections on Fe scaled by 0.2 (black) for each composition as as reference

with substitution. The slight shifts of the Fe peaks are of the same order of magnitude like the respective rigid band shift.

To interpret the spectra of the substituents, some interesting related data are listed in Tab. 5.3. ϵ_0 is the mean value of the d -orbital DOS which was extracted from calculating the first statistic moment of the respective DOS in an energy window between -9 eV and 2 eV. This provides a well defined way to extract the mean value independent of the detailed structure of the spectra which can contain several side maxima like for Fe or just one single maximum like for Zn. Of course this can only serve to get a rough quantitative estimate of the shifts. The $V_{l,m}$ are the differences of the diagonal elements of the TM block and the Fe block of the respective onsite Hamiltonians $H^{TM, TM} - H^{Fe, Fe}$ with $l = 2$ (the l -offdiagonal elements are zero) as a measure for the impurity potential. The shifts of the substituent peaks with respect to the Fe peak correlate well with the impurity potentials. The impurity potential is to zeroth order determined by the different pseudopotentials of the substituent, which arise from the respective core sizes, configuration of the core electrons and nuclear charges. Additionally it is influenced by the surrounding atoms in

TM	$\approx \epsilon_0 - \epsilon_0^{Fe}$ (eV)	$V_{2,0}$ (eV)	$V_{2,1}$ (eV)	$V_{2,-1}$ (eV)	$V_{2,2}$ (eV)	$V_{2,-2}$ (eV)
Mn	0.157	0.250	0.201	0.201	0.190	0.259
Fe	0.000	0.000	0.000	0.000	0.000	0.000
Co	-0.276	-0.292	-0.259	-0.259	-0.266	-0.312
Ni	-0.855	-0.917	-0.866	-0.866	-0.877	-0.906
Cu	-2.213	-2.350	-2.243	-2.243	-2.211	-2.220
Zn	-5.646	-6.102	-5.935	-5.935	-5.873	-5.888

Table 5.3.: Shift of substituent d -spectra in orbital DOS compared with difference of diagonal elements $V_{l,m}$ with $l = 2$ of onsite Hamiltonians

the disordered compound, in particular by hybridization with As.

5.3.2. Band renormalization

Bloch spectral function

As already outlined in Sec. 4.3, the Bloch spectral function $A(\omega, \mathbf{k})$ given by Eq. (2.72) contains all information about the band structure of a disordered system and thus is the basic quantity to study momentum resolved disorder effects in more detail. To extend the analysis of the DOS carried out in the previous section, which provided relatively coarse grained averages over all bands, in this section I want to present a systematic scheme for the investigation of the impact of disorder on particular bands contributing to the Fermi surface. In Fig. 5.12 (a) $A(\omega, \mathbf{k})$ of substitutionally disordered $\text{Ba}(\text{Fe}_{0.9}\text{Ni}_{0.1})_2\text{As}_2$ is shown together with the band structure of the parent compound. Obviously all bands get shifted to lower energies as already observed in the DOS in the last section. Moreover, this plot reveals that these level shifts are band selective and momentum dependent - essentially meaning that they are non rigid, an information which the DOS could not provide. But it would be desirable to quantify this non-rigidness to be able to shed light on the initially mentioned controversy between charge doping and unchanged TM-valence reported by different experimental techniques. Furthermore, in the color plot the disordered bandstructure seems to exhibit band selective and \mathbf{k} -dependent spectral broadenings, but also here it is difficult to separate spectral broadenings from high spectral weight due to crossings of multiple bands. To be able to quantify such effects, we have to look at the spectral function in more detail. For that purpose in Fig. 5.12 (b), $A(\omega, \mathbf{k})$ is plotted against energy at three subsequent \mathbf{k} -points in the region next to the X-point where the electron bands cross the Fermi level. These \mathbf{k} -points are marked by the red vertical lines in the color plot. Obviously, the spectral function contains multiple peaks which causes complications when the impact of disorder on one particular band shall be investigated: This example contains for $\mathbf{k} = 0.17\bar{\text{X}}\bar{\Gamma}$ and $\mathbf{k} = 0.2\bar{\text{X}}\bar{\Gamma}$ the pathological case where the two electronic bands just get very close and cross themselves such that their spectra overlap. This results in the respective double peaks next to the Fermi level. From such a double peak it is difficult to extract the behavior of an individual band next to the Fermi. Thus, a single peaked, disentangled spectral function for each individual band would be much more suitable to trace its position in energy and its spectral width.

Projection technique

A promising ansatz for disentangling the spectral peaks of the individual bands consists in projecting the \mathbf{k} -dependent Green's function $S(\mathbf{k})\Gamma(\mathbf{k}, \omega)S(\mathbf{k})$ involved in the calculation of $A(\omega, \mathbf{k})$, being a matrix in the extended BEB orbital Hilbert space, on the eigenvectors of the parent compound. The idea behind this is that we are interested how the bands of the parent compound, having well-defined eigenvectors, will be affected by disorder. Mathematically this is accomplished by defining a band-projected Green's function

$$G_n(\mathbf{k}, \omega) \equiv \sum_{i,j \in \text{parent}} c_{n,i}^*(\mathbf{k}) [S(\mathbf{k})\Gamma(\mathbf{k}, \omega)S(\mathbf{k})]_{i,j} c_{n,j}(\mathbf{k}) \quad (5.7)$$

where $c_{n,j}$ is the j th orbital component of the eigenvector of band n . Because these eigenvectors are only defined in the smaller Hilbert space of the parent compound, the sum in

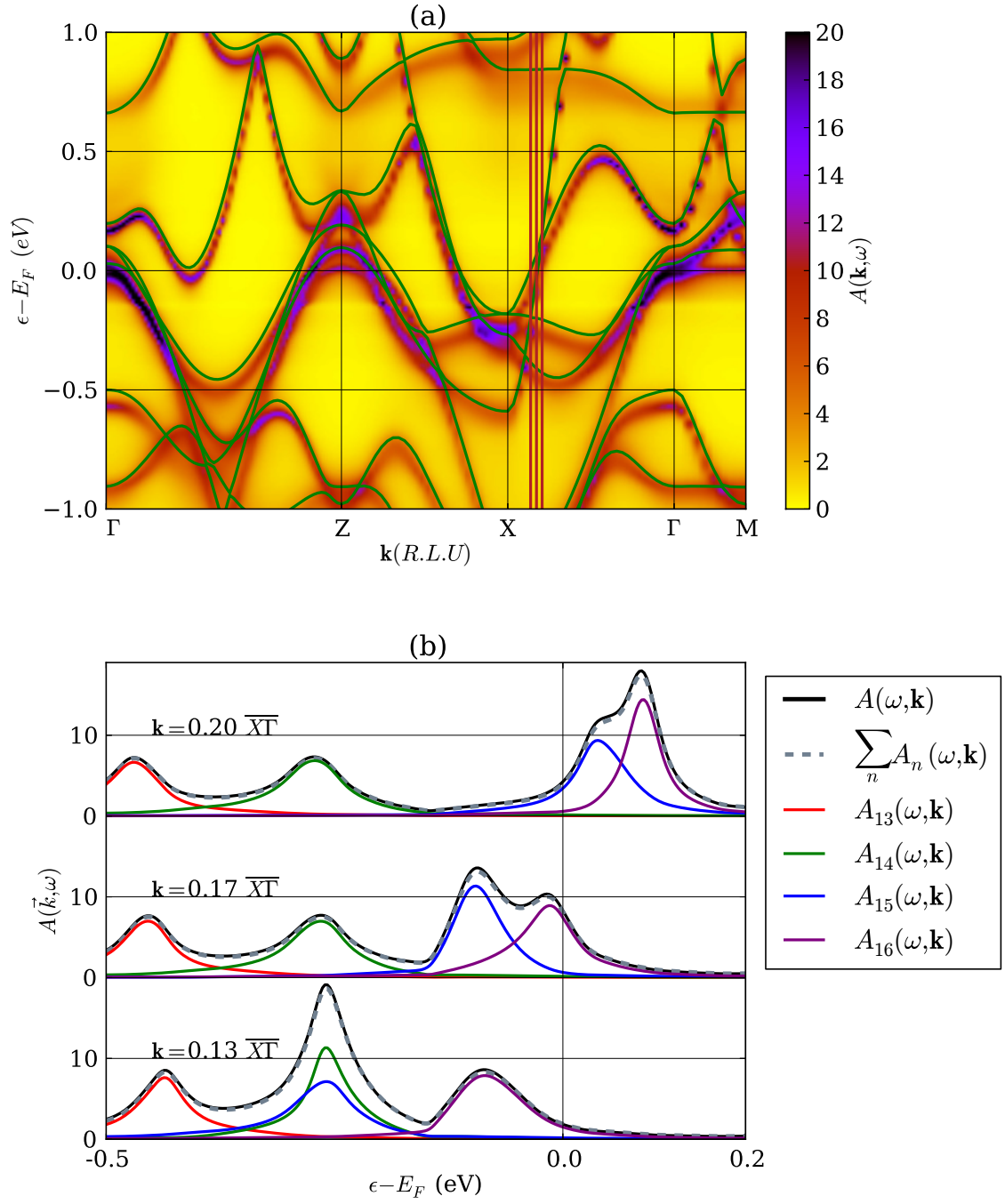


Figure 5.12.: (a) Bloch spectral function of disordered $\text{Ba}(\text{Fe}_{0.9}\text{Ni}_{0.1})_2\text{As}_2$ together with band structure of the parent compound (green solid lines); (b) Bloch spectral function of $\text{Ba}(\text{Fe}_{0.9}\text{Ni}_{0.1})_2\text{As}_2$ at three \mathbf{k} -points [vertical red lines in (a)] together with projections (colors) on bands of the parent compound and sum over all bands

Eq. (5.7) only runs over orbital indices belonging to the subspace of the parent compound. This projection from a larger Hilbert space down to a smaller one is valid if the changes of the bands due to disorder are not too large. This is supposed to be the case in the regime of small impurity concentrations which fortunately is just the regime we are interested in. The resulting band projected spectral functions are shown in various colors in Fig. 5.12 (b). Each of them only contains a single well defined peak and in particular they disentangle the double peak corresponding to the crossing of the two electron bands. If this method was exact, the sum over all projected bands would give the total spectral function. To test the accuracy, the sum over just these four bands (out of 45) is also plotted and fulfills this sum rule astonishingly well. This demonstrates that this projection is valid even at an impurity concentration $x = 0.1$.

Having available a single spectral function for each band, the impact of disorder on a selected band of the parent compound can be studied by comparing its spectral function in the parent compound to that in the disordered system. The positions of the spectral peaks can easily be extracted by searching the maximum of the associated projected spectral function $A_n(\mathbf{k}, \omega) = \frac{-1}{\pi} \text{Im} G_n(\mathbf{k}, \omega)$. Comparing them between the parent compound and the disordered system gives rise to a level shift $\Delta\epsilon_n$ due to disorder. To facilitate the extraction of the spectral broadening we make a further approximation and assume the following functional form for a band-projected Green's function

$$G_n(\mathbf{k}, \omega) = \frac{1}{\omega + i\delta - (\epsilon_n(\mathbf{k}) - E_F^0) - \Sigma_n} \quad (5.8)$$

where $\epsilon_n(\mathbf{k})$ is the dispersion of band n in the parent compound with respect to its Fermi level E_F^0 . The disorder effects on band n are considered by the complex self-energy $\Sigma_n \equiv \Sigma_n^R + i\Sigma_n^I$. The imaginary part of this self energy is negative. The full Green's function in practice is evaluated at a slightly complex frequency $\omega + i\delta$, which also has to be accounted for. The self energy in principle could be extracted from finding the poles of G_n in complex frequency. In practice we choose a different approach based on the knowledge that the real part of the pole is just the position $\omega_p = \epsilon_n^d(\mathbf{k}) - E_F$ of the peak in energy which we already know. Here $\epsilon_n^d(\mathbf{k})$ is the band dispersion and E_F the Fermi level in the disordered system. It follows

$$\text{Re} \frac{1}{G_n(\mathbf{k}, \omega_p)} = 0 = \underbrace{\epsilon_n^d(\mathbf{k}) - E_F - (\epsilon_n(\mathbf{k}) - E_F^0)}_{\Delta\epsilon_n} - \Sigma_n^R \quad (5.9)$$

Then the band Green's function evaluated at ω_p , but still at a small δ far off the actual pole becomes

$$G_n(\mathbf{k}, \omega_p) = \frac{1}{i(\delta - \Sigma_n^I)} \quad (5.10)$$

which is purely imaginary. This finally yields for the real and imaginary part of the band self-energy

$$\Sigma_n^R = \Delta\epsilon_n \quad (5.11)$$

$$\Sigma_n^I = \frac{1}{\text{Im} G_n(\mathbf{k}, \omega_p)} + \delta = \frac{-1}{\pi A_n(\mathbf{k}, \omega_p)} + \delta = -\Delta\sigma_n \quad (5.12)$$

where $\Delta\sigma_n$ is the spectral broadening of band n . This allows to extract the spectral width and broadening provided the peak position is known.

In the following, self-energy effects on the three hole-like bands next to the Γ -point and on the two electron-like bands next to the X-point will be analyzed. For the rest of this work, only a cut through the full Fermi surface of the parent compound (see Fig. 5.4) in the $(\mathbf{k}_x, \mathbf{k}_y)$ plane at $\mathbf{k}_z = 0$ will be considered, as shown in Fig. 5.13. In the Brillouin

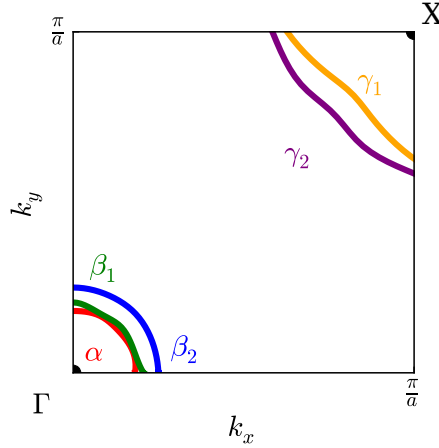


Figure 5.13.: Fermi surface of the parent compound in the $(\mathbf{k}_x, \mathbf{k}_y)$ plane at $\mathbf{k}_z = 0$ mapped out via DFT on a coarse-grained \mathbf{k} -mesh

zone corresponding to the tetragonal unit cell with two iron atoms, this planar projection essentially consists of three hole-like circles around the zone center $\Gamma = (0, 0, 0)$ and two electron-like ellipses around the zone corner $X = (1, 1, 0)$. In all what follows, the conventions for labelling of bands which were introduced in Fig. 5.13 will be used. The inner hole band is called α , the two outer hole bands β_1 and β_2 as well as the inner electron band γ_1 and the outer electron band γ_2 . Information about the orbital composition of band n , which of course depend on \mathbf{k} , can be obtained from the components of its eigenvector $c_{n,i}(\mathbf{k})$. In Fig. 5.14, the modulus squared of each eigenvector component at the respective Fermi wave vectors \mathbf{k}_F in the Γ -Z direction for the hole bands and the X- Γ direction for the electron bands is plotted.

The dominant orbital composition is listed in Tab. 5.4 where $\text{Lin}\{\dots\}$ means a linear combination.

Band	Type	l	m	Orbital
α	Fe	2	2	$d_{x^2-y^2}$
β_1	Fe	2	1	d_{xz}
β_2	Fe	2	-1	d_{yz}
γ_1	Fe	2	$\text{Lin}\{1, -1, 2\}$	$\text{Lin}\{d_{xz}, d_{yz}, d_{x^2-y^2}\}$
γ_2	Fe	2	2	$d_{x^2-y^2}$

Table 5.4.: Orbital composition (dominant contributions) of electron and hole bands at the Fermi level

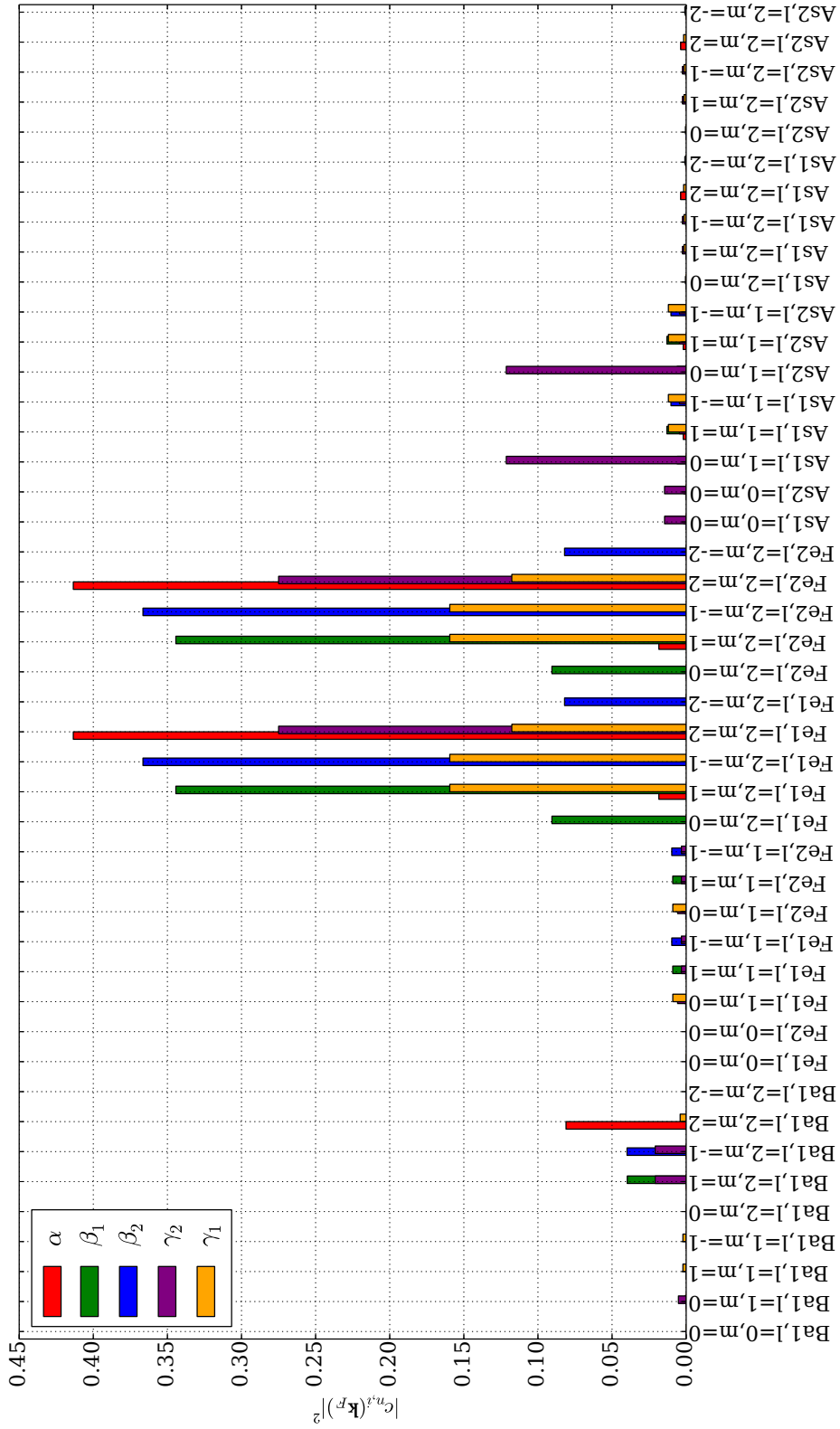


Figure 5.14.: Modulus squared of the orbital components of the eigenvectors for each band at the respective Fermi wave vector

The coordinate system is chosen such that x and y point along the projections of the FeAs bonds into the Fe planes. To get an impression how these orbitals are oriented with respect to the FeAs bonds, Fig. 5.15 shows a three dimensional plot of these five spherical harmonics.

Level shifts

In Fig. 5.16 the level shifts or real parts of the band self-energy Σ_n of the three hole bands (α , β_1 and β_2) and the two electron bands (γ_1 and γ_2) are plotted against impurity concentration x for different transition metal substitutions in $Ba(Fe_{1-x}TM_x)_2As_2$. These level shifts were taken at the Fermi wave vector \mathbf{k}_F of the respective disordered system and are measured parallel to the energy axis. This convention for the level shifts will also be chosen in the next sections if not mentioned otherwise. The calculations were carried out at impurity concentrations $x \in \{0.01, 0.03, 0.05, 0.07, 0.1\}$. For some bands and substitutions, not all points in the concentration range are shown because at a certain concentration threshold depending on the substituent species, the bands do not cross the Fermi level anymore. In this concentration range, the shifts behave linearly to good approximation. For this reason, lines were fitted to the data. The slopes for each substituent will be compared later for all substitutions (e.g. also at the pnictogen site) performed in this work. First of all, the level shifts increase in magnitude with an increasing difference of valence electron number between host and substituent. In particular, for Mn substitution the level shifts have a different sign as for the remaining TM substitutions because Mn has valence electrons less than Fe as opposed to the other TM which have more. The dashed lines show the respective rigid band shifts calculated from Eq. (5.6) expected in the picture of charge doping. Obviously, the level shifts in general are non-rigid, band-

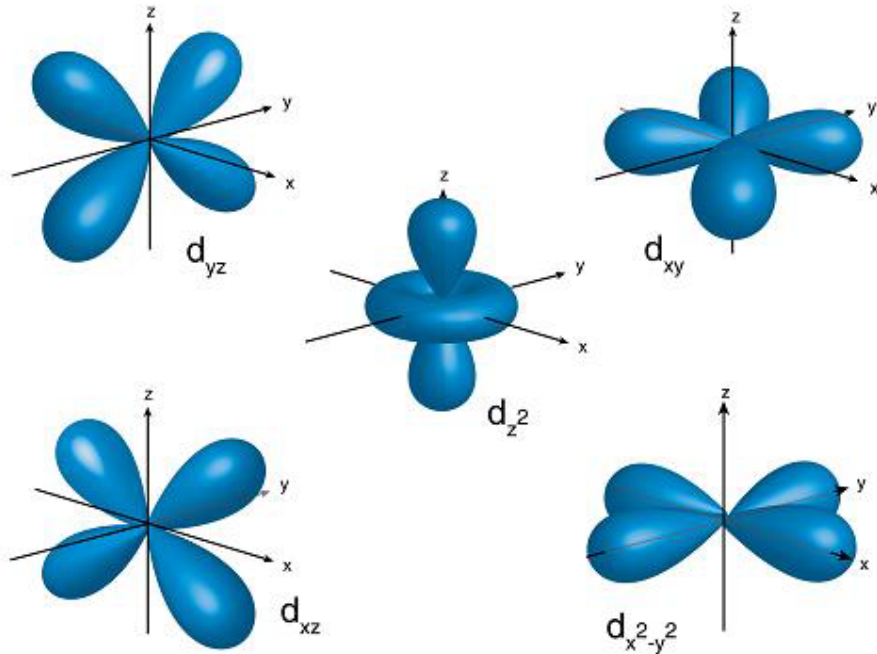


Figure 5.15.: The orientation of the five d -orbitals, figure from [112]

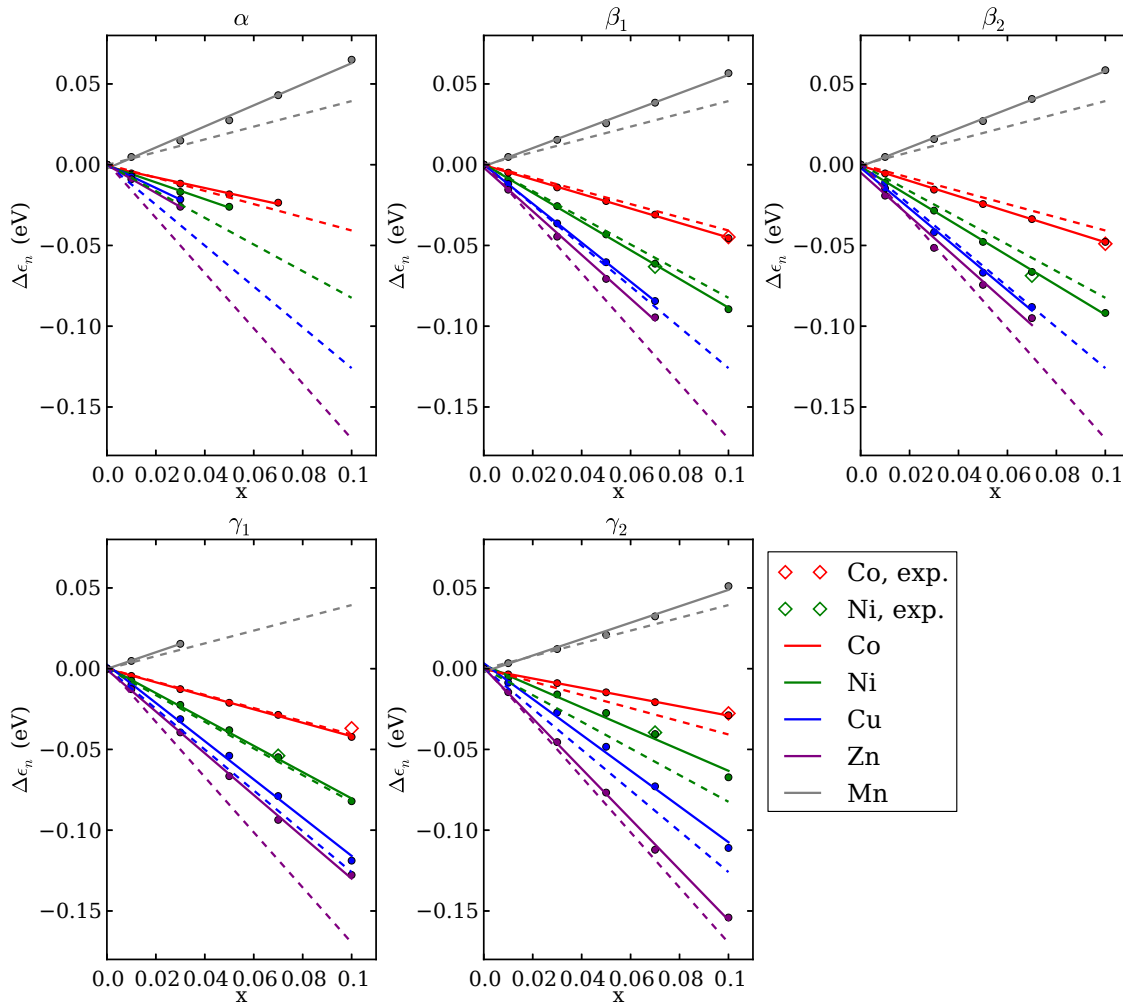


Figure 5.16.: Band shifts of the three hole bands (α , β_1 and β_2) and the two electron bands (γ_1 and γ_2) against impurity concentration x for different transition metal substitutions (colors) in $\text{Ba}(\text{Fe}_{1-x}\text{TM}_x)_2\text{As}_2$. Solid lines: fits to the closed symbols, dashed lines: rigid band shift, open symbols: calculation at experimental structure

selective and depend (see Tab. 5.4) on the orbital composition of the band. The β bands (apart from Mn substitution) and the γ_1 band (apart from Zn substitution) behave the most rigid-like. These bands also have a similar orbital composition. The α and γ_2 band, which have dominant $d_{x^2-y^2}$ character, exhibit more pronounced deviations from a rigid band shift. Apparently, if the lobes of the orbitals point into the direction of the FeAs bonds, this leads to larger deviations from a rigid band shift. At least for Co substitution (apart from the γ_2 band) the overall behavior suggests a rigid band shift to be a reasonable description which would support the charge doping scenario. For the other species, this is not so clear anymore, at best the directions of the shifts follow the naive picture.

As initially mentioned, for all calculations the crystal structure of stoichiometric BaFe_2As_2 was used and not changed with x . In order to see to what extent structural changes influence these results, the calculations for 10% Co substitution and 7% Ni substitution

were repeated, using the crystal structures measured by Peter Schweiss in four circle X-ray diffraction experiments [113] at the respective impurity concentrations. This was done because on the one hand, the present methodology does not yet provide access to the total energy (which has to be implemented in the future) and on the other hand, DFT-based approaches are well known to fail in predicting a realistic crystal structure upon minimizing the total energy for these compounds. These additional calculations are shown by the open symbols in Fig. 5.16 and are not included in the fits. Obviously, for these substitutions at this low concentration range, there are no substantial changes due to structural effects.

Spectral broadenings

In Fig. 5.17 the spectral broadenings of the three hole bands (α , β_1 and β_2) and the two electron bands (γ_1 and γ_2) are plotted against impurity concentration x for different transition metal substitutions in $Ba(Fe_{1-x}TM_x)_2As_2$ for the same range of concentrations as already the level shifts were calculated. Again, the broadenings were taken at the Fermi wave vector k_F of the disordered system which will also be done in the next sections, if not mentioned otherwise. As before, data points do not exist if the bands do not cross Fermi level anymore at that impurity concentration. Like the level shifts, the broadenings (apart from the α band at Mn substitution) show a linear behavior in this impurity concentration range and lines were fitted of which the slopes will be compared later. Also the spectral broadenings get enhanced with increasing difference in valence electron number of the substituent with respect to the host apart from the α band, which exhibits also the strongest deviations from the linear behavior. Whereas for most other bands Zn substitution leads to the strongest impurity scattering, for the α band this at least is not clear. The α band apparently exhibits an anomalous behavior. The β bands and the γ_1 band, being of similar orbital composition, are most affected by impurity scattering. These are the bands which exhibit the most rigid-like band shifts. The α and γ_2 band, being both of $d_{x^2-y^2}$ orbital character, behave differently and at least the two strongest scatterers Cu and Zn affect them weaker than the other bands. This suggests that an orbital character, where the lobes point into the direction of the FeAs bonds, makes the associated bands more robust against strong impurity scattering.

Also for the spectral broadenings, effects due to structural changes for Co and Ni substitution are negligible in the considered impurity concentration range. Similar trends concerning the dependence of the spectral broadenings on the substituent species can be found in the inverse charge carrier relaxation time $1/\tau'$ for low temperatures from optical measurements in Tab. 4 on page 848 of Ref. [114].

5.4. 4d and 5d transition metal substitution

In the last section, I discussed the changes in electronic structure of randomly substituting both Fe atoms with another 3d transition metal by moving horizontally to the left and right side of Fe in the periodic table. This section deals with moving vertically in the periodic table and the substitution of Fe by Ni (which was already shown before) will be compared with substitution of Fe by Pd, which is a 4d transition metal and Pt being a 5d transition metal. Because these are isovalent substitutions, we expect to see the same effects of Fermi level shifts for all three substituents.

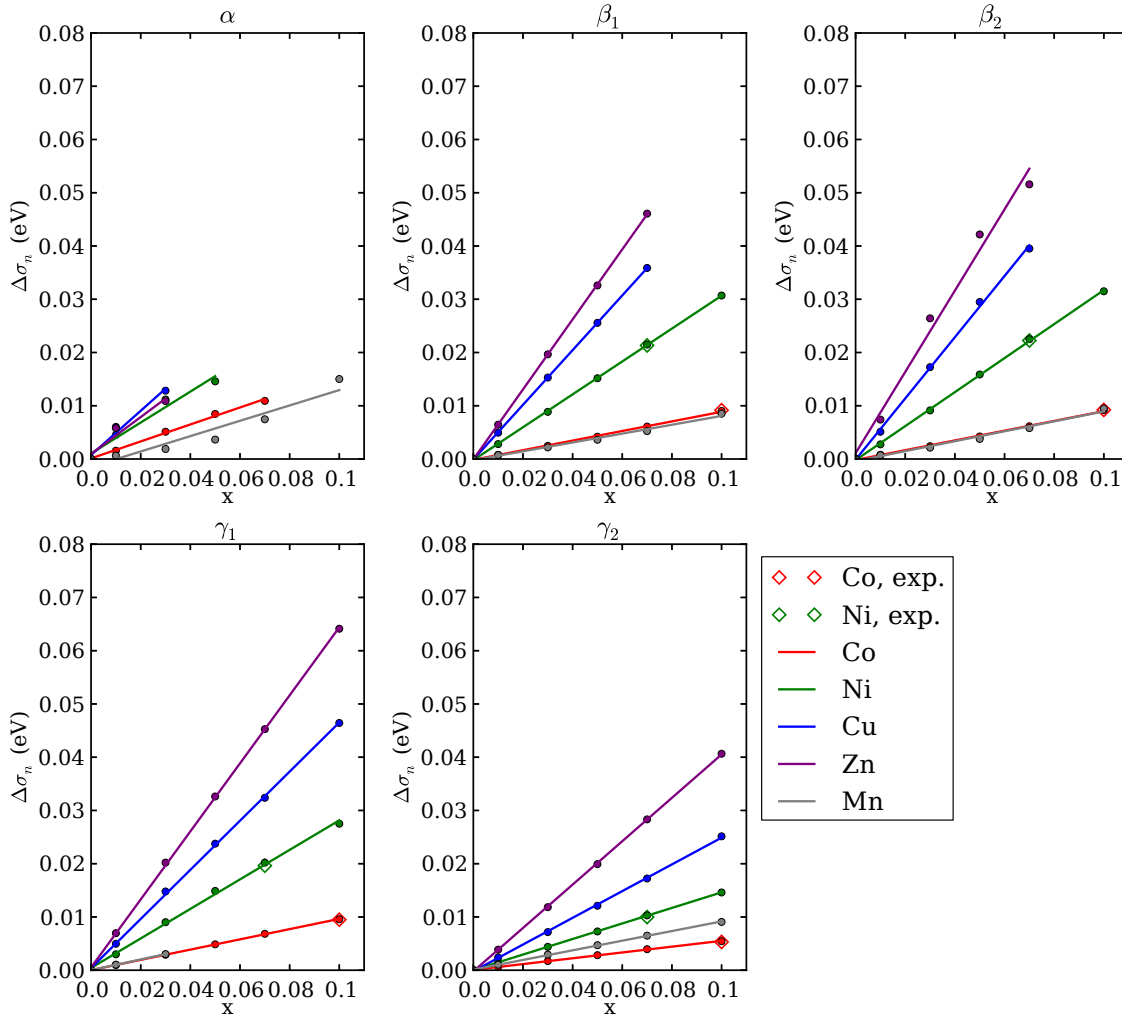


Figure 5.17.: Spectral broadenings of the three hole bands (α , β_1 and β_2) and the two electron bands (γ_1 and γ_2) against impurity concentration x for different transition metal substitutions (colors) in $\text{Ba}(\text{Fe}_{1-x}\text{TM}_x)_2\text{As}_2$. Solid lines: fits to the closed points, Open symbols: calculations at experimental structure

In this section the same route will be followed as before. First of all, we look at the total DOS at 5% substitution which is shown in Fig. 5.18 to get an overall impression. On the larger energy range, nothing interesting happens so this plot only shows a narrow energy window around the Fermi level. Obviously, the DOS of the Pd and Pt substitutions get shifted in the same way, as expected. The Ni substitution also is very close to the other two but it behaves slightly different. This finite change of the DOS cannot be attributed to the number of valence electrons and thus must originate from the different pseudopotential arising from a different configuration of the core electrons, core size and nuclear charge.

These effects are more obvious in the angular momentum and species projected DOS shown in Fig. 5.19. The Fe- d spectra shift hardly due to substitution as expected. The Pd- d and Pt- d DOS exhibit a similar form and are slightly shifted with respect to each other. The

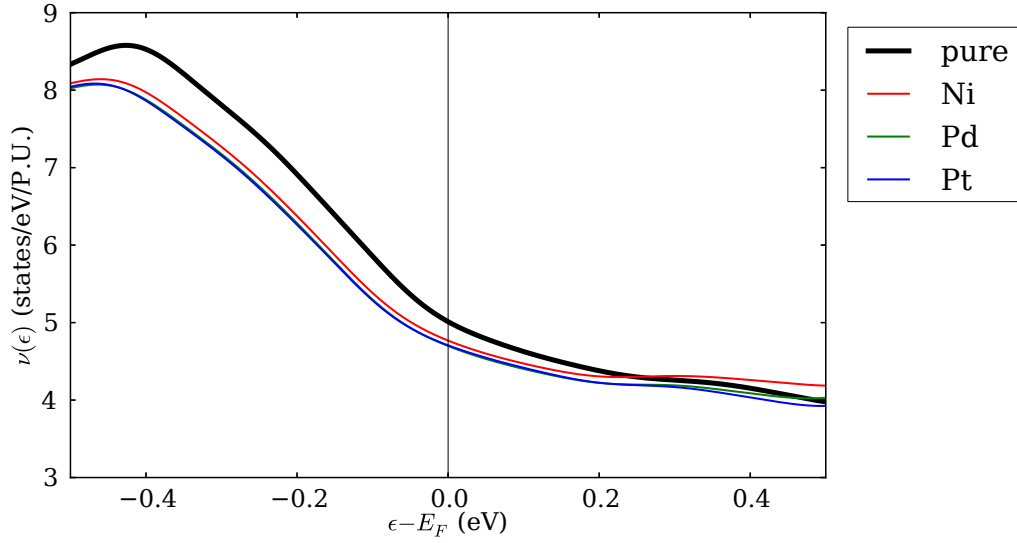


Figure 5.18.: Total DOS of pure BaFe_2As_2 (black) together with disordered $\text{Ba}(\text{Fe}_{0.95}\text{TM}_{0.05})_2\text{As}_2$ with $\text{TM} \in \{\text{Ni}, \text{Pd}, \text{Pt}\}$ (colors) in a small energy range around the Fermi level of the respective composition

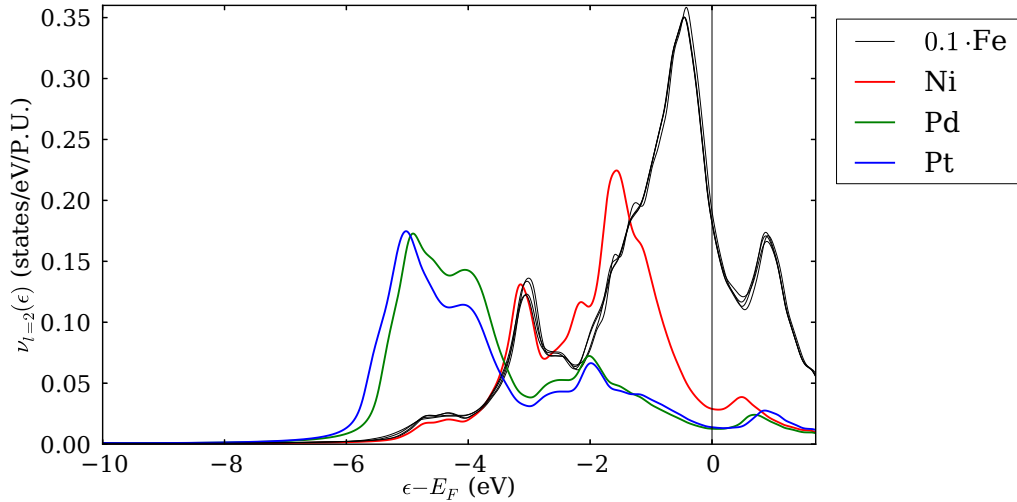


Figure 5.19.: Sum over all $l = 2$ contributions of angular momentum resolved and TM -projected DOS of disordered $\text{Ba}(\text{Fe}_{0.95}\text{TM}_{0.05})_2\text{As}_2$ with $\text{TM} \in \{\text{Ni}, \text{Pd}, \text{Pt}\}$ (colors) together with the respective projections on Fe scaled by 0.1 (black) for each composition as a reference

differences in their form can be attributed to their position in energy with respect to the energy levels of the other atoms which influences in particular the hybridization with As. But the form and especially the position of the Ni- d DOS are considerably different in spite of them all having the same number of valence electrons. For further analysis, in Tab. 5.5 the mean value of the Fe and substituent spectra obtained from calculation of the first statistic moment are compared with the impurity potentials from the difference of the diagonal d onsite Hamiltonian matrix elements. For Ni the shift of the spectrum

TM	$\approx \epsilon_0 - \epsilon_0^{\text{Fe}}$ (eV)	$V_{2,0}$ (eV)	$V_{2,1}$ (eV)	$V_{2,-1}$ (eV)	$V_{2,2}$ (eV)	$V_{2,-2}$ (eV)
Fe	0.000	0.000	0.000	0.000	0.000	0.000
Ni	-0.870	-0.928	-0.877	-0.877	-0.888	-0.920
Pd	-2.523	-2.761	-2.860	-2.860	-2.873	-2.771
Pt	-2.532	-2.736	-2.939	-2.939	-2.970	-2.805

Table 5.5.: Shift of substituent peak in orbital DOS compared with difference of diagonal elements with $l = 2$ of onsite Hamiltonians

correlates well with the impurity potential, for Pd and Pt the shifts show the same trends as the impurity potentials but the deviations between impurity potentials and shifts are larger. This essentially means that the offsite Hamiltonian matrix elements play a more important role for the spectra in case of Pd and Pt substitution than for Ni. This can be attributed to a stronger hybridization, being an offsite effect, of the Pd and Pt atoms with the surrounding atoms due to their larger core size and larger extent of the d wavefunctions.

Let me now discuss the level shifts and spectral broadenings as these concepts are already established from the last section. The level shifts for the concentrations $x \in \{0.01, 0.03, 0.05\}$ are compared for Ni, Pd and Pt substitution and a rigid band shift, which is the same for all considered substituents, in Fig. 5.20. Again, the level shifts are band selective and depend on their orbital character. Lines were fitted because like before they exhibit a linear behavior. As already outlined in the discussion of the DOS, just from the number of valence electrons we would expect the same shifts for all substituents. This is only the case for the β_2 -band but even these level shifts deviate from a rigid band shift. For the α and γ_2 bands the shifts caused by Pt substitution behave the most rigid-like but this is not true for the other bands. At least, this seems to be an effect of Pt substitution on bands with dominant $d_{x^2-y^2}$ orbital character. In general, the β and γ_1 bands, being of similar orbital composition behave the most rigid like, which is the same trend as already reported for the $3d$ - TM substitutions. This, together with the preceding analysis of the $3d$ - TM substitutions, shows that the picture of charge doping connected with a rigid band shift works best in the case of Co and Pt substitution. Also on this smaller energy scale, there are no substantial effects due to structural changes for Ni substitution.

The respective spectral broadenings are shown in Fig. 5.21 for the same range of concentrations. Again, they depend linearly on the concentration apart from the α band, where the linear fits could be argued. As before, they are band selective. Unlike the level shifts, the spectral broadenings exhibit a clear trend for the substituent species: for all bands, Ni causes the strongest broadenings, followed by Pd and Pt which has the weakest effects. For the $3d$ - TM substitutions the trends of the broadenings were correlated to the shifts of the respective TM d -spectra in the orbital DOS and thereby were also correlated with the impurity potential. For moving vertically in the periodic table, this trend does not hold anymore - at least not for the impurity potentials. This can be attributed to an enhanced significance of environmental disorder effects for increasing ionic radius and extent of the d wavefunctions. The last point gives rise to a stronger hybridization which clearly is an offsite effect. The changes of the spectral broadenings due to an experimental crystal structure are negligible.

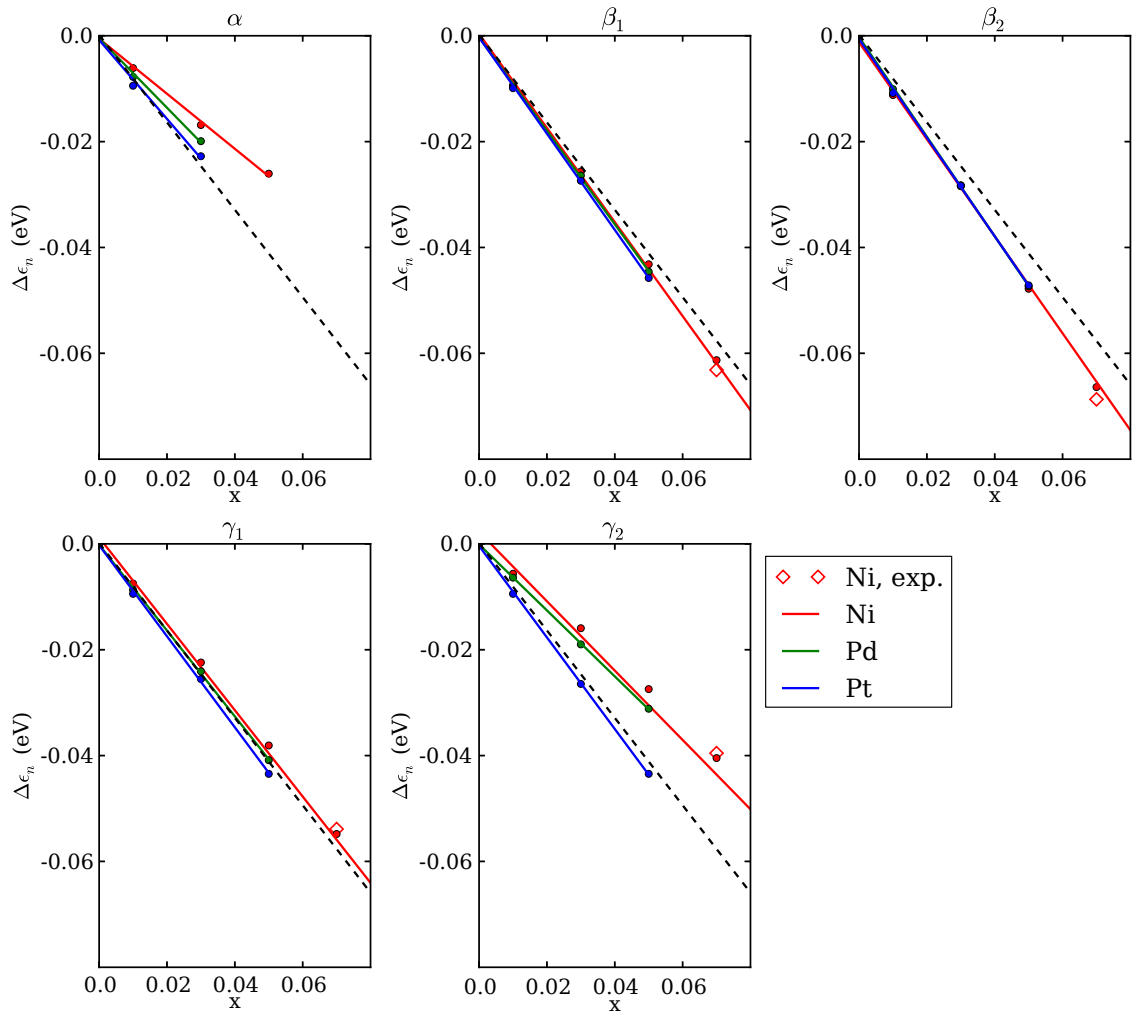


Figure 5.20.: Band shifts of the three hole bands (α , β_1 and β_2) and the two electron bands (γ_1 and γ_2) against impurity concentration x for Ni, Pd and Pt substitution (colors) in $\text{Ba}(\text{Fe}_{1-x}\text{TM}_x)_2\text{As}_2$. Solid colored lines: fits to the closed points, solid black line lines: rigid band shift, Open Symbols: calculations at experimental structure for 7% Ni substitution

5.5. K and P substitution

Until now, various substitutions at the Fe site of BaFe_2As_2 were considered in the present work. This section is devoted to substitutions at the other sites namely Ba by K and As by P. Especially, the $\text{Ba}_{1-x}\text{K}_x\text{Fe}_2\text{As}_2$ system was intensively studied in the past (also at our institute in particular). Apart from the usual tiny deviations of the DOS next to the Fermi level, neither the total DOS nor the orbital projected DOS exhibit considerable effects as in the case of *TM* substitution. The valence states which are *s* states for (Ba,K) and *p* states for (As,P) are far below the Fermi level. For this reason I immediately turn to the discussion of the band selective effects because from them we can learn the most about these substitutions. One important remark has to be made: until now the impurity concentration x was always a site related quantity. But whereas in the case of substi-

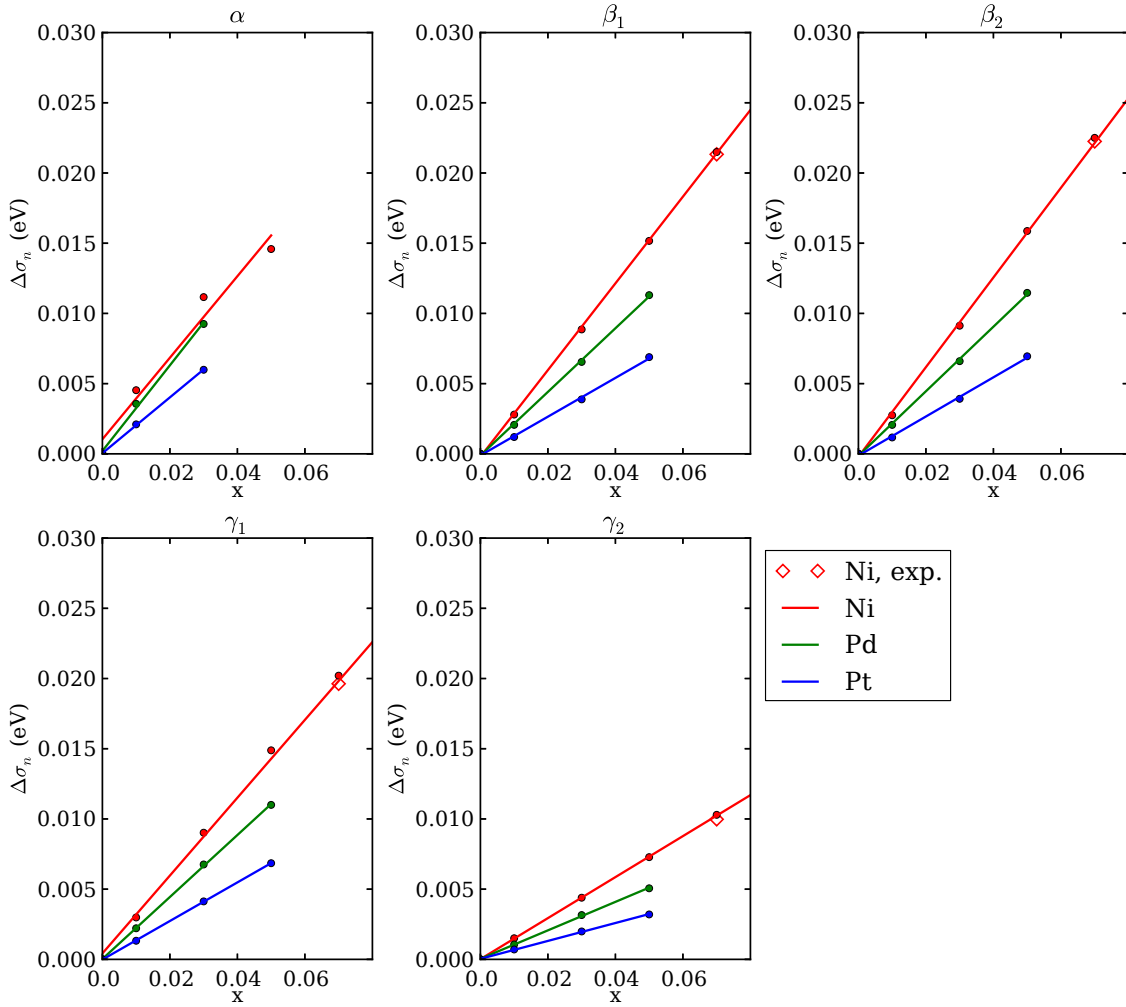


Figure 5.21.: Spectral broadenings of the three hole bands (α , β_1 and β_2) and the two electron bands (γ_1 and γ_2) against impurity concentration x for Ni, Pd and Pt substitution (colors) in $\text{Ba}(\text{Fe}_{1-x}\text{TM}_x)_2\text{As}_2$. Solid lines: fits to the closed points, Open Symbols: calculations at experimental structure for 7% Ni substitution

tutions at the Fe or the As sites always both atoms are substituted at a concentration x , at the Ba site only one atom is substituted. So for the same x in case of TM or P substitution, effectively twice as many atoms are substituted per unit cell as in the case of K substitution. In this section, the effects of K and P substitution are compared with each other and, as a reference, against Co substitution. To be able to do that, the effective percentage of substitutions per unit cell y will be considered. In the case of K substitution $y = x$ but for Co and P substitution $y = 2x$ will be plotted.

The respective level shifts are shown in Fig. 5.22. Due to the linear behavior of the level shifts with impurity concentration, lines were fitted. The level shifts for P substitution are negligible. From the fact that As and P are isovalent this is no surprise and shows that for P substitution the picture of a rigid band shift is well suited. K substitution causes level shifts which are of the same order of magnitude as for Co substitution but have the

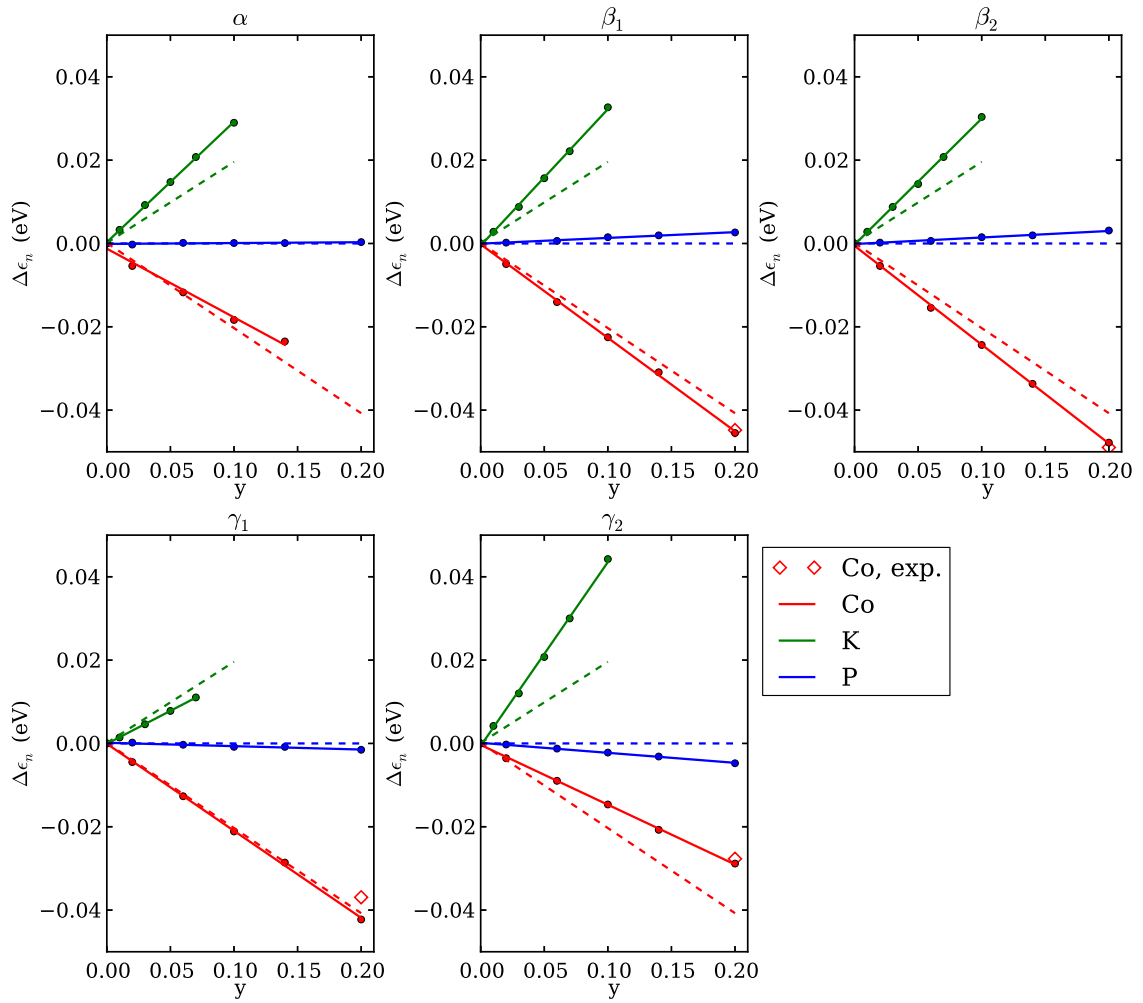


Figure 5.22.: Band shifts of the three hole bands (α , β_1 and β_2) and the two electron bands (γ_1 and γ_2) against effective impurity concentration y in the whole crystal for Co, K and P substitution (colors). Solid lines: linear fits to the closed points, dashed lines: rigid band shift, Open Symbols: calculations at experimental structure for 10% Co substitution

opposite sign. In the charge doping picture this means that K introduces holes to the system (as also Mn did). The level shifts depend on the orbital character of the band and are less well described by a rigid band shift than in the case of Co substitution. Only the γ_1 band behaves rigid-like. This is at least partly the same trend as for Co, Ni, Cu, Pd and Pt substitution but there also the β bands behaved more rigid-like which for K is not the case. Also on this smaller energy scale the structural changes at 10%Co substitution only have a small impact on the level shifts.

The spectral broadenings are shown in Fig. 5.23. Here, the broadenings for Co, which were plotted as a reference, are scaled by a factor of 0.1 because the broadenings for K substitution are 1-2 orders of magnitude smaller than for Co substitution. For P substitution they are even more than 3 orders of magnitude smaller for the hole bands. This is one of the most important results of this whole chapter: my calculations show that the lifetimes

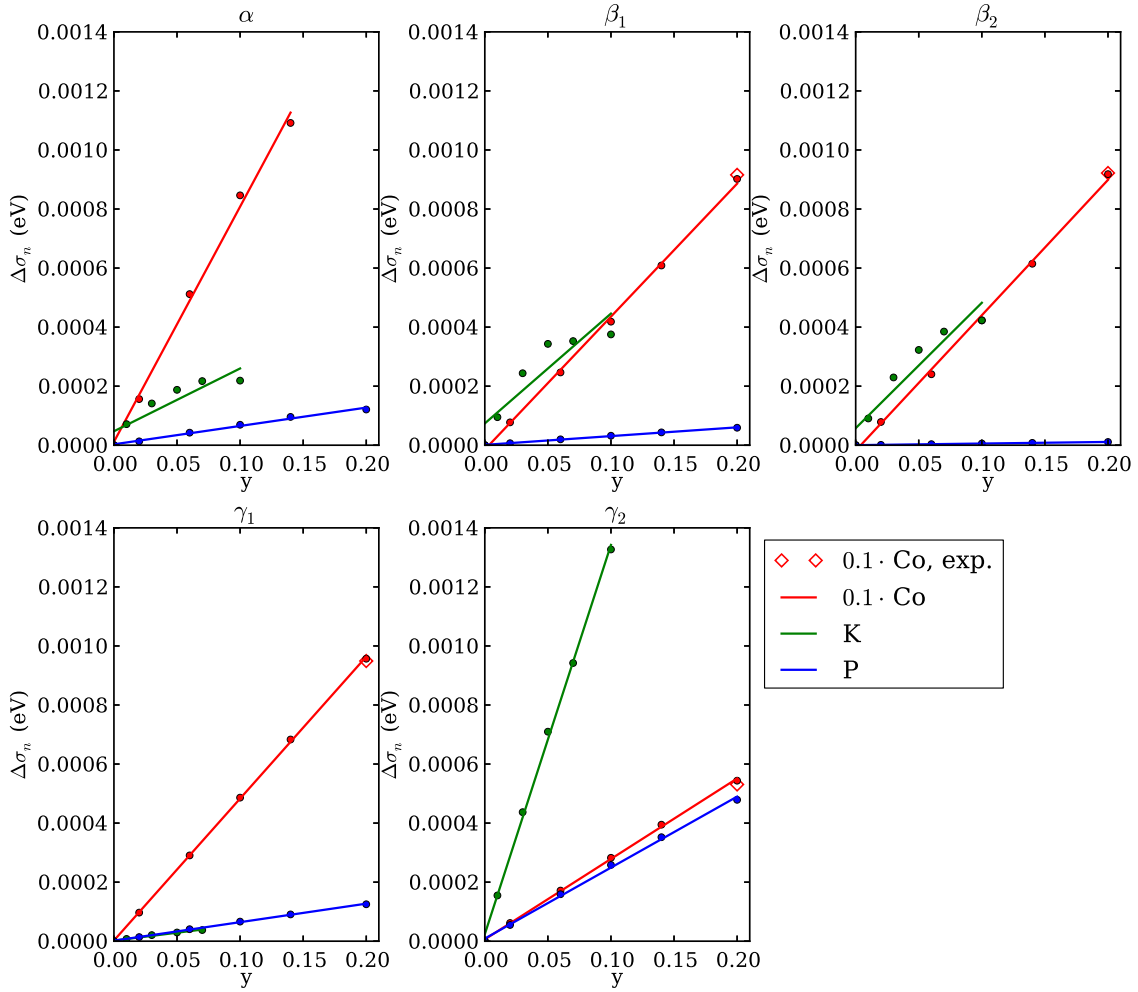


Figure 5.23.: Spectral broadenings of the three hole bands (α , β_1 and β_2) and the two electron bands (γ_1 and γ_2) against effective impurity concentration y in the whole crystal for Co, K and P substitution (colors). Solid lines: linear fits to the closed points, Open Symbols: calculations at experimental structure for 10% Co substitution

of the states at the Fermi level get only considerably affected by impurity scattering if the substitution occurs in the Fe planes, whereas the out-of plane substitutions only lead to negligible effects.

Nevertheless, even if these effects are negligible compared to the *TM* substitutions, let me also discuss them in detail. The P substitutions cause the smallest broadenings. The broadenings behave perfectly linear and lines were fitted. In general, the electron bands are more affected than the hole bands. The broadenings due to K substitutions are larger. For the electron bands they are linear with impurity concentration, for the hole bands this is not the case. So it is only justified to fit lines for the electron bands but nevertheless this was also done for the hole bands in order to have one central concentration-independent quantity to compare later between all species. This issue will be discussed again in the next section. Both substitutions differ in the trends when comparing different bands with each other as for *TM* substitutions.

Also on this energy scale, the spectral broadenings do not get considerably affected by structural changes. As a general trend, the considered structural effects for Co and Ni substitution are at best small for the level shifts but for the spectral broadenings they are negligible at all.

5.6. General trends of band renormalization

In the last sections, in particular the behavior of the level shifts and spectral broadenings on electron and hole bands next to the Fermi level were analyzed in detail depending on the impurity concentration for different substitutions separately. In most cases, they depend linearly on the impurity concentration so let me finally compare the slopes of these quantities to conclude the discussion of the essential effects of different substitutions on the individual bands for small impurity concentrations.

In Fig. 5.24 the slopes of the level shifts of the three hole bands α , β_1 , β_2 and the two electron bands γ_1 , γ_2 are plotted against substituent species together with the rigid band shift. In general, for $3d$ -TM substitution the level shifts follow the trend of the rigid band shift and the deviations grow upon moving horizontally in the periodic table to the right or left away from Fe. On the electron doped side for Co, Ni, and Cu substitution, the β and γ_1 bands, being of similar orbital composition, behave the most rigid-like. Especially the α band, which has $d_{x^2-y^2}$ orbital character, considerably deviates from the rigid band shift. In Sec. 5.1.3, experimental results [28] were introduced which showed a coincidence of the superconducting domes obtained from resistivity measurements, when they are plotted over the number of extra electrons expected from a rigid band shift. Provided that the $d_{x^2-y^2}$ orbitals do not significantly contribute to the pairing state, the rigidness of the remaining band shifts obtained in this work for Co and Ni substitution agree with these experimental findings. Mn substitution essentially introduces holes into the system. Here the two electron bands behave the most rigid-like. K substitution also introduces holes to the system but here the γ_2 band deviates the strongest from the rigid band shift. At

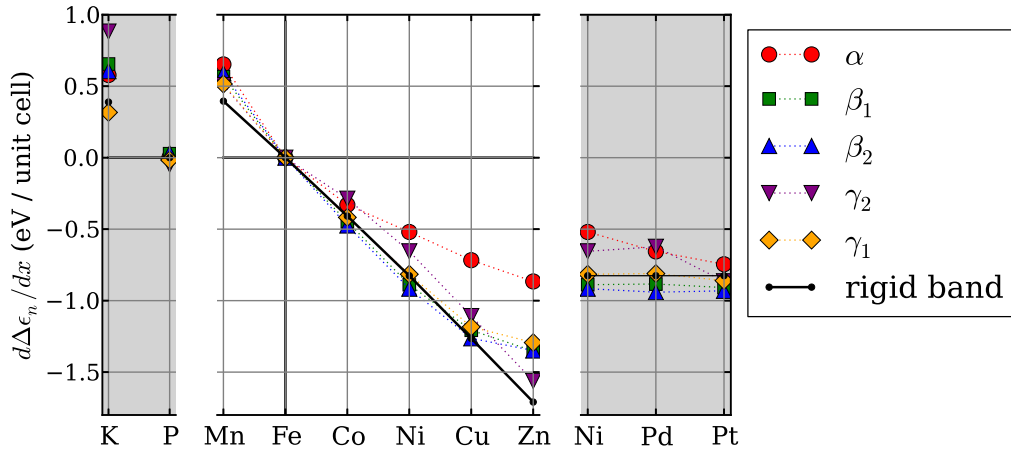


Figure 5.24.: Slopes of level shifts plotted over substituent (points) together with rigid band shift (solid line). Besides the $3d$ -TM substitution series for Fe, substitutions of K for Ba and P for As are shown to the left as well as substitutions of Pd and Pt for Fe to the right (shaded)

least considering the last statement about states with $d_{x^2-y^2}$ character, this fits into the general trend. P substitution causes no shifts due to its isovalence with As.

For the Ni, Pd, Pt substitution series, apparently an inverse trend seems to be fulfilled: moving vertically down in the periodic table, i.e. increasing the core size causes a decrease in the deviations from the rigid band shift. In general, these results demonstrate the applicability of the picture of charge doping in zeroth order but if we look into the details, the deviations from the rigid band shift depend on the orbital composition of the bands.

After having a complete picture about the level shifts, let me now draw general conclusions about the spectral broadenings. In Fig. 5.25 the dependence of the slopes of the spectral broadenings on substitution is shown. As already mentioned in last section, the most obvious feature which is also one of the most important conclusions of this study, is the fact that the spectral broadenings are only relevant for substitutions in the Fe planes. K and P substitution, both occurring outside these planes, have negligible broadening effects. Thus, also the deviations from the linear behavior of the spectral broadenings for K substitutions are negligible on this scale. For 3d-TM substitution the broadenings in general increase upon moving horizontally away from Fe in the periodic table. As already was the case for the level shifts, also the broadenings of the β and the γ_1 bands, being of similar orbital composition, show the same trend. Again, the bands with $d_{x^2-y^2}$ orbital character, α and γ_2 , behave differently.

As for the deviations of the level shifts from the rigid band shift, a similar trend can be attributed to the spectral broadenings for the Ni, Pd, Pt series. Moving vertically downwards in the periodic table, i.e. increasing the ionic radius causes a reduction of the spectral broadenings. This can be attributed to an increasing significance of environmental disorder effects because Pd and Pt substitutions come along with an extent of the d wave functions which gives rise to a stronger hybridization. This issue will again be important in Sec. 5.7.3 where intraband and interband scattering are compared.

In addition, from both the level shifts and the spectral broadening we can make the general statement that bands with $d_{x^2-y^2}$ orbital character, where the lobes of the orbitals mainly

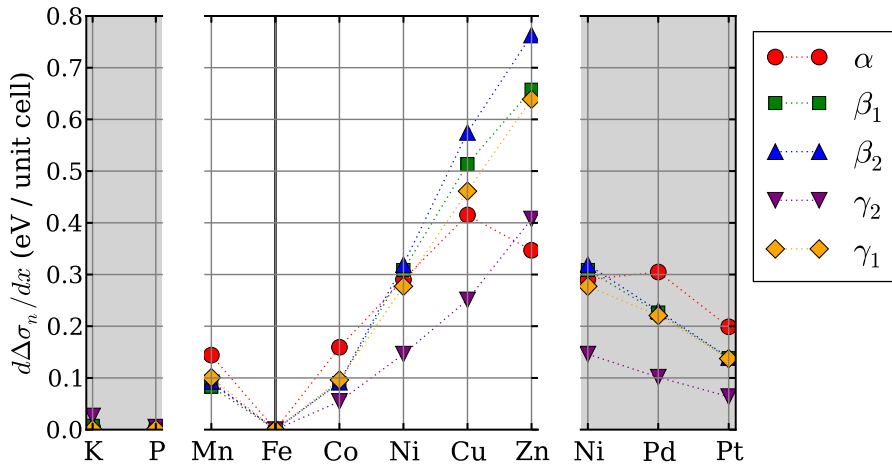


Figure 5.25.: Slopes of the spectral broadenings plotted over substituent. Besides the 3d-TM substitution series for Fe, substitutions of K for Ba and P for As are shown to the left as well as substitutions of Pd and Pt for Fe to the right (shaded)

point into the directions of the Fe-As bonds, show an anomalous behavior compared to the remaining bands.

At least to my knowledge, no direct measurements of spectral broadenings are published to further discuss these findings even if such broadenings in principle should be accessible by ARPES. At least for comparison with residual resistivity there are better formal approaches than these broadenings to derive them from the present calculations which should be done in future work.

5.7. Impact of impurity scattering on superconductivity

Looking back at the phase diagram Fig.5.3, it is obvious that substitutional disorder plays an important role in enhancing and suppressing superconductivity in BaFe_2As_2 . As already mentioned in the introduction into the present chapter, it is by now well established that the iron pnictides are unconventional superconductors. Furthermore, strong evidence is found by experimental [91–93] and theoretical [34–36] works that the superconducting order parameter in BaFe_2As_2 exhibits s -wave symmetry, meaning that it obeys the same symmetry as the crystal, but changes sign between the hole and electron Fermi surfaces (see Fig. 5.13). This structure of the order parameter is called an s^{+-} state. For investigating the influence of impurity scattering on such an s^{+-} superconductor it turns out important to distinguish between intraband and interband scattering. For such an analysis, which the rest of this chapter is devoted to, a further computational approach needs to be developed in addition to the CPA. Let me therefore first briefly summarize some general statements about impurity scattering in an s^{+-} superconductor.

5.7.1. Dirty superconductors: theory essentials

In conventional superconductors, the famous Anderson theorem [108] states that only magnetic impurities are pair breaking, i.e. suppress T_c , whereas nonmagnetic impurities do not affect the superconducting state. The Abrikosov-Gorkov (AG) theory [115] puts this statement on a quantitatively more profound level. This theory, which has been reviewed for example in [104], considers a conventional s -wave superconductor in the presence of impurities. In the following, a hat (e.g. \hat{U}) denotes an operator acting in Nambu space where the field operators are spinors $\Psi^\dagger = (\psi_\uparrow^\dagger, \psi_\downarrow^\dagger, \psi_\uparrow, \psi_\downarrow)$. The impurity potential was introduced by (notation in the following adapted to [104])

$$\hat{U}_{imp}(\mathbf{k} - \mathbf{k}') = U_{pot}(\mathbf{k} - \mathbf{k}')\tau_3 + J(\mathbf{k} - \mathbf{k}')\mathbf{S} \cdot \boldsymbol{\alpha} \quad (5.13)$$

where

$$\boldsymbol{\alpha} = \frac{1}{2} [(1 + \tau_3)\boldsymbol{\sigma} + (1 - \tau_3)\sigma_3\boldsymbol{\sigma}\sigma_3] \quad (5.14)$$

and the σ_i are Pauli matrices in spin space, $\boldsymbol{\sigma}$ is a vector of the three σ_i and τ_i are Pauli matrices in particle-hole space. U_{pot} is a potential scattering term describing scattering on nonmagnetic impurities and J accounts together with the spin \mathbf{S} of the impurity for magnetic impurities. The Green's function of the superconducting state is written as

$$\hat{G}(\mathbf{k}, \omega) = [i\omega_n - \xi(\mathbf{k})\tau_3 - \Delta\sigma_2\tau_2 - \hat{\Sigma}]^{-1} \equiv [i\tilde{\omega}_n - \tilde{\epsilon}(\mathbf{k}) - \tilde{\Delta}\sigma_2\tau_2]^{-1} \quad (5.15)$$

where $\xi(\mathbf{k})$ is the dispersion of the quasiparticles, ω_n are fermionic Matsubara frequencies, Δ is the superconducting gap in the clean case and $\hat{\Sigma}$ the self-energy due to impurities. $\tilde{\omega}_n$, $\tilde{\epsilon}(\mathbf{k})$ and $\tilde{\Delta}$ are the respective impurity-renormalized frequency, quasiparticle dispersion and gap. AG then found the equations for renormalization of the gap and frequencies

$$\tilde{\omega} = \omega + (\gamma_p + \gamma_s) \frac{\tilde{\omega}}{\sqrt{\tilde{\omega}^2 + \tilde{\Delta}^2}} \quad (5.16)$$

$$\tilde{\Delta} = \Delta + (\gamma_p - \gamma_s) \frac{\tilde{\Delta}}{\sqrt{\tilde{\omega}^2 + \tilde{\Delta}^2}} \quad (5.17)$$

where γ_p is the scattering rate due to nonmagnetic impurities and γ_s the scattering rate on magnetic impurities. Introducing the ratios $a \equiv \Delta/\omega$ and $\tilde{a} \equiv \tilde{\Delta}/\tilde{\omega}$, these two equations can be rewritten after some manipulations into

$$\tilde{a} = a \left(1 - 2\gamma_s \frac{\tilde{a}}{\Delta\sqrt{1 + \tilde{a}^2}} \right) \quad (5.18)$$

The superconducting gap is determined from the self-consistent equation

$$\Delta(\hat{k}) = \pi T N_0 \sum_{\tilde{a}_n} \int d\hat{k}' V(\hat{k}, \hat{k}') \frac{\tilde{a}_n(\hat{k}')}{\sqrt{1 + \tilde{a}_n^2(\hat{k}')}} \quad (5.19)$$

where \hat{k} is a unit \mathbf{k} -vector, the integration is performed over solid angle, N_0 is the DOS in the normal state and V is the pairing potential. The important outcome of this theory is that the renormalization of the ratio of the gap and frequencies via Eq. (5.18) only depends on the scattering rate γ_s on magnetic impurities. If there are no magnetic impurities, Eq. (5.19) resembles just the same gap equation as in the clean case. So the gap would not be changed by nonmagnetic impurities at all which is the essence of the Anderson theorem.

Golubov and Mazin [33] have extended this theory to multiband superconductors, where several bands contribute to the pairing. For such a case, they found that impurities which lead to interband scattering, no matter if they are magnetic or not, as well as intraband scattering caused by magnetic impurities suppress superconductivity. Superconductivity in multiband systems is only robust against intraband scattering caused by nonmagnetic impurities. Furthermore, these authors find that in the special case of a two-band system, due to symmetries only magnetic interband scattering suppresses T_c . In addition, they also considered a two-band system with a sign change in the order parameter between the two bands, which, as mentioned above, is a promising candidate for the iron pnictides, and found out that only nonmagnetic interband scattering is pair breaking.

This last statement about the s^{+-} scenario was rederived in a compact form by Vorontsov et al. [37] in connection with the iron-based superconductors: according to their work, Eq. (5.18) then becomes (adapted to the present notation)

$$\tilde{a} = a \left(1 - 2\gamma_\pi \frac{\tilde{a}}{\Delta\sqrt{1 + \tilde{a}^2}} \right) \quad (5.20)$$

which is formally the same result as in conventional AG theory but with the interband scattering rate on nonmagnetic impurities γ_π appearing instead of γ_s . Due to their analysis,

the nonmagnetic interband scattering alone leads to pair breaking in an s^{+-} superconductor whereas the intraband scattering influences the residual resistivity.

As a matter of completeness, it should be mentioned that Hoyer et al. [116] provided an alternative and more generic approach to this problem: based on symmetry considerations they derived a generalization of the Anderson theorem to s^{+-} superconductors. It states that in such systems superconductivity is robust against interband scattering on time-reversal antisymmetric impurities and intraband scattering on time-reversal symmetric impurities. The time-reversal symmetric impurities represent the nonmagnetic impurities where the discussion in the present work is restricted to.

Going back to the schematic phase diagram Fig. 5.3, the superconducting transition temperature T_c not only drops with increasing impurity concentration: At low impurity concentrations (the so-called underdoped region) it first *rises* with impurity concentration up to a maximum (at the so-called optimally doped impurity concentration) and *then* drops with increasing impurity concentration (in the so-called overdoped region). But the theoretical considerations reviewed so far only describe the suppression of T_c due to (interband) impurity scattering, i.e. only properly explain the overdoped region of the superconducting dome. The rise of T_c in the underdoped region can be explained with the interplay between superconductivity and antiferromagnetism: At low impurity concentrations, long-range antiferromagnetic order forms and suppresses superconductivity. Upon increasing the impurity concentration, the antiferromagnetic order gets suppressed which enhances superconductivity up to the optimal doping. Then, superconductivity gets suppressed by impurity scattering. This rather qualitative discussion has been formulated in a quantitatively more profound model study by Fernandes et al. [117]. From this discussion it is clear that when comparing scattering rates with experimental transition temperatures considering pair breaking, on the one hand the height of the superconducting dome is important but also its width on the concentration axis gives information about how strong a certain amount of impurities suppresses superconductivity.

5.7.2. Intraband and interband scattering from first principles

From these statements it is obvious that only the spectral broadenings alone, analyzed so far in this work, are not sufficient to study the aspect of pair breaking for the various considered substitutions. These broadenings contain all accumulated scattering effects onto a single band but do not provide explicit information about scattering *between* two bands.

The goal of this section is to set up a formalism suited for calculating scattering rates between two arbitrary bands of the parent compound from first principles, of course trying to benefit from the quantities provided by the CPA calculations so far. For simplicity, only a single impurity will be considered in order to gain information about interband and intraband contributions to the spectral broadenings obtained above. In the end, a formula will be derived which gives the interband and intraband scattering rates per impurity introduced into the system. The linearity of the spectral broadenings in the impurity concentration justifies to extrapolate these results to finite impurity concentrations where the actual suppression of superconductivity due to impurity scattering occurs, as explained in the last section.

The appropriate quantity to study the effects of a localized perturbation, is the transition matrix T . It is related to the Green's function in the following way in the tight-binding

language

$$G = G_0 + G_0 T G_0 \quad (5.21)$$

$$T = V + V G_0 V + V G_0 V G_0 V + \dots \quad (5.22)$$

where again G (G_0) are the full (unperturbed) Green's functions, respectively, and V is the impurity potential. This shows that T essentially is a summation of all repeated scatterings up to infinite order on the same impurity. How can we use this to consider scatterings between bands?

The Lippmann-Schwinger equation of scattering theory relates a perturbed state $|\psi\rangle$ to an unperturbed state $|\phi\rangle$ in the following form

$$|\psi\rangle = |\phi\rangle + \hat{G}_0 \hat{V} |\psi\rangle \quad (5.23)$$

where \hat{V} is the operator of the scattering potential, in our case the impurity potential, and $\hat{G}_0 = (\omega - \hat{H}_0)^{-1}$ is the Green's function operator of the unperturbed system with Hamiltonian \hat{H}_0 , which in our case is the parent compound. The T -matrix operator can then be defined (see for example [118]) as

$$\hat{T}|\phi\rangle = \hat{V}|\psi\rangle \quad (5.24)$$

Application of \hat{V} to both sides of Eq. (5.23) from the left

$$\hat{V}|\psi\rangle = \hat{V}|\phi\rangle + \hat{V}\hat{G}_0\hat{V}|\psi\rangle \quad (5.25)$$

and the use of Eq. (5.24) yields

$$\hat{T}|\phi\rangle = \hat{V}|\phi\rangle + \hat{V}\hat{G}_0\hat{T}|\phi\rangle \quad (5.26)$$

which only contains unperturbed states and thus serves as a convenient starting point for the evaluation of the T -matrix in a special basis. We are interested in the influence of the scattering on selected bands. Thus, the unperturbed states will be band states of the parent compound $|n, \mathbf{k}\rangle$ and the equation is

$$\hat{T}|n, \mathbf{k}\rangle = \hat{V}|n, \mathbf{k}\rangle + \hat{V}\hat{G}_0\hat{T}|n, \mathbf{k}\rangle \quad (5.27)$$

These band states $|n, \mathbf{k}\rangle$ can be expressed in the local basis $|i\mu\rangle$ via the band eigenvector components $c_{n,i\mu}(\mathbf{k})$ which were already used in the projection technique for the spectral function

$$|n, \mathbf{k}\rangle = \sum_{i\mu} c_{n,i\mu}(\mathbf{k}) e^{i\mathbf{k}\mathbf{R}_i} |i\mu\rangle \quad (5.28)$$

where i is a site and μ an orbital index and \mathbf{R}_i the vector of the site. Projection of Eq. (5.27) on a local basis state $\langle i\mu|$ from the left and the use of Eq. (5.28) yields the matrix equation

$$\sum_{j\nu} \langle i\mu | \hat{T} | j\nu \rangle c_{n,j\nu}(\mathbf{k}) e^{i\mathbf{k}\mathbf{R}_j} = \sum_{j\nu} \langle i\mu | \hat{V} + \hat{V}\hat{G}_0\hat{T} | j\nu \rangle c_{n,j\nu}(\mathbf{k}) e^{i\mathbf{k}\mathbf{R}_j} \quad (5.29)$$

Before proceeding, the matrix element $\langle i\mu | \hat{V}\hat{G}_0\hat{T} | j\nu \rangle$ has to be evaluated in order to see which Green's function matrices G or \mathcal{G} (see Eqs (2.63) and (2.64)) enter the expression. For the moment, let me suppress the index μ and use a combined orbital and site index i

$$\begin{aligned} \langle i | \hat{V}\hat{G}_0\hat{T} | j \rangle &= \sum_{a,b,c,d} \langle i | \hat{V} | a \rangle S_{a,b}^{-1} \langle b | \hat{G}_0 | c \rangle S_{c,d}^{-1} \langle d | \hat{T} | j \rangle \\ &= \sum_{a,b,c,d} V_{i,a} S_{a,b}^{-1} (S\mathcal{G}_0S)_{b,c} S_{c,d}^{-1} T_{d,j} \\ &= \sum_{a,d} V_{i,a} \mathcal{G}_{0,a,d} T_{d,j} = (V\mathcal{G}_0T)_{i,j} \end{aligned} \quad (5.30)$$

where the unity operator in the nonorthogonal basis $\mathbf{1} = \sum_{a,b} |a\rangle S_{a,b}^{-1} \langle b|$ was used¹. Absorbing the phase factor together with the eigenvectors into a new coefficient $a_{n,i\mu}(\mathbf{k}) \equiv c_{n,i\mu}(\mathbf{k})e^{i\mathbf{k}\mathbf{R}_i}$ and arranging these coefficient into a matrix $A(\mathbf{k})$, Eq. (5.29) can be converted into the matrix equation

$$TA(\mathbf{k})|_{i\mu,n} = (V + V\mathcal{G}_0T)A(\mathbf{k})|_{i\mu,n} \quad (5.31)$$

which can be rearranged into a closed expression for the T -matrix

$$TA(\mathbf{k})|_{i\mu,n} = (1 - V\mathcal{G}_0)^{-1} VA(\mathbf{k})|_{i\mu,n} \quad (5.32)$$

Converting this expression back to the old notation gives the equivalent equation

$$\langle i\mu | \hat{T} | n, \mathbf{k} \rangle = \sum_{j\nu} \left[(1 - V\mathcal{G}_0)^{-1} V \right]_{i\mu,j\nu} c_{n,j\nu}(\mathbf{k}) e^{i\mathbf{k}\mathbf{R}_j} \quad (5.33)$$

In this section, we are interested in transition between different bands at different \mathbf{k} -points $\langle n'\mathbf{k}' | \hat{T} | n, \mathbf{k} \rangle$. Using Eq. (5.28) to convert the left terminal band to the local basis and then inserting Eq. (5.33) finally gives

$$\begin{aligned} \langle n'\mathbf{k}' | \hat{T} | n, \mathbf{k} \rangle &= \sum_{i\mu} \langle i\mu | \hat{T} | n, \mathbf{k} \rangle c_{n',i\mu}^*(\mathbf{k}') e^{-i\mathbf{k}'\mathbf{R}_i} \\ &= \sum_{i\mu,j\nu} c_{n',i\mu}^*(\mathbf{k}') \left[(1 - V\mathcal{G}_0)^{-1} V \right]_{i\mu,j\nu} c_{n,j\nu}(\mathbf{k}) e^{-i\mathbf{k}'\mathbf{R}_i} e^{i\mathbf{k}\mathbf{R}_j} \end{aligned} \quad (5.34)$$

which is nothing else than the T -matrix in the local basis representation transformed to the band basis. Until now, the impurity potential V was not specified in further detail. In order to describe the physical situation of replacing one single host atom of species p at site s by an impurity of species q , a realistic formulation in the BEB-language would be

$$\begin{aligned} V_{i\mu,j\nu}^{P,Q} &= \left(H_{i\mu,j\nu}^{P,Q} \delta_{P,q} - H_{i\mu,j\nu}^{P,Q} \delta_{P,p} \right) \delta_{i,s} + \left(H_{i\mu,j\nu}^{P,Q} \delta_{Q,q} - H_{i\mu,j\nu}^{P,Q} \delta_{Q,p} \right) \delta_{j,s} \\ &\quad - \left(H_{i\mu,j\nu}^{P,Q} \delta_{P,q} \delta_{Q,q} - H_{i\mu,j\nu}^{P,Q} \delta_{P,p} \delta_{Q,p} \right) \delta_{i,s} \delta_{j,s} \end{aligned} \quad (5.35)$$

¹According to [118], the Green's function operator \hat{G}_0 involved in the Lippmann-Schwinger equation is just the resolvent operator $(\omega - \hat{H})^{-1}$. In App. D.3 it is shown that the matrix elements of the resolvent operator in a nonorthogonal basis are just identical to our Green's matrix $G = S\mathcal{G}S$ connected with annihilation and creation operators.

where the second line is just a double counting correction for terms appearing both in the first and second term of the first line and H always means the total Hamiltonian, i.e. the sum of onsite and offsite contributions. This expression for the impurity potential is the most accurate one based on the Hamiltonian matrix elements available in the present framework. It contains not only the difference in onsite energies arising from the impurity, it moreover accounts for the environment, i.e. the modifications in the hopping terms induced by the impurity. For the most cases, the onsite contributions are expected to be dominant. To facilitate the problem, I thus once again will resort to the single-site approximation where the impurity potential reads

$${}^{q_s}V_{i\mu,j\nu}^{P,Q} = \left(H_{i\mu,i\nu}^{q,q} \delta_{P,q} \delta_{Q,q} - H_{i\mu,i\nu}^{p,p} \delta_{P,p} \delta_{Q,p} \right) \delta_{i,s} \delta_{i,j} \quad (5.36)$$

which is nothing else than the difference between the substituent species block of the onsite Hamiltonian of the substitutional end member and the host species block of the onsite Hamiltonian of the parent compound. This approximation has the further advantage that for \mathcal{G}_0 appearing in Eq. (5.34) just the CPA effective medium Green's function Γ of the parent compound, being an onsite quantity as well, can be used. Then, the expression for the single-site T -matrix becomes

$${}^{q_s}T_{n\mathbf{k},n'\mathbf{k}'}(\omega) = \sum_{\mu\nu} c_{n,i\mu}^*(\mathbf{k}) \left[(1 - {}^{q_s}V\Gamma(\omega))^{-1} {}^{q_s}V \right]_{i,\mu\nu} c_{n',i\nu}(\mathbf{k}') e^{i(\mathbf{k}'-\mathbf{k})\mathbf{R}_i} \quad (5.37)$$

Going beyond this onsite approximation would require to evaluate the impurity potential and related summations in Eq. (5.34) for a couple of sites surrounding s which results in the inversion of rather big matrices. All quantities are available from the CPA calculations and the evaluation of Eq. (5.37) is restricted to just one single substitutional site in one unit cell. In practical calculations, we take the charge self-consistent Green's function Γ and for the terms in Eq. (5.36) for the impurity potential associated with the host $H_{i\mu,i\nu}^{p,p}$ the charge self consistent onsite Hamiltonian of the parent compound. The terms in Eq. (5.36) associated with the substituent $H_{i\mu,i\nu}^{q,q}$ are taken from the charge self-consistent calculation of a disordered system at low concentrations ($x = 0.01$) to incorporate at least some of the environmental effects neglected by the single-site approximation. In order that a difference of matrix blocks, which were evaluated in different sets of orbitals, is calculated in Eq. (5.36), the impurity part is transformed from the impurity orbitals $|s, \mu, i\rangle$ where it was originally evaluated with respect to in the CPA calculation to the host orbitals $|s, \mu, h\rangle$ according to

$$\langle s, \mu, h | \hat{H}_i | s, \nu, h \rangle = \sum_{\mu', \nu'} S_{\mu, \mu'}^{h, i} \langle s, \mu', i | \hat{H}_i | s, \nu', i \rangle S_{\nu', \nu}^{i, h} \quad (5.38)$$

Here $S_{\mu, \mu'}^{h, i} = \langle \mu, h | \mu', i \rangle$ is the overlap matrix between the impurity and host orbitals. The actual scattering rate from band n at \mathbf{k}_F to band n' at \mathbf{k}'_F at the Fermi level then can be readily calculated from Fermi's golden rule (see for example [119])

$$w_{n\mathbf{k}_F, n'\mathbf{k}'_F} = \frac{2\pi}{\hbar} x \left| {}^{q_s}T_{n\mathbf{k}_F, n'\mathbf{k}'_F}(E_F) \right|^2 \nu_{n'}(E_F) \quad (5.39)$$

where the initial and final band as well as the T -matrix are taken at the Fermi-level due to energy conservation because we assume elastic scattering. $\nu_{n'}(E_F)$ is the band projected

density of states of the final band, as required by Fermi's golden rule. This leads to the general property $w_{n\mathbf{k}_F, n'\mathbf{k}'_F} \neq w_{n'\mathbf{k}'_F, n\mathbf{k}_F}$ which can be understood by the fact that the elastic scattering rate of course depends on the number of available final states with the appropriate energy. Because the T -matrix itself only considers the effect of a single impurity, the result needs to be scaled by the impurity concentration x to obtain the rate at a finite number of impurities which is valid as long as environmental disorder effects are neglected.

5.7.3. Intraband versus interband scattering comparing different substitutions

In Fig. 5.26 the scattering rate from the α -band at the Fermi wave vector in the (1,1,0)-direction (marked with an arrow) into all bands on the Fermi surface cross-section of the parent compound in the $(\mathbf{k}_x, \mathbf{k}_y)$ -plane (see also Fig. 5.13) is shown as a color-plot for Co substitution. Obviously, the scattering rate highly depends on the final band and on the scattering vector. The scattering rate into the same band at the same \mathbf{k} -point is the highest, as naively might have been expected. The scattering rate into the same band in general decreases as the angle between the initial and final \mathbf{k} -point increases to $\varphi = \pi$ and then increases again as the angle further increases to $\varphi = 2\pi$. Also this seems intuitive, apart from the "singular" points at $\varphi = n\pi/2$ where the rate assumes almost the

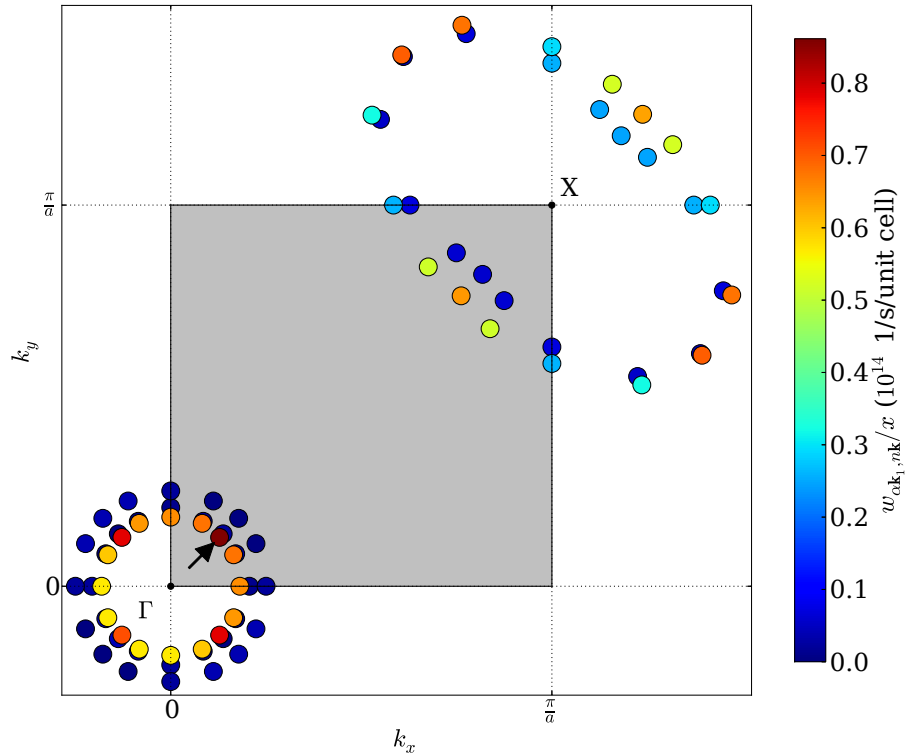


Figure 5.26.: Plot of the concentration normalized scattering rate $w_{\alpha\mathbf{k}_1, n\mathbf{k}}/x$ (colors) due to Co substitution on the Fermi surface of the parent compound in the $(\mathbf{k}_x, \mathbf{k}_y)$ -plane starting from band α at $\mathbf{k}_1 = k_F(1,1,0)$ (marked with an arrow) into all other bands, Shaded area: first Brillouin zone

same value as at $\varphi = 0$. The physical origin of this behavior is not clear - at least it is solely determined by the eigenvectors of the parent compound and might be related to the tetragonal symmetry. The scattering rate into the other two hole bands (β_1, β_2) is negligible. The scattering rate into the outer electron band γ_2 , being of similar dominant orbital character $d_{x^2-y^2}$ as the initial α -band, shows a similar behavior as the scattering rate into the same band. The maximum rates, which exhibit the same fourfold symmetry at $\phi = n\pi/2$ counted from the (1,1,0)-direction with respect to the X -point, are smaller and the fluctuations are larger. In addition, there are two "absolute" maxima at $\phi = \pi/2$ and $\phi = 3\pi/2$ instead of one at $\phi = 0$. Compared to this, the rate into the inner electron band γ_1 is relatively small and monotonously decreases as ϕ increases from 0 to π . To a certain extent, the \mathbf{k} -space anisotropy of the scattering into the two electron bands mutually cancels, a point to which I will come back later.

At least from this special case of the scattering from the α -band at $k_F(1,1,0)$ for Co substitution, we can learn apart from the \mathbf{k} -space anisotropy that the intraband hole-hole scattering is the largest, followed by an interband hole-electron scattering which still is considerable and finally a negligible interband hole-hole scattering. We are interested in more general trends using different initial bands and especially comparing different substitutions. For this purpose, a fully \mathbf{k} -resolved analysis contains too much detail information. Therefore, in spite of the \mathbf{k} -space anisotropy, let me now average over the respective Fermi sheets in \mathbf{k} -space

$$\frac{w_{n_i, n_f}}{x} = \frac{1}{N_i N_f} \sum_{\mathbf{k}_i, \mathbf{k}_f} \frac{w_{n_i \mathbf{k}_i, n_f \mathbf{k}_f}}{x} \quad (5.40)$$

where N_i (N_f) are the numbers of initial (final) \mathbf{k} -points, such that we are left with \mathbf{k} -independent scattering rates, still between all five bands. The results are shown in Fig. 5.27. In each plot, the scattering rate starting from the same initial band is plotted against substitution in the same manner as was already done for the slopes of the level shifts and broadenings. The color code distinguishes between the different final bands and the respective intraband scattering rate is emphasized by larger symbols.

First of all, the results exhibit a similar overall trend as already the spectral broadenings (see Sec. 5.6): for TM substitution the scattering rates grow upon moving horizontally in the periodic table whereas the effects are much smaller for substitution outside the Fe planes. For P substitution the rates are negligible and for K substitution solely the intraband scattering rate $w_{\alpha, \alpha}$ plays a small role. Only the series Ni, Pd, Pt behaves differently than the spectral broadenings. Whereas the spectral broadenings systematically decreased upon moving vertically downwards in the periodic table (apart from the α -band) this is not the case for the scattering rates. They increase from Ni to Pd to a value almost as large as for Cu substitution and then decrease again from Pd to Pt to a value in the middle between Ni and Cu. As discussed above, the behavior of the shifts in the spectra of the orbital DOS was not the same as that of the onsite matrix elements (see Fig. 5.19 and Tab. 5.5). This discrepancy and the fact that for Pd and Pt substitution, the spectral broadenings do not show the same trends as the shifts in the orbital DOS, in contrast to the systematic trends for 3d TM substitution, was attributed to a stronger influence of environmental disorder effects for Pd and Pt substitution. On the other hand, the increase in the scattering rate from Ni to Pd in general follows the trends of the shift of the spectra of the projected DOS and the onsite Hamiltonian matrix elements. Bearing in mind that the single-site T -matrix only depends on the onsite Hamiltonian matrix elements, this behavior can be understood. The scattering rates for Pt substitution in addition do not

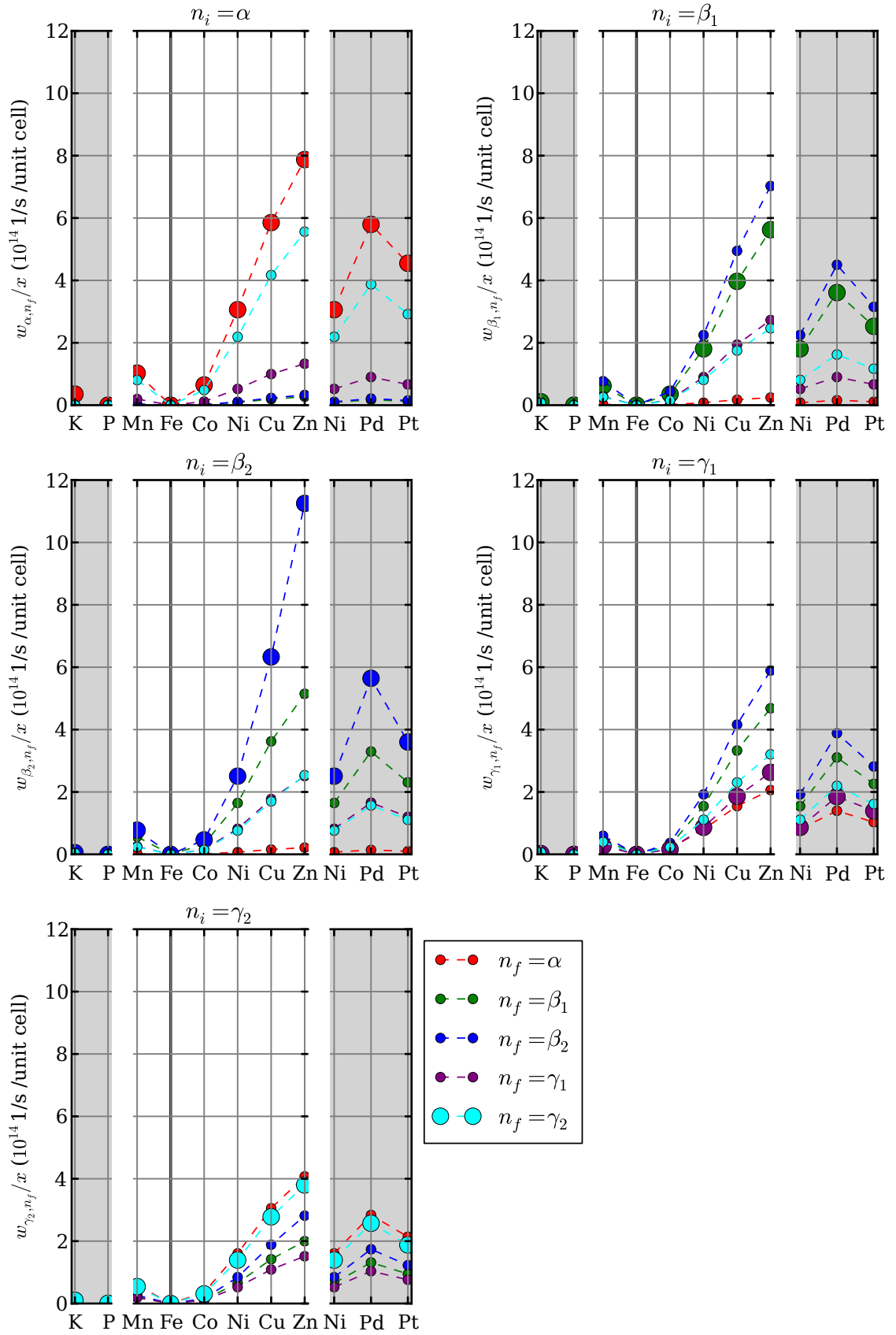


Figure 5.27.: Concentration normalized, k -averaged scattering rate $w_{n_i, n_f}/x$ against substituent, each plot corresponds to a fixed initial band n_i , points for intraband scattering are larger, different final bands n_f are color-coded

follow the trend of the shifts of the projected DOS and instead decrease again with respect to Pd. This originates from the basis transformation of the orbitals Eq. (5.38) which was verified by an additional calculation without this transformation. All this strongly suggests that whereas for $3d$ -TM, K and P substitution the onsite approximation in the calculation of the T -matrix was sufficient, this is not the case anymore for $4d$ and $5d$ TM substitution, where the ionic radii of the substituents considerably increase with respect to the host atom. As already stated above, for such larger atoms also the d wave functions become more extended and thus hybridization effects, being offsite phenomena, play a more important role. The spectral broadenings do not suffer from this shortcomings because these were derived from the BEB-CPA calculations which accounts for the influence of disorder on the hybridization and makes no further single site approximation. Thus, for $4d$ and $5d$ TM substitution we trust more in the spectral broadenings.

The hole-hole scattering rates are the largest for all substitutions. In case of the α or β_2 -band being the initial band, these are also intraband scattering rates. If the β_1 -band is the initial one, the rate w_{β_1, β_2} is the largest but the intraband rate w_{β_1, β_1} is almost as large. This is another manifestation that the two β -bands behave similarly: they show similar level shifts, broadenings and exhibit a similar dominant orbital character.

In all cases, the hole-electron scattering is smaller than the hole-hole scattering. For the α -band as initial state, the hole-electron scattering is the second largest, for the β bands as initial states it is the third largest. If the electron bands are the initial states, the largest scattering rate is an electron-hole rate (in case of γ_2 being the initial state, the second largest electron-electron intraband scattering rate is however almost the same). In general, for the largest rates a similar dominant orbital character of the initial and final band seems to be an important condition (which in the case of intraband scattering as for α and β_2 as initial states is of course trivial).

We cannot extract further general trends from this data so far. To make the study more transparent, let me now average over the two outer hole bands $(\beta_1, \beta_2) \rightarrow \beta$ based on their similar behavior in all quantities analyzed so far and the two electron bands $(\gamma_1, \gamma_2) \rightarrow \gamma$ based on the argument that their \mathbf{k} -space anisotropy mutually cancels, as mentioned above. As an example, for this effective three-band system the scattering rate on the Fermi surface for Co substitution, again starting from the α -band at $k_F(1,1,0)$ is plotted in Fig. 5.28. Considering the scattering rates between the hole bands, nothing has drastically changed. The scattering into the electron band now is more isotropic.

5.7.4. Implications for pair breaking

For the general, substitution dependent trends, the scattering rates for the reduced electronic structure to effectively three bands again were averaged over all \mathbf{k} -points on the respective Fermi surface sheet. The results are shown in Fig. 5.29, where the concentration normalized intraband scattering rates \mathcal{V} are shown on left side and the interband rates \mathcal{U} on the right side. What do these results imply for the pair breaking strength of the individual substitutions? First of all, the scattering in case of P substitution is negligible like the spectral broadenings. Secondly and most importantly, for all substitutions the hole-hole intraband scattering is larger than the hole-electron and electron-hole interband scattering. For TM substitution, the hole-hole intraband scattering is enhanced by more than a factor of two compared to the electron-hole scattering, for K substitution this factor is even larger. The electron-electron intraband scattering is of the same order of magnitude as the hole-electron interband scattering. The interband scattering between different

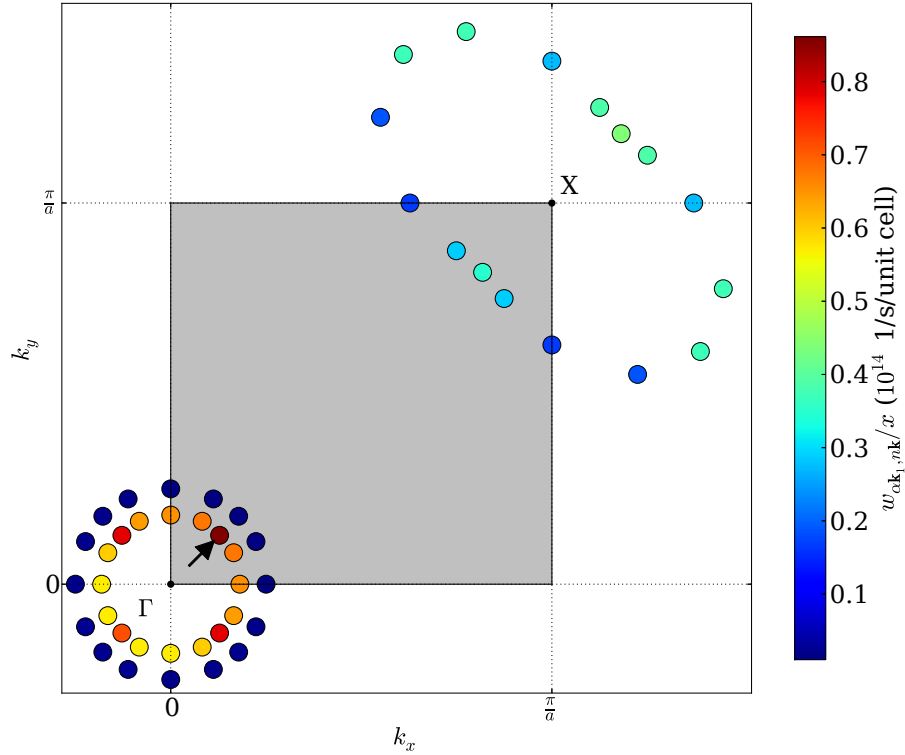


Figure 5.28.: Plot of the concentration normalized scattering rate $w_{\alpha k_1, n k} / x$ (colors) due to Co substitution on the Fermi surface in the $(\mathbf{k}_x, \mathbf{k}_y)$ -plane for the electronic structure reduced to three bands starting from band α at $\mathbf{k}_1 = k_F(1, 1, 0)$ (marked with an arrow) into all other bands, shaded area: first Brillouin zone

hole bands is negligible. This behavior gives an argument based on first principles, that an s^{+-} pairing scenario in these system is in no contradiction to the evident considerable impurity scattering, because the latter is dominated by intraband scattering which is not pair breaking. This considerable impurity scattering is real and has been experimentally observed in the residual resistivity [28, 120]. The linear dependence of the spectral broadenings on impurity concentration obtained in this work (see Secs. 5.3-5.5), suggests that this dominating intraband scattering found in the dilute limit can also be assumed at finite impurity concentrations. Assuming s^{+-} -pairing this explains why superconductivity is still present in these systems at higher impurity concentrations. On the other hand, these findings cannot prove that the gap structure necessarily *has* to be s^{+-} because we cannot rule out other possible pairing scenarios.

From transport measurements it is reported [120] that for Co substitution hole carriers are more affected by impurity scattering and the transport is thus dominated by electrons. This is consistent with the present results because the intraband scattering, which gives rise to the residual resistivity, is larger for the holes than for the electrons.

Furthermore, the interband scattering is smallest for P substitution, slightly larger for K substitution and further increases along the TM series. Bearing in mind that solely the interband scattering suppresses T_c in an s^{+-} superconductor, the present results suggest that pair breaking is stronger for Co than for K substitution and further increases for TM

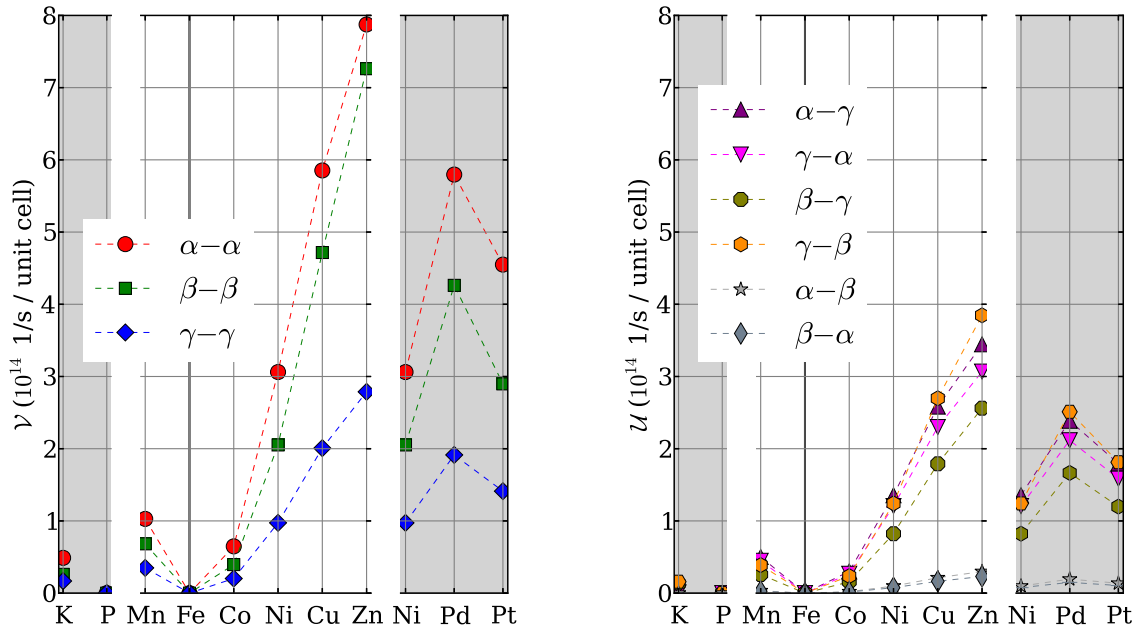


Figure 5.29.: Concentration normalized, k -averaged intraband \mathcal{V} and interband \mathcal{U} scattering rates against substituent, electronic structure reduced to two hole bands and one electron band

substitution upon moving horizontally in the periodic table. For K, Co, Ni and Cu substitution this qualitatively agrees with experiments [28, 95, 99, 121] because the observed T_c at optimal doping is the highest for K substitution, is lower for Co substitution and successively decreases along the TM series (see also Figs. 5.3 and 5.5 at the beginning of this chapter). In addition, these experiments reveal that the widths of the superconducting domes show the same trends - K substitution shows the broadest dome and upon TM substitution the width successively gets reduced. This shows that for K substitution the impurities are the least effective in suppressing superconductivity. For Co substitution the dome gets narrower, i.e. a smaller amount of impurities is needed to destroy superconductivity. This again manifests that Co is more pair breaking than K which under the assumption of s^{+-} pairing agrees with present results for Co leading to a larger interband scattering. The same discussion is valid for the remaining $3d$ TM substitutions.

According to transport measurements [122], the superconducting domes of $\text{Ba}(\text{Fe}_{1-x}\text{Ni}_x)_2\text{As}_2$ and $\text{Ba}(\text{Fe}_{1-x}\text{Pd}_x)_2\text{As}_2$ coincide. This is clearly not reproduced by the present interband scattering rates which would rather suggest a considerably stronger suppression of T_c by Pd substitution than for Ni substitution. I already stated that for $4d$ and $5d$ TM substitution the onsite approximation in the T -matrix calculation may not be valid anymore. In the $\text{Sr}(\text{Fe}_{1-x}\text{Ni}_x)_2\text{As}_2$, T_c seems to be the same as for $\text{Sr}(\text{Fe}_{1-x}\text{Pd}_x)_2\text{As}_2$ [123] as well. In that work, it is additionally reported that the superconducting dome is larger for Pt substitution than for Ni substitution and thus also larger than for Pd substitution. Assuming that Ba-122 behaves similarly to the Sr-122 system, at least this trend comparing Pd and Pt substitution would surprisingly be reproduced by the present interband scatterings despite the fact that those trends do not fit together with the $3d$ TM substitutions. If this is just by chance or systematic cannot be answered at this stage.

For Mn substitution, in experiment no superconductivity is found at all as for example

studied in detail in [124]. In contrast, the present findings under the assumption of s^{+-} superconductivity would suggest a suppression of T_c ranging between that of Co and Ni substituted BaFe₂As₂. This discrepancy is likely due to the fact that for Mn substitution magnetic effects have to be considered, but the present calculations could not take this into account because spin polarization is not yet implemented in the program package developed in this work. Hints for Mn being a magnetic impurity have for example been pointed out in recent electron spin resonance studies [125].

There are no substantial scattering effects, neither interband, nor intraband, due to P substitution - a trend which already the spectral broadenings showed. But from experiment [126], the height and width of the superconducting dome for P substitution ranges in between of those for Co and K substitution. This at least under the assumption of s^{+-} pairing is not consistent with the present scattering rates and their implications for pair breaking as in the case of 3d TM and K substitution. For P substitution more pronounced structural changes arise where in experiment two different distances from the Fe planes for the As and P atoms have been observed [127], respectively. This distance is known to have a larger influence on the bandstructure than the structural changes due to TM substitution considered above. If the position of the P atom gets closer to the Fe planes, hybridization effects with states at the Fermi surface, which are not present in the stoichiometric crystal structure, might lead to scattering and spectral broadening effects. This more sophisticated structural changes could eventually be treated in future work by introducing an additional site for P in the unit cell and then substituting As by vacancies and at the P site substitute vacancies by P.

6. Summary and conclusions

In the first part of this thesis, a charge self-consistent extension of the coherent potential approximation (CPA) [1, 2] after Blackman, Esterling and Berk (BEB) [4] was developed within a pseudopotential density functional theory (DFT) framework based on earlier work [11]. This method is dedicated to the calculation of the electronic structure of substitutionally disordered, arbitrarily complex real materials from first principles at arbitrary impurity concentrations without the need of supercells. Compared to the conventional CPA, which can only handle disorder in the onsite Hamiltonian matrix elements, this particular extension allows in addition to incorporate the disordered environment of a site via disorder in the hopping terms. In the BEB-formalism, this is accomplished without giving up the approximation of a single site self-energy which makes this approach computationally effective. On the background of recent computationally expensive efforts to incorporate off-diagonal disorder by the nonlocal CPA and related approaches [18, 62, 64], the BEB approach in my opinion deserves more attention. To my knowledge, the present work provides the first implementation of this method based on pseudopotentials. In the past, CPA-like methods were mainly applied within the Kohn-Korringa-Rostoker (KKR) framework [12–19] but rarely within other frameworks, which mostly address the problem of substitutional disorder via supercells. In contrast, the pseudopotential framework is one of the most frequently used in *ab-initio* electronic structure calculations (for example the famous Vienna *ab initio* simulation package (VASP) [128] or Quantum Espresso [129] both rely on pseudopotentials). I hope that this work might contribute in making this powerful class of CPA-like methods accessible to a larger community.

The BEB-CPA scheme itself was validated on a tight binding model against exact diagonalization of a randomly occupied cluster. Thereby, the BEB-CPA overall performs well in taking into account also effects of the disordered environment surrounding a site in the disordered medium. Only the random formation of clusters of one species which can give rise to localized states was shown to be not captured by the BEB-CPA.

The developed *ab-initio* implementation was tested for binary $\text{Cu}_{1-x}\text{Zn}_x$ alloys which represent a typical benchmark for this type of methods. The present results agree well with those obtained by other, already established KKR-CPA implementations [18]. From theoretical considerations, it is known (e.g. [3]) that opposed to simpler approaches like in particular the virtual crystal approximation (VCA) [50], the CPA correctly describes the split-band limit of a disordered system. The present calculations also show that the $\text{Cu}_{1-x}\text{Zn}_x$ alloys provide a realization of this split-band limit in nature and thus emphasize the necessity for the efforts of developing CPA-like methods.

In the second part of this thesis the developed methodology was used to systematically investigate a variety of substitutions in one of the most prominent representatives of the iron-based superconductors (FeSC) - the BaFe_2As_2 system. This material class is subject of intensive ongoing research since its discovery in 2008 [20]. Hereby the focus was set on the impact of substitutional disorder on individual bands near the Fermi level. To address the question if substitution leads to charge doping in this material class, disorder induced level shifts of the three hole-like bands near the center of the first Brillouin zone

and the two electron-like bands at the zone edge were considered. Except for isovalent P substitution for As, all investigated substitutions lead to band selective level shifts. To first approximation, these level shifts follow the trend of a simple rigid band shift, which describes a shift of the Fermi energy due to the introduction of extra charge carriers to the system. Looking at the details, there are deviations of the level shifts from the rigid band shift which depend on the orbital composition of the bands and at least for $3d$ transition metal (TM) substitution systematically get enhanced the more the number of valence electrons between host and substituent differ from each other. For Co, Mn and Pt substitution the deviations from the rigid band shift are the smallest. The strongest deviations from the rigid band shift occur for bands with $d_{x^2-y^2}$ orbital character. Apart from these bands, the behavior of the remaining bands is very rigid like for $3d$ TM substitution. Thus, apart from the effects on the inner hole band α with $d_{x^2-y^2}$ orbital character, which vanishes already at low impurity concentrations, these results suggest that the primary effect accomplished by TM and P substitution is charge doping. Provided that the $d_{x^2-y^2}$ bands do not significantly contribute to the pairing state, this supports the viewpoint of [28] based on thermodynamic and transport measurements that for Co and Ni substitution charge doping governs the shapes of the superconducting domes.

Besides charge doping, another important physical effect induced by substitutional disorder are spectral broadenings, i.e. finite lifetimes of the electronic quasiparticle states. Significant effects only occur for substitutions in the Fe planes. Along the $3d$ TM series, the spectral broadenings increase with growing difference in the number of valence electrons between host and impurity. For moving vertically downwards in the periodic table starting at Ni, the broadenings decrease with increasing ionic radius and increasing extent of the d wavefunctions. These are the same trends as observed for the deviations of the level shifts from the rigid band shift. Also considering the spectral broadenings, the $d_{x^2-y^2}$ bands behave differently from the remaining bands. Physically, these results suggest that K and P only act as weak scatterers in this system, or more generally, substitutions outside the Fe planes do not cause large impurity scattering effects. Along the $3d$ TM series, Co is the weakest scatterer and the impurity scattering successively increases up to Zn, which is the strongest scatterer. Pd and Pt are weaker scatterers than Ni but stronger than Co. In the future it would be interesting to perform experiments where such spectral broadenings or lifetime effects can be extracted to directly compare them with the present predictions (in principle, such information should be encoded in the various angle-resolved photo emission spectroscopy (ARPES) measurements performed on these compounds but at least to my knowledge, the required data is not published).

For all considered substitutions at impurity concentrations below 10%, the level shifts and spectral broadenings in good approximation behave linearly with impurity concentration. For Co and Ni substitution, at least for impurity concentrations up to 10% the level shifts and spectral broadenings are not significantly affected by substitution induced structural changes. For P substitution, where the structural changes are more complicated, this situation eventually could be different and should be verified in future work.

Several earlier theoretical and experimental works [34–37, 91–93] (only to list a few) provided strong hints to the structure and symmetry of the superconducting gap in the FeSC to be of s^{+-} type. This means that the order parameter exhibits s -wave symmetry, i.e. the same symmetry as the crystal structure, but changes sign between different Fermi surface sheets. For conventional superconductors due to the Anderson theorem [108] and Abrikosov-Gorkov (AG) theory [104, 115] only scattering on magnetic impurities is pair

breaking and scattering on nonmagnetic impurities does not affect the superconducting state. It was shown for an s^{+-} pairing scenario [33, 37, 116] that it is important to distinguish between intra- and interband scattering where for nonmagnetic impurities only interband scattering is pair breaking whereas intraband scattering influences the residual resistivity.

Thus, to study the impact of the various substitutions on superconductivity, it was essential to go beyond the spectral broadenings because they only provide direct access to all accumulated scattering effects on one single band. Therefore in the last part of this work a T -matrix approach was developed to obtain additional information about the impurity scattering between different bands from first principles. To my knowledge, such a study from first principle has not been performed before. To reveal general trends, an average was taken over the two outer hole bands β_1 and β_2 and the two electron bands so that we are effectively left with two hole bands and one electron band. This analysis for the various substitutions in the dilute concentration limit reveals that intraband scattering is always enhanced by more than a factor of two compared to interband scattering. In this context interband scattering means scattering between hole and electron bands because scattering between different hole bands turned out to be negligible. This confirms the robustness of an s^{+-} pairing state even at higher total impurity scattering as revealed by measurements of the residual resistivity because the latter is only an intraband scattering effect which is harmless for superconductivity. Furthermore, the intraband scattering in hole bands is by more than a factor of two larger than intraband scattering in the electron band. At least for Co substitution this is consistent with transport measurements [120] which find that hole carriers are more affected by impurity scattering and transport, being governed by intraband scattering, is dominated by electrons.

By comparing the interband scattering among the different substitutions, under the assumption of s^{+-} pairing it was possible to compare their pair breaking strength: The interband scattering successively gets increased from K to Co, over Ni and Cu up to Zn substitution which then implies that the pair breaking strength gets enhanced. This directly can be related to the phase diagrams obtained by several experimental techniques (see Figs. 5.3 and 5.5 and refs. [28, 95, 99, 121]) where the superconducting domes along the same series successively get suppressed, i.e. they get narrower on the concentration axis and lower on the temperature scale. The primary increase of T_c with substitution at small impurity concentrations can be explained [117] with the successive suppression of the antiferromagnetic order by substitution which competes with superconductivity. Moreover, it is the overdoped (impurity concentrations larger than optimal doping) region of the superconducting dome which is solely governed by pair breaking effects and should be considered for comparison with the present results. The linear dependence of the spectral broadenings on finite impurity concentration can be used to extrapolate the results obtained by the T -matrix approach working in the dilute limit to the concentration regime of physical interest at finite concentrations. There, the increasing suppression of the superconducting domes from K substitution along the $3d$ TM series qualitatively shows the same trend as the increase in interband scattering i.e. pair breaking under the assumption of s^{+-} pairing. This shows for K and $3d$ TM substitution that the suppression of superconductivity in the overdoped region originates from interband scattering on nonmagnetic impurities.

The scattering effects for Mn substitution cannot be related to experiment [124] most probably because the present calculations do not incorporate magnetism.

The present results for P substitution do not agree with the experimental trend which could originate from more substantial structural changes due to P substitution which were not considered in this work. Along the substitution series from Ni over Pd to Pt, experiments [123] (partly using Sr instead of Ba, unfortunately) the pair breaking decreases. This trend is reproduced by the spectral broadenings obtained in the present work but not by the interband scattering from the T -matrix approach, which is the relevant quantity to compare with. This disagreement of the T -matrix with experiment and the spectral broadenings most probably is a consequence of the single-site approximation imposed for the T -matrix where the scattering potential is site diagonal and environmental effects are neglected. Instead, the spectral broadenings which were directly calculated by the BEB-CPA contain environmental disorder effects, which shows the necessity of such approaches beyond the conventional CPA for a realistic description of disorder in FeSC.

In future work it would be important to include spin polarization into the developed program package to consider also the effect of magnetic impurities. Structural effects should be incorporated into the study about BaFe_2As_2 for all substitutions. Furthermore, transport coefficients should be extracted from the CPA calculations to have further quantities which can be compared with experiments. Finally, the T -matrix approach should be improved beyond the single site approximation to see if the trends for Pd and Pt substitution can be better related to experiment. Lastly, it might be interesting to combine the present T -matrix analysis with realistic model based approaches explicitly working in the superconducting state.

A. The full *ab-initio* program

In Secs. 2.2.4 and 2.3 the general principle of the charge self-consistent pseudopotential LCAO-CPA method was outlined. In this appendix chapter an overview about the actual implementation shall be given. The whole charge self-consistent scheme depicted in Fig. 2.2 was implemented as a completely separate program which takes the relevant information generated by the LCAO part of the individual MBPP calculations as input. This program is written in Fortran90 (except for the Broyden mixing scheme which is written in Fortran77) and has an overall length of roughly 12500 code lines up to now. Among them ca. 8200 lines were written in this work and the rest are library routines which were mainly taken from the MBPP. The several code files and their purposes are listed in Tab. A.1. In App. B the detailed mathematical expressions for the matrix elements

File	Developed	Short description
broyd.f	H.Winter	Broyden mixing for charge self-consistency
excorr.f90	MBPP	Routines for exchange-correlation (XC) potential
funkt.f90	MBPP	Mathematical functions, in particular cubic harmonics, Legendre polynomials, Gaunt coefficients and Wigner matrices
geo.f90	MBPP	Investigate bonds to neighboring atoms
specialpar.f90	MBPP	Special parameters, e.g. fundamental constants
cpa.f90	This work	The main program
cpaSolver.f90	This work	BEB-CPA impurity solver, calculation of DOS, spectral function, Fermi level and charge self-consistency
density.f90	This work	Electronic density (initially and in charge self-consistency)
hamilton.f90	This work	Hamiltonian matrix elements
input.f90	This work	Processing of necessary input data, set up indices
overlap.f90	This work	Overlap matrix elements
potential.f90	This work	Local potential including V_{XC} decomposition
symmetry.f90	This work	Symmetrization of matrix elements
tools.f90	This work	Help routines (scalar products, radial Fourier transformation, ...)

Table A.1.: All source code files the CPA-program consist of

and the density are derived in a form convenient for numerical implementation. There also the relevant subroutines where this expressions are implemented will be mentioned. Currently, a simple shared-memory parallelization using `OpenMP` is built into the program, which allows to use all cores within one node on a cluster machine. A distributed-memory parallelization (e.g. `mpi`) to use multiple nodes in parallel is not implemented until now.

In addition, the program needs to be linked with the common open-source mathematical libraries BLAS (Basic Linear Algebra subprograms) [130] and LAPACK (Linear Algebra Package) [131] which are in particular used for matrix diagonalization and inversion.

A.1. How to perform calculations

The MBPP was slightly modified in this work in order to provide all data required for a CPA calculation. The most data is collected in a new file `cpaprep.f90` and additionally the file `lcao.f90` was slightly modified for an output of the optimized local orbitals in high numerical precision. The user has to set up an MBPP calculation as usual with an LCAO fit in the end. Additionally the directive `#define CPA_PREP` has to be set which then forces this special MBPP version to provide all relevant information which will be stored in formatted ASCII files with the prefix `CPA_*`. The CPA program then expects to look up all information concerning the parent compound, crystal structure, symmetries, which just have to be read once in the "master" directory (which can be a symbolic link to the actual directory the MBPP calculation was running in) which has to be named `CM`. Then, for each substitution in a complex compound, a "slave" calculation has to be provided, where the CPA program looks up pseudopotentials and wavefunctions of the substituent. Therefore, depending on the number of substituents, the program expects further directories (which again can be symbolic links) named `CS i` where $i \in [1, 9]$ is the index of the substituent.

However, even if this all runs automatically, the user has to specify additional information like the number of substituents, which species to substitute, cutoff parameters for summations, energy intervals, etc. in a formatted input file `CPA_INP`. This file up to now does not have the convenient identifiers like the `INP` files of an MBPP calculation. So the order of the lines and position of newline characters really matters! The most generic form of such an input file `CPA_INP` is shown in Listing A.1.

Listing A.1: Generic example for the file `CPA_INP`

```

1  Ntypes
2  NslaveCalc
3  NvalenceElectrons
4  cutoff_k lmcutExtern lmcutIntern
5  shapeFuncType shapeFuncPar
6  hostTypeIndex nameHostAtom impurityTypeIndex nameImpurityAtom
7  concenTypeAtom1 ... concenTypeAtomN shapeFuncCutoffRadius
8  leften numleft fermileften numfermi fermirighten numright righten
   numimag topen
9  maxCpaIter cpaTol fermiIter fermiTol cpaNtemp csItemp
10 cpaTemp1 ... cpaTempN
11 dosleft dosright numdos dosSmear
12 csStartIter csMaxIter linMix denTol csTol
13 bdstrucNline
14 bdstrucSmear
15 startpoint endpoint nk nameDirection
16 ibandprojLow ibandprojUp bandIntLow bandIntUp

```

The parameters in the individual lines have the following meaning:

1. `Ntypes` (**integer**): Total number of different atomic types, including all substituents
2. `NslaveCalc` (**integer**): Number of slave calculations (=number of substituent species)

-
3. **NvalenceElectrons (float)**: Number of valence electrons in charge neutral compound, $z_{val} = \sum_{i,P} c_i^P z_{val,i}^P$
 4. Cutoffs for summations and Fourier transformations
 - **cutoff_k (float)**: Cutoff radius in atomic units up to which the radial Fourier transformation of the wavefunctions shall be calculated; also used for evaluation of matrix elements (for the local pseudopotentials two times this cutoff is used)
 - **lmcutExtern (integer)**: Cutoff for internal summations over orbital quantum numbers l, m . The individual quantum numbers are connected to the combined lm index like $l(lm) = 0, 1, 1, 1, 2, 2, 2, 2, \dots = (l+1)^2$ and $m(lm) = 0, 0, 1, -1, 0, 1, -1, 2, -2, \dots$ which is defined in `specialpar.f90`. So a maximum angular momentum of $l = 2$ requires an $lm = 9$, for example.
 - **lmcutIntern (integer)**: A separated cutoff for internal summations for the B -coefficients Eq. (B.25) - was originally introduced to reduce computation time but is only used for the density and not really necessary anymore to be treated separately (`lmcutExtern = lmcutIntern` usually is a secure choice)
 5. Specification of shape functions
 - **shapeFuncType (integer)**: The functional type (equal for each type and site) of the shape functions to be used according to Eq. (B.50)
 - **shapeFuncPar (float)**: The parameter of the shape functions γ in Eq. (B.50)
 6. This line will be read `NslaveCalc` times
 - **hostTypeIndex (integer)**: Index of the atomic type of the host atom in the parent compound (equivalent to the order the types are specified in the MBPP calculation)
 - **nameHostAtom (char[2])**: Name of the atomic type of the host to be replaced by the considered slave
 - **impurityTypeIndex (integer)**: Index of the atomic type of the substituent in the slave calculation (in most cases the same as `hostTypeIndex`, is never allowed to exceed the number of types in the parent compound or the substitutional end member!)
 - **nameImpurityAtom (char[2])**: Name of the atomic type of the substituent considered in the slave calculation
 7. This line will be read `Ntypes` times
 - **concentTypeAtom1 (float)**: Atomic concentration of the first atom of the considered type
 - **concentTypeAtomN (float)**: Atomic concentration of the last atom of the considered type
 - **shapeFuncCutoffRadius (float)**: Cutoff radius of the shape function associated with the considered type

If an atom of a certain type is located on several sites in the unit cell but not at all sites substitutions should occur, then the concentrations at these sites shall be set to zero but they have to be provided here. If an atom of one species appears

more times in the crystal than the other types, then the number of concentrations to be provided for *every* type has to be always that maximum number of atoms of the same type (called **natomax** in the MBPP and the CPA-code). If an atomic type appears less often, the respective superfluous concentrations have to be assigned a zero value. The index of a concentration of a certain type is the same as the site index in the unit cell which was specified when setting up the MBPP calculation.

8. Specification of the closed curve (half-box in the upper complex half plane, see Sec. 2.3 and App. C) needed for integrations involved in the calculation of the Fermi level and the charge self-consistency. The region around the estimated Fermi level needs to be sampled finer and thus has to be extra defined.
 - **leften (float)**: Lower boundary (Ry) of the box on the real axis far below the Fermi level
 - **numleft (integer)**: Number of sampling points in that region
 - **fermyleften (float)**: Lower boundary (Ry) of the region the Fermi level is supposed to lie in
 - **numfermi (integer)**: Number of sampling points in that region
 - **fermirighten (float)**: Upper boundary (Ry) of the region the Fermi level is supposed to lie in
 - **numright (integer)**: Number of sampling points in the region above the Fermi level
 - **righten (float)**: Upper boundary (Ry) of the box on the real axis
 - **numimag (integer)**: Number of sampling points on the positive imaginary axis
 - **topen (float)**: Upper boundary (Ry) of the box on the imaginary axis

The numbers given here have to be dividable by six plus one ($6n + 1$, n integer) required by the special integration method.

9. Information for the CPA cycle
 - **maxCpaIter (integer)**: Maximum number of iterations for the CPA solver (the inner loop in Fig. 2.2, to avoid endless loops at poor convergence)
 - **cpaTol (float)**: The convergence criterion (Ry) for the CPA solver the self-energy change has to fall below
 - **fermiIter (integer)**: Maximum number of iterations in the bisection method for determination of the Fermi level from the number of valence electrons
 - **fermiTol (float)**: The minimal difference (Ry) between the left and right approximation to the Fermi level in the bisection method
 - **cpaNtemp (integer)**: The number of temperatures the chemical potential should be calculated for to extrapolate to $T = 0$ for the Fermi level. Currently for **cpaNtemp**=1 the Fermi level is chosen identically to the chemical potential and for **cpaNtemp**≥2 a linear extrapolation to $T = 0$ using the chemical potential at the lowest and highest temperature is implemented.
 - **csItemp (integer)**: The index of the temperature the charge self-consistency should be calculated at. Currently no extrapolation for $T = 0$ is implemented for the charge self-consistency.

-
10. **cpaTemp (float)**: The **cpaNtemp** temperatures the chemical potential shall be calculated for. To be specific, $k_B T$ has to be given here in Ry.
 11. Boundaries for the calculation of the DOS. Apart from the smearing parameter, these boundaries will also be used for the evaluation of the Bloch spectral function.
 - **dosleft (float)**: The lower boundary (Ry) of the energy interval, the DOS shall be evaluated within. Here, the Fermi level is not yet assumed to define the energy zero! In spite of that, in the output file **CPA_TOTDOS**, the energy scale will be converted to eV and the energy zero will be shifted to the Fermi level.
 - **dosright (float)**: The upper boundary (Ry) of this energy interval
 - **numdos (integer)**: The number of sampling points for this energy interval
 - **dosSmear (float)**: The imaginary part δ in the complex frequency of the retarded Green's function the DOS is calculated from
 12. Control parameters for the charge self-consistency
 - **csStartIter (integer)**: The number of the charge iteration the program will be started with. Initially, when a calculation is set up from the scratch, this should be 1. Note that for this special value some parts of the program (especially in the calculation of the charge density) behave differently. When a calculation for example reaches the time limit on a shared computer, this number can be increased to restart the calculation provided the densities and eventually the Hamiltonian from the last calculations can be read.
 - **csMaxIter (integer)**: The maximum number of charge iterations (at the moment not more than 2 digits shall be used because otherwise the names of the output files are not human readable anymore)
 - **linMix (float)**: In the first step the Broyden mixing scheme performs a linear mixing to build up the Jacobi matrix which needs to be specified here. Never use numbers > 0.05 because this can drive the algorithm far away from the solution.
 - **denTol (float)**: A limit beyond which an orbital density component is assumed by the program to vanish for symmetry reasons. This analysis is only carried out in the first charge iteration and the orbital indices which vanish or are relevant are then stored in the files **CPA_ZERO_DEN** and **CPA_UPDATE_DEN**, respectively. This should make the scheme more robust against numerical errors which possibly could violate the symmetry of the considered compound and eventually lead to a faster convergence.
 - **csTol (float)**: The maximal density difference between two iterations below which all orbital contributions have to fall to indicate convergence
 13. **bdstrucNline (integer)**: Number of sequential directions in \mathbf{k} -space the Bloch spectral function should be evaluated along. If this is zero, the Bloch spectral function will not be evaluated and lines 14 and 15 do not have to be provided.
 14. **bdstrucSmear (float)**: The parameter δ in the complex frequency for the evaluation of the Bloch spectral function (usually it has to be chosen smaller than **dosSmear** to resolve all bands).

15. Specification of a direction in \mathbf{k} -space for calculation of the Bloch spectral function, this line will be read `bdstrucNline` times
 - `startpoint (float[3])`: Reciprocal lattice coordinates of the startpoint of a direction
 - `endpoint (float[3])`: Reciprocal lattice coordinates of the endpoint of a direction
 - `nk (integer)`: Number of sampling points along that line
 - `nameDirection (char[2])`: Name of the direction (e.g. letters of start and endpoint)

16. Control parameters for the projection of the spectral function on eigenstates of the parent compound
 - `ibandprojLow (integer)`: Lower band index for the projection
 - `ibandprojUp (integer)`: Upper band index for the projection (the spectral function will be projected on all bands lying in between those indices)
 - `bandIntLow (float)`: The projected spectral functions need to be normalized - lower energy limit (Ry) for the integration.
 - `bandIntUp (float)`: Upper energy limit (Ry) for the integration

A typical c-shell script for the example of disordered $\text{Ba}(\text{Fe}_{0.9}\text{Co}_{0.1})_2\text{As}_2$ is shown in Listing A.2.

Listing A.2: Example csh-script for disordered $\text{Ba}(\text{Fe}_{0.9}\text{Co}_{0.1})_2\text{As}_2$

```

1  #!/bin/csh
2  # set up cpa-Calculation for Co substituted BaFe2As2
3  # command: job_submit -t 4000 -m 64000 -c p -p 1/16 -J "bfa_0.1Co-subst" -e
   err_bfa_0.9_0.1 -o run_bfa_0.9_0.1 calcCpa_bfa_Fe0.9_Co0.1
4  setenv OMP_NUM_THREADS 16
5
6  set baconc = 1.0
7  set fe1conc = 0.9
8  set fe2conc = 0.9
9  set as1conc = 1.0
10 set as2conc = 1.0
11 set co1conc = 0.1
12 set co2conc = 0.1
13
14 set zval = 28.2
15
16 set cpaMaster = $HOME/BaFe2As2/cpa_prep_bfa/
   e22g30k84s01exp_867_cpaPrep_noppw
17 set cpaSlave1 = $HOME/BaFe2As2/cpa_prep_bca/
   e22g30k168s01expfe_867_cpaPrep_noppw
18 set cpaProg = $HOME/Version_5_CPA/cpa_v30/cpa
19 set linMix = 0.005
20 set denUpdtBound = 0.00000001
21 set chargeScfLim = 0.00000001
22
23 set wd = $WORK/bafe2as2/cpa_bfa_Fe${fe1conc}_Co${co1conc}
24 set savedir = $HOME/BaFe2As2/cpa_300K/cpa_bfa_Fe${fe1conc}_Co${co1conc}
25

```

```

26
27 if ( ! -d $savedir) then
28     mkdir $savedir
29 endif
30
31 if ( ! -d $wd) then
32     mkdir $wd
33 endif
34
35 cd $wd
36
37 if (-f CPA_OUT) then
38     rm CPA_OUT
39 endif
40
41 ln -sf $cpaMaster CM
42 ln -sf $cpaSlave1 CS1
43
44 cp -v $HOME/BaFe2As2/cpa_300K/cpa_pure_BaFe2As2/CPA_CLEANEIGEN_* .
45
46 cat > CPA_INP << END
47 4
48 1
49 $zval
50 14.8 49 49
51 8 32.8
52 2 Fe 2 Co
53 $baconc 0.0 10.5
54 $fe1conc $fe2conc 6.9
55 $as1conc $as2conc 6.5
56 $co1conc $co2conc 6.9
57 -20.0 121 -0.45 601 -0.15 181 30.0 61 10.0
58 200 0.000001 40 0.000000001 2 2
59 0.0019 0.005
60 -1.2 -0.22 5000 0.01
61 1 50 $linMix $denUpdtBound $chargeScfLim
62 4
63 0.0005
64 0.0 0.0 0.0 -0.5 0.5 0.5 60 GZ
65 -0.5 0.5 0.5 0.0 0.0 0.5 30 ZX
66 0.0 0.0 0.5 0.0 0.0 0.0 30 XG
67 0.0 0.0 0.0 0.5 0.5 -0.5 10 GM
68 10 17 -0.42 -0.27
69 END
70
71 time $cpaProg > dump_bfa

```

A.2. Output Files

The program produces a huge amount of data, all written in formatted files which was needed for testing. First the program writes a lot of status remarks, some intermediate results as well as error and warning messages directly to standard output which particularly was needed for debugging. For that reason one should pipe the output of the program into a file as shown in the last line of the shell script Listing A.2. The more important data like geometry information, Fermi level, integrals of the orbital charge densities calculated

during the self-consistency cycle and so on are written to the file CPA_OUT. Up to now, both files are redundant in some aspects and not always nicely structured which should be improved in the future. In addition, important results like densities, DOS, spectral functions and so on are written in many well-structured output files of which the most important shall be briefly mentioned in what follows.

- CPA_DEN_<type>_<atomNumber>_l_m_<chargeIter>: Species and atom resolved radial contributions (angular quantum numbers l and m) to the electronic density in real space
- CPA_ZERO_DEN: A list of the density components which the program assumes to vanish by symmetry - the threshold for this assumption is given via the control parameter `denTol` in CPA_INP - and will not be updated in the charge self-consistency loop for improving the robustness of the numerics. This file is generated in the first charge iteration and is read (has to be provided, otherwise the program crashes) in all further charge iterations. I do not recommend to manipulate it!
- CPA_UPDATE_DEN: The complementary information: A list of density components the program shall update in charge self-consistency, also generated in the first iteration and needed for all further iterations.
- CPA_HMIXK_REAL_<chargeIter>: The real part of the \mathbf{k} -dependent mixing Hamiltonian ${}^{mix}H(\mathbf{k}) + {}^{mix,nl}H(\mathbf{k}) + T(\mathbf{k})$ from Eqs (B.64) and (B.67) plus the kinetic term which reduces to the crystal Hamiltonian in the clean case
- CPA_HMIXK_IMAG_<chargeIter>: The imaginary part of the same quantity
- CPA_VMIXK_<chargeIter>: Just the mixing potential ${}^{mix}H(\mathbf{k}) + {}^{mix,nl}H(\mathbf{k})$ like before without the kinetic term
- CPA_VMIXK_REAL_<chargeIter>: The real part of the mixing potential
- CPA_VMIXK_IMAG_<chargeIter>: The imaginary part of the mixing potential
- CPA_VMIX_ONSITE_<chargeIter>: The onsite mixing potential - is needed when a calculation is restarted, especially if just a bandstructure calculation is performed without recalculating all matrix elements
- CPA_HOFFSITE_<chargeIter>: The full \mathbf{k} -dependent offsite Hamiltonian - can be useful when a calculation is restarted
- CPA_HOFFSITE_REAL_<chargeIter>: The real part of this quantity
- CPA_HOFFSITE_IMAG_<chargeIter>: The imaginary part of this quantity
- CPA_TOFFSITE_<chargeIter>: The \mathbf{k} -dependent kinetic energy (calculated from Eq. (B.74) without onsite corrections). Is needed when a calculation is restarted, especially if just a bandstructure calculation is performed without recalculating all matrix elements
- CPA_TOFFSITE_REAL_<chargeIter>: Its real part
- CPA_TOFFSITE_IMAG_<chargeIter>: Its imaginary part

- CPA_VOFFSITE_<chargeIter>: The full \mathbf{k} -dependent potential (calculated from Eq. (B.75) without onsite corrections). Is needed when a calculation is restarted, especially if just a bandstructure calculation is performed without recalculating all matrix elements
- CPA_VOFFSITE_REAL_<chargeIter>: Its real part
- CPA_VOFFSITE_IMAG_<chargeIter>: Its imaginary part
- CPA_HONSITE_<chargeIter>: The full onsite Hamiltonian - can be useful when a calculation is restarted
- CPA_HONSITE_REAL_<chargeIter>: Its real part
- CPA_HONSITE_IMAG_<chargeIter>: Its imaginary part
- CPA_VXC_<type>_<atomNumber>_l_m_<chargeIter>: Species and atom resolved radial contributions (angular quantum numbers l and m) to the exchange and correlation potential in real space
- CPA_VXCK_<type>_<atomNumber>_l_m_<chargeIter>: The same in reciprocal space
- CPA_TOTDOS_<chargeIter>: The total density of states, energy in eV with respect to the Fermi level, DOS in 1/(eV unit cell)
- CPA_ORBDOS_<type>_<atomNumber>_l_m_<chargeIter>: Orbital decomposed density of states, same units as CPA_TOTDOS
- CPA_CLEANBDSTRUC_<bandIndex>_<direction>: Bandstructure of the parent compound - eigenvalues of mixing Hamiltonian, only calculated if NslaveCalc is zero
- CPA_CLEANEIGEN_<direction>: All eigenvectors of the crystal Hamiltonian of the parent compound, only calculated if NslaveCalc is zero and needed as input for the projection on clean bands
- CPA_CLEANEIGEN_REG: The respective eigenvectors on a regular \mathbf{k} -mesh
- CPA_KDOS_<direction>: The total Bloch spectral function, first column: \mathbf{k} , second column: energy with respect to Fermi level in eV, third column: spectral function in 1/(eV unit cell). For the length of the path in \mathbf{k} -space the same conventions are chosen as in the MBPP: the length of the first direction is normalized to unity and all further direction lengths are rescaled to that unit.
- CPA_KDOS_<direction>_<type>_l: A species and l -decomposed version of the spectral function
- CPA_PROJSPECFUNC_<bandIndex>_<direction>: The spectral function projected on a band of the parent compound
- CPA_PSFFWHM2_<bandIndex>_<direction>: Essential properties of a band-projected spectral function: first column: \mathbf{k} , second column: energy of peak, third column: spectral half width (HWHM), fourth column: spectral broadening (half width minus band smearing), fifth column: norm (integral over energy)

- CPA_BDOS_<bandIndex>_<chargeIter>: Density of states of a certain band (similar to a band projected spectral function but summed over a regular \mathbf{k} -mesh) needed for calculating scattering rates using the T -matrix

A.3. How to modify the behavior of the code

The main program is set up in the file `cpa.f90`. In principle only subroutines which do the essential work, are called here. If the calculation is started from the scratch it first reads all required data and calculates the electronic density for each slave calculation (the master then is counted as `islave=0`) *independently*. This is due to the fact, that the densities in the first step can only be calculated like in an ordered compound because the Green's function is not yet established and the expansion coefficients of the Kohn-Sham orbitals with respect to the local basis have to be used instead as shown later in Eq. (B.27) in Sec. B.3. These are provided by the MBPP and thus are only defined for an ordered system. The calculations have to be carried out for the full parent compound and substitutional end member because the bond routines (defined in `geo.f90`) which generate a list of bonds to neighbouring atoms within a certain cutoff radius need the full crystal structure to operate reasonably. These densities then are written on file and all other data, essentially the bond list, is destroyed.

Then all relevant data is again read for the full calculation of the disordered system, the overlap matrix is calculated and the charge self-consistency loop is started. Therein, first the densities are calculated (in the first step they are just read from file, otherwise they are mixed with the previous densities using the Broyden scheme) and the convergence of the charge self-consistency is checked. Relying on these densities, the potentials are calculated. Afterwards, the onsite and the offsite Hamiltonian matrix elements are calculated which together with the mixing potential needs the most time. Then the CPA medium Green's function is calculated along the integration path (box in upper half plane). From that the chemical potential and Fermi level are calculated. After that, the density of states is evaluated. Finally, if the charge self-consistency is not yet converged, the A -coefficients Eq. (B.26) for the new charge densities are calculated from the Green's function and the loop is iterated. If the charge density is converged or the loop is finished because the maximum number of charge iterations was exceeded, the Bloch spectral function is evaluated. Currently, the behavior of the code when restarting a calculation can be manually influenced by changing some boolean control variables in the beginning of `cpa.f90`. The relevant lines are shown in Listing A.3

Listing A.3: Beginning of `cpa.f90`

```
39  calcOvlp = .true.
40  calcHamiltonian = .true.
41  allocPot = .true.
42  readOldRadDen = .false.
43  irkmax = 2
44  chargeScIter = 1
45  symm = .true.
46  chargeConverged = .false.
```

The overlap matrix does not change with charge iteration so it only has to be calculated once - `calcOvlp` can be set to `.false.` when a calculation is restarted. The calculation of the Hamiltonian matrix is controlled by `calcHamiltonian`. When a calculation is

restarted and the Hamiltonian matrix elements were already written on file in the start iteration (`csStartIter`) of the restarted calculation, setting this variable to `.false.` can save time. In the next charge iteration (if needed) the program automatically resets it to `.true.` `allocPot` shall not be changed. The parameter `readOldRadDen` decides whether the old densities should be read from file or if they should be calculated. Setting this to `.true.` is the minimal requirement if a calculation which is not yet charge self-consistent and reached the time limit shall be restarted. If additionally `calcHamiltonian` should be set to `.false.` depends on how far the program proceeded in the last charge iteration. `irkmax`, `chargeScIter` and `symm` shall not be changed. Finally, `chargeConverged` gives information if the charge self-consistency was already achieved. This is very useful when setting up a different bandstructure calculation on an already charge self-consistent effective medium and Hamiltonian - then one should set this parameter to `.true.` In future work all of this should be incorporated into the file `CPA_INP` which will make recompilation for the user unnecessary and thus may contribute to avoid mistakes.

A.4. Data structure

At this stage some important remarks about the data organization in the code have to be made. This discussion will not be complete because all details are again commented in the source code files but it is helpful to get a general understanding. First of all, a generic compound contains different atomic types `itype = 1 ... ntype` and each of them has a name stored in the `char[2]` array `nameat(itype)`. In some subroutines this atomic type or species index `itype` is also called `spec`. Each atomic type can occur several times in the unit cell which is stored in the integer array `natom(itype)` of which the maximum number is `natomax`. The sum over this array is `natcel` which in a disordered compound is different to the physical number of atoms because it also counts multiple occupancies of a site by several species. The physical number of atoms in the unit cell is `totNum_atoms` which essentially is the value of `natcel` for the parent compound. This gives rise to an atomic index `iat = 1 ... natom(itype)` which has a different range for each type. Each atom is located at an individual site whose lattice coordinates are stored in the double precision array `coorat(3,iat,itype)`. Therefore, the order of the index `iat` is meaningful. The compound index `(iat,itype)` thus allows to uniquely specify an atom. For the disordered compound also a site dependent atomic concentration is important which is stored in the double precision array `conc_iat_spec(iat,itype)`. This is of course allocated from `1 ... natomax` and `1 ... ntype` which is the reason for always requiring `natomax` concentrations for each type in the input file as discussed in Sec A.1.

All orbital matrix elements are stored in a compound index `iao` which was taken from the MBPP for historic reasons but is far from being intuitive. Therefore it is first important to memorize the combined (l, m) index `lm` which was defined before. It is constructed in the following way

<code>lm</code>	1	2	3	4	5	6	7	8	9	...
<code>l</code>	0	1	1	1	2	2	2	2	2	...
<code>m</code>	0	0	1	-1	0	1	-1	2	-2	...

then the `iao` index is defined in the following way, shown here for the simplified example of type 1 having 2 atoms with orbital angular momentum up to $l = 1$ (`lm=4`):

<code>iao</code>	1	2	3	4	5	6	7	8	9	...
<code>itype</code>	1	1	1	1	1	1	1	1	2	...
<code>iat</code>	1	2	1	1	1	2	2	2	1	...
<code>lm</code>	1	1	2	3	4	2	3	4	1	...

In the program, several index arrays are constructed to translate these indices into each other. This `iao` index is convenient for matrix element evaluation. A problem arises, when for example coincidences of sites have to be verified - simply testing if `iat1 = iat2` is not sufficient because the `iat` index can be associated with a different site for one species than for the other species. Additionally, in the CPA-solver, matrix inversions of site diagonal blocks have to be performed where the `iao`-index as well as the `iat`-index are not well suited for. For that purpose, in the subroutine `rebuild_iat` and subroutine `buildSiteData` an alternative site index is built up. Here the central quantity is the site of which the maximum number is `num_sites`. Each site has a certain number `ntype_site(isite)` of possible types `itype_site(1:ntype_site, isite)` to be occupied with. Then, at each site another combined type and `lm` index, called `t1m` is established in the following, more intuitive way (for the same example as before with angular momentum up to $l = 1$):

<code>t1m</code>	1	2	3	4	5	...
<code>itype</code>	1	1	1	1	2	...
<code>lm</code>	1	2	3	4	1	...

Of course, again a couple of index arrays have to be built up which relate the site data structure to the `iao` index but they are commented in the code and are mostly self-explaining. As a last detail, the subroutine `rebuild_iat` changes the initial index `iat` when an atomic concentration for `iat < natom(itype)` is below a certain threshold that it would be considered as zero for the rest of the program.

B. Matrix elements

B.1. Basis set

In this section, the properties of the nonorthogonal, atom-centered basis functions will be discussed in full detail. All matrix elements which are needed throughout the whole program implemented in this work and will be discussed in the following sections, are evaluated with respect to these basis functions. The analytical calculations involved in deriving the final expressions of the matrix elements which will be presented below, sometimes are quite lengthy. But with the help of all useful properties of the involved quantities presented below, they are rather straight forward to derive so I will in general not present all intermediate steps and restrict myself to the final results.

B.1.1. Localized orbitals in real space

In three dimensional real space, each basis function referring to a given set of quantum numbers, is defined in the following form

$$\phi_{Lslm}^Q(\mathbf{r}) = \phi_{lm}^Q(\mathbf{r} - \mathbf{R}_L - \mathbf{R}_s) \quad (\text{B.1})$$

where the quantum numbers have the following meaning:

- l : orbital angular momentum
- m : magnetic quantum number $m = -l, \dots, l$
- L : index of unit cell in Bravais lattice
- s : index of atomic site in unit cell
- Q : index of atomic species

An additional principal quantum number n is omitted in this work because, following the MBPP, only one orbital per angular momentum is assumed which is sufficient for the treatment of valence electrons in the pseudopotential framework. In the main text, Chap. 2, the quantum numbers l and m have been abbreviated by a combined index μ . Here, this is not done anymore because these distinct indices are important for the details of matrix element evaluation. The angular momentum dependence of these basis functions is described by cubic harmonics or real spherical harmonics $K_{lm}(\hat{r})$:

$$\phi_{lm}^Q(\mathbf{r}) = i^l f_l^Q(r) K_{lm}(\hat{r}) \quad (\text{B.2})$$

where $\hat{r} = \mathbf{r}/r$ is a unit vector pointing into the direction of \mathbf{r} and $r = |\mathbf{r}|$ is the modulus of vector \mathbf{r} . The K_{lm} and all related routines and coefficients are taken from the MBPP (in particular subroutine `k1m` in file `funkt.f90`) and the above unit vector is the angular part $\hat{r} = (\vartheta, \varphi)$ of the spherical coordinates (r, ϑ, φ) used in some of these routines. The

only material specific quantities important for disorder and generated by the LCAO fit are the radial functions $f_l^Q(r)$ which are given numerically on an equidistant radial grid with a finite, species- and l -dependent cutoff radius $R_{C,l}^Q$ which is defined by the user in the LCAO-fit of the MBPP (see for example Tabs. 4.1 and 5.1).

B.1.2. Localized orbitals in reciprocal space

The orbitals in real space introduced above have a representation in reciprocal space connected by Fourier transformation

$$\phi_{lm}^Q(\mathbf{k}) = \frac{1}{\sqrt{\Omega_C}} \int d^3r \phi_{lm}^Q(\mathbf{r}) e^{-i\mathbf{k}\mathbf{r}} \quad (\text{B.3})$$

$$\phi_{lm}^Q(\mathbf{r}) = \frac{\sqrt{\Omega_C}}{(2\pi)^3} \int d^3k \phi_{lm}^Q(\mathbf{k}) e^{i\mathbf{k}\mathbf{r}} \quad (\text{B.4})$$

where $\int d^3r e^{-i\mathbf{k}\mathbf{r}} = (2\pi)^3 \delta(\mathbf{k})$ was used and Ω_C is the unit cell volume. As a matter of convention, in this work the Fourier transformations of the orbitals *unlike* the potentials are always associated with a factor of $\sqrt{\Omega_C}$. At this point it is useful to define a radial Fourier transformation

$$f_l^Q(k) \equiv 4\pi \int dr r^2 f_l^Q(r) j_l(kr) \quad (\text{B.5})$$

$$f_l^Q(r) \equiv \frac{1}{2\pi^2} \int dk k^2 f_l^Q(k) j_l(kr) \quad (\text{B.6})$$

where the j_l are spherical Bessel functions which are implemented by the MBPP-routine `subroutine bsj` in file `funkt.f90`. The conventions historically chosen in this work unfortunately are *not* the same as in the MBPP. The radial Fourier transformation Eq. (B.5) is implemented in the `subroutine rft_rToK` and the inverse transformation Eq. (B.6) in the `subroutine rft_kToR` in the file `tools.f90`. The involved one dimensional integrations are performed numerically by means of the Simpson method [68, 69, 77]. This will also be the case for all other one dimensional radial integrals (in r -space and k -space) appearing throughout this chapter, if not mentioned otherwise. Via these radial Fourier transformations the angular decomposition in \mathbf{k} -space follows

$$\phi_{lm}^Q(\mathbf{k}) = \frac{1}{\sqrt{\Omega_C}} f_l^Q(k) K_{lm}(\hat{k}) \quad (\text{B.7})$$

which in contrast to Eq. (B.2) is a real quantity.

B.1.3. Useful properties of real spherical harmonics

The cubic harmonics used in this work have some well known advantageous properties which often will be referred to when evaluating the matrix elements and shall be summarized in the following. First of all they are orthonormal

$$\int d\Omega K_{lm}(\hat{r}) K_{l'm'}(\hat{r}) = \delta_{ll'} \delta_{mm'} \quad (\text{B.8})$$

where in spherical coordinates it is useful to introduce an element of solid angle via $\int d^3r = \int dr r^2 d\Omega$. As an extension of Eq. (B.8) one often encounters angular overlap integrals of

three cubic harmonics which are called Gaunt coefficients

$$C(lm, l'm', l''m'') = \int d\Omega K_{lm}(\hat{r}) K_{l'm'}(\hat{r}) K_{l''m''}(\hat{r}) \quad (\text{B.9})$$

They exhibit several well-known symmetries and thus can be efficiently calculated as implemented in the MBPP-routine subroutine `clgd` in file `funkt.f90`. Another useful relation of the cubic harmonics is

$$e^{i\mathbf{k}\mathbf{r}} = \sum_{lm} 4\pi i^l j_l(kr) K_{lm}(\hat{r}) K_{lm}(\hat{k}) \quad (\text{B.10})$$

Provided a translationally invariant effective medium, it is more convenient to calculate some of the multi-center integrals in reciprocal space and Fourier transform them back on the lattice to real space using the convention

$$A_{s,t}(\mathbf{k}) = \frac{1}{(2\pi)^3} e^{-i\mathbf{k}(\mathbf{R}_s - \mathbf{R}_t)} \sum_L e^{-i\mathbf{k}\mathbf{R}_L} A_{Ls,t}$$

where $A_{Ls,t}$ abbreviates $A_{Ls,0t}$. When dealing with such discrete Fourier transformations, the following relations can be helpful

$$\sum_L e^{-i\mathbf{k}\mathbf{R}_L} = N_{\mathbf{k}} \sum_{\mathbf{G}} \delta_{\mathbf{k}\mathbf{G}} = \frac{(2\pi)^3}{\Omega_C} \sum_{\mathbf{G}} \delta(\mathbf{G} - \mathbf{k})$$

where $\mathbf{R}_L \in \text{Bravais-lattice}$, $\mathbf{G} \in \text{reciprocal lattice}$ and $N_{\mathbf{k}}$ is the number of \mathbf{k} -points in the first Brillouin zone.

B.1.4. Translation of the orbitals

Due to the fact that some of the matrix elements to be calculated are multi-center integrals, knowledge about the behavior of the basis functions in an orbital representation like Eqs. (B.2) or (B.7) under a translation in real space is essential. Using the definitions and conventions from above this can be written

$$\phi_{Lslm}^Q(\mathbf{r}) = \frac{\sqrt{\Omega_C}}{(2\pi)^3} \int d^3k e^{-i\mathbf{k}(\mathbf{R}_L + \mathbf{R}_s)} e^{i\mathbf{k}\mathbf{r}} \phi_{lm}^Q(\mathbf{k}) \quad (\text{B.11})$$

$$= \frac{1}{(2\pi)^3} \int d^3k e^{-i\mathbf{k}(\mathbf{R}_L + \mathbf{R}_s)} e^{i\mathbf{k}\mathbf{r}} f_l^Q(k) K_{lm}(\hat{k}) \quad (\text{B.12})$$

$$= \frac{1}{(2\pi)^3} \int d^3k d^3r' e^{-i\mathbf{k}(\mathbf{R}_L + \mathbf{R}_s)} e^{i\mathbf{k}\mathbf{r}} \phi_{lm}^Q(\mathbf{r}') e^{-i\mathbf{k}\mathbf{r}'} \quad (\text{B.13})$$

where the advantage of evaluating K_{lm} or f_l^Q only with respect to an unshifted origin is always paid by the price of additional integrations.

B.2. Overlap matrix elements

With the definitions and relations of the last sections every ingredient needed for the calculation of the overlap matrix elements is now available.

B.2.1. Onsite overlap

Just for a matter of completeness and as an instructive example, the easiest matrix elements are the onsite terms of the overlap matrix. They can be simplified to the following expression

$$\dot{S}_{s,lm,tl'm'}^{PQ} = \langle sPlm | sPl'm' \rangle \delta_{PQ} = \int d^3r \left[\phi_{lm}^P(\mathbf{r} - \mathbf{R}_s) \right]^* \phi_{l'm'}^P(\mathbf{r} - \mathbf{R}_s) \delta_{PQ} \quad (\text{B.14})$$

$$= \delta_{ll'} \delta_{mm'} \int dr r^2 \left(f_l^P(r) \right)^2 \delta_{PQ} \quad (\text{B.15})$$

where once again δ_{PQ} is a consequence of the BEB-rules Eq.(2.28) but apart from that only the properties of the K_{lm} have been used. As already discussed in Sec.2.2.4, in the special basis set chosen in this work, the orbitals of the same atomic type are normalized meaning that the onsite overlap becomes unity

$$\dot{S} = \mathbf{1} \quad (\text{B.16})$$

However, for the sake of consistency checks, Eq. (B.15) has been implemented in the code in the subroutine `calcOverlapOnsite` in the file `overlap.f90`.

B.2.2. Offsite terms

More important but also more complicated are the offsite terms of the overlap matrix. As already stated, due to the translational invariance of the underlined quantities in the extended Hilbert space of the BEB-formalism it is more convenient to first evaluate the total overlap matrix for generic indices in reciprocal space

$$S_{slm,tl'm'}^{PQ}(\mathbf{k}) = \frac{1}{(2\pi)^3} \sum_L e^{-i\mathbf{k}\mathbf{R}_L} e^{-i\mathbf{k}(\mathbf{R}_s - \mathbf{R}_t)} \times \\ \times \int d^3r \left[\phi_{lm}^P(\mathbf{r} - \mathbf{R}_L - \mathbf{R}_s) \right]^* \phi_{l'm'}^Q(\mathbf{r} - \mathbf{R}_t) \quad (\text{B.17})$$

$$= \frac{1}{\Omega_C} \sum_G e^{-i\mathbf{G}(\mathbf{R}_s - \mathbf{R}_t)} f_l^P(k - G) K_{lm}(\widehat{k - G}) \times \\ \times f_{l'}^Q(k - G) K_{l'm'}(\widehat{k - G}) \quad (\text{B.18})$$

Using Eq. (B.18) and the trivial result for the onsite overlap, the offsite overlap matrix elements can be calculated via

$$\check{S}_{slm,tl'm'}^{PQ}(\mathbf{k}) = S_{slm,tl'm'}^{PQ}(\mathbf{k}) - \delta_{s,t} \dot{S}_{s,lm,tl'm'}^{PQ} = S_{slm,tl'm'}^{PQ}(\mathbf{k}) - \delta_{PQ} \delta_{st} \delta_{ll'} \delta_{mm'} \quad (\text{B.19})$$

These expressions are implemented in the code via the subroutine `calcOverlapOffsite` in the file `overlap.f90`. The results of evaluating Eq. (B.18) are stored in the complex array `ovlp_k(irk,iao1,iao2)` where `irk` is a \mathbf{k} -point index and `(iao1,iao2)` are described in Sec. A.4. The true offsite overlap matrix elements due to Eq. (B.19) are stored in the complex array `sOffsite(irk,iao1,iao2)`.

B.3. Electronic density

As already discussed in Sec. 2.3, in the BEB-formalism the density is calculated in the following local decomposition for internal calculations like improving the Hamiltonian

$$n(\mathbf{r}) = \sum_{LsP} \eta_{Ls}^P n_{Ls}^P(\mathbf{r}) \quad (\text{B.20})$$

Due to the fact that in the BEB formalism the η are just used for transformation but in the end only configurational averages are quantities of interest, Eq. (B.20) is never evaluated in practical calculations (except for the case if the total density in real space is desired where then the η have to be replaced by atomic concentrations as already discussed in Sec. 2.3). Moreover what really has to be evaluated in the charge self-consistency cycle are the local species resolved density components which in Sec. 2.3 were shown to be (after Eq. (2.81))

$$n_{Ls}^P(\mathbf{r}) = -\frac{1}{\pi} \frac{1}{c_s^P} \sum_{\substack{MtQ \\ lml'm'}} \phi_{Lslm}^P(\mathbf{r}) \int_{-\infty}^{E_F} d\omega \operatorname{Im} \Gamma_{Lslm, Mt'l'm'}^{PQ}(\omega^+) \left(\phi_{Mt'l'm'}^Q(\mathbf{r}) \right)^* \quad (\text{B.21})$$

$$\equiv -\frac{1}{\pi} \sum_{\substack{MtQ \\ lml'm'}} A_{Lslm, Mt'l'm'}^{PQ} \left[\phi_{Mt'l'm'}^Q(\mathbf{r}) \right]^* \phi_{Lslm}^P(\mathbf{r}) \quad (\text{B.22})$$

As stated several times before, the effective medium Green's function $\Gamma_{Lslm, Mt'l'm'}^{PQ}$ is translationally invariant (in L, M) which means that the coefficients $A_{Lslm, Mt'l'm'}^{PQ}$ only depend on the difference $L - M$ which is a simplification. Furthermore, in practice it is necessary to introduce a cutoff radius R_{cut} for the summation - usually it is chosen such that atoms (Q, Mt) with distance beyond this cutoff have no overlap to the reference atom (P, Ls) in the sense that the other atoms have to be located in a region where the radial wavefunction of the reference atom is nonvanishing.

According to the conventions selected in this work, a multipole expansion of these density components n_{Ls}^P then reads

$$n_{Ls}^P(\mathbf{r}) = \sum_{lm} n_{Ls, lm}^P(r) K_{lm}(\hat{r}) \quad (\text{B.23})$$

where the translation of the second orbital located at (M, t) to the origin of the reference atom (L, s) can be readily performed by the formal apparatus outlined in Secs. B.1.1 - B.1.4 which yields

$$\begin{aligned} n_{Ls, lm}^P(r) = & -\frac{1}{\pi} \sum_{MtQ} \sum_{l'm'l''m''} \sum_{l''m''} i^{l'} A_{Lsn'l'm', Mtn''l''m''}^{PQ} C(lm, l'm', l''m'' \times \\ & \times \left[B_{n''l''m'', l''m''}^Q(r, \mathbf{R}_M - \mathbf{R}_L + \mathbf{R}_t - \mathbf{R}_s) \right]^* \times \\ & \times f_{n'l'}^P(r) \end{aligned} \quad (\text{B.24})$$

where the coefficients B depending on the actual translation vector are a shorthand notation for

$$B_{lm,l'm'}^Q(r, \mathbf{R}) = \frac{2}{\pi} \sum_{l''m''} C(lm, l'm', l''m'') K_{l''m''}(\hat{R}) i^{l'-l''} \times \int dk k^2 j_{l''}(kr) j_{l''}(kR) f_l^Q(k) \quad (\text{B.25})$$

The computation of the radial orbital densities after Eq. (B.24) are implemented in the source code via the `subroutine denSpecOrb` which is called by the `subroutine init_density` in the file `density.f90`. In this subroutine the symmetrized radial orbital densities in real space are stored in the double precision array `orb_rad_den_r(ir, ilm, iat, itype)` where `ir` is the radial index on an equidistant r -grid, `ilm` the combined (l, m) -index, `iat` an atomic index and `itype` an atomic type or species index. In this routine also the Broyden mixing of the new (calculated from the Green's function) and the old charge densities is performed by calling the `subroutine broyd` defined in `broyd.f` when the charge iteration is greater than one. Also the maximal density difference as convergence criterion for the charge self-consistency is calculated here. The radial Fourier transformations of the radial orbital densities to k -space are performed in the `subroutine init_density` and stored in the array `orb_rad_den_k`. The B -coefficients as defined by Eq. (B.25) are calculated by the `subroutine denCalcB`. The A -coefficients, being essentially the integrals of the Green's function, are given by the expressions derived in Sec. 2.3

$$A_{Lslm, Mtl'm'}^{PQ} = \frac{1}{c_s^P} \frac{1}{N_{\mathbf{k}}} \text{Im} \sum_{\mathbf{k}} e^{i\mathbf{k}(\mathbf{R}_L + \mathbf{R}_s - \mathbf{R}_M - \mathbf{R}_t)} \left[\oint_{\text{box}} \Gamma_{slm, t'l'm'}^{PQ}(\omega) f(\omega, T) d\omega - \sum_n \frac{2n\pi i}{\beta} \Gamma_{slm, t'l'm'}^{PQ}(\mu + i\omega_n) \right] \quad (\text{B.26})$$

where again the integration is performed around a rectangular path in the upper half plane at finite temperature T , $f(\omega, T)$ is the Fermi distribution and the integral is corrected for the poles at the fermionic Matsubara frequencies $\omega_n = (2n + 1)\pi k_B T$ (for more details see App. C below). In the program code, Eq. (B.26) is implemented in the `subroutine cpa_calcDenA` in the file `cpaSolver.f90` because this is closely related to the CPA cycle. In the first step where only the orbitals, potentials and crystal structure from the DFT calculation but no Green's function are known, the A have to be calculated from the respective DFT bandstructures of the parent compound and the substitutional end members

$$A_{Lslm, Mtl'm'}^{PQ} = \frac{-2\pi}{N_{\mathbf{k}}} \sum_{\mathbf{k}, j} \text{occup}(\mathbf{k}, j) e^{i\mathbf{k}(\mathbf{R}_L + \mathbf{R}_s - \mathbf{R}_M - \mathbf{R}_t)} c_{lm,s}^{Pkj} \left(c_{l'm',t}^{Qkj} \right)^* \quad (\text{B.27})$$

where j runs over all bands of the parent compound, $\text{occup}(\mathbf{k}, j)$ are the fractional occupation numbers of band j at point \mathbf{k} and $c_{lm,s}^{Pkj}$ expansion coefficients of the LCAO Bloch-basis with respect to the original Kohn-sham bands both taken from the DFT calculation. This expression was derived by a combination of the expression of the total density in the original mixed basis and the representation of the Bloch basis in LCAO wavefunctions as given in [9]. It is implemented in the `subroutine denCalcA_first` in the file

density.f90.

B.4. Hamiltonian matrix elements

After having outlined how to calculate the overlap matrix elements and the electronic density in an analytical form which can directly be translated into source code it is time to do the same for the Hamiltonian matrix elements. Therefore it is first of all important to do the same analysis as was already done for the local orbitals in Sec.B.1 for the contributions to the local potential. Here, one general remark has to be made about the actual storage of the potentials in the CPA program: like in the MBPP, for the radial potentials in real space $r \cdot V(r)$ and for the radial potentials in reciprocal space $k^2 \cdot V(k)$ is stored and calculated because this has numerical advantages in avoiding divergences. The only exception to that is the exchange and correlation potential in reciprocal space $V_{XC}(k)$ but this is commented in the source code.

B.4.1. Potential contributions

As already outlined in Sec. 2.2.4 the DFT potential consists of the following contributions

$$V(\mathbf{r}) = V_{Pseudo}(\mathbf{r}) + V_{Hartree}(\mathbf{r}) + V_{XC}(\mathbf{r}) \quad (\text{B.28})$$

namely the Hartree term describing the interaction of one electron with the total electronic density, the pseudopotential modelling the electron-ion interaction screened by the core electrons and the exchange and correlation part containing in principle all remaining many body effects not considered by the other terms and corrections to the kinetic term. In particular, in the MBPP the pseudopotential is divided into a local and a nonlocal part

$$\begin{aligned} V_{Pseudo}(\mathbf{r}) &= V_{loc}^{PS}(\mathbf{r}) + \sum_{lm} [V_l^{PS}(\mathbf{r}) - V_{loc}^{PS}(\mathbf{r})] |lm\rangle\langle lm| \\ &= V_{loc}^{PS}(\mathbf{r}) + \sum_{lm} V_l^{PS,nl}(\mathbf{r}) |lm\rangle\langle lm| \end{aligned} \quad (\text{B.29})$$

The reason for this is that in order to construct the total ionic pseudopotential, one has to construct a pseudopotential for each angular momentum component separately as discussed in more detail in [9]. Outside the core region all angular momentum components exhibit the same long range behavior as $\frac{-Ze^2}{r}$ making it convenient to separate this general long ranged contribution from the others and absorb it into the term $V_{loc}^{PS}(\mathbf{r})$. The remaining angular momentum dependent nonlocal parts then are short ranged and only play a role inside the core region. There is a free choice of the local part which is also an option in the MBPP and technically maintained by the array `vidx` which was also taken over into the CPA code. But in practice this option is hardly used, so in this work it was assumed that the local part is *always* the $l = 0$ component. For using the full functionality of selections stored in `vidx` the CPA code has to be extended in the places where the pseudopotential is treated.

B.4.2. The local potential

For all local contributions to the potential, the following decomposition is required by the pseudopotential-LCAO-CPA scheme

$$V(\mathbf{r}) = \sum_{LsQ} \eta_{Ls}^Q V_{Ls}^Q(\mathbf{r}) = \sum_{LsQ} \eta_{Ls}^Q V_s^Q(\mathbf{r} - \mathbf{R}_L) \quad (\text{B.30})$$

where in contrast to the wave functions the atomic index in the unit cell s does *not* indicate a translation of the potential by \mathbf{R}_s . The index s is needed because specifying only the species is not sufficient in a disordered system - moreover the information, which site in the unit cell is occupied by which species becomes important. If a translation by \mathbf{R}_s is performed, this will be explicitly indicated in the argument of the potential. The individual contributions of the local potential are

$$V_s^Q(\mathbf{r}) = V_{Hartree_s}^Q(\mathbf{r}) + V_{loc_s}^{PSQ}(\mathbf{r}) + V_{XC_s}^Q(\mathbf{r}) \quad (\text{B.31})$$

Thereby V_{loc}^{PS} is already decomposed by construction in the MBPP and is the only contribution where the index s is obsolete because the pseudopotentials are only generated species- and angular momentum-wise. For the other contributions, the decompositions have to be worked out in the following sections and due to inhomogeneities in the density arising from disorder the index s is meaningful.

For the Fourier transformation the following conventions are used

$$V_s^Q(\mathbf{k}) = \frac{1}{\Omega_C} \int d^3r V_s^Q(\mathbf{r}) e^{-i\mathbf{k}\mathbf{r}} \quad (\text{B.32})$$

$$V_s^Q(\mathbf{r}) = \frac{\Omega_C}{(2\pi)^3} \int d^3k V_s^Q(\mathbf{k}) e^{i\mathbf{k}\mathbf{r}} \quad (\text{B.33})$$

which are obviously different from the ones for the orbitals because here Ω_C and *not* its square root appears. Secondly, a multipole expansion to account for angular momentum decomposition is used in the following form

$$V_s^Q(\mathbf{r}) = \sum_{lm} V_{s,lm}^Q(r) K_{lm}(\hat{r}) \quad (\text{B.34})$$

which, unlike the orbitals is *not* defined with an additional factor i^l . This definition yields

$$V_s^Q(\mathbf{k}) = \frac{4\pi}{\Omega_C} \int dr r^2 \sum_{lm} (-i)^l j_l(kr) K_{lm}(\hat{k}) V_{s,lm}^Q(r) \quad (\text{B.35})$$

and can be rewritten as

$$V_s^Q(\mathbf{k}) = \frac{1}{\Omega_C} \sum_{lm} (-i)^l V_{s,lm}^Q(k) K_{lm}(\hat{k}) \quad (\text{B.36})$$

where again radial Fourier transformation was introduced in exactly the *same* way as for the basis orbitals Eq. (B.5)

$$V_{s,lm}^Q(k) = 4\pi \int dr r^2 j_l(kr) V_{s,lm}^Q(r) \quad (\text{B.37})$$

Again, this is different from the convention of the MBPP which made it necessary to rescale some of the k -dependent potentials imported from MBPP by $\frac{1}{4\pi}$ but this is commented in the source code.

Then the translation of the origins where the local potentials are referring to, is carried out in a similar way as for the basis orbitals

$$V_{Ls}^Q(\mathbf{r} - \mathbf{R}_s) = \frac{\Omega_C}{(2\pi)^3} \int d^3k e^{-i\mathbf{k}(\mathbf{R}_L + \mathbf{R}_s)} e^{i\mathbf{k}\mathbf{r}} V_s^Q(\mathbf{k}) \quad (\text{B.38})$$

$$= \frac{1}{(2\pi)^3} \int d^3k d^3r' e^{-i\mathbf{k}(\mathbf{R}_L + \mathbf{R}_s)} e^{i\mathbf{k}\mathbf{r}} V_s^Q(\mathbf{r}') e^{-i\mathbf{k}\mathbf{r}'} \quad (\text{B.39})$$

B.4.3. The nonlocal pseudopotential

The same considerations have to be carried out for the nonlocal contributions of the pseudopotential, which have to be treated differently because they depend on two coordinates \mathbf{r} and \mathbf{r}'

$${}^{nl}V_{Ls}^Q(\mathbf{r}, \mathbf{r}') = {}^{nl}V_s^Q(\mathbf{r} - \mathbf{R}_L, \mathbf{r}' - \mathbf{R}_L) \quad (\text{B.40})$$

Moreover, such a contribution is a nonlocal operator and thus, being evaluated between two orbitals, its action on a wavefunction is important. According to [9] this is given by

$$\begin{aligned} {}^{nl}V_{0s}^Q|00Q\mu\rangle &= \int d^3r' {}^{nl}V_s^Q(\mathbf{r}, \mathbf{r}') \phi_{l'm'}^Q(\mathbf{r}') \\ &= \sum_{l,m} \int d^3r' \frac{1}{r^2} \delta(r - r') {}^{nl}V_{s,l}^Q(r) K_{lm}(\hat{r}) K_{lm}(\hat{r}') \phi_{l'm'}^Q(\mathbf{r}') \end{aligned} \quad (\text{B.41})$$

and in reciprocal space it reads

$${}^{nl}V_s^Q(\mathbf{k}, \mathbf{k}') = \frac{4\pi}{\Omega_C} \sum_l (2l+1) P_l(\hat{\mathbf{k}} \cdot \hat{\mathbf{k}}') \int dr r^2 j_l(kr) {}^{nl}V_{s,l}^Q(r) j_l(k'r) \quad (\text{B.42})$$

where the P_l are Legendre polynomials.

B.4.4. The Hartree potential

The Hartree potential depends on the electronic density and is given in real space via

$$V_{Hartree}(\mathbf{r}) = e^2 \int \frac{n(\mathbf{r}')}{|\mathbf{r} - \mathbf{r}'|} d^3r' \quad (\text{B.43})$$

It turns out that its evaluation is more convenient in reciprocal space. The electronic density can be Fourier transformed

$$\begin{aligned} n(\mathbf{k}) &= \frac{1}{\Omega_C} \int n(\mathbf{r}) e^{-i\mathbf{k}\mathbf{r}} d^3r \\ &= \frac{1}{\Omega_C} \sum_{sP} \eta_s^P \sum_{lm} (-i)^l K_{lm}(\hat{\mathbf{k}}) n_{s,lm}^P(k) \\ &\equiv \sum_{sP} \eta_s^P n_s^P(\mathbf{k}) \end{aligned} \quad (\text{B.44})$$

where the radial Fourier transformation $n_{Ls,lm}^P(k)$ is defined as usual in this work. Fourier transformation of the Hartree potential yields

$$V_H(\mathbf{k}) = e^2 n(\mathbf{k}) \frac{4\pi}{k^2} = e^2 \frac{4\pi}{k^2} \sum_{sP} \eta_s^P n_s^P(\mathbf{k}) \equiv \sum_{sP} \eta_s^P {}^{(H)}V_s^P(\mathbf{k}) \quad (\text{B.45})$$

This directly leads to a species and site resolved decomposition of the Hartree potential in the sense of the BEB formalism which can be calculated from the densities via

$$\begin{aligned} {}^{(H)}V_s^P(\mathbf{k}) &= \frac{1}{\Omega_C} \frac{4\pi e^2}{k^2} \sum_{lm} (-i)^l n_{s,lm}^P(k) K_{lm}(\hat{k}) \\ &\equiv \frac{1}{\Omega_C} \sum_{lm} (-i)^l {}^{(H)}V_{s,lm}^P(k) K_{lm}(\hat{k}) \end{aligned} \quad (\text{B.46})$$

with the radial angular and species resolved local contributions to the Hartree potential

$${}^{(H)}V_{s,lm}^P(k) = \frac{4\pi e^2}{k^2} n_{s,lm}^P(k) \quad (\text{B.47})$$

where in the units used within the MBPP and the CPA program $e^2 = 2$. Due to the fact, that in the implementation only $k^2 V(k)$ is calculated, Eq. (B.47) can be evaluated without the $\frac{1}{k^2}$ term in order to avoid the occurrence of any divergences for $k \rightarrow 0$ which was directly implemented when summing up all contributions to the local potential in k -space in the subroutine `calcLocPot` in the file `potential.f90`.

The respective components in real space can be obtained by the usual radial Fourier transformation

$${}^{(H)}V_{s,lm}^P(r) = \frac{1}{2\pi^2} \int dk k^2 j_l(kr) {}^{(H)}V_{s,lm}^P(k) = \frac{4\pi e^2}{2\pi^2} \int dk j_l(kr) n_{s,lm}^P(k) \quad (\text{B.48})$$

where by inserting Eq. (B.47) the critical factor $\frac{1}{k^2}$ dropped out and also this expression can be directly implemented which was done in the subroutine `calcHartree` in the file `potential.f90`.

B.4.5. Exchange and correlation

As already discussed in Sec. 2.2.4 the exchange and correlation potential (XC) can only approximately be decomposed into the local species resolved contributions required by the BEB formalism due to its nonlinear dependence on the electronic density and it was motivated that this is accomplished via shape functions in this work. With every atom, a certain radially symmetric shape function \mathcal{S}_i^P is associated

$$\mathcal{S}_i^P(\mathbf{r}) = \mathcal{S}_i^P(|\mathbf{r}|) = \mathcal{S}^P\left(\frac{|\mathbf{r}|}{C R_i^P}\right) \quad \mathcal{S}^P(1) = 0 \quad (\text{B.49})$$

and each of them is characterized by the functional form itself as well as by a distinct cutoff radius $C R_i^P$. Here the index i is understood to label a single site in the whole crystal, i.e. it is a combination of (L, s) . In the actual implementation the functional form of all shape

functions is chosen to be the same and is characterized by two parameters $n \in \mathbb{N}$ and γ

$$\mathcal{S}^P(x) = \begin{cases} 1 & \text{for } n = 0 \\ e^{-\gamma x^2} & \text{for } n = 1 \\ 1 - e^{-\gamma(1-x)^n} & \text{for } n \geq 2 \end{cases} \quad (\text{B.50})$$

such that the distinction between different atoms is only made by the cutoff radii. Moreover, in the current implementation the cutoff radii are only species-dependent and thus get their site dependence only from the atomic sublattice of a certain species which was sufficient for BaFe₂As₂. In future applications to other materials this might be changed. The sum over all site centered shape functions evaluated at an arbitrary point \mathbf{r} can be understood as a kind of norm:

$$\mathcal{N}_i^P(\mathbf{r}) = \mathcal{S}_i^P(\mathbf{r}) + \sum_{j \neq i, Q} c_j^Q \mathcal{S}_j^Q(\mathbf{r} - (\mathbf{R}_j - \mathbf{R}_i)) \quad (\text{B.51})$$

Then, an arbitrary local and species decomposition of the XC-potential can be obtained via

$${}^{XC}V_i^P(\mathbf{r}) = V_{XC} \left[{}^{XC}n_i^P(\mathbf{r}) \right] \frac{\mathcal{S}_i^P(\mathbf{r})}{\mathcal{N}_i^P(\mathbf{r})} \quad (\text{B.52})$$

Here, ${}^{XC}n_i^P(\mathbf{r})$ is the the density averaged under the condition that site i is occupied with species P

$$\begin{aligned} {}^{XC}n_i^P(\mathbf{r}) = & {}^{PC}n_i^P(r) + \sum_{lm} n_{i,lm}^P(r) K_{lm}(\hat{\mathbf{r}}) \\ & + \sum_{j \neq i, Q} \sum_{lm} c_j^Q n_{j,lm}^Q(|\mathbf{r} - (\mathbf{R}_j - \mathbf{R}_i)|) K_{lm}(\mathbf{r} - \widehat{\mathbf{R}_j + \mathbf{R}_i}) \end{aligned} \quad (\text{B.53})$$

and ${}^{PC}n_i^P(r)$ is the partial-core charge density as obtained from the MBPP (like the pseudopotential only defined type-wise but has to be added for every atom). This conditionally averaged density is calculated via the `double precision function calcXCDen_spec` in the file `potential.f90`. Thereby, the bond sum over neighbors is restricted to bonds with length less than two times the cutoff radius of the local orbitals.

The norm Eq.(B.51) by entering the decomposition Eq.(B.52) ensures that even if the shape functions are heavily overlapping, no double counting like in an atomic sphere approximation (ASA) occurs. Unlike in the ASA, the shape functions are even required to overlap each other to accomplish that every point in space lies within some of the shape functions. Such a decomposition is considered to be good if $\mathcal{N}(\mathbf{r})$ evaluated at several points in the unit cell exhibits the lowest possible spatial fluctuations. The quality of the approximation can also be tested by comparing the bandstructures of a clean CPA calculation (a CPA calculation without any substitutions) with the respective DFT bandstructure because the bandstructure tends to be sensitive to the choice of the shape functions.

Having achieved a local decomposition of the XC-potential, a further angular momentum decomposition of these local contributions is necessary. Due to the nonlinear functional dependence of the XC-potential on the density resulting in a purely numerical local decomposition of the XC-potential, also the angular momentum decomposition has to be carried out numerically - in contrast to the other potential contributions for which the

multipole terms could be defined analytically. For the desired decomposition

$${}^{XC}V_s^P(\mathbf{r}) = \sum_{lm} {}^{XC}V_{s,lm}^P(r)K_{lm}(\hat{r}) \quad (\text{B.54})$$

the radial angular decomposed components can be obtained using the orthogonality Eq. (B.8) of the cubic harmonics

$${}^{XC}V_{s,lm}^P(r) = \int {}^{XC}V_s^P(\mathbf{r})K_{lm}(\hat{r})d\Omega \quad (\text{B.55})$$

where the integration over solid angle has to be carried out numerically. For this task the use of spherical coordinates where the element of solid angle is given via $d\Omega = d\varphi d\cos\vartheta$ is convenient. For the integration over φ the whole interval from 0 to 2π is divided into N_φ equidistant points. The integration can then simply be accomplished by the trapezoidal rule [68, 69, 132]

$$\begin{aligned} \int_0^{2\pi} f(\varphi)d\varphi &= \int_0^{\frac{2\pi}{N_\varphi}} f(\varphi)d\varphi + \int_{\frac{2\pi}{N_\varphi}}^{\frac{4\pi}{N_\varphi}} f(\varphi)d\varphi + \dots + \int_{(N_\varphi-1)\frac{2\pi}{N_\varphi}}^{N_\varphi\frac{2\pi}{N_\varphi}} f(\varphi)d\varphi \\ &= \frac{2\pi}{N_\varphi} \frac{f_0 + f_1}{2} + \frac{2\pi}{N_\varphi} \frac{f_1 + f_2}{2} + \dots + \frac{2\pi}{N_\varphi} \frac{f_{N_\varphi-1} + f_{N_\varphi}}{2} \\ &= \frac{2\pi}{N_\varphi} \left[\frac{f_0 + f_{N_\varphi}}{2} + \sum_{j=1}^{N_\varphi-1} f_j \right] \\ &= \frac{2\pi}{N_\varphi} \sum_{j=0}^{N_\varphi-1} f_j \end{aligned} \quad (\text{B.56})$$

where $f_j = f(j\frac{2\pi}{N_\varphi})$ and in the last step $f_0 = f_{N_\varphi}$ as a consequence of the 2π periodicity of the spherical coordinates was used. The integration over ϑ is slightly more complicated and is performed via a Gauß- Legendre quadrature [68–71]

$$\int d\cos\vartheta f(\vartheta) = \sum_{i=1}^{N_\vartheta} w_i f(x_i) \quad (\text{B.57})$$

where the special weight factors are defined by

$$w_i = \frac{2}{(1-x_i^2) \left[P'_{N_\vartheta}(x_i) \right]^2} \quad (\text{B.58})$$

and the P'_{N_ϑ} are the first derivatives of Legendre polynomials. The optimal x_i and associated w_i for a number of N_ϑ sampling points are tabulated and can be found for example on the web [71]. In the code they were already needed for the gaunt coefficients and thus are taken from the file `funkt.f90` (arrays `x_clgd` and `w_clgd`). Finally the whole scheme of orbital decomposition of the site and species resolved contributions of the XC-potential works as follows

$${}^{XC}V_{s,lm}^P(r) = \sum_{i=1}^{N_\vartheta} w_i \frac{2\pi}{N_\varphi} \sum_{j=1}^{N_\varphi} {}^{XC}V_s^P(\mathbf{r}_{i,j})K_{lm}(x_i, \varphi_j) \quad (\text{B.59})$$

where $x_i = (\cos \theta)_i$. In this work it was found that for $N_\varphi = 17$ and $N_\theta = 10$ the orthogonality of the K_{lm} serving as a benchmark for this integration method is fulfilled up to $l = 8$ within an accuracy of 10^{-14} . All this is essentially implemented in the subroutine `calcVxc` in the file `potential.f90`.

B.4.6. The mixing-potential or averaged crystal potential

In the Hamiltonian Eqs. (2.50) and (2.51) the pseudopotential LCAO-CPA is based on, weighted restricted sums appear as for example for the offsite Hamiltonian

$$\left\langle iP\mu \left| \sum_{k \neq (i,j), R} c_k^R V_k^R \right| jQ\nu \right\rangle \quad (\text{B.60})$$

It is convenient to first evaluate this sum without the restriction and afterwards subtract the respective terms which have to be excluded. Secondly, in a clean compound without disorder, where all atomic concentrations are equal to one, an unrestricted version of Eq. (B.60) is nothing else but the crystal potential. Being able to evaluate the crystal Hamiltonian of the parent compound within the CPA program on the one hand can serve for the purpose of validation when setting up a new calculation and comparing with the LCAO matrix elements in the MBPP (and was of course helpful for the implementation). On the other hand the diagonalisation of this crystal Hamiltonian is helpful to analyze self-energy effects in the disordered compound. For historical reasons, this unrestricted sum is called "mixing-potential" in this work and is given by

$$\begin{aligned} V_{mix}(\mathbf{r}) &= \sum_{NuR} c_u^R V_{Nu}^R(\mathbf{r} - \mathbf{R}_u) = \frac{\Omega_C}{(2\pi)^3} \sum_{NuR} c_u^R \int d^3k e^{-i\mathbf{k}(\mathbf{R}_N + \mathbf{R}_u)} e^{i\mathbf{k}\mathbf{r}} V_u^R(\mathbf{k}) \\ &= \sum_{GuR} c_u^R e^{-i\mathbf{G}\mathbf{R}_u} e^{i\mathbf{G}\mathbf{r}} V_u^R(\mathbf{G}) \equiv \sum_{\mathbf{G}} e^{i\mathbf{G}\mathbf{r}} V_{mix}(\mathbf{G}) \end{aligned} \quad (\text{B.61})$$

N being a lattice index, u an atomic index within the unit cell, R being a species index and \mathbf{G} is a vector of the reciprocal lattice. Additionally the abbreviation $V_{mix}(\mathbf{G})$ was introduced meaning

$$\begin{aligned} V_{mix}(\mathbf{G}) &= \sum_{uR} c_u^R e^{-i\mathbf{G}\mathbf{R}_u} V_u^R(\mathbf{G}) \\ &= \frac{1}{\Omega_C} \sum_{uRlm} c_u^R e^{-i\mathbf{G}\mathbf{R}_u} (-i)^l V_{u,lm}^R(\mathbf{G}) K_{lm}(\hat{\mathbf{G}}) \end{aligned} \quad (\text{B.62})$$

Then the onsite matrix elements of the mixing potential are readily found after some manipulations to be

$$\begin{aligned} \langle sPlm | V_{mix} | sPl'm' \rangle &= 4\pi \sum_{\mathbf{G}} e^{i\mathbf{G}\mathbf{R}_s} V_{mix}(\mathbf{G}) \sum_{l''m''} i^{l'+l''-l} K_{l''m''}(\hat{\mathbf{G}}) \times \\ &\quad \times C(lm, l'm', l''m'') \int dr r^2 j_{l''}(Gr) f_l^P(r) f_{l'}^P(r) \end{aligned} \quad (\text{B.63})$$

Furthermore V_{mix} is lattice-periodic. For the clean limit this is clear because V_{mix} then reduces to the crystal potential as discussed before and for a disordered system this property follows directly from Eq. (B.61). This allows to evaluate the matrix elements between

arbitrary sites in \mathbf{k} space for convenience

$$\begin{aligned}
 {}^{(mix)}H_{slm,tl'm'}^{PQ}(\mathbf{k}) &= \sum_L \langle LsPlm | V_{mix} | 0tQl'm' \rangle e^{-i\mathbf{k}\mathbf{R}_L} e^{-i(\mathbf{R}_s - \mathbf{R}_t)} \\
 &= \frac{1}{\Omega_C} \sum_{\mathbf{G}\mathbf{G}'} e^{-i\mathbf{G}\mathbf{R}_s} e^{i\mathbf{G}'\mathbf{R}_t} f_l^P(\mathbf{k} - \mathbf{G}) K_{lm}(\widehat{\mathbf{k} - \mathbf{G}}) \times \\
 &\quad \times V_{mix}(\mathbf{G}' - \mathbf{G}) f_{l'}^Q(\mathbf{k} - \mathbf{G}') K_{l'm'}(\widehat{\mathbf{k} - \mathbf{G}'}). \tag{B.64}
 \end{aligned}$$

This expression for V_{mix} is only valid for the local potential. In Sec. B.4.3 the existence of the nonlocal pseudopotential was discussed which, being a nonlocal operator, has to be treated differently:

$$V_{mix}^{nl} = \sum_{NuR} c_u^R {}^{nl}V_{Nu}^R \tag{B.65}$$

Then, after some manipulations the onsite terms can be found to be

$$\begin{aligned}
 \langle sPlm | V_{mix}^{nl} | sPl'm' \rangle &= \frac{\Omega_C}{(2\pi)^3} \sum_{\mathbf{G}uR} c_u^R \int d^3k e^{i\mathbf{G}(\mathbf{R}_s - \mathbf{R}_u)} [\phi_{nlm}^P(\mathbf{k})]^* \times \\
 &\quad \times {}^{nl}V_u^R(\mathbf{k}, \mathbf{k} - \mathbf{G}) \phi_{l'm'}^P(\mathbf{k} - \mathbf{G}) \tag{B.66}
 \end{aligned}$$

Unfortunately, this expression cannot be further simplified and obviously it contains a three dimensional integration in reciprocal space. This makes it necessary to calculate all matrix elements in reciprocal space which after a lengthy calculation are given by

$$\begin{aligned}
 {}^{mix,nl}H_{slm,tl'm'}^{PQ}(\mathbf{k}) &= \sum_L \langle LsPlm | V_{mix}^{nl} | 0tQl'm' \rangle e^{-i\mathbf{k}\mathbf{R}_L} e^{-i(\mathbf{R}_s - \mathbf{R}_t)} \\
 &= \sum_{\mathbf{G}\mathbf{G}'uR} c_u^R e^{-i\mathbf{G}\mathbf{R}_s} e^{i\mathbf{G}'\mathbf{R}_t} e^{i(\mathbf{G} - \mathbf{G}')\mathbf{R}_u} \times \\
 &\quad \times [\phi_{lm}^P(\mathbf{k} - \mathbf{G})]^* {}^{nl}V_u^R(\mathbf{k} - \mathbf{G}, \mathbf{k} - \mathbf{G}') \phi_{l'm'}^Q(\mathbf{k} - \mathbf{G}') \tag{B.67}
 \end{aligned}$$

The calculation of the total \mathbf{k} -dependent mixing potential containing the local Eq. (B.64) and nonlocal contribution Eq. (B.67) is implemented in the program via the subroutine `calcVmix_k` in the file `hamilton.f90` and is stored in the complex array `vmix_k(irk,iao1,iao2)`. The onsite terms are then obtained via discrete Fourier transformation of Eqs. (B.64) and (B.67) which is implemented in the subroutine `calcMixOnsite` in the file `hamilton.f90`.

B.4.7. Onsite Hamiltonian matrix elements

At this stage, all necessary ingredients and simplifications are prepared on the route to the final evaluation of the Hamiltonian matrix elements in an analytical form which is well suited for implementation in a source code. The onsite Hamiltonian matrix elements contain the following contributions

$$\dot{H}_{s,lm,l'm'}^{PP} = \dot{T}_{s,lm,l'm'}^{PP} + \dot{W}_{s,lm,l'm'}^{PPP}$$

$$+ \underbrace{\sum_{\substack{(N,u) \neq (0,s) \\ R}} \langle sPlm | c_u^R (V_{Nu}^R + {}^{nl}V_{Nu}^R) | sPl'm' \rangle}_{\equiv R.S.} \quad (B.68)$$

Among these contributions, the kinetic term is found to be

$$\dot{T}_{s,lm,l'm'}^{PQ} \equiv \langle sPlm | \hat{t} | sQl'm' \rangle = \delta_{ll'} \delta_{mm'} \frac{\hbar^2}{2m} \frac{1}{(2\pi)^3} \int dk k^4 f_l^P(k) f_l^Q(k) \quad (B.69)$$

where in the atomic units used in this work and the MBPP $\frac{\hbar^2}{2m} = 1$. The onsite matrix elements of the local potential and the nonlocal pseudopotential are given by

$$\begin{aligned} \langle sPlm | V_s^R | sQl'm' \rangle &= \sum_{l''m''} i^{l'-l} C(lm, l'm', l''m'') \int dr r^2 f_l^P(r) V_{s,l''m''}^R(r) f_{l'}^Q(r) \\ \langle sPlm | {}^{nl}V_s^R | sQl'm' \rangle &= \delta_{ll'} \delta_{mm'} \theta(l-1) \theta(l_{max} - l) \int dr r^2 f_l^P(r) {}^{nl}V_{s,l}^R(r) f_l^Q(r) \end{aligned}$$

which then finally give

$$\dot{W}_{s,lm,l'm'}^{PRQ} \equiv \langle sPlm | V_s^R | sQl'm' \rangle + \langle sPlm | {}^{nl}V_s^R | sQl'm' \rangle \quad (B.70)$$

with an extra species index R for the potential. Such potential matrix elements containing three different species will be needed for calculating the offsite matrix elements. Finally the restricted sum can then be evaluated via

$$R.S. = \langle sPlm | V_{mix} + V_{mix}^{nl} | sPl'm' \rangle - \sum_R c_s^R \dot{W}_{s,lm,l'm'}^{PRP} \quad (B.71)$$

All the equations presented in this subsection are implemented in the subroutine `calchOnsite` in the file `hamilton.f90` and are stored in the complex arrays `vOnsite(iao1,itype,iao2)` (\dot{W}), `tOnsite(iao1,iao2)` (\dot{T}) and `hOnsite(iao1,iao2)` (\dot{H}).

B.4.8. Offsite Hamiltonian matrix elements

The offsite Hamiltonian matrix elements exhibit similar contributions as the onsite matrix elements (first two lines) plus additional correction terms which maintain the $1 - \delta_{ij}$ offsite property (last three lines)

$$\begin{aligned} \check{H}_{slm,tl'm'}^{PQ}(\mathbf{k}) &= T_{slm,tl'm'}^{PQ}(\mathbf{k}) + W_{slm,tl'm'}^{PPQ}(\mathbf{k}) + [W_{tl'm',slm}^{QQP}(\mathbf{k})]^* \\ &+ \underbrace{\sum_{\substack{(N,u) \neq (0,s), (0,t) \\ R}} \langle sPlm | c_u^R (V_{Nu}^R + {}^{nl}V_{Nu}^R) | tQl'm' \rangle(\mathbf{k})}_{\equiv R.S.} \\ &- \delta_{s,t} \left[\dot{T}_{s,lm,l'm'}^{PQ} + \dot{W}_{s,lm,l'm'}^{PPQ} + (\dot{W}_{s,l'm',lm}^{QQP})^* \right] \\ &- \delta_{s,t} \langle sPlm | V_{mix} + V_{mix}^{nl} | sQl'm' \rangle \end{aligned}$$

$$+ \delta_{s,t} \sum_R c_s^R \left[\dot{W}_{s,lm,tl'm'}^{PRQ} + \left(\dot{W}_{s,tl'm',lm}^{QRP} \right)^* \right] \quad (\text{B.72})$$

because only the first two lines alone would still allow for onsite contributions. The correction terms are the reason for the need to evaluate the onsite potential matrix elements with three different species \dot{W}^{PRQ} discussed in the last section. In the third term of the first line, originally being a term where the potential is centered at the right terminal site (see Eq. (2.51)), the hermiticity of the Hamiltonian operator was used

$$\langle sPlm | V_t^Q | tQl'm' \rangle = \langle tQl'm' | V_t^Q | sPlm \rangle^* \quad (\text{B.73})$$

because in the following only matrix elements where the potential is centered at the left terminal site are considered. The kinetic contribution is given by

$$T_{slm,tl'm'}^{PQ}(\mathbf{k}) = \frac{\hbar^2}{2m\Omega_C} \sum_{\mathbf{G}} (\mathbf{k} - \mathbf{G})^2 e^{-i\mathbf{G}(\mathbf{R}_s - \mathbf{R}_t)} f_l^P(k - G) K_{lm}(\widehat{k - G}) \times \\ \times f_{l'}^Q(k - G) K_{l'm'}(\widehat{k - G}) \quad (\text{B.74})$$

Next, the left centered matrix elements for arbitrary sites are best evaluated in reciprocal space and a tedious calculation yields

$$\langle sPlm | V_s^R | tQl'm' \rangle(\mathbf{k}) = \frac{4\pi}{\Omega_C} \sum_{l''m'',l''m'''} i^{l''m''-l} C(lm, l''m'', l''m''') \times \\ \times \sum_{\mathbf{G}} e^{-i\mathbf{G}(\mathbf{R}_s - \mathbf{R}_t)} K_{l'm'}(\widehat{k - G}) K_{l''m'''}(\widehat{k - G}) \times \\ \times f_{l'}^Q(k - G) \int dr r^2 j_{l''}((k - G)r) f_l^P(r) V_{s,l''m''}^R(r) \\ \langle sPlm | {}^{nl}V_s^R | tQl'm' \rangle(\mathbf{k}) = \frac{4\pi}{\Omega_C} \sum_{\mathbf{G}} e^{-i\mathbf{G}(\mathbf{R}_s - \mathbf{R}_t)} f_{l'}^Q(k - G) K_{lm}(\widehat{k - G}) \times \\ \times K_{l'm'}(\widehat{k - G}) \int dr r^2 j_l((k - G)r) f_l^P(r) {}^{nl}V_{s,l}^R(r)$$

which in total leads to

$$W_{slm,tl'm'}^{PRQ}(\mathbf{k}) \equiv \langle sPlm | V_s^R | tQl'm' \rangle(\mathbf{k}) + \langle sPlm | {}^{nl}V_s^R | tQl'm' \rangle(\mathbf{k}) \quad (\text{B.75})$$

Finally, the restricted sum can be written as

$$R.S. = {}^{mix}H_{slm,tl'm'}^{PQ}(\mathbf{k}) + {}^{mix,nl}H_{slm,tl'm'}^{PQ}(\mathbf{k}) \\ - \sum_R \left(c_s^R W_{slm,tl'm'}^{PRQ}(\mathbf{k}) + c_t^R \left[W_{tl'm',slm}^{QRP}(\mathbf{k}) \right]^* \right) \quad (\text{B.76})$$

The equations presented in this subsection are implemented in the subroutine `calcHOffsite_lr` in the file `hamilton.f90` and are stored in the complex arrays `vOffsite(irk,iao1,ittype,iao2)` (W), `tOffsite(irk,iao1,iao2)` (T) and `hOffsite(irk,iao1,iao2)` (\check{H}).

B.5. Symmetrization

The lattice of a generic crystalline material can, depending on the space group, contain several symmetries. As already mentioned, an advantageous property of the BEB formalism is the fact that all quantities in the extended Hilbert space preserve those symmetries of the parent compound. The MBPP makes extensive use of symmetries which comes especially into play when \mathbf{k} -dependent quantities are calculated. Instead of calculating a quantity for all the \mathbf{k} -points on a regular mesh the first Brillouin zone is discretized by, the use of symmetries allows to restrict the calculation to only the irreducible part of the first Brillouin zone and then obtain the quantities at other \mathbf{k} -points just by applying symmetry operations. In particular, in all processes involving Brillouin zone integration, instead of summing over all points of the regular mesh it is sufficient to just sum over the irreducible part and afterwards symmetrize the integral. Depending on the number of symmetries, this can lead to a drastic speedup of the program. In the MBPP the full machinery of finding symmetries is already implemented so it was obvious to import this list of symmetries generated by the MBPP for the parent compound and benefit from this speedup in the CPA program. Thus it has to be derived how the individual quantities, of which the calculation involves Brillouin zone integration, namely the electronic density, onsite mixing matrix elements and the effective medium Greens function, have to be symmetrized. How this is accomplished, will be sketched in this section.

A generic symmetry operation g can always be written as a combination of a rotation D and a translation $\boldsymbol{\tau}$

$$g = (D, \boldsymbol{\tau}) \quad g(\mathbf{r}) = D\mathbf{r} + \boldsymbol{\tau} \quad (\text{B.77})$$

where D is a rotation matrix. If such an operation g is an actual symmetry of the crystal it transforms an atom located at site s into another atom located at site s'

$$s' = g(s) \quad g(\mathbf{R}_s) = D\mathbf{R}_s + \boldsymbol{\tau} = \mathbf{R}_{s'} + \mathbf{R}_L \quad (\text{B.78})$$

where always a nontrivial lattice vector \mathbf{R}_L may be involved. Next, the behavior of the local basis functions under symmetry operations has to be concerned. Without loss of generality the species index will be omitted in the following because the symmetry operations only occur between atoms of the same type. The wave functions are

$$\phi_{lm}(\mathbf{r}) = i^l f_l(r) K_{lm}(\hat{r}) \quad \phi_{Ls,lm}(\mathbf{r}) = \phi_{lm}(\mathbf{r} - \mathbf{R}_s - \mathbf{R}_L) \quad (\text{B.79})$$

The transformations then read

$$\begin{aligned} \phi_{Ls,lm}[g(\mathbf{r})] &= \phi_{Ls,lm}(D\mathbf{r} + \boldsymbol{\tau}) = \phi_{lm}(D\mathbf{r} + \boldsymbol{\tau} - \mathbf{R}_s - \mathbf{R}_L) \\ &= \phi_{lm} \left[D \left(\mathbf{r} + \underbrace{D^{-1}\boldsymbol{\tau} - D^{-1}\mathbf{R}_s - D^{-1}\mathbf{R}_L}_{-g^{-1}(\mathbf{R}_s) + \mathbf{R}_{L'}} \right) \right] \\ &= \phi_{lm} \left[D(\mathbf{r} - \mathbf{R}_{g^{-1}(s)} - \mathbf{R}_{L''}) \right] \end{aligned} \quad (\text{B.80})$$

When applying a rotation to a local orbital ϕ one needs knowledge about the transformation of the cubic harmonics under such a rotation. This can be written in terms of Wigner

matrices $W_{m,m'}^l(g)$

$$K_{lm}(D\hat{r}) = \sum_{m'} W_{m,m'}^l(g) K_{lm'}(\hat{r}) \quad W_{m,m'}^l(g) = \int d\Omega K_{lm}(D\hat{r}) K_{lm'}(\hat{r}) \quad (\text{B.81})$$

which then leads to

$$\begin{aligned} \phi_{Ls,lm} [g(\mathbf{r})] &= \sum_{m'} W_{m,m'}^l(g) \phi_{lm'}(\mathbf{r} - \mathbf{R}_{g^{-1}(s)} - \mathbf{R}_{L''}) \\ &= \sum_{m'} W_{m,m'}^l(g) \phi_{L''g^{-1}(s),lm'}(\mathbf{r}) \end{aligned} \quad (\text{B.82})$$

Taking into account the above considerations a generic matrix element of a symmetry invariant operator \hat{A} can be written after some manipulations

$$\begin{aligned} A_{s_1 l_1 m_1, s_2 l_2 m_2}(D_g \mathbf{k}) &= \sum_{m'_1, m'_2} A_{g^{-1}(s_1) l_1 m'_1, g^{-1}(s_2) l_2 m'_2}(\mathbf{k}) W_{m_1, m'_1}^{l_1}(g) W_{m_2, m'_2}^{l_2}(g) \times \\ &\quad \times e^{iD_g \mathbf{k}(\mathbf{R}_{s_1} - \mathbf{R}_{s_2})} e^{-i\mathbf{k}(\mathbf{R}_{g^{-1}(s_1)} - \mathbf{R}_{g^{-1}(s_2)})} \end{aligned} \quad (\text{B.83})$$

or more compactly written in matrix form

$$A(D_g \mathbf{k}) = T_g A(\mathbf{k}) T_g^\dagger \quad (\text{B.84})$$

$$T_{g,slm,s'l'm'} = \delta_{l,l'} \delta_{s',g^{-1}(s)} W_{m,m'}^l(g) e^{iD_g \mathbf{k} \mathbf{R}_s} e^{-i\mathbf{k} \mathbf{R}_{g^{-1}(s)}} \quad (\text{B.85})$$

Then the sum of such a matrix element over all \mathbf{k} -points becomes

$$S = \sum_{\mathbf{k}} A(\mathbf{k}) = \sum_{\boldsymbol{\kappa}} \sum_{g(\boldsymbol{\kappa})} A(D_g \boldsymbol{\kappa}) = \sum_{\boldsymbol{\kappa}} \sum_g \frac{1}{n_{inv}(\boldsymbol{\kappa})} T_g A(\boldsymbol{\kappa}) T_g^\dagger \quad (\text{B.86})$$

where $\boldsymbol{\kappa}$ belongs to the irreducible part of the first Brillouin zone and $n_{inv}(\boldsymbol{\kappa})$ is the number of all symmetry operations which map $\boldsymbol{\kappa}$ on itself. In the second equality, the $\sum_{g(\boldsymbol{\kappa})}$ runs only over a subset of symmetry operations which generate the symmetry related set of \mathbf{k} -points belonging to $\boldsymbol{\kappa}$, the so called "star" of $\boldsymbol{\kappa}$. In the last step, the \sum_g is performed over all symmetry operations, which was compensated by the factor $\frac{1}{n_{inv}(\boldsymbol{\kappa})}$. When calculating onsite matrix elements where the T_g do not depend on $\boldsymbol{\kappa}$ anymore because then the phase factors get trivial in Eq. (B.85) this allows to perform the sum over the symmetry operations g independently from that over $\boldsymbol{\kappa}$

$$S = \sum_g T_g \left(\sum_{\boldsymbol{\kappa}} \frac{1}{n_{inv}(\boldsymbol{\kappa})} A(\boldsymbol{\kappa}) \right) T_g^\dagger \equiv \frac{1}{N_g} \sum_g T_g \left(\sum_{\boldsymbol{\kappa}} w(\boldsymbol{\kappa}) A(\boldsymbol{\kappa}) \right) T_g^\dagger \quad (\text{B.87})$$

where in the last equality N_g is just the number of symmetry operations (`nsympop` in the code) and $w(\boldsymbol{\kappa})$ are symmetry dependent weight factors (`weight_irk` in the code) which are delivered by the MBPP program. This in principle allows to first calculate all \mathbf{k} -dependent matrix elements only for vectors $\boldsymbol{\kappa}$ inside the irreducible part of the first Brillouin zone and then sum over them using the weight factors which is the inner sum in Eq. (B.87). Afterwards, to include also the terms lying outside the irreducible part, this sum is symmetrized which is the outer sum in Eq. (B.87). This allows to implement a

generic symmetrization routine for onsite matrix elements which does nothing but

$${}^{sym}S_{s,l_1m_1,l_2m_2} = \frac{1}{N_g} \sum_g \sum_{m'_1,m'_2} W_{m_1,m'_1}^{l_1}(g) S_{g^{-1}(s),l_1m'_1,l_2m'_2} W_{m_2,m'_2}^{l_2}(g) \quad (\text{B.88})$$

where S is just the unsymmetrized sum over the irreducible part of their first Brillouin zone. This is applied when calculating the onsite mixing terms and the onsite effective medium Green's function and implemented in the `subroutine symmetrizeOnsiteGmat` taking care of the special site-indices of the effective medium Green's function and `subroutine symmetrizeOnsiteCmat` for a general complex onsite matrix in `iao` orbital indices in the file `symmetry.f90`

For the electronic density this becomes slightly different. Here the Brillouin zone summation is only involved in the A -coefficients Eqs. (B.26) and (B.27). These summations are only performed over the κ -vectors inside the irreducible part and instead of the factor $\frac{1}{N_k}$ the appropriate weight factor $w(\kappa)$ is taken into account in the summation (these weight factors reduce to $\frac{1}{N_k}$ when no symmetries are present). Then, after having calculated the radial orbital densities $n_{Ls,lm}(r)$ (including all the summations over the B -coefficients) they get symmetrized according to

$${}^{sym}n_{Ls,lm}(r) = \frac{1}{N_g} \sum_g \sum_{m'} W_{m,m'}^l(g) n_{Lg^{-1}(s),lm'}(r) \quad (\text{B.89})$$

where still the species indices were omitted without loss of generality. This is implemented in the `subroutine denSpecOrb` in the file `density.f90`.

All symmetry operations $s' = g(s)$ which are found in a crystal by the MBPP are stored in an "atomic transformation table" being realized as an integer array `iatrans(isym,iat,itpe)` in the code which gives the transformed atomic index corresponding to an initial atomic index `iat` of species `itpe` under a symmetry operation `isym`.

C. The impurity solver

This chapter is devoted to a brief discussion of some details about the CPA-solver, being the "heart piece" of the implemented program. All subroutines, if nothing else is mentioned, can be found in the file `cpaSolver.f90`. Usually, a calculation is carried out in the following way: First, the CPA effective medium Green's function is calculated along a rectangular path in the upper complex frequency half-plane as already mentioned several times in this work. This is done in the subroutine `cpaCalcMedium` for several temperatures. Essentially this routine, as also other routines do, only calls the subroutine `cpaCycleEnergy` where the actual work is done. This subroutine implements the inner self-consistency loop shown in Fig 2.2 for a single complex frequency (called `energy` in the code) where the impurity problem is solved numerically by iterating the following equations

$$\underline{\Gamma}_{i,\mu\nu}^{PQ} = \int_{1.BZ} d^3k \left[\omega \left(\mathbf{1} + \check{\underline{S}}(\mathbf{k}) \right) - \check{\underline{H}}(\mathbf{k}) - \underline{\Sigma} \right]^{-1} \Big|_{i\mu, i\nu}^{PQ} \quad (\text{C.1})$$

$$d\underline{\Sigma}_{i,\mu\nu}^{PQ} = \left(\underline{\Gamma}_i^{-1} \right)_{\mu\nu}^{PQ} + \sum_q \frac{1}{c_i^q} \left[\check{\underline{H}}_i - \underline{\Sigma}_i - \underline{\Gamma}_i^{-1} \right]_{\mu\nu}^{qq} \delta_{PQ} \delta_{Pq} \quad (\text{C.2})$$

which were already explained in detail in Sec. 2.2.4. This scheme provides a self-consistent, fully symmetrized onsite medium Green's function $\underline{\Gamma}$ in the site data structure in the complex array `greenSite(tlm1, tlm2, isite)`. Having obtained a converged self-energy it also provides the \mathbf{k} -dependent Green's function in the irreducible part of the first Brillouin zone without performing the summation over all \mathbf{k} -points

$$\underline{\Gamma}(\mathbf{k}) = \left[\omega \left(\mathbf{1} + \check{\underline{S}}(\mathbf{k}) \right) - \check{\underline{H}}(\mathbf{k}) - \underline{\Sigma} \right]^{-1} \quad (\text{C.3})$$

which is used for most physical observables in the program like for example the density of states Eq. (2.71). $\underline{\Gamma}(\mathbf{k})$ is given in the `iao` indices in the complex array `greenOrbK(iao1, iao2, irk)`. The involved matrix inversions are performed by LAPACK (Linear Algebra Package) routines [131]. Back in the subroutine `cpaCalcMedium` this Green's function then is summed over all irreducible \mathbf{k} -points and symmetrized. Also the product $\underline{S}(\mathbf{k})\underline{\Gamma}(\mathbf{k})$ is calculated. This is used to calculate the chemical potential μ and Fermi level in the subroutine `cpaCalcFermi` via calculating the particle number

$$N = -\frac{2}{\pi} \text{Im} \oint d\omega \text{Tr} \left[\int_{1.BZ} d^3k \underline{S}(\mathbf{k}) \underline{\Gamma}(\mathbf{k}, \omega) \right] f(\omega, \mu, T) - 2\pi i k_B T \sum_n \text{Tr} \left[\int_{1.BZ} d^3k \underline{S}(\mathbf{k}) \underline{\Gamma}(\mathbf{k}, \omega_n) \right] \quad (\text{C.4})$$

where $f(\omega, \mu, T) = 1/(1 + \exp(\frac{\omega - \mu}{k_B T}))$ is the Fermi-Dirac distribution function, k_B the Boltzmann constant and the frequency integration is performed along a rectangular path surrounding the real frequency axis (which by symmetry arguments can be restricted to

the upper complex half-plane). This procedure was chosen because unlike integrating the DOS this particle number does not depend on the infinitesimal imaginary part of the frequency which strongly influences the fine structure of the DOS. The boundaries of the closed path have to be chosen large enough (far way from the "interesting region") such that the result does not depend anymore on these boundaries. This procedure has the disadvantage that for numerical reasons it has to be performed at finite temperature T because the zero temperature limit of $f(\omega, \mu, T)$, being just a step function $\theta(\omega - E_F)$, changes too abruptly for numerical integration and needs an extremely fine sampling. This temperature is an artificial electronic temperature and should not be confused with the thermodynamic temperature of the physical system which is beyond the scope of this work. The Fermi-Dirac distribution function exhibits equidistant poles on a vertical line parallel to the imaginary frequency axis cutting the real axis at the chemical potential μ with imaginary parts at the fermionic Matsubara frequencies $\omega_n = (2n + 1)\pi k_B T$, n being an integer. The expression for the particle number has to be corrected for these additional poles which is achieved by the second term. The chemical potential is then adjusted by an iterative bisection method until the true particle number, fixed by the constraint of a charge neutral alloy, is found within a certain accuracy. The chemical potential obtained in this way can, depending on the user's choice, be calculated at multiple temperatures. For one temperature the Fermi energy E_F is set identical to the chemical potential, for more than one temperatures at the moment E_F is obtained by a linear extrapolation to $T = 0$ from the chemical potentials at the highest and lowest temperature. Of course, higher order extrapolations could be implemented in the future.

The effective medium Green's function on a closed cycle as obtained by the subroutine `cpaCalcMedium` is also necessary for the A -coefficients appearing the charge self-consistency computed in the subroutine `cpa_calcDenA` which was described earlier in Secs. 2.3 and B.3. The actual integral expression Eq. (B.26) is similar to the particle number and carried out in the same way. The charge self-consistency is only carried out at one temperature which can be specified by the user.

Usually, apart from the angular integration involved in the orbital decomposition of the XC-potential, all numerical integrations in this work are performed by the Simpson method [68, 69, 77], being a summed second order Newton-Cotes formula [68, 69, 78, 79]. This works as follows

$$\int_a^b dx f(x) \approx \frac{h}{3} [f(x_0) + 4f(x_1) + 2f(x_2) + 4f(x_3) + \dots + 2f(x_{N-2}) + 4f(x_{N-1}) + f(x_N)] \quad (\text{C.5})$$

where $h = (b - a)/N$ and the interval $[a, b]$ was divided into N equidistant partial intervals centered around x_i and having a width of $2h$. In practical benchmark tests (an integration of \underline{ST} over the closed complex frequency path should always give the number of orbitals) this method turned out to be not sufficiently accurate for the frequency integration involved in the Fermi level calculation or charge self-consistency. Therefore, a higher order Newton-Cotes formula had to be used and the summed one of sixth order is given by the so-called Weddle rule [68, 69, 79]

$$\int_a^b dx f(x) \approx \frac{h}{840} \left[41f(x_0) + 216f\left(x_0 + \frac{h}{6}\right) + 27f\left(x_0 + \frac{2h}{6}\right) + 272\left(x_0 + \frac{3h}{6}\right) \right]$$

$$\begin{aligned}
&+27 \left(x_0 + \frac{4h}{6} \right) + 216f \left(x_0 + \frac{5h}{6} \right) + 41f(x_1) \\
&+41f(x_1) + 216f \left(x_1 + \frac{h}{6} \right) + \dots + 41f(x_N) \Big] \tag{C.6}
\end{aligned}$$

where $h = (b - a)/N$ and the number of sampling points N has to be dividable by six plus one. This integration method (taking into account the appropriate signs when following the closed path) is implemented in the `subroutine cpaComplexIntegrateBox`. The density of states and orbital projections are calculated in the `subroutine cpaDosPlot` via

$$\nu(\omega) = -\frac{2}{\pi} \text{Im Tr} \left[\int_{1.BZ} d^3k S(\mathbf{k}) \Gamma(\mathbf{k}, \omega^+) \right] \tag{C.7}$$

again using the central `subroutine cpaCycleEnergy` - this time not on a closed path but parallel to the real axis with a slightly complex frequency $\omega^+ = \omega + i\delta$. As mentioned before, the fine structure of the DOS strongly depends on δ which should not be chosen too small. This subroutine also provides the self-energy which is later needed in the calculation of the Bloch spectral function. For this self-energy, in most cases a smaller imaginary part δ than for the DOS has to be chosen in order to resolve the bands in \mathbf{k} -space.

Finally, the `subroutine cpaBandsAlongLine` calculates the Bloch spectral function via

$$A(\mathbf{k}, \omega) = -\frac{1}{\pi} \text{Im Tr} \left[\underline{S}(\mathbf{k}) \underline{\Gamma}(\mathbf{k}, \omega^+) \right] \tag{C.8}$$

along one direction in \mathbf{k} -space. The \mathbf{k} -mesh which has been used before throughout the program was a regular one suited for Brillouin zone integration. But here now a direction has to be discretized and in order to still use all the subroutines which do not perform a \mathbf{k} -summation, a new \mathbf{k} -mesh has to be generated. Therefore, all the \mathbf{k} -dependent quantities like offsite overlap, offsite Hamiltonian, mixing potential are deleted or deallocated. Then, they are recalculated on the new \mathbf{k} -mesh. This only works if the onsite terms of which at least parts cannot be calculated in absence of a regular \mathbf{k} -mesh were kept. As mentioned above, this was done for the self energy being an onsite quantity - due to the fact that in the CPA-solver a Brillouin zone integration is involved, here the usual procedure of determining the effective medium via the `subroutine cpaCycleEnergy` cannot be applied anymore. For that reason, $\underline{\Gamma}(\mathbf{k}, \omega^+)$ is calculated *without* any iterations from the charge self-consistent effective medium self-energy Σ . Finally, the projections of the spectral function on the subspace of the parent compound are performed as described in Sec. 5.3.2.

D. Green's functions in a nonorthogonal basis

The BEB-CPA method developed in this work uses a nonorthogonal LCAO basis with respect to which in particular the Green's functions are defined. This causes some peculiarities which are not contained in the standard textbooks on many body theory. Due to the fact that I was lacking of a coherent review about this topic, when I developed the program, I decided to summarize the essential facts in this chapter. Some of the symbolism can be found for example in the papers of Stollhoff, Heilingbrunner, Horsch and Fulde, e.g. [72, 73].

D.1. Local basis and field operators

We start from the same set of orbitals $\phi_i(\mathbf{r})$ as already defined in Sec. B.1.1 which are nonorthogonal

$$\langle i|j\rangle = \int d^3r \phi_i^*(\mathbf{r})\phi_j(\mathbf{r}) = S_{i,j} \quad (\text{D.1})$$

where i, j are combined orbital and site indices and S is the overlap matrix. The unit operator in such a basis is given via

$$\mathbf{1} = \sum_{i,j} |i\rangle S_{i,j}^{-1} \langle j| \quad (\text{D.2})$$

where in the whole chapter the shorthand notation $S_{i,j}^{-1} = (S^{-1})_{i,j}$ denotes the (i, j) th element of the inverse overlap matrix unless mentioned otherwise. The fermionic field operators $\psi^\dagger(\mathbf{r})$ ($\psi(\mathbf{r})$) which create (annihilate) an electron at position \mathbf{r} then are given by

$$\psi^\dagger(\mathbf{r}) = \sum_i \phi_i^*(\mathbf{r}) c_i^\dagger \quad \psi(\mathbf{r}) = \sum_i \phi_i(\mathbf{r}) c_i \quad (\text{D.3})$$

where the fermionic, second quantized operators c_i^\dagger, c_i are hermitian conjugates of each other but unlike the usual orthogonal case are *no* creation and annihilation operators anymore! The commutation relations of the field operators are defined as in the orthogonal case

$$\{\psi(\mathbf{r}), \psi^\dagger(\mathbf{r}')\} = \delta(\mathbf{r} - \mathbf{r}') \quad (\text{D.4})$$

where $\{A, B\} = AB + BA$ denotes an anticommutator and $\delta(\mathbf{r} - \mathbf{r}')$ is the Dirac delta distribution. From this requirement the commutation relations of the c_i can be derived to be

$$\{c_i, c_j^\dagger\} = S_{i,j}^{-1} \quad (\text{D.5})$$

Another set of second quantized fermionic operators a_i^\dagger (a_i) can be defined which really create (annihilate) an electron in state i

$$a_i^\dagger|0\rangle = |i\rangle \quad (\text{D.6})$$

where $|0\rangle$ is the vacuum state. Also these operators are hermitian conjugates. Evaluating the vacuum expectation value of the anticommutator and using Eq. (D.6) yields the commutation relations

$$\{a_i, a_j^\dagger\} = S_{i,j} \quad (\text{D.7})$$

which reduces to $\delta_{i,j}$ for an orthonormal basis. With these a_i operators no field operators can be defined anymore because Eq. (D.4) then would not be fulfilled anymore. But via the commutation relations these two sets of second quantized operators can be converted into each other

$$c_i = \sum_j S_{i,j}^{-1} a_j \quad (\text{D.8})$$

D.2. Bloch basis and field operators

For the calculation of quantities which exhibit the translational symmetry of the lattice it is useful to perform a superposition to Bloch orbitals

$$\phi_{i,\mathbf{k}}(\mathbf{r}) = \frac{1}{(2\pi)^{3/2}} \sum_L e^{i\mathbf{k}(\mathbf{R}_L+\mathbf{R}_i)} \phi_i(\mathbf{r} - \mathbf{R}_L) = \frac{1}{(2\pi)^{3/2}} \sum_L e^{i\mathbf{k}(\mathbf{R}_L+\mathbf{R}_i)} \phi_{iL}(\mathbf{r}) \quad (\text{D.9})$$

or

$$|i\mathbf{k}\rangle = \frac{1}{(2\pi)^{3/2}} \sum_L e^{i\mathbf{k}(\mathbf{R}_L+\mathbf{R}_i)} |iL\rangle \quad (\text{D.10})$$

where L indicates lattice vectors. With these Bloch orbitals, the matrix elements of a translational invariant operator A (e.g. the offsite Hamiltonian and overlap matrix in Chap. B) in \mathbf{k} -space

$$A_{i,j}(\mathbf{k}) = \frac{1}{(2\pi)^3} e^{-i\mathbf{k}(\mathbf{R}_i-\mathbf{R}_j)} \sum_L e^{-i\mathbf{k}\mathbf{R}_L} A_{Li,j} \quad (\text{D.11})$$

can be written in the form

$$\langle i\mathbf{k} | \hat{A} | j \rangle = (2\pi)^{3/2} e^{-i\mathbf{k}\mathbf{R}_j} A_{i,j}(\mathbf{k}) \quad (\text{D.12})$$

Also for the Bloch orbitals it is useful to define field operators

$$\psi_{\mathbf{k}}(\mathbf{r}) = \frac{1}{(2\pi)^{3/2}} \sum_L e^{-i\mathbf{k}\mathbf{R}_L} \psi(\mathbf{r} - \mathbf{R}_L) \equiv \sum_i \phi_{i\mathbf{k}}(\mathbf{r}) c_{i\mathbf{k}} \quad (\text{D.13})$$

where

$$\{\psi_{\mathbf{k}}(\mathbf{r}), \psi_{\mathbf{k}'}^\dagger(\mathbf{r}')\} = \delta_{\mathbf{k},\mathbf{k}'} \delta(\mathbf{r} - \mathbf{r}') \quad (\text{D.14})$$

from which again it can be derived that

$$\{c_{i\mathbf{k}}, c_{j\mathbf{k}'}^\dagger\} = \delta_{\mathbf{k},\mathbf{k}'} S_{i,j}^{-1}(\mathbf{k}) \quad (\text{D.15})$$

Also here, a set of creation and annihilation operators can be defined

$$a_{i\mathbf{k}}^\dagger|0\rangle = |i\mathbf{k}\rangle \quad \{a_{i\mathbf{k}}, a_{j\mathbf{k}'}^\dagger\} = \delta_{\mathbf{k},\mathbf{k}'} S_{i,j}(\mathbf{k}) \quad (\text{D.16})$$

and the two sets of second quantized operators are related to each other via

$$c_{i\mathbf{k}} = \sum_j S_{i,j}^{-1}(\mathbf{k}) a_{j\mathbf{k}} \quad (\text{D.17})$$

D.3. Retarded Green's function

We define the retarded, time dependent Green's function in the usual way by creation and annihilation operators

$$G_{i,j}(t) = -i\theta(t) \langle 0 | \{a_i(t), a_j^\dagger\} | 0 \rangle \quad (\text{D.18})$$

where $\theta(t)$ is the Heaviside step function. Due to the fact that in this work only noninteracting electronic Green's functions are considered, it is sufficient to take the vacuum expectation value here which will make life easier later in the derivation. The time dependent operators $a_i(t)$ are given in the Heisenberg picture

$$a_i(t) = e^{i\hat{H}t} a_i e^{-i\hat{H}t} \quad a_i = a_i(t=0) \quad a_j^\dagger = a_j^\dagger(t=0) \quad (\text{D.19})$$

where \hat{H} is the full Hamiltonian *operator* of the problem. As is well known from standard textbooks like [74] we assume that the eigenvalue problem of Hamiltonian operator \hat{H} is solved

$$\hat{H}|n\rangle = \epsilon_n|n\rangle \quad \sum_n |n\rangle\langle n| = \mathbf{1} \quad (\text{D.20})$$

and we can always find an orthogonal eigenbasis $|n\rangle$ with eigenvalues ϵ_n . Furthermore, we choose the vacuum energy to be zero $\hat{H}|0\rangle = 0$. We now insert two $\mathbf{1}$ into Eq. (D.18)

$$G_{i,j}(t) = -i\theta(t) \sum_n \langle 0 | e^{i\hat{H}t} a_i e^{-i\hat{H}t} |n\rangle \langle n| a_j^\dagger + a_j^\dagger e^{i\hat{H}t} |n\rangle \langle n| a_i^{-i\hat{H}t} | 0 \rangle \quad (\text{D.21})$$

$$= -i\theta(t) \left(\sum_n e^{-i\epsilon_n t} \langle 0 | a_i |n\rangle \langle n | a_j^\dagger | 0 \rangle + \sum_n e^{i\epsilon_n t} \langle 0 | a_j^\dagger |n\rangle \langle n | a_i | 0 \rangle \right) \quad (\text{D.22})$$

$$= -i\theta(t) \sum_n e^{-i\epsilon_n t} \langle 0 | a_i |n\rangle \langle n | a_j^\dagger | 0 \rangle \quad (\text{D.23})$$

Later we are interested in the Fourier transformation

$$G_{i,j}(\omega) = \int dt e^{i\omega t} G_{i,j}(t) \quad (\text{D.24})$$

$$= \sum_n \left\langle 0 \left| a_i \frac{|n\rangle\langle n|}{\omega + i\delta - \epsilon_n} a_j^\dagger \right| 0 \right\rangle \quad (\text{D.25})$$

This is nothing but the spectral representation of the resolvent operator $\hat{G}(\omega)$

$$G_{i,j}(\omega) = \langle 0 | a_i \hat{G}^R(\omega) a_j^\dagger | 0 \rangle = \langle i | \hat{G}(\omega) | j \rangle \quad \hat{G}(\omega) = (\omega + i\delta - \hat{H})^{-1} \quad (\text{D.26})$$

To further proceed, consider the matrix elements of the inverse of the resolvent operator

$$\langle i | \hat{G}^{-1}(\omega) | j \rangle = \langle i | \omega + i\delta - \hat{H} | j \rangle = S_{i,j}(\omega + i\delta) - H_{i,j} \quad (\text{D.27})$$

where the Hamiltonian *matrix* $H_{i,j} = \langle i | \hat{H} | j \rangle$ was introduced. Clearly, the following relation has to be fulfilled

$$\langle i | \hat{G}^{-1}(\omega) \hat{G}(\omega) | j \rangle = S_{i,j} \quad (\text{D.28})$$

Introduction of a $\mathbf{1}$ by Eq. (D.2) and use of Eq. (D.27) yields

$$\sum_{i',j'} [(\omega + i\delta)S - H]_{i,i'} S_{i',j'}^{-1} G_{j',j}(\omega) = S_{i,j} \quad (\text{D.29})$$

Solving this matrix equation for G finally yields the Green's function matrix elements

$$G_{i,j}(\omega) = S [(\omega + i\delta)S - H]^{-1} S \Big|_{i,j} \equiv S\mathcal{G}(\omega)S \Big|_{i,j} \quad (\text{D.30})$$

with the conventions for G and \mathcal{G} used several times in this thesis. When calculating an observable from the Green's function in a nonorthogonal basis, one has always to take care about how it is expressed in the second quantized operators to find out, which of the Green's function G or \mathcal{G} to be used.

For the important case of the density of states (DOS), this is

$$\nu(\omega) = -\frac{1}{\pi} \text{Im} \sum_i (G(\omega)S^{-1})_{i,i} = -\frac{1}{\pi} \text{Im} \sum_i [S\mathcal{G}(\omega)]_{i,i} \quad (\text{D.31})$$

which can be verified by inserting the spectral representation Eq. (D.25) which finally yields $\sum_n \delta(\omega - \epsilon_n)$ which is just the definition of the DOS.

For the Green's function in real space we can write

$$G(\mathbf{r}, \mathbf{r}', \omega) = \int dt e^{i\omega t} G(\mathbf{r}, \mathbf{r}', t) = \int dt e^{i\omega t} \langle 0 | \{ \psi(\mathbf{r}, t), \psi^\dagger(\mathbf{r}', 0) \} | 0 \rangle \quad (\text{D.32})$$

Using our initially defined field operators and choosing the same route as before (inserting a set of eigenstates of \hat{H}) yields

$$G(\mathbf{r}, \mathbf{r}', \omega) = \langle 0 | \psi(\mathbf{r}) \hat{G}(\omega) \psi^\dagger(\mathbf{r}') | 0 \rangle = \sum_{i,j} \phi_i(\mathbf{r}) \mathcal{G}_{i,j}(\omega) \phi_j^*(\mathbf{r}') \quad (\text{D.33})$$

which is just the expression used for the charge self-consistency.

D.4. Bloch spectral function

The Bloch spectral function is usually defined as

$$A(\mathbf{k}, \omega) = -\frac{1}{\pi} \text{Im} G(\mathbf{k}, \omega) \quad (\text{D.34})$$

where

$$G(\mathbf{k}, \omega) = \frac{1}{(2\pi)^{3/2}} \sum_L e^{-ik\mathbf{R}_L} \int d^3r G(\mathbf{r} - \mathbf{R}_L, \omega) \quad (\text{D.35})$$

where again L indicates lattice vectors. This can be rewritten using the field operators

$$G(\mathbf{k}, \omega) = \frac{1}{(2\pi)^{3/2}} \sum_L \int d^3 r e^{-i\mathbf{k}\mathbf{R}_L} \langle 0 | \psi(\mathbf{r} - \mathbf{R}_L) \hat{G}(\omega) \psi^\dagger(\mathbf{r}) | 0 \rangle \quad (\text{D.36})$$

$$= \int d^3 r \langle 0 | \psi_{\mathbf{k}}(\mathbf{r}) \hat{G}(\omega) \psi^\dagger(\mathbf{r}) | 0 \rangle \quad (\text{D.37})$$

where we have a field operator for the Bloch basis on the left side and a normal field operator on the right side. This can be further simplified

$$G(\mathbf{k}, \omega) = \int d^3 r \sum_{i,j} \phi_{i\mathbf{k}}(\mathbf{r}) \phi_j^*(\mathbf{r}) \langle 0 | c_{i\mathbf{k}} \hat{G}(\omega) c_j^\dagger | 0 \rangle \quad (\text{D.38})$$

$$= (2\pi)^{3/2} \sum_{ij} e^{i\mathbf{k}\mathbf{R}_j} S_{j,i}(\mathbf{k}) \langle 0 | c_{i\mathbf{k}} \hat{G}(\omega) c_j^\dagger | 0 \rangle \quad (\text{D.39})$$

Transformation of the c operators to the a operators by Eqs. (D.8) and (D.17) this finally yields

$$G(\mathbf{k}, \omega) = (2\pi)^{3/2} \sum_{ij} e^{i\mathbf{k}\mathbf{R}_i} \underbrace{\langle i\mathbf{k} | \hat{G}(\omega) | j \rangle}_{=(2\pi)^{3/2} e^{-i\mathbf{k}\mathbf{R}_j} G_{i,j}(\mathbf{k}, \omega)} S_{i,j}^{-1} \quad (\text{D.40})$$

With the same logic as before starting from $\langle i\mathbf{k} | \hat{G}^{-1} \hat{G} | j \rangle$ we obtain

$$G_{i,j}(\mathbf{k}, \omega) = S(\mathbf{k}) [(\omega + i\delta)S(\mathbf{k}) - H(\mathbf{k})]^{-1} S(\mathbf{k}) \Big|_{i,j} = S(\mathbf{k}) \mathcal{G}(\mathbf{k}, \omega) S(\mathbf{k}) \Big|_{i,j} \quad (\text{D.41})$$

Inserting this into Eq. (D.40) finally yields after some manipulations

$$G(\mathbf{k}, \omega) = \sum_i [S(\mathbf{k}) \mathcal{G}(\mathbf{k}, \omega)]_{i,i} \quad (\text{D.42})$$

which is the expression referred to in the rest of this work for the calculation of a Bloch spectral function.

List of Figures

2.1. Cartoon of the CPA condition after [57]	15
2.2. Schematic working flow of the ab-initio program	30
3.1. Total DOS for simple model within CPA vs. Lanczos for several onsite energies	32
3.2. Total DOS for simple model within CPA vs. Lanczos for several concentrations	33
3.3. Fano lineshapes from [83]	33
3.4. Total DOS for simple model within CPA vs. Lanczos, clusters removed . . .	34
3.5. Total DOS for simple model BEB-CPA vs. Lanczos for various species diagonal hoppings	35
4.1. Randomly occupied bcc and sc structures, ordered sc CuZn compound . . .	37
4.2. Radial basis functions for $\text{Cu}_{1-x}\text{Zn}_x$ -alloys	39
4.3. Bandstructures for Cu, DFT vs. LCAO-fit	39
4.4. Density of states of pure Cu (left) and pure Zn (right) obtained within the CPA (red) after one charge iteration against DFT (black)	40
4.5. Total DOS of ordered CuZn vs. disordered $\text{Cu}_{0.5}\text{Zn}_{0.5}$ vs. [18]	41
4.6. Densities of states of disordered $\text{Cu}_{1-x}\text{Zn}_x$ obtained after one charge iteration for several compositions	42
4.7. Bloch spectral function of disordered $\text{Cu}_{0.5}\text{Zn}_{0.5}$	43
4.8. Orbital projected Bloch spectral function of disordered $\text{Cu}_{0.5}\text{Zn}_{0.5}$	44
4.9. Crystal structure of partially substituted CuZn alloy	44
4.10. Total DOS of partially substituted CuZn alloy	45
5.1. Crystal structures of four most prominent families of FeSC, from [94]	49
5.2. Crystal structure of BaFe_2As_2 , from [96]	49
5.3. Compilation of temperature - substitution phase diagrams for BaFe_2As_2 , from [26]	50
5.4. Fermi surface of BaFe_2As_2 , from [98]	51
5.5. Temperature - substitution / doping phase diagram for TM substituted BaFe_2As_2 , from [28]	52
5.6. Radial wavefunctions for Ba, Fe and As	55
5.7. Bandstructure of BaFe_2As_2 DFT vs. LCAO-fit	56
5.8. Bandstructure of BaFe_2As_2 DFT vs. CPA	56
5.9. Total DOS of $\text{Ba}(\text{Fe}_{0.9}\text{Zn}_{0.1})_2\text{As}_2$, charge self-consistency	57
5.10. Total DOS of BaFe_2As_2 vs. $\text{Ba}(\text{Fe}_{0.9}\text{TM}_{0.1})_2\text{As}_2$	59
5.11. Orbital, <i>TM</i> -projected DOS for $l = 2$ of $\text{Ba}(\text{Fe}_{0.9}\text{TM}_{0.1})_2\text{As}_2$	60
5.12. Bloch spectral function of $\text{Ba}(\text{Fe}_{0.9}\text{Ni}_{0.1})_2\text{As}_2$ and band projections	62
5.13. Fermi surface of BaFe_2As_2 in $(\mathbf{k}_x, \mathbf{k}_y)$ plane at $\mathbf{k}_z = 0$	64
5.14. Orbital composition of band eigenvectors	65

5.15. Orientation of d -orbitals, from [112]	66
5.16. Band shifts for TM substitution	67
5.17. Spectral broadenings for TM substitution	69
5.18. Total DOS for Ni, Pd and Pt substitution	70
5.19. Orbital, TM projected DOS for $l = 2$ for Ni, Pd and Pt substitution	70
5.20. Bandshifts for Ni, Pd and Pt substitution	72
5.21. Spectral broadenings for Ni, Pd and Pt substitution	73
5.22. Bandshifts for K and P substitution	74
5.23. Spectral broadenings for K and P substitution	75
5.24. Slopes of level shifts against substituent	76
5.25. Slopes of spectral broadenings against substituent	77
5.26. Intra- / interband scattering rate on Fermi surface for Co substitution	84
5.27. Intra- / Interband scattering rates averaged over \mathbf{k} against substituent	86
5.28. Intra- / interband scattering rate on Fermi surface for Co substitution, reduced to 3 bands	88
5.29. Intra- / interband scattering rates reduced to 3 bands averaged over \mathbf{k} against substituent	89

Bibliography

- [1] P. Soven, “Coherent-Potential Model of Substitutional Disordered Alloys,” Phys. Rev. **156**, 809–813 (1967).
- [2] D. W. Taylor, “Vibrational Properties of Imperfect Crystals with Large Defect Concentrations,” Phys. Rev. **156**, 1017–1029 (1967).
- [3] R. J. Elliott, J. A. Krumhansl, and P. L. Leath, “The theory and properties of randomly disordered crystals and related physical systems,” Rev. Mod. Phys. **46**, 465–543 (1974).
- [4] J. A. Blackman, D. M. Esterling, and N. F. Berk, “Generalized Locator-Coherent-Potential Approach to Binary Alloys,” Phys. Rev. B **4**, 2412–2428 (1971).
- [5] P. Hohenberg and W. Kohn, “Inhomogeneous Electron Gas,” Phys. Rev. **136**, B864–B871 (1964).
- [6] W. Kohn and L. J. Sham, “Self-Consistent Equations Including Exchange and Correlation Effects,” Phys. Rev. **140**, A1133–A1138 (1965).
- [7] D. Vanderbilt, “Optimally smooth norm-conserving pseudopotentials,” Phys. Rev. B **32**, 8412–8415 (1985).
- [8] S. G. Louie, K.-M. Ho, and M. L. Cohen, “Self-consistent mixed-basis approach to the electronic structure of solids,” Phys. Rev. B **19**, 1774–1782 (1979).
- [9] B. Meyer, F. Lechermann, C. Elsässer, and M. Fähnle, “Fortran90 Program for Mixed-Basis Pseudopotential Calculations for Crystals,” Max-Planck-Institut für Metallforschung, Stuttgart (unpublished).
- [10] B. Meyer, *Entwicklung eines neuen ab-initio "mixed-basis"-Pseudopotentialprogrammes und Untersuchung atomarer Fehlstellen in Molybdän und intermetallischen Verbindungen* (Cuvillier Verlag Göttingen, 1999), Dissertation.
- [11] K. Koepf, B. Velický, R. Hayn, and H. Eschrig, “Self-consistent LCAO-CPA method for disordered alloys,” Phys. Rev. B **55**, 5717–5729 (1997).
- [12] J. Korringa, “On the calculation of the energy of a Bloch wave in a metal,” Physica **13**, 392 – 400 (1947).
- [13] W. Kohn and N. Rostoker, “Solution of the Schrödinger Equation in Periodic Lattices with an Application to Metallic Lithium,” Phys. Rev. **94**, 1111–1120 (1954).
- [14] A. Bansil, L. Schwartz, and H. Ehrenreich, “Electronic structure of disordered CuNi alloys,” Phys. Rev. B **12**, 2893–2907 (1975).

- [15] G. M. Stocks, W. M. Temmerman, and B. L. Gyorffy, “Complete Solution of the Korringa-Kohn-Rostoker Coherent-Potential-Approximation Equations: Cu-Ni Alloys,” *Phys. Rev. Lett.* **41**, 339–343 (1978).
- [16] G. M. Stocks and H. Winter, “Self-consistent-field-Korringa-Kohn-Rostoker-coherent-potential approximation for random alloys,” *Zeitschrift für Physik B Condensed Matter* **46**, 95–98 (1982).
- [17] H. Winter and G. M. Stocks, “Calculation of self-consistent potentials for substitutionally disordered systems with application to the $\text{Ag}_x - \text{Pd}_{1-x}$ alloy series,” *Phys. Rev. B* **27**, 882–904 (1983).
- [18] D. A. Rowlands, J. B. Staunton, B. L. Györffy, E. Bruno, and B. Ginatempo, “Effects of short-range order on the electronic structure of disordered metallic systems,” *Phys. Rev. B* **72**, 045101 (2005).
- [19] D. A. Rowlands, “Short-range correlations in disordered systems: nonlocal coherent-potential approximation,” *Reports on Progress in Physics* **72**, 086501 (2009).
- [20] Y. Kamihara, T. Watanabe, M. Hirano, , and H. Hosono, “Iron-Based Layered Superconductor $\text{LaO}_{1-x}\text{F}_x\text{FeAs}$ ($x = 0.05-0.12$) with $T_c = 26$ K,” *Journal of the American Chemical Society* **130**, 3296–3297 (2008), pMID: 18293989.
- [21] R. Zhi-An, L. Wei, Y. Jie, Y. Wei, S. Xiao-Li, Zheng-Cai, C. Guang-Can, D. Xiao-Li, S. Li-Ling, Z. Fang, and Z. Zhong-Xian, “Superconductivity at 55 K in Iron-Based F-Doped Layered Quaternary Compound $\text{SmO}_{1-x}\text{F}_x\text{FeAs}$,” *Chinese Physics Letters* **25**, 2215 (2008).
- [22] W. Meissner and R. Ochsenfeld, “Ein neuer Effekt bei Eintritt der Supraleitfähigkeit,” *Naturwissenschaften* **21**, 787–788 (1933).
- [23] F. Hardy, P. Burger, T. Wolf, R. A. Fisher, P. Schweiss, P. Adelman, R. Heid, R. Fromknecht, R. Eder, D. Ernst, H. v. Löhneysen, and C. Meingast, “Doping evolution of superconducting gaps and electronic densities of states in $\text{Ba}(\text{Fe}_{1-x}\text{Co}_x)_2\text{As}_2$ iron pnictides,” *EPL (Europhysics Letters)* **91**, 47008 (2010).
- [24] N. Ni, A. Thaler, J. Q. Yan, A. Kracher, E. Colombier, S. L. Bud’ko, P. C. Canfield, and S. T. Hannahs, “Temperature versus doping phase diagrams for $\text{Ba}(\text{Fe}_{1-x}\text{TM}_x)_2\text{As}_2$ (TM = Ni, Cu, Cu/Co) single crystals,” *Phys. Rev. B* **82**, 024519 (2010).
- [25] A. E. Böhmer, P. Burger, F. Hardy, T. Wolf, P. Schweiss, R. Fromknecht, H. v. Löhneysen, C. Meingast, H. K. Mak, R. Lortz, S. Kasahara, T. Terashima, T. Shibauchi, and Y. Matsuda, “Thermodynamic phase diagram, phase competition, and uniaxial pressure effects in $\text{BaFe}_2(\text{As}_{1-x}\text{P}_x)_2$ studied by thermal expansion,” *Phys. Rev. B* **86**, 094521 (2012).
- [26] A. E. Böhmer, *Competing Phases in Iron-Based Superconductors Studied by High-Resolution Thermal-Expansion and Shear-Modulus Measurements*, Ph.D. thesis (2014), Karlsruhe, KIT, Diss., 2014.

-
- [27] R. M. Fernandes, A. V. Chubukov, and J. Schmalian, “What drives nematic order in iron-based superconductors?” *Nature Physics* **10**, 97–104 (2014).
- [28] P. C. Canfield, S. L. Bud’ko, N. Ni, J. Q. Yan, and A. Kracher, “Decoupling of the superconducting and magnetic/structural phase transitions in electron-doped BaFe_2As_2 ,” *Phys. Rev. B* **80**, 060501 (2009).
- [29] C. Liu, T. Kondo, R. Fernandes, A. Palczewski, E. Mun, N. Ni, A. Thaler, A. Bostwick, E. Rothenberg, J. Schmalian, S. Bud’ko, P. Canfield, and A. Kaminski, “Evidence for a Lifshitz transition in electron-doped iron arsenic superconductors at the onset of superconductivity,” *Nat. Phys.* **6**, 419 (2010).
- [30] M. Neupane, P. Richard, Y.-M. Xu, K. Nakayama, T. Sato, T. Takahashi, A. V. Federov, G. Xu, X. Dai, Z. Fang, Z. Wang, G.-F. Chen, N.-L. Wang, H.-H. Wen, and H. Ding, “Electron-hole asymmetry in the superconductivity of doped BaFe_2As_2 seen via the rigid chemical-potential shift in photoemission,” *Phys. Rev. B* **83**, 094522 (2011).
- [31] E. M. Bittar, C. Adriano, T. M. Garitezi, P. F. S. Rosa, L. Mendonça Ferreira, F. Garcia, G. d. M. Azevedo, P. G. Pagliuso, and E. Granado, “Co-Substitution Effects on the Fe Valence in the BaFe_2As_2 Superconducting Compound: A Study of Hard X-Ray Absorption Spectroscopy,” *Phys. Rev. Lett.* **107**, 267402 (2011).
- [32] M. Merz, F. Eilers, T. Wolf, P. Nagel, H. v. Löhneysen, and S. Schuppler, “Electronic structure of single-crystalline $\text{Sr}(\text{Fe}_{1-x}\text{Co}_x)_2\text{As}_2$ probed by x-ray absorption spectroscopy: Evidence for effectively isovalent substitution of Fe^{2+} by Co^{2+} ,” *Phys. Rev. B* **86**, 104503 (2012).
- [33] A. A. Golubov and I. I. Mazin, “Effect of magnetic and nonmagnetic impurities on highly anisotropic superconductivity,” *Phys. Rev. B* **55**, 15146–15152 (1997).
- [34] I. I. Mazin, D. J. Singh, M. D. Johannes, and M. H. Du, “Unconventional Superconductivity with a Sign Reversal in the Order Parameter of $\text{LaFeAsO}_{1-x}\text{F}_x$,” *Phys. Rev. Lett.* **101**, 057003 (2008).
- [35] J. Zhang, R. Sknepnek, R. M. Fernandes, and J. Schmalian, “Orbital coupling and superconductivity in the iron pnictides,” *Phys. Rev. B* **79**, 220502 (2009).
- [36] R. Sknepnek, G. Samolyuk, Y.-B. Lee, and J. Schmalian, “Anisotropy of the pairing gap of FeAs-based superconductors induced by spin fluctuations,” *Phys. Rev. B* **79**, 054511 (2009).
- [37] A. B. Vorontsov, M. G. Vavilov, and A. V. Chubukov, “Superfluid density and penetration depth in the iron pnictides,” *Phys. Rev. B* **79**, 140507 (2009).
- [38] J. Bardeen, L. N. Cooper, and J. R. Schrieffer, “Theory of Superconductivity,” *Phys. Rev.* **108**, 1175–1204 (1957).
- [39] W. Metzner and D. Vollhardt, “Correlated Lattice Fermions in $d = \infty$ Dimensions,” *Phys. Rev. Lett.* **62**, 324–327 (1989).
- [40] A. Georges and G. Kotliar, “Hubbard model in infinite dimensions,” *Phys. Rev. B* **45**, 6479–6483 (1992).

- [41] A. Georges, G. Kotliar, W. Krauth, and M. J. Rozenberg, “Dynamical mean-field theory of strongly correlated fermion systems and the limit of infinite dimensions,” *Rev. Mod. Phys.* **68**, 13–125 (1996).
- [42] A. Herbig, “Ab-Initio-Berechnung von elektronischen Eigenschaften und Gitterdynamik von Arsen und Eisen-Arsenid,” Diploma Thesis, Institut für Festkörperphysik, Karlsruher Institut für Technologie (unpublished).
- [43] M. Born and R. Oppenheimer, “Zur Quantentheorie der Molekeln,” *Annalen der Physik* **389**, 457–484 (1927).
- [44] H. Hellmann, “A New Approximation Method in the Problem of Many Electrons,” *The Journal of Chemical Physics* **3**, 61–61 (1935).
- [45] R. Heid and K.-P. Bohnen, “Linear response in a density-functional mixed-basis approach,” *Phys. Rev. B* **60**, R3709–R3712 (1999).
- [46] B. Amadon, F. Lechermann, A. Georges, F. Jollet, T. O. Wehling, and A. I. Lichtenstein, “Plane-wave based electronic structure calculations for correlated materials using dynamical mean-field theory and projected local orbitals,” *Phys. Rev. B* **77**, 205112 (2008).
- [47] J. Bednorz and K. Müller, “Possible high T_c superconductivity in the Ba–La–Cu–O system,” *Zeitschrift für Physik B Condensed Matter* **64**, 189–193 (1986).
- [48] W. Ku, T. Berlijn, and C.-C. Lee, “Unfolding First-Principles Band Structures,” *Phys. Rev. Lett.* **104**, 216401 (2010).
- [49] T. Berlijn, C.-H. Lin, W. Garber, and W. Ku, “Do Transition-Metal Substitutions Dope Carriers in Iron-Based Superconductors?” *Phys. Rev. Lett.* **108**, 207003 (2012).
- [50] R. H. Parmenter, “Energy Levels of a Disordered Alloy,” *Phys. Rev.* **97**, 587–598 (1955).
- [51] O. De la Peña Seaman, R. de Coss, R. Heid, and K.-P. Bohnen, “Effects of al and c doping on the electronic structure and phonon renormalization in mgb₂,” *Phys. Rev. B* **79**, 134523 (2009).
- [52] O. De la Peña Seaman, R. de Coss, R. Heid, and K.-P. Bohnen, “Electron-phonon coupling and two-band superconductivity of Al- and C-doped MgB₂,” *Phys. Rev. B* **82**, 224508 (2010).
- [53] J. Faulkner, “The Modern Theory of Alloys,” *Prog. Mat. Sci.* **27**, 1–& (1982).
- [54] J. Korringa, “Dispersion theory for electrons in a random lattice with applications to the electronic structure of alloys,” *Journal of Physics and Chemistry of Solids* **7**, 252 – 258 (1958).
- [55] J. L. Beeby and S. F. Edwards, “The Electronic Structure of Liquid Insulators,” *Proceedings of the Royal Society of London A: Mathematical, Physical and Engineering Sciences* **274**, 395–412 (1963).
- [56] J. L. Beeby, “Electronic Structure of Alloys,” *Phys. Rev.* **135**, A130–A143 (1964).

-
- [57] H. Shiba, “A Reformulation of the Coherent Potential Approximation and Its Applications,” *Progress of Theoretical Physics* **46**, 77–94 (1971).
- [58] F. Brouers, M. Cyrot, and F. Cyrot-Lackman, “Bethe-Peierls Approximation in the Electronic Theory of Disordered Materials,” *Phys. Rev. B* **7**, 4370–4373 (1973).
- [59] P. L. Leath, “Equivalence of Expanding in Localized or Bloch States in Disordered Alloys,” *Phys. Rev. B* **2**, 3078–3087 (1970).
- [60] T. Matsubara and Y. Toyozawa, “Theory of Impurity Band Conduction in Semiconductors: An Approach to Random Lattice Problem,” *Progress of Theoretical Physics* **26**, 739–756 (1961).
- [61] M. Tsukada, “Contribution to the Many Site Theory of the Disordered System,” *Journal of the Physical Society of Japan* **32**, 1475–1485 (1972).
- [62] M. Jarrell and H. R. Krishnamurthy, “Systematic and causal corrections to the coherent potential approximation,” *Phys. Rev. B* **63**, 125102 (2001).
- [63] A. N. Rubtsov, M. I. Katsnelson, and A. I. Lichtenstein, “Dual fermion approach to nonlocal correlations in the Hubbard model,” *Phys. Rev. B* **77**, 033101 (2008).
- [64] H. Terletska, S.-X. Yang, Z. Y. Meng, J. Moreno, and M. Jarrell, “Dual fermion method for disordered electronic systems,” *Phys. Rev. B* **87**, 134208 (2013).
- [65] A. Gonis and J. W. Garland, “Rederivation and proof of analyticity of the Blackman-Esterling-Berk approximation,” *Phys. Rev. B* **16**, 1495–1502 (1977).
- [66] D. Sanchez-Portal, E. Artacho, and J. M. Soler, “Projection of plane-wave calculations into atomic orbitals,” *Solid State Comm.* **95**, 685 – 690 (1995).
- [67] D. Sánchez-Portal, E. Artacho, and J. M. Soler, “Analysis of atomic orbital basis sets from the projection of plane-wave results,” *J. Phys. Cond. Mat.* **8**, 3859 (1996).
- [68] J. B. Scarborough, *Numerical Mathematical Analysis* (The Johns Hopkins Press, Baltimore, 1966).
- [69] J. Stoer, *Numerische Mathematik 1* (Springer-Verlag Berlin Heidelberg New York, 1999).
- [70] C. G. J. Jacobi, “Ueber Gaußs neue Methode, die Werthe der Integrale näherungsweise zu finden,” *Journal für die reine und angewandte Mathematik* **1**, 301 (1826).
- [71] “<https://pomax.github.io/bezierinfo/legendre-gauss.html>,” .
- [72] P. Horsch and P. Fulde, “On the theory of electronic correlations in solids,” *Zeitschrift für Physik B Condensed Matter* **36**, 23–35 (1979).
- [73] G. Stollhoff and A. Heilingbrunner, “Coupled-cluster-equations for the local ansatz,” *Zeitschrift für Physik B Condensed Matter* **83**, 85–91 (1991).
- [74] A. A. Abrikosov, L. P. Gorkov, and I. E. Dzyaloshinski, *Methods of quantum field theory in statistical physics* (Dover Publications, Inc., New York, 1969).

- [75] K. Koepnick, B. Velický, R. Hayn, and H. Eschrig, “Analytic properties and accuracy of the generalized Blackman-Esterling-Berk coherent-potential approximation,” *Phys. Rev. B* **58**, 6944–6962 (1998).
- [76] D. D. Johnson, “Modified Broyden’s method for accelerating convergence in self-consistent calculations,” *Phys. Rev. B* **38**, 12807–12813 (1988).
- [77] “https://en.wikipedia.org/wiki/Simpson's_rule,” .
- [78] “https://en.wikipedia.org/wiki/Newton-Cotes_formulas,” ().
- [79] “<https://de.wikipedia.org/wiki/Newton-Cotes-Formeln>,” ().
- [80] R. Eder, (2013), Private communication: program for exact diagonalization, Institut für Festkörperphysik, Karlsruhe.
- [81] C. Lanczos, “An Iteration Method for the Solution of the Eigenvalue Problem of Linear Differential and Integral Operators,” *Journal of Research of the National Bureau of Standards* **45**, 255 (1950).
- [82] J. D. Hunter, “Matplotlib: A 2D graphics environment,” *Comput. Sci. Eng.* **9**, 90–95 (2007).
- [83] U. Fano, “Effects of Configuration Interaction on Intensities and Phase Shifts,” *Phys. Rev.* **124**, 1866–1878 (1961).
- [84] “<https://en.wikipedia.org/wiki/Brass>,” .
- [85] H. J. Monkhorst and J. D. Pack, “Special points for Brillouin-zone integrations,” *Phys. Rev. B* **13**, 5188–5192 (1976).
- [86] R. Heid, (2014), Private communication: pseudopotentials for CuZn-alloys, Institut für Festkörperphysik, Karlsruhe.
- [87] L. Hedin and B. I. Lundqvist, “Explicit local exchange-correlation potentials,” *Journal of Physics C: Solid State Physics* **4**, 2064 (1971).
- [88] L. N. Cooper, “Bound Electron Pairs in a Degenerate Fermi Gas,” *Phys. Rev.* **104**, 1189–1190 (1956).
- [89] A. D. Christianson, E. A. Goremychkin, R. Osborn, S. Rosenkranz, M. D. Lumsden, C. D. Malliakas, I. S. Todorov, H. Claus, D. Y. Chung, M. G. Kanatzidis, R. I. Bewley, and T. Guidi, “Unconventional superconductivity in Ba_{0.6}K_{0.4}Fe₂As₂ from inelastic neutron scattering,” *NATURE* **456**, 930–932 (2008).
- [90] M. D. Lumsden, A. D. Christianson, D. Parshall, M. B. Stone, S. E. Nagler, G. J. MacDougall, H. A. Mook, K. Lokshin, T. Egami, D. L. Abernathy, E. A. Goremychkin, R. Osborn, M. A. McGuire, A. S. Sefat, R. Jin, B. C. Sales, and D. Mandrus, “Two-dimensional resonant magnetic excitation in BaFe_{1.84}Co_{0.16}As₂,” *Phys. Rev. Lett.* **102**, 107005 (2009).
- [91] X. Zhang, Y. S. Oh, Y. Liu, L. Yan, K. H. Kim, R. L. Greene, and I. Takeuchi, “Observation of the Josephson Effect in Pb/Ba_{1-x}K_xFe₂As₂ Single Crystal Junctions,” *Phys. Rev. Lett.* **102**, 147002 (2009).

-
- [92] C. T. Chen, C. C. Tsuei, M. B. Ketchen, Z. A. Ren, and Z. X. Zhao, “Integer and half-integer flux-quantum transitions in a niobium-iron pnictide loop,” *NATURE PHYSICS* **6**, 260–264 (2010).
- [93] T. Hanaguri, S. Niitaka, K. Kuroki, and H. Takagi, “Unconventional s-Wave Superconductivity in Fe(Se,Te),” *SCIENCE* **328**, 474–476 (2010).
- [94] J. ichi Shimoyama, “Potentials of iron-based superconductors for practical future materials,” *Superconductor Science and Technology* **27**, 044002 (2014).
- [95] M. Rotter, M. Tegel, and D. Johrendt, “Superconductivity at 38 K in the Iron Arsenide $(\text{Ba}_{1-x}\text{K}_x)\text{Fe}_2\text{As}_2$,” *Phys. Rev. Lett.* **101**, 107006 (2008).
- [96] A. F. Kemper, C. Cao, P. J. Hirschfeld, and H.-P. Cheng, “Effects of cobalt doping and three-dimensionality in BaFe_2As_2 ,” *Phys. Rev. B* **80**, 104511 (2009).
- [97] S. Drotziger, P. Schweiss, K. Grube, T. Wolf, P. Adelman, C. Meingast, and H. v. Löhneysen, “Pressure versus Concentration Tuning of the Superconductivity in $\text{Ba}(\text{Fe}_{1-x}\text{Co}_x)_2\text{As}_2$,” *J. Phys. Soc. Jpn.* **79**, 124705 (2010).
- [98] D. J. Singh, “Electronic structure and doping in BaFe_2As_2 and LiFeAs : Density functional calculations,” *Phys. Rev. B* **78**, 094511 (2008).
- [99] N. Ni, A. Thaler, J. Q. Yan, A. Kracher, E. Colombier, S. L. Bud’ko, P. C. Canfield, and S. T. Hannahs, “Temperature versus doping phase diagrams for $\text{Ba}(\text{Fe}_{1-x}\text{TM}_x)_2\text{As}_2$ (TM = Ni, Cu, Cu/Co) single crystals,” *Phys. Rev. B* **82**, 024519 (2010).
- [100] H. Wadati, I. Elfimov, and G. A. Sawatzky, “Where Are the Extra d Electrons in Transition-Metal-Substituted Iron Pnictides?” *Phys. Rev. Lett.* **105**, 157004 (2010).
- [101] R. Balian and N. R. Werthamer, “Superconductivity with Pairs in a Relative p Wave,” *Phys. Rev.* **131**, 1553–1564 (1963).
- [102] J. Annett, N. Goldenfeld, and S. R. Renn, “Interpretation of the temperature dependence of the electromagnetic penetration depth in $\text{YBa}_2\text{Cu}_3\text{O}_{7-\delta}$,” *Phys. Rev. B* **43**, 2778–2782 (1991).
- [103] A. P. Mackenzie and Y. Maeno, “The superconductivity of Sr_2RuO_4 and the physics of spin-triplet pairing,” *Rev. Mod. Phys.* **75**, 657–712 (2003).
- [104] A. V. Balatsky, I. Vekhter, and J.-X. Zhu, “Impurity-induced states in conventional and unconventional superconductors,” *Rev. Mod. Phys.* **78**, 373–433 (2006).
- [105] H. Alloul, J. Bobroff, M. Gabay, and P. J. Hirschfeld, “Defects in correlated metals and superconductors,” *Rev. Mod. Phys.* **81**, 45–108 (2009).
- [106] V. G. Kogan, “Pair breaking in iron pnictides,” *Phys. Rev. B* **80**, 214532 (2009).
- [107] P. J. Hirschfeld, M. M. Korshunov, and I. I. Mazin, “Gap symmetry and structure of Fe-based superconductors,” *Rep. Prog. Phys.* **74**, 124508 (2011).
- [108] P. Anderson, “Theory of dirty superconductors,” *J. Phys. Chem. Solids* **11**, 26 – 30 (1959).

- [109] A. Herbig, R. Heid, and J. Schmalian, “Charge doping versus impurity scattering in chemically substituted iron-pnictides,” arXiv:1510.06941v1 (2015).
- [110] J. P. Perdew and Y. Wang, “Accurate and simple analytic representation of the electron-gas correlation energy,” *Phys. Rev. B* **45**, 13244–13249 (1992).
- [111] R. Heid, (2015), Private communication: pseudopotentials for chemical substitutions in BaFe_2As_2 , Institut für Festkörperphysik, Karlsruhe.
- [112] “https://upload.wikimedia.org/wikipedia/commons/5/58/d_orbitals.png,” .
- [113] M. Merz, P. Schweiss, P. Nagel, M.-J. Huang, R. Eder, T. Wolf, H. von Löhneysen, and S. Schuppler, “Of Substitution and Doping: Spatial and Electronic Structure in Fe Pnictides,” *Journal of the Physical Society of Japan* **85**, 044707 (2016).
- [114] D. C. Johnston, “The puzzle of high temperature superconductivity in layered iron pnictides and chalcogenides,” *Advances in Physics* **59**, 803–1061 (2010).
- [115] A. Abrikosov and L. Gorkov, “Contribution to the Theory of Superconducting Alloys with Paramagnetic Impurities,” *Zhur. Eksptl. i Teoret. Fiz.* **39**, 1781 (1960).
- [116] M. Hoyer, M. S. Scheurer, S. V. Syzranov, and J. Schmalian, “Pair breaking due to orbital magnetism in iron-based superconductors,” *Phys. Rev. B* **91**, 054501 (2015).
- [117] R. M. Fernandes, M. G. Vavilov, and A. V. Chubukov, “Enhancement of T_c by disorder in underdoped iron pnictide superconductors,” *Phys. Rev. B* **85**, 140512 (2012).
- [118] J. Ziman, *Elements of Advanced Quantum Theory* (Cambridge University Press, 1975).
- [119] J. Sakurai, *Modern Quantum Mechanics revised edition* (Addison-Wesley Publishing Company, 1994).
- [120] F. Rullier-Albenque, D. Colson, A. Forget, and H. Alloul, “Hall Effect and Resistivity Study of the Magnetic Transition, Carrier Content, and Fermi-Liquid Behavior in $\text{Ba}(\text{Fe}_{1-x}\text{Co}_x)_2\text{As}_2$,” *Phys. Rev. Lett.* **103**, 057001 (2009).
- [121] H. Chen, Y. Ren, Y. Qiu, W. Bao, R. H. Liu, G. Wu, T. Wu, Y. L. Xie, X. F. Wang, Q. Huang, and X. H. Chen, “Coexistence of the spin-density wave and superconductivity in $\text{Ba}_{1-x}\text{K}_x\text{Fe}_2\text{As}_2$,” *EPL (Europhysics Letters)* **85**, 17006 (2009).
- [122] N. Ni, A. Thaler, A. Kracher, J. Q. Yan, S. L. Bud’ko, and P. C. Canfield, “Phase diagrams of $\text{Ba}(\text{Fe}_{1-x}\text{M}_x)_2\text{As}_2$ single crystals ($M = \text{Rh}$ and Pd),” *Phys. Rev. B* **80**, 024511 (2009).
- [123] K. Kirshenbaum, S. R. Saha, S. Ziemak, T. Drye, and J. Paglione, “Universal pair-breaking in transition-metal-substituted iron-pnictide superconductors,” *Phys. Rev. B* **86**, 140505 (2012).
- [124] A. Thaler, H. Hodovanets, M. S. Torikachvili, S. Ran, A. Kracher, W. Straszheim, J. Q. Yan, E. Mun, and P. C. Canfield, “Physical and magnetic properties of $\text{Ba}(\text{Fe}_{1-x}\text{Mn}_x)_2\text{As}_2$ single crystals,” *Phys. Rev. B* **84**, 144528 (2011).

-
- [125] P. F. S. Rosa, C. Adriano, T. M. Garitezi, M. M. Piva, K. Mydeen, T. Grant, Z. Fisk, M. Nicklas, R. R. Urbano, R. M. Fernandes, and P. G. Pagliuso, “Possible unconventional superconductivity in substituted BaFe_2As_2 revealed by magnetic pair-breaking studies,” *SCIENTIFIC REPORTS* **4** (2014), 10.1038/srep06252.
- [126] S. Jiang, H. Xing, G. Xuan, C. Wang, Z. Ren, C. Feng, J. Dai, Z. Xu, and G. Cao, “Superconductivity up to 30 K in the vicinity of the quantum critical point in $\text{BaFe}_2(\text{As}_{1-x}\text{P}_x)_2$,” *Journal of Physics: Condensed Matter* **21**, 382203 (2009).
- [127] P. Schweiss, Private communication: different As heights in P-substituted BaFe_2As_2 , Institut für Festkörperphysik, Karlsruhe.
- [128] “<https://www.vasp.at/>,” .
- [129] “<http://www.quantum-espresso.org/>,” .
- [130] “<http://www.netlib.org/blas/>,” .
- [131] “<http://www.netlib.org/lapack/>,” .
- [132] “<https://de.wikipedia.org/wiki/Trapezregel>,” .

Acronyms

This thesis contains a couple of acronyms. For better readability of this thesis, I tried to explain acronyms in every chapter anew. However, the most frequently used acronyms in this thesis are listed below.

AG	Abrikosov-Gorkov
BEB	Blackman, Esterling and Berk
BLAS	Basic Linear Algebra Subprograms
CPA	coherent potential approximation
DFT	density functional theory
DOS	density of states
FeSC	iron based superconductors
KKR	Kohn-Korringa-Rostoker
LAPACK	Linear Algebra Package
LCAO	linear combination of atomic orbitals
MBP	mixed-basis pseudopotential
MBPP	mixed-basis pseudopotential program
TM	transition metal
VCA	virtual crystal approximation

Danksagung

Diese Arbeit, die in den letzten drei Jahren entstanden ist, wäre ohne einige Personen so nicht zustande gekommen und ich möchte die Gelegenheit nutzen, diesen Personen zu danken.

Zunächst möchte ich mich bei Hilbert von Löhneysen für die Übernahme des Referats und dafür bedanken, dass er die Anfertigung dieser Arbeit am Institut für Festkörperphysik ermöglicht hat und ich mir während dieser Zeit keine Sorgen um meinen Lebensunterhalt machen musste (was leider nicht selbstverständlich ist).

Dann möchte ich mich bei Jörg Schmalian für die Übernahme des Korreferats, das Lesen dieses Manuskripts und einige hilfreiche Diskussionen und das Beisteuern einiger interessanter Ideen bedanken, die diese Arbeit von typischen *ab-initio* Arbeiten unterscheidet, insbesondere hinsichtlich der T -Matrix-Analyse.

Mein ganz besonderer Dank gilt meinem Betreuer Rolf Heid, der die entscheidende Idee zu dieser Arbeit hatte, mir bei der Methodenentwicklung mit seiner ganzen Erfahrung immer zur Seite stand und auch bei der Fehlersuche in der Testphase der Methode einen wichtigen Beitrag geleistet hat. Zudem möchte ich ihm für das Lesen dieses Manuskripts danken.

Weiterhin möchte ich mich bei Robert Eder bedanken, ohne dessen Ideen der impurity-solver und die Ladungsselbstkonsistenz wahrscheinlich heute noch nicht gut laufen würden und der die Idee zu dem Vergleich mit exakter Diagonalisierung hatte und das entsprechende Programm dazu beigesteuert hat.

Dann möchte ich mich bei Kai Grube, Frédéric Hardy, Roland Hott, Mareike Hoyer, Christoph Meingast, Michael Merz, Roland Schäfer, Mathias Scheurer, Stefan Schuppler, Peter Schweiss, Frank Weber und Diego Zocco für hilfreiche Diskussionen und Vorschläge bedanken.

Für die angenehme Arbeitsatmosphäre möchte ich allen Mitarbeitern am IFP danken, darunter besonders auch den "guten Seelen" des Instituts, allen voran Klaus-Peter Bohnen sowie Carmen Dörflinger und Otto Walz.

Den "jüngeren" (teilweise ehemaligen) IFP Mitarbeitern (vor allem Doktoranden und Diplomanden / Masterstudenten) Anna Böhmer, Philipp Burger, Felix Eilers, Mingquan He, Cornelia Hintze, Mareike Hoyer, Andreas Kapuvari, Maximilian Kauth, Sven Kranich, Sebastian Kuntz, Philipp Kurzhals, Michael Maschek, Matthias Mörtter, Aaron Sauer, Liran Wang und Karsten Wolff möchte ich für die schöne gemeinsame Zeit während der letzten drei Jahre und einige Kneipenabende und Feiern danken.

Dann gilt mein Dank noch der Dekanatssekretärin Regina Hühn für ihre unendliche Geduld und Hilfsbereitschaft.

Last but not least möchte ich noch meinen Eltern Rainer und Irene Herbig danken, insbesondere für die finanzielle Unterstützung während meines Studiums und die moralische Unterstützung während dieser Arbeit.